

2016

Catalytic upgrading of phenolic compounds using ceria-based materials

Nicholas Nelson
Iowa State University

Follow this and additional works at: <https://lib.dr.iastate.edu/etd>

 Part of the [Chemistry Commons](#)

Recommended Citation

Nelson, Nicholas, "Catalytic upgrading of phenolic compounds using ceria-based materials" (2016). *Graduate Theses and Dissertations*. 15983.

<https://lib.dr.iastate.edu/etd/15983>

This Dissertation is brought to you for free and open access by the Iowa State University Capstones, Theses and Dissertations at Iowa State University Digital Repository. It has been accepted for inclusion in Graduate Theses and Dissertations by an authorized administrator of Iowa State University Digital Repository. For more information, please contact digirep@iastate.edu.

Catalytic upgrading of phenolic compounds using ceria-based materials

by

Nicholas C. Nelson

A dissertation submitted to the graduate faculty
in partial fulfillment of the requirements for the degree of

DOCTOR OF PHILOSOPHY

Major: Chemistry

Program of Study Committee:
Igor I. Slowing, Co-Major Professor
Aaron D. Sadow, Co-Major Professor
Wenyu Huang
Marek Pruski
L. Keith Woo

Iowa State University

Ames, Iowa

2016

Copyright © Nicholas C. Nelson, 2016. All rights reserved.

TABLE OF CONTENTS

	Page
ACKNOWLEDGMENTS	iv
ABSTRACT.....	v
CHAPTER 1. INTRODUCTION	1
General Introduction	1
Structural Properties of Ceria and its Related Oxides	6
Synthesis of Ceria and Ceria-Based Materials.....	14
Ceria-Based Materials for Biomass Upgrading Reactions	23
Concluding Remarks.....	28
References.....	29
CHAPTER 2. SELECTIVE HYDROGENATION OF PHENOL CATALYZED BY PALLADIUM ON HIGH-SURFACE-AREA CERIA AT ROOM TEMPERATURE AND AMBIENT PRESSURE.....	42
Abstract.....	42
Introduction.....	43
Experimental.....	45
Results and Discussion	51
Conclusions.....	70
Acknowledgments.....	71
References.....	71
Appendix of Supporting Information.....	75
CHAPTER 3. TRANSFER HYDROGENATION OVER SODIUM-MODIFIED CERIA: ENRICHMENT OF REDOX SITES ACTIVE FOR ALCOHOL DEHYDROGENATION	83
Abstract.....	83
Introduction.....	83
Experimental.....	86
Results and Discussion	97
Conclusions.....	114
Acknowledgments.....	114
References.....	114
Appendix of Supporting Information.....	119

CHAPTER 4. STABILITY OF Pd/CeO ₂ CATALYST DURING TRANSFER HYDROGENATION: PRIMARY VS. SECONDARY ALCOHOLS	139
Abstract	139
Introduction.....	139
Experimental.....	141
Results.....	145
Discussion.....	152
Conclusions.....	155
Acknowledgments.....	156
References.....	156
Appendix of Supporting Information.....	159
 CHAPTER 5. PHOSPHATE MODIFIED CERIA AS A BRØNSTED ACIDIC/REDOX MULTIFUNCTIONAL CATALYST	 165
Abstract	165
Introduction.....	165
Experimental.....	168
Results and Discussion	174
Conclusions.....	190
Acknowledgments.....	191
References.....	191
Appendix of Supporting Information.....	197
 CHAPTER 6. CONCLUSIONS AND OUTLOOK	 204

ACKNOWLEDGMENTS

I express my sincere gratitude to Dr. Igor Ivan Slowing for providing me the opportunity to realize my goals. I would not be writing this today if it weren't for you. Your guidance and constant questioning clearly demonstrated how to be an effective mentor and scientist. I would also like to thank my committee members both past and present, Dr. Aaron D. Sadow, Wenyu Huang, Marek Pruski, Theresa Windus, and Keith Woo for their valuable time, support, instrument use, and collaborations.

I would like to thank my lab mates, past and present, for keeping things interesting. It was a pleasure working with you all. I would especially like to thank Sebastian for perspective on scientific matters and fruitful discussions pertaining to lab and life (P.S. you suck). I would also like to thank Dr. Ashley Dreis for her enthusiasm towards science that greatly influenced my own enthusiasm.

I would also like to thank my wife, April, for her continued love and support during our time in Ames. You have always been there for me and I appreciate that very much. Finally, I would also like to thank my parents for their unwavering love, kindness, and support throughout the years that allowed me to get to this point.

This work was supported by the U.S. Department of Energy (DOE), Office of Basic Energy Sciences, Division of Chemical Sciences, Geosciences, and Biosciences, through the Ames Laboratory Catalysis Science program. at the Ames Laboratory under contract number DE-AC02-07CH11358. The Ames Laboratory is operated for the DOE by Iowa State University. The document number assigned to this dissertation is IS-T 3190.

ABSTRACT

This dissertation describes the catalytic upgrading of phenolic compounds over ceria-based materials. The work was motivated by the need to find alternative industrial uses for the light rare earth elements (e.g. cerium) as part of the Critical Materials Institute. Cerium is typically encountered in the +3 or +4 oxidation state and its dioxide is the most technologically advanced cerium compound. Cerium dioxide (ceria) is best known for its ability to release and store oxygen, thereby acting as an oxygen buffer in many catalytic systems. The oxygen storage and release capability has been exploited in three-way catalysis and is one of the most industrialized uses of cerium. Traditionally, ceria has been explored for small molecule (e.g. CO) oxidation catalysis, while its utility as a catalyst for organic oxidations has been gaining attention. The unique oxygen-activating property of ceria has delayed its study as a catalyst component for reductive transformations.

Phenolics represent an interesting class of oxygenates for transformation over ceria-based materials. The chemistry of hydroxyl-containing compounds over ceria is well-studied and is often preceded by reactive adsorption to form activated intermediates. The economic importance of phenolics as precursors for nylon production and the oxygenate-activating ability of ceria-based materials provide a good starting point for determining alternative industrial uses for cerium. Furthermore, phenolics can be derived from renewable resources, an industrial sector that is expected to see large growth during the current century. Identifying active, selective, and environmentally friendly catalytic systems that convert biorenewable compounds into commodity chemicals is thus critical for ushering in the biorefinery era. The catalytic systems described here demonstrate ceria-based materials are active for the reductive transformation of phenolics using molecular hydrogen and aliphatic alcohols.

Palladium supported on high-surface-area ceria was found to effectively catalyze the hydrogenation of phenol to cyclohexanone at atmospheric pressure and room temperature under batch conditions. The activity was highly dependent on the catalyst prerduction temperature which led to optimization of Pd dispersion and metal-support interactions. Analogous to alkyl alcohols, phenol underwent dissociative adsorption on ceria to yield cerium-bound phenoxy and water. The phenoxy species were activated toward dearomatization by molecular hydrogen.

Palladium supported on high-surface-area ceria (Pd/CeO₂) and sodium-modified ceria (Pd/Ce-Na) were used as catalysts for the aqueous-phase transfer hydrogenation of phenol using 2-propanol under flow conditions. Both catalysts were active and showed constant activity for 7 days on-stream. Pd/Ce-Na showed a marked increase (6x) in transfer hydrogenation activity over Pd/CeO₂. Modification of ceria by sodium provided more 2-propanol adsorption sites and redox active sites (i.e. defects) for 2-propanol dehydrogenation which resulted in higher phenol transfer hydrogenation activity. For primary alcohols, reduction of the ceria support to form cerium hydroxy carbonate occurred and led to irreversible deactivation of the catalyst. A deactivation mechanism involving C-C scission of acyl and carboxylate intermediates to form CO was proposed.

Deposition of trimethylphosphate onto ceria followed by thermal treatment resulted in formation of surface phosphates with retention of redox activity. The introduction of phosphates generated Brønsted acidic sites and decreased the number of Lewis acidic sites on the surface. Upon deposition of Pd, the multifunctional material showed enhanced activity for phenolic hydrogenolysis compared to Pd on the unmodified ceria support. This was attributed to the cooperativity between the Lewis acid sites, which activate phenolics for dearomatization, and the redox/acid property, which catalyzes hydrogenolysis.

CHAPTER 1

INTRODUCTION.

General Introduction

The inevitable depletion of fossil fuels and the environmental controversies that surround their use makes it imperative to develop sustainable, economical, and efficient alternatives to the production of petrochemicals. Most carbon-based products pervasive in modern society are derived from petroleum sources and our continued reliance on them is problematic in many ways. Since the end of the 20th century, significant time and effort has been devoted to finding alternative resources and effective catalytic processes to curb our reliance on petroleum. The most noteworthy renewable sources of carbon that have large-scale capability are plants (i.e. biomass) and atmospheric carbon dioxide.¹ Of the possible options, biomass seems to be the most promising, sustainable, and carbon-neutral alternative to lessen our reliance on petroleum-based products mainly due to the infancy of CO₂ conversion technology.² Biomass is an umbrella term for organic matter derived from living or recently living organisms, and includes plant- and animal-based matter that can be converted into desired chemical products (i.e. platform molecules). The platform molecules may be used to derive economically important chemicals that are traditionally obtained from petroleum.³⁻⁴ The source of biomass is broadly categorized into food- and non-food-based biomass. First generation biomass refining or biorefinery plants typically use food-based sources to derive important chemicals (e.g. ethanol). However, this is undesirable because it compounds the food shortage problem through direct competition.⁵ Using non-food biomass for producing valuable chemical intermediates is thus far more appropriate towards developing sustainable alternatives to petroleum. Most non-food biomass is in the form of lignocellulose and the efficient degradation and separation of

lignocellulose into its constituents for chemical upgrading has been the focus of contemporary biomass research.

Lignocellulose is composed of carbohydrate polymers (cellulose and hemicellulose) and an aromatic polymer (lignin).⁶ The polysaccharide component (celluloses) is tightly bound to lignin through ester and ether linkages.⁶ This structure has evolved to impart hydrolytic stability and structure robustness to plant cell walls and is therefore highly recalcitrant to chemical modification.⁷ The efficient depolymerization of lignocellulose is therefore a significant hurdle that must be overcome before large-scale implementation as a substitute for petroleum-based products is achieved.⁷ Polysaccharide upgrading technology is significantly further along than lignin upgrading due to it constituting the bulk of biomass (70-85 wt. %) and the well-known chemistry for transformation of carbohydrates.² Once separated from lignin, the polysaccharides can be depolymerized into C5 (hemicellulose) and C6 (cellulose) sugars through acid-catalyzed hydrolysis to yield valuable platform molecules that are poised for catalytic upgrading (Figure 1). The lignin component is often more recalcitrant and harsher conditions are needed to depolymerize it.

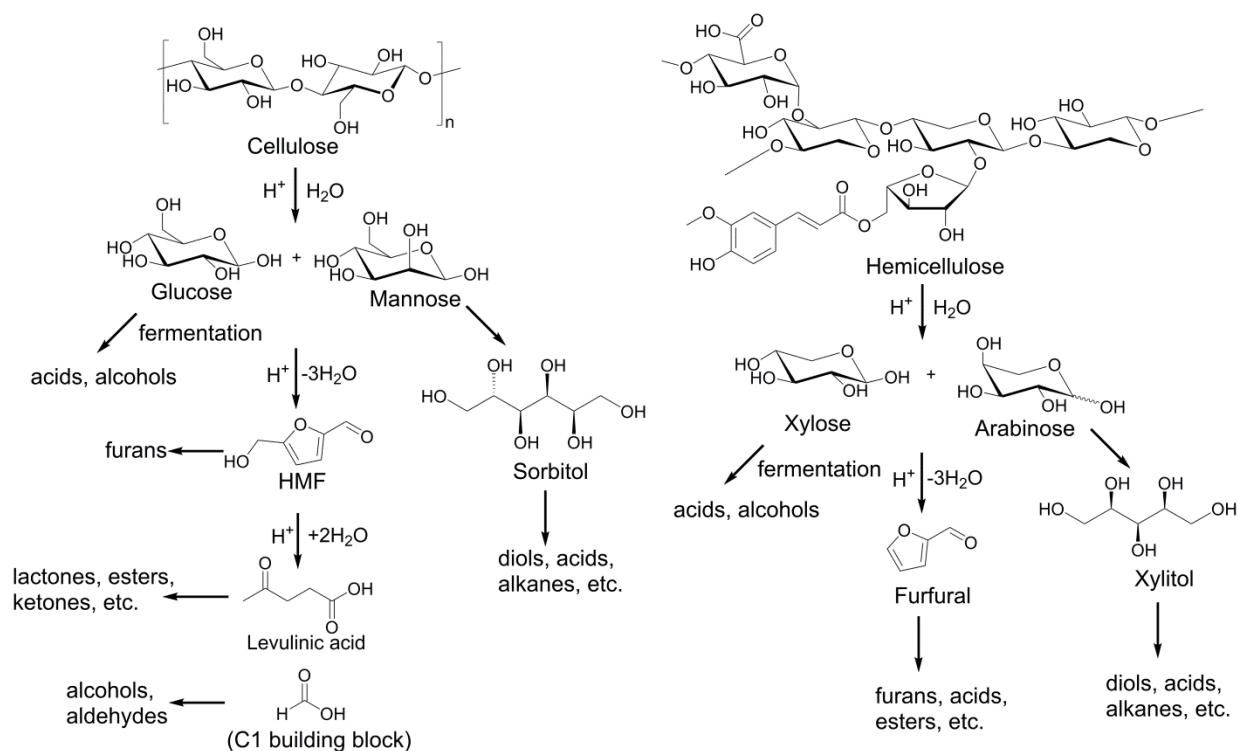


Figure 1. Platform molecules derived from the hydrolysis of polysaccharides and their possible chemically upgraded products.²

Lignin is a heterogeneous, alkyl-aromatic amorphous polymer comprised of methoxylated phenylpropane.⁸ The lignin fraction of lignocellulose constitutes about 15-30 wt. % depending on the source and is typically underused as a chemical feedstock.⁹ Lignin is mainly a by-product of the paper industry and within this context finds niche uses in low-value markets with the majority of it burned as a low-value fuel for industrial plant processes.⁷ Its inherent heterogeneity and recalcitrance make it difficult to depolymerize and separate into smaller compounds that can be catalytically upgraded to high-value chemicals and fuels. Because of this, lignin waste production is expected to increase with the onset of lignocellulose biorefineries.¹⁰ Even though lignin represents a minor component of lignocellulose, its efficient utilization could have major economic impact for the production of fuels and specialty chemicals due to its unique aromatic structure.¹¹ In fact, lignin is the only large-scale renewable source of aromatics from

which many important commodity chemicals can be derived and its valorization remains a significant, yet promising challenge.⁷ The lignin structure is believed to originate from the random polymerization of p-coumaryl alcohol, coniferyl alcohol, and sinapyl alcohol (Figure 2a).¹² Figure 2b shows a pictorial structure of lignin with typical bonding patterns that are representative for the various sources of lignin.¹³⁻¹⁴ Given the rich aromatic structure, lignin chemical conversion into valuable aromatics (e.g. benzene, anisole, phenol, etc.) has been the subject of numerous investigations.¹⁵⁻¹⁶ The obvious and urgent needs for more sustainable chemical processes will likely lead to the development of lignin-based technologies and allow it to become a significant source of renewable aromatics.¹⁷ However, in order to take full advantage of renewable aromatic feedstocks, sustainable and economical downstream processes that selectively convert lignin/lignocellulose depolymerization products into high-value commodity chemicals need to be developed in concert.

A wide range of heterogeneous catalysts and catalytic processes have been developed for lignocellulose upgrading to platform molecules.¹⁸⁻²⁰ Unlike the catalysts used for petroleum upgrading that are optimized to introduce functionality, catalysts for lignocellulose platform molecules often need to reduce functionality, especially as it pertains to fuel and monoaromatic production.¹⁹ Although some guidance can be offered from the catalysts and catalytic systems used in petroleum upgrading, new catalysts must be developed for lignocellulosic platform molecule conversion into high-value specialty chemicals. The biorefinery concept calls for the development of catalytic systems that keep with the green metrics (e.g. green solvents, energy non-intensive, earth abundant materials, etc.) and show high selectivity for specific bonding motifs to lessen the burdens associated with separation. Chemical upgrading usually involves reforming, hydrogenolysis, hydrogenation, oxidation, hydrolysis, and C-C coupling reactions

among others. Given the large number of platform molecules that can be derived from lignocellulose and the even larger number of chemical pathways leading to desired products, catalysts exhibiting multifunctional properties are preferred.²¹ Multifunctional materials can provide increased catalytic activity, modify selectivity, improve catalyst stability, and allow for tandem processes to occur that eliminate synthetic steps.^{18, 22} Therefore, significant effort must be focused on identifying these catalytic systems for efficient upgrading technologies.

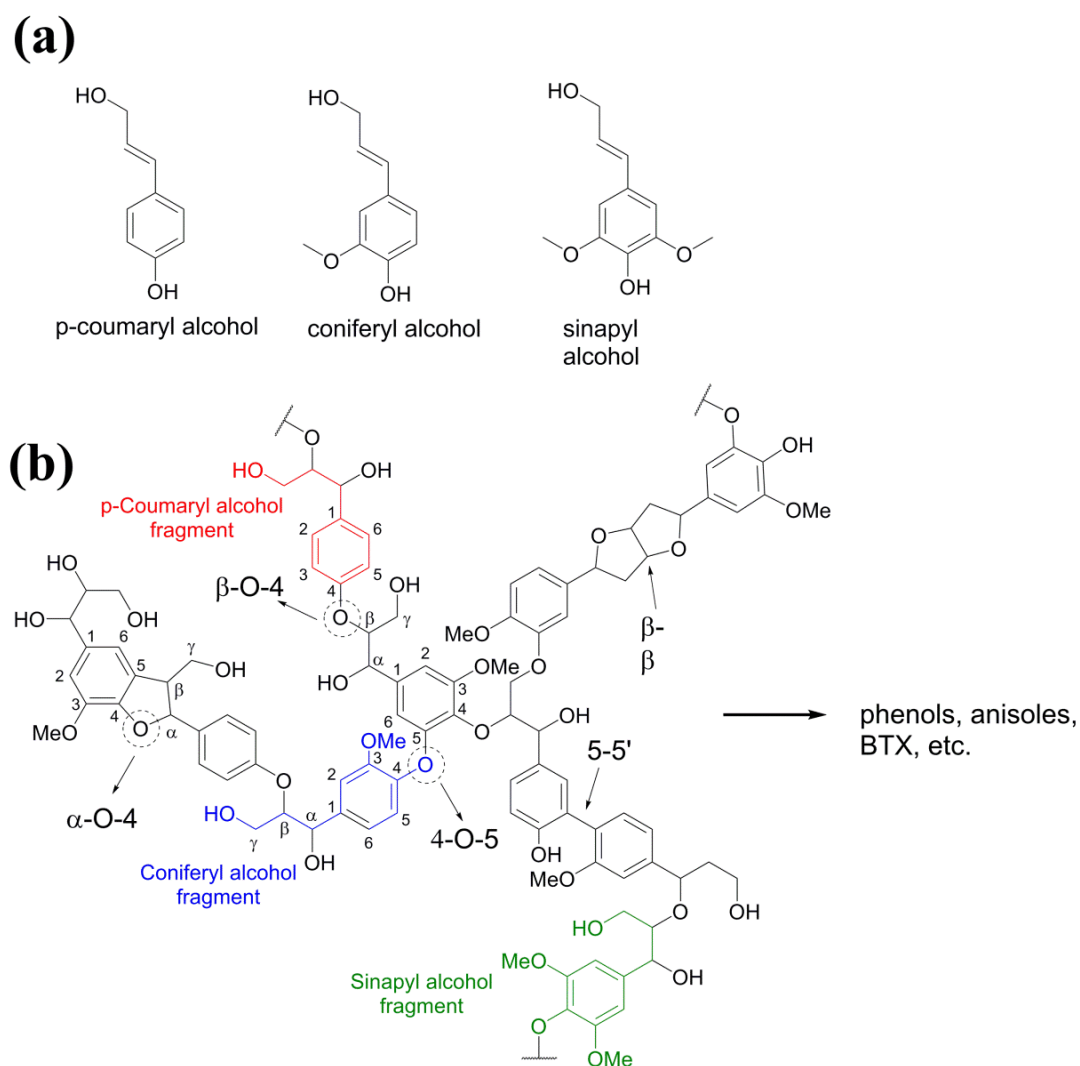


Figure 2. (a) Monolignols that provide the framework for lignin. (b) Representative structure of lignin with some common bonding motifs.¹³⁻¹⁴

This thesis describes the efforts made towards converting phenolic compounds into valuable chemical intermediates over ceria-based catalysts. Phenolic compounds are prevalent depolymerization products of lignin²³⁻²⁴ and are valuable precursors for plastics and pharmaceutical compounds.²⁵ Therefore, continued development of highly active, selective, and environmentally friendly catalysts that transform phenolics under milder conditions than their industrial analogs is needed to help usher in the biorefinery era. Ceria is a redox active rare-earth oxide most notably known for its ability to release and store oxygen. Because of this property, ceria has found widespread use in oxidation catalysis. Under reducing environments (e.g. H₂), ceria readily loses lattice oxygen and becomes an oxygen sink that can promote deoxygenation reactions.²⁶ Furthermore, supporting transition metals onto ceria can result in unique, synergistic interactions between the metal and support that endow the material with activity towards other hydrotreating reactions.²⁷⁻²⁸ In order to understand the role that ceria-based catalysts can play in biorefineries, an understanding of the structural and chemical properties must precede its use.

Structural Properties of Ceria and Its Related Oxides.

Cerium is the most abundant rare-earth lanthanide element and is mainly recovered from bastnäsite, monazite, and loparite minerals.²⁷ The most widely known use for metallic cerium is in mischmetal alloy used for lighter flints and other metallurgy applications.²⁷ Due to its high reactivity, cerium is often utilized in one of two valence states, Ce(III) and Ce(IV). Many cerium-based applications are related to the ability of cerium to cycle between the Ce³⁺ and Ce⁴⁺ oxidation states. This phenomenon is most widely recognized in cerium(IV) dioxide (CeO₂, ceria) and therefore can be a valuable catalyst, co-catalyst, or promoter in organic transformations, especially those that involve redox chemistry.

Ceria finds many uses in large-scale commodity chemical manufacturing processes. For instance, ceria is used as a catalyst component in refinery operations to convert crude oil into lower molecular-weight fractions, a process called fluid catalytic cracking (FCC).²⁹ It is also used to promote the dehydrogenation of ethylbenzene to styrene and the ammoxidation of propylene to acrylonitrile.²⁹ Perhaps the most significant technological application is the ability of ceria to act as an oxygen reservoir for vehicle emission control.³⁰ This is related to the relative ease with which cerium can cycle between its oxidation states allowing it to promote the oxidation of hydrocarbons and carbon monoxide found in vehicle exhaust. In relation, ceria has been gaining attention for its ability to reduce particle emissions in diesel and also to control sulfur oxide emissions.³⁰ Ceria and its analogs have also been studied as solid electrolytes for solid oxide fuel cell applications due to the high oxygen ion conductivity of doped ceria.³⁰ The chemistry of ceria and ceria-related materials is diverse due to the unique structural and chemical properties of ceria, its ability to incorporate an extensive list of heteroatoms into the lattice, and its unique interaction with supported transition metals.²⁷⁻²⁸ This section will primarily deal with the structural aspects of ceria and its related oxides.

Cerium oxide can exist as a sesquioxide (Ce_2O_3), dioxide (CeO_2), or as an intermediate oxide between the two extremes (CeO_x , $1.5 \leq x \leq 2$). Cerium(III) oxide forms a hexagonal crystal structure ($P32/m$, $a=0.389$ nm, $c=0.607$ nm) upon reduction of CeO_2 ,³¹ while other forms of the sesquioxide are known to exist.³²⁻³⁵ Cerium(IV) oxide crystallizes in the cubic fluorite structure ($Fm3m$, $a=0.541134$ nm)²⁷ and is the most common oxidic phase encountered. The fluorite structure of ceria is characterized by a face-centered-cubic (f.c.c.) array of cerium atoms that are coordinated by eight equivalent nearest-neighbor oxygen anions (Figure 3a). The oxygen atoms fill all tetrahedral holes of the cationic sub-lattice and are coordinated by four equivalent

nearest-neighbor cerium cations. Alternatively, the unit cell can be redrawn to form a primitive cubic array of oxygen atoms which clearly shows the eight-coordinate sites are alternatively empty (Figure 3b). This is believed to impart ceria with unique properties, especially as they pertain to oxygen mobility and incorporation of dopants.²⁷

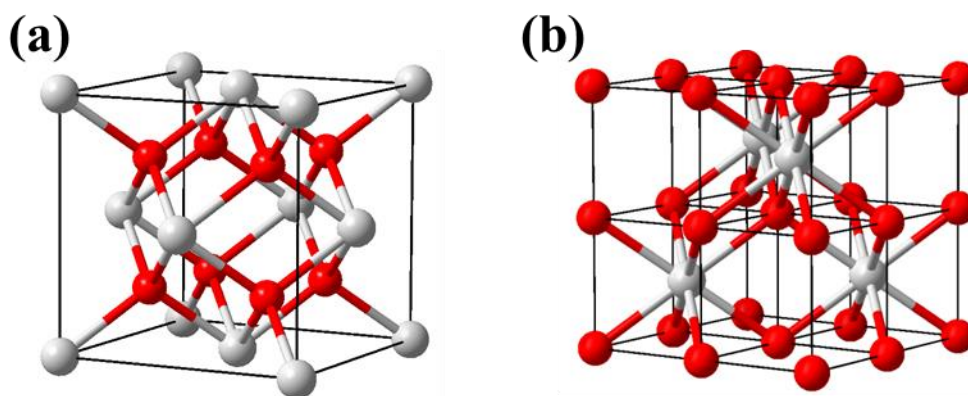
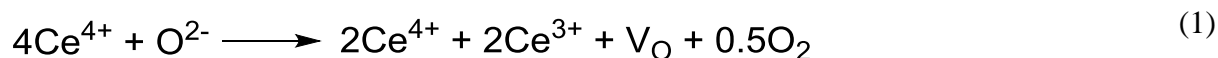


Figure 3. (a) CeO₂ unit cell constructed as f.c.c. array of cerium atoms. (b) Redrawn as a primitive cubic array of oxygen atoms.

The higher oxides of ceria (CeO_x, $x \geq 1.714$) can be prepared from the removal of O²⁻ anions through thermal treatment under reducing conditions (e.g. H₂) or through thermal treatment at low oxygen pressures according to the following reaction scheme (Eq 1):



where V_O represents a vacancy formed from the removal of lattice O. Charge balance is maintained from the removal of lattice O by reduction of two cerium cations. Several studies have indicated that CeO₂ exhibits a continuum of oxygen-deficient, non-stoichiometric disordered phases above 685 °C.^{32, 36-37} Upon cooling, these amorphous phases become ordered into a series of fluorite-related phases with compositions ranging from CeO_{1.714} to CeO₂.

Throughout this composition range the cerium and oxygen atoms remain essentially in the same position as shown in Figure 3, but much of the cubic symmetry is lost due to oxygen removal, and at certain stoichiometric ratios (e.g. $\text{CeO}_{1.714}$) can result in the ordering of oxygen vacancies.³⁸ The lower oxides of ceria (i.e. CeO_x , $1.5 \leq x \leq 1.714$) give rise to a non-stoichiometric phase (σ) at high temperatures that crystallize into a body-centered cubic type-C rare earth oxide.²⁷ The end member of the non-stoichiometric σ -phase forms the C-type sesquioxide ($\text{CeO}_{1.50-1.53}$) that crystallizes in the bixbyite structure where oxygen atoms occupy three quarters of the octahedral holes.³⁹ The formation of the C-type sesquioxide over the A-type (hexagonal) has been suggested to be favored upon reducing the size of ceria crystallite to 1.5 nm.³⁹ The result is consistent with the stabilization of vacancies on the surface as compared to the bulk⁴⁰ and the higher propensity for reduction of small ceria crystallites.⁴¹ The stabilization mechanism for small ceria crystallites gives rise to unique material properties that can be exploited for redox applications.

Defects are an important intrinsic property of ceria and their presence is closely related to the redox properties. Thus, elucidation of their structure and formation mechanism are valuable for the design of materials with high defect concentrations and to understand their role during chemical processes. Defects arising from thermal disorder or redox processes occurring on the surface are described as intrinsic, while those resulting from doping are considered extrinsic.²⁷ The intrinsic defects generated from thermal disorder can be described as either Schottky- (Eq. 2) or Frenkel- (Eqs. 3 and 4) type and are represented using Kröger and Vink⁴² point defect notation:





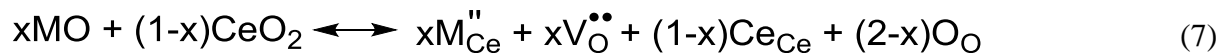
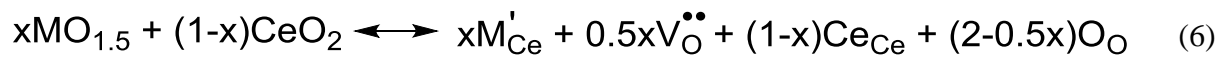
where Ce_{Ce} and O_O represent cerium and oxygen at their respective lattice sites, V_{Ce} and V_O represent a cerium and oxygen vacancy, and Ce_i and O_i represent a cerium and oxygen at an interstitial position. The effective charge is expressed in terms of the charge normally present in the same position in the host lattice and is indicated by a dot (\bullet) and a prime ($'$) for each positive and negative charge, respectively. The most energetically accessible defect is of the anion Frenkel variety⁴³ and is often the dominant defect in bulk, polyhedron ceria.²⁷ The defect does not result in stoichiometric deviation and is seemingly related to the oxygen storage capacity and mobility of ceria and its analogs.⁴⁴⁻⁴⁵ Defects arising through redox processes occurring on the surface of ceria are often associated with the removal of lattice oxygen. In this case, ceria becomes anion-deficient and charge balance must be compensated for by introduction of two electrons. Previous studies have shown that the lattice parameter of ceria increases as the degree of non-stoichiometry increases even when corrected for thermal dilation.⁴⁶⁻⁴⁷ The lattice expansion is attributed to the formation of the larger Ce^{3+} upon removal of oxygen. Furthermore, X-ray⁴⁸ and neutron⁴⁹ diffraction studies showed that the cerium cationic sublattice is not strongly perturbed upon removal of oxygen, while strong perturbation of the oxygen sublattice is observed. The data put forth suggests that the charge compensating mechanism for non-stoichiometry in ceria is accomplished through the reduction of two Ce cations from +4 to +3 for each lattice oxygen removed (Eq. 5). This can be represented through Kröger-Vink notation as:



Although Eq. 5 suggests the defects formed upon removal of lattice oxygen are isolated, their formation results in the expansion of Ce atoms around the oxygen-vacant site accompanied by contraction of oxygen atoms around the vacancy.³⁸ The structural rearrangement or defect cluster eventually leads to ordering of vacancies for CeO_{1.714}. Esch *et al.*⁵⁰ used high-resolution scanning tunneling microscopy and density functional calculations to unravel the local structure of surface and subsurface oxygen vacancies on the (111) surface. On the slightly reduced surface, single vacancies corresponding to surface and subsurface were the dominant defects and found to be in equal proportions. The vacancies were shown to result in relaxation of the surface structure through the expansion Ce cations and contraction or outward relaxation of O anions depending on the type of single vacancy. At higher non-stoichiometry linear surface oxygen vacancy clusters were formed. The vacancy clusters expose Ce³⁺ cations and the adjacent cerium cations remain as Ce⁴⁺. The authors suggest that the removal of a subsurface oxygen vacancy is a prerequisite to the formation of vacancy clusters. The presence and concentration of vacancies or vacancy clusters is often correlated with enhanced redox property and catalytic activity.

The fluorite structure of ceria can tolerate a wide range of metal dopants due to the open structure (Figure 3) with concomitant introduction of extrinsic defect sites. Incorporation of zirconium into the ceria lattice to form a continuum of ceria-zirconia mixed oxides is the most widely studied ceria-doped system. Ceria-zirconia mixed oxides are known to retain their redox properties under high temperature conditions, while significant redox inhibition is observed for ceria under similar conditions.⁵¹ Zirconium is valence isoelectronic with cerium and its incorporation does not necessitate the formation of charge-compensating vacancies. The enhanced redox thermal stability of ceria-zirconia mixed oxides has been associated with the stability of anionic Frenkel defects (Eq. 4).⁴⁴ For ceria, the Frenkel defects annihilate at high

temperature, while for ceria-zirconia there appears to be a high activation barrier for this process. This is possibly due to the restriction of oxygen interstitials to tetrahedral sites caused by the smaller zirconium cations. Interestingly, the presence of extrinsic oxygen vacancies were observed for ceria-zirconia mixed oxides even though zirconium is valence isoelectronic with cerium. This again was attributed to the smaller ionic radius of zirconium eliminating the strain associated with forming the larger Ce^{3+} .⁴⁴ The ceria-zirconia mixed oxide system reflects that extrinsic vacancies can be formed upon valence isoelectronic doping of ceria due to subtle size/strain effects. Ceria doped with aliovalent metals (M^{2+} and M^{3+}) has been achieved using transition,⁵² alkaline earth,⁵³ and rare earth metals.⁵⁴ In this instance, incorporation of the heteroatoms into the ceria framework does necessitate the formation of charge-compensating vacancies. The preferred charge-compensating mechanism is related to the formation of oxygen vacancies.^{43, 55-56} The charge compensation mechanism for tri- (Eq. 6) and di-valent (Eq. 7) cation dopants can be written as:



Introduction of aliovalent heteroatoms into the ceria framework can result in enhanced redox properties through the formation of charge-compensating vacancies that increase the number of defect sites and thereby promote redox chemistry.⁵⁷⁻⁶⁰ The ease with which cerium cation can cycle between its oxidation states appears to not only be related to the concentration of vacancies,⁴¹ but also to the size of the heteroatom dopant.⁶¹ That is, for a fixed dopant level or oxygen vacancy concentration, larger dopant ions (e.g. Ca^{2+} , La^{3+}) may better accommodate the

strain associated with the formation of the larger Ce^{3+} cation upon reduction. The oxygen mobility is also enhanced upon aliovalent doping by providing a more open framework (due to oxygen vacancy formation) allowing facile oxygen diffusion from the bulk to the surface.⁶²⁻⁶³ This phenomenon is closely related to the redox ability, especially when a continuous supply of active oxygen species from the bulk to the surface is needed under oxygen poor conditions. Aliovalent-doped ceria materials have also been observed to enhance ionic conductivity through oxygen vacancy formation making them interesting materials for solid state conductor applications.⁶⁴

The defect chemistry of ceria dominates its redox properties. As such, unraveling the local structure of defect sites and their oxidation properties has been the subject of numerous investigations. Notably, Onishi *et al.*⁶⁵⁻⁶⁶ probed the defect sites of well-outgassed and partially reduced ceria through O_2 adsorption monitored by infrared spectroscopy. Adsorbed superoxide species were observed for both samples while peroxide species were also observed for the partially reduced ceria sample. The results imply that there are one- and two-electron defect sites on the surface of ceria and that the degree of non-stoichiometry dictates the population of the defects. Similarly, d'Itri *et al.*⁶⁷ studied adsorbed dioxygen on ceria reduced with H_2 and CO through *in situ* Raman spectroscopy. They provided spectroscopic evidence for the formation of planar bridging and η^1 superoxo dioxygen species. The peroxide species were suggested to form non-planar bridging and η^2 peroxo species. In addition, they were able to distinguish between peroxide species adsorbed on isolated and aggregated two-electron defect sites. Using CO oxidation as a probe molecule, they observed that adsorbed superoxide species (i.e. one-electron defect sites) were more active for low temperature CO oxidation than two-electron defect sites. Superoxide species were also observed to be active for low temperature CO oxidation in ceria-

zirconia mixed oxides⁶⁸ and gold supported on ceria.⁶⁹ Overbury and Wu⁷⁰ probed the defect sites of ceria with specific surface terminations through O₂ adsorption. They observed that both the quantity and quality of defect sites were dependent on the surface termination. Intrinsic defects were most abundant and clustered on particles with (110) surface termination and least abundant and clustered on the (111) surface. In addition, superoxides were not formed on the (100) and (111) surfaces. The results are consistent with the CO oxidation activity over the different surfaces.⁷¹⁻⁷² Finally, Ramaswamy *et al.*⁷³ studied the defect sites of ceria with electron paramagnetic resonance and correlated the concentration of one-electron defect sites to the activation temperature for ethylbenzene oxidative dehydrogenation with nitrous oxide. The results suggested that the one-electron defect sites are responsible for the activation of α and β -hydrogen of ethylbenzene. The aforementioned studies correlate defect structure to catalytic activity and can aid in the rational design of ceria-based materials for redox catalysis.

Synthesis of Ceria and Ceria-Based Materials.

Cerium dioxide can be easily prepared through thermal treatment (i.e. pyrolysis) of cerium salts in air to afford the oxide with cubic fluorite structure.⁷⁴⁻⁷⁵ This is most often accomplished through the use of cerium salts that undergo pyrolysis to yield ceria and gas (e.g. Ce(NO₃)₃). Although this method is straightforward and simple, it can lead to bulk-like materials whose properties are often correlated to low activity in catalytic applications. Controlling the size and shape of ceria and related materials on the nanometer scale can lead to increased surface area, defect-enriched surfaces, and facet-dependent phenomena. These morphology-controlled synthetic procedures have proven to be a fruitful approach for the design of ceria-based materials with distinctive properties relative to their bulk and polyhedron counterparts. This section

highlights research efforts focused on the controlled synthesis and assembly of ceria and ceria-based materials and how the specific morphologies dictate material properties.

The synthesis of ceria can be achieved by a wide variety of methods.⁷⁶⁻⁸¹ Typically, an alkali solution is added to a Ce(III) or Ce(IV) salt to promote hydrolysis which affords the Ce(III) or Ce(IV) hydroxide.²⁷⁻²⁸ Sodium hydroxide⁸²⁻⁸³ and ammonia⁸⁴⁻⁸⁵ are the two most common precipitating agents used, but others, such as urea⁸⁶ and sodium carbonate⁸⁷, have also been employed. The metal hydroxide can be readily oxidized and/or dehydrated by thermal treatment under oxygen or air (i.e. calcination) to afford cubic fluorite ceria. This synthetic approach affords small (<50 nm), isotropic polycrystalline ceria particles whose size can be heavily influenced by the calcination temperature (>400 °C) used in order to improve crystallinity and/or remove surface impurities.⁸⁸ The precipitation route primarily leads to (111) terminated ceria particles in the absence of suitable ligands/conditions that can selectively control the exposed crystal planes. However, given the polycrystalline nature of the materials prepared via precipitation, there is undoubtedly other surface terminations present, although far less prevalent than the (111).^{70, 89} Related synthetic procedures for the formation of ceria include hydrothermal^{54, 89}, solvothermal⁷³, sonochemical⁹⁰, solution combustion⁹¹⁻⁹², sol-gel⁹³⁻⁹⁴, microwave⁹⁵, and microemulsion methods⁹⁶⁻⁹⁷. Considering the facile formation of ceria, the aforementioned methods and their variations are devised to invoke unique material characteristics that may impart increased activity during chemical transformations. In many cases, the desired characteristics are enrichment of defects and high surface-to-volume ratio which can be achieved by decreasing the particle/crystallite size and/or imparting the material with well-defined structure (e.g. pores and shape).

Perhaps the most widely known size-dependent phenomenon is the ability to tune the bandgap of inorganic semiconducting materials by controlling the physical size of the semiconductor crystal.⁹⁸ The above-mentioned synthetic procedures used to prepare ceria can be manipulated to attain size selectivity through judicious choice of reaction temperature⁸⁵, solvent⁹⁹, time¹⁰⁰, surfactant¹⁰¹, precursor¹⁰², etc. For instance, Zhang and coworkers¹⁰³ prepared sub-5 nm colloidal ceria particles via a polyol method. The colloids exhibited size-dependent optical properties showing a 0.35 eV reduction of the band gap relative to bulk ceria (3.54 eV). Similarly, Ghosh and coworkers⁸⁴ were able to prepare 2.3 nm ceria nanoparticles through ammonia precipitation of cerium(III) nitrate in a mixed glycol-water solvent. They observed a significant decrease (1.29 eV) of the nanoparticle band gap relative to bulk ceria. These two examples indicate that the band gap of ceria is size-dependent, but does not obey the traditional quantum confinement effect which usually results in an increase of the band gap with decreasing particle size. However, the simple quantum size effect assumes no significant dependence of the chemical structure on size.¹⁰⁴ Several studies have shown that the surface structure of ceria undergoes substantial changes as the size of the particle decreases, especially below 10 nm. Wu et al.¹⁰⁵ measured the Ce³⁺ content of ceria particles with varying diameters through the white-line ratios (M_5/M_4) of the electron energy loss spectra (EELS). The fraction of Ce³⁺ ions in the particle were found to increase with decreasing particle size below about 15 nm. It was also observed from the EELS spectrum that the reduction of cerium ions occurs mainly at the surface, forming a CeO_{1.5} layer and leaves the core essentially as CeO₂. Quite remarkably, they observed complete reduction of ceria to CeO_{1.5} for particle diameters below 3 nm while retaining the cubic fluorite structure. The increased Ce³⁺/Ce⁴⁺ ratio as the particle size decreases has also been corroborated by other groups.¹⁰⁶⁻¹⁰⁹ Tsunekawa¹¹⁰ proposed that the enrichment of Ce³⁺ as the

ceria particle size decreases was due to lattice relaxation through removal of half surface oxygen and a lower nominal valence from -2 (O^{2-}) to -1 (O_2^{2-}). This model agreed well with the observed lattice constant change and implies that the cause of the lattice relaxation is due to the formation of peroxides on the inner surface. In any case, the band gap redshift observed for small ceria particles is not due to the quantum confinement effect itself, but to the existence of Ce^{3+} on the surface of the material.¹¹¹ The enrichment of surface Ce^{3+} implies the formation of vacancies which can alter the properties of the material especially as they pertain to redox ability.

It is very well known that the propensity of ceria to facilitate redox reactions is directly related to the amount of defect sites present. Thus, the enrichment of surface Ce^{3+} through formation of oxygen vacancies (i.e. defects) can be controlled by tuning the polyhedron particle size and has led to enhanced reactivity for chemical conversion. For instance, Colvin^{102, 112} and coworkers prepared 3-10 nm diameter ceria colloids coated with a thin stabilizer (e.g. polyacrylic acid) and their activity for hydrogen peroxide disproportionation was monitored. They observed increased activity as the particle size decreased and this size-dependent trend was correlated with the amount of surface Ce^{3+} . The higher activity of the smaller ceria particles was attributed to the higher concentration of Ce^{3+} , thus providing more active sites for the Ce^{3+}/Ce^{4+} redox cycle. Another example of ceria particle size-activity relationship was shown by Adachi.⁹⁷ In this study, ceria particles with average diameters from 2.6-4.1 nm were prepared using a microemulsion method and their activity tested for carbon monoxide (CO) oxidation. Their alumina supported nanoparticulate ceria showed a lower temperature to achieve 50 % conversion of the CO stream compared to their bulk-like precipitated counterpart. The enhanced activity was again attributed to a higher concentration of redox active sites due to the small particle size. The ability to control the amount of defect sites on the surface of ceria by size manipulation has proven to be a

valuable approach towards increasing the catalytic activity in many systems. However, ceria is notoriously known for its facile ability to crystallize at high temperatures and can result in the coalescence of small particles which often leads to decreased catalytic activity through defect healing and decreased surface area. Thus, synthetic methods that impart ceria-based materials with permanent porosity (i.e. high surface area) through strict geometric control are necessary.

High surface area materials are desirable for many applications. In theory, the activity of a material exhibiting high surface area should be enhanced relative to its low surface area counterpart due to higher amounts of exposed surface atoms that dictate heterogeneous catalytic processes. Enhancement of surface area is typically achieved through use of surfactants which provide the template for precursor self-assembly. Post-synthesis removal of the surfactant by various means results in void spaces and therefore enhances the number of surface atoms exposed. In many cases, the presence of surfactants within a synthetic procedure will lead to enhanced surface area, but perhaps more desirable (and difficult) is to prepare materials with atomic and structural order through self-assembly processes. Interest and progress in this research field has exploded since the discovery of ordered mesoporous silica in the early 1990's¹¹³⁻¹¹⁴ and has led to the development of other structurally ordered materials (e.g. MOF, COF, etc.).¹¹⁵⁻¹¹⁶ The two most common approaches for introducing structural order is through molecular self-assembly using structure-directing agents (i.e. supramolecular assembly) or through the self-assembly of individual particles.¹¹⁷ The two approaches have been utilized to synthesize ceria-based materials with ordered structures whose nanocrystal assemblies can lead to non-additive properties. Structural ordering can allow control over chemical processes (e.g. catalysis, separation, etc.) by tuning pore dimensions and also provides a unique platform to study the effect of confinement on elementary processes.¹¹⁸⁻¹²² The specific arrangement of

particles to form hierarchical structures can also result in unique properties not observed in the bulk.¹⁰⁴

The inherent difficulty for the supramolecular self-assembly approach for structurally ordered ceria lies within the ability of ceria to crystallize or sinter at modest temperatures (<400 °C). The crystallization process is desirable and necessary to form cubic fluorite oxide from the inorganic-organic matrix. However, the temperatures needed for crystallization and pore wall densification, which provides structural integrity, often leads to crystallite growth. This can have detrimental effects on the structural order. Lyons *et al.*¹²³ were able to sufficiently control the reaction and calcination conditions to prevent structural degradation using the neutral surfactant hexadecylamine and cerium(III) acetate precursor. After the initial crystallization and densification the material retained its structural integrity at temperatures up to 600 °C. The formation of stable mesoporous phases was said to relate to low temperature removal of templating molecules and the use of cerium acetate to direct wall condensation. Considering the inherent difficulties of forming structurally-ordered ceria mentioned previously, the incorporation of heteroatoms within the ceria matrix has been used to reduce the facile crystallite growth upon organic template removal and pore wall densification. Ceria-zirconia mixed oxides are known for their enhanced oxygen uptake/release properties and their thermal stability under high temperature conditions (>600 °C) relative to ceria. These properties make it desirable and feasible to fabricate nanostructures with ordered structures.¹²⁴⁻¹²⁵ Yuan *et al.*¹²⁶ were able to develop a sol-gel evaporation-induced self-assembly process to synthesize ordered 2D hexagonal mesoporous $\text{Ce}_{1-x}\text{Zr}_x\text{O}_2$ ($x = 0.4-0.8$) solid solutions with crystalline walls. The mixed oxides were stable up to 600 °C and exhibited high surface area ($100-130 \text{ m}^2 \text{ g}^{-1}$) with pore sizes ranging from 3.2-3.7 nm.

The other commonly encountered approach to synthesize ceria and ceria-based materials with structural order is through self-assembly of preformed ceria crystallites. The advantage of this approach over supramolecular self-assembly is that the ceria building block size and shape can be controlled prior to the self-assembly process. By employing this strategy 2D and 3D structures can be obtained with unique properties. Corma *et al.*¹⁰⁴ were able to prepare high-surface-area, thermally stable, mesostructured ceria through self-assembly of individual 5 nm ceria particles using a solution-based method and nonionic surfactant. The material showed well-defined hexagonal symmetry with wall thickness of 6 nm. The similarity of wall thickness and nanoparticle diameter indicated an assembly process involving a monolayer of individual particles. The assembly displayed a unique photovoltaic response not observed in bulk ceria and operational organic-dye-free solar cells were constructed using the material as the active component. In a similar approach, Chane-Ching *et al.*¹²⁷ self-assembled 5 nm ceria particles using aminocaproic acid. The bifunctional amino acid was able to interact with the ceria particle and surfactant through the carboxylic acid and amine, respectively. The procedures outlined above are non-trivial and require careful control over reaction conditions (e.g. volume fraction of nanoparticles, size matching between particle and hydrophilic component of surfactant, pH, etc.) which could be the reason for the limited success in developing straightforward, easily reproducible synthetic methods for the synthesis of structurally ordered ceria.¹²⁸

The most significant ceria synthetic procedures developed in the past decade, especially in terms of understanding structure-activity relationships, have been materials with well-defined shapes. Structure plays an essential role in heterogeneous catalysis through the specific arrangement of atoms that can lead to electronic, thermodynamic, and geometric properties that activate substrates or stabilize intermediates for desired catalytic functions. The host structure

can exist or be fine-tuned in a wide variety of ways that can ultimately lead to preferential formation of one reaction pathway over another or result in increased activity. In 2004, Li *et al.*¹²⁹ showed the crystal plane of ceria plays an essential role in determining its catalytic oxidation properties. In the seminal report, single-crystalline ceria nanorods with well-defined crystal planes were synthesized by a solution-based hydrothermal method. The rods showed higher CO oxidation rates (3x) than ceria nanoparticles with ill-defined shape even though the latter material contained more corner and edge atoms due to the smaller size. High-resolution transmission electron microscopy (HRTEM) showed the rods exposed the (100) and (110) planes, whereas the particles only exposed the (111) planes. Thus, a correlation was drawn between the catalytic performance and the exposed crystal planes. Shortly thereafter, Yan *et al.*¹³⁰ showed the removal of oxygen from the ceria lattice was structure sensitive by synthesizing single-crystalline nanopolyhedra, nanorods, and nanocubes through an alkaline hydrothermal route. According to HRTEM, the uniform shapes had different exposed planes: (111) and (100) for polyhedra, (110) and (100) for rods, and (100) for cubes. The key factors leading to their growth were attributed to the formation of hexagonal $\text{Ce}(\text{OH})_3$ intermediate species and their transformation into CeO_2 at elevated temperature together with the sodium hydroxide concentration. Oxygen storage capacity (OSC) measurements at 400 °C revealed that lattice oxygen removal was restricted to the surface on polyhedra, but was able to take place on the surface and subsurface for rods and cubes. The results suggested that the (100)/(110) planes were more reactive toward removal of lattice oxygen than the (111) planes, in accordance with Li *et al.* Furthermore, theoretical work has shown that the oxygen vacancy formation energy increases in the following sequence $(110) < (100) < (111)$ ¹³¹⁻¹³³ and is in general agreement with the

aforementioned studies. Both reports showed that ceria materials can be easily prepared with high oxidation activity for technological applications and fundamental research.

Since then there have been numerous reports on the synthesis of ceria shapes with well-defined facets^{79, 81, 134-136} including wires,¹³⁷⁻¹⁴³ tubes,^{137, 144-146} and other shapes.¹⁴⁷⁻¹⁵¹ Notably, Gao *et al.*¹⁵² reported the shape- and size-controlled synthesis of ceria nanocubes bounded by six (200) planes and their two- and three-dimensional self-assembly on a substrate. The cubes were prepared hydrothermally through a mixed phase system containing water, toluene, ceria precursor, oleic acid, and *tert*-butylamine. The size tunability was achieved through modification of synthetic conditions and attributed to the oriented aggregation mediated precursor growth mechanism of colloidal nanoparticles. Adschiri *et al.*¹⁵³ prepared single-crystalline cerium oxide nanocrystals with dimensions of about 10 nm with (100) facets via organic ligand-assisted supercritical hydrothermal synthesis. The cubes showed significant OSC at relatively low temperature (150 °C) compared to irregularly shaped ceria. Similarly, Murray *et al.*¹⁵⁴ prepared two-dimensional (2D) ceria nanocrystals by thermal decomposition of cerium acetate at 320-330 °C in the presence of oleic acid and oleylamine stabilizers and sodium diphosphate or sodium oleate as mineralizers. The length of the nanoplates could be controlled by the mineralizer and the height was found to be around 2 nm. The plates were either enclosed by six (100) facets or a combination of two (100) facets and four (110) facets. OSC measurements were performed at 300 °C and suggested that oxygen storage was not limited to the surface of the plates. The synthetic control demonstrated from these and other studies allow for structure-activity relationships to be established under realistic catalytic conditions.¹⁵⁵ The shape-control, which is closely related to defect-site-control, can also allow activity and selectivity tuning for specific catalytic applications.

Ceria-Based Materials for Biomass Upgrading Reactions.

Ceria and ceria-based materials have been successfully used for several organic transformations and their activity is often attributed to the redox and acid-base properties.¹⁵⁶ The cerium cations are weak Lewis acids, but can catalyze dehydration¹⁵⁷⁻¹⁵⁸ and hydrolysis¹⁵⁹ reactions. Overall, ceria is a mildly basic oxide and its amphoteric properties make it an interesting catalyst that potentially offers acid-base pair cooperativity for selective chemical conversions.¹⁶⁰⁻¹⁶¹ The acid-base properties of ceria can be modified through incorporation¹⁶² or deposition¹⁶³ of transition metals, thus providing synthetic control and acid-base property tuning for specific tasks. The inherent redox property and oxygen buffering capacity allow ceria-based materials to be used as oxidation or reduction catalysts simply by switching the gaseous environment (e.g. O₂ and H₂).¹⁶⁴ The redox property can also be controlled through metal doping, metal deposition, size, and shape manipulations to optimize reactivity and selectivity.^{27-28, 165} The control over acid-base and redox properties make ceria-based materials interesting for biorefinery applications. This section attempts to summarize reactions over ceria-based materials that are expected to play a role in biorefineries.

Ceria has been explored in C-C coupling reactions through aldol condensation. This carbon-carbon bond formation reaction is important for renewable fuel applications by creating higher carbon chains from small platform molecules (e.g. furfural). For example, the aldol condensation/hydrogenation reaction of 2-hexanone was studied over Pd/CeZrO_x at 350 °C and 5 bar H₂ with a weight hourly space velocity (WHSV) of 1.92 h⁻¹.¹⁶⁶⁻¹⁶⁷ 2-hexanone can be derived from the deoxygenation of carbohydrates and used as a building block for diesel and jet fuels. The aldol condensation/hydrogenation reaction over Pd/CeZrO_x catalysts resulted in the preferential formation of saturated, single-branched C₁₂ ketones, which could be subsequently

hydrogenated and dehydrated to yield C₁₂ alkanes within a biorefinery. Over Pd/CeO₂, the conversion was 40 % with a selectivity of 77 %. Incorporation of zirconium to form ceria-zirconia solid solutions resulted in increased conversion while the selectivity remained more or less constant. Over Pd/Ce₂Zr₅O_x, the conversion and selectivity to the C₁₂ ketone reached 84 % and 77 %, respectively. The increase in activity with increasing zirconia content in the mixed-oxide catalyst was attributed to changes in the acid-base properties and/or increased resistance to water inhibition. The presence of CO₂ in the reactant stream led to strong inhibition of the self-coupling activity of 2-hexanone and was attributed to basic site quenching.

Ketonization is another important class of carbon-carbon bond forming reactions. In ketonization reactions, two carboxylic acids combine to form ketone and by-products (CO₂ and water). Carboxylic acids can be obtained from carbohydrates through deoxygenation and have been shown to undergo ketonization over ceria¹⁶⁸⁻¹⁶⁹ and ceria-based catalysts.¹⁷⁰⁻¹⁷³ The ketonization and aldol condensation reactions are closely related in the sense that both carboxylic acids and ketones can be derived from carbohydrates. As alluded to previously, the carboxylic acid could quench the active basic sites necessary for aldol condensation reactions. The separation of acids, ketones, and aldehydes is one option to avoid the quenching, but is undesirable due to the associated time and cost factors. Therefore, it is beneficial to develop catalytic systems that are able to catalyze ketonization and aldol condensation reactions together. Dumesic *et al.*¹⁷⁴ were able to transform two important biomass-derived carbohydrates (glucose and sorbitol) into transportation fuels through a two-step process. The oxygen content of the feedstock was reduced over a Pt-Re/C catalyst at 230 °C to generate C₄-C₆ monofunctional oxygenated alcohols, ketones, and carboxylic acids. Upgrading through ketonization using Ce_{0.5}Zr_{0.5}O₂ catalyst afforded 98 % conversion of the carboxylic acids in the feed to C₇-C₁₁

ketones at 300 °C. The ketones in the ketonized stream (34 %), along with the other monofunctional oxygenates, were subjected to aldol condensation (off-line) over a Pd/Ce_{0.5}Zr_{0.5}O₂ catalyst to increase the yield of C₇₊ products. At 350 °C, 57 % of the total carbon was in the form of C₇₊ ketones. The ketones were readily hydrogenated/dehydrated to C₇₊ alkanes over Pt/NbOPO₄ catalyst. Due to the high conversion of carboxylic acids over Ce_{0.5}Zr_{0.5}O₂, deactivation of Pd/Ce_{0.5}Zr_{0.5}O₂ by carboxylic acids was avoidable. For on-line purposes, the CO₂ by-product from ketonization can be easily scrubbed from the system before reaching the Pd/Ce_{0.5}Zr_{0.5}O₂ catalyst bed.

Ceria-based catalysts have also found use for hydrodeoxygenation reactions. Sievers *et al.*²⁶ studied the hydrodeoxygenation of lignin-derived guaiacol over bulk ceria and ceria-zirconia catalysts in a flow reactor at 1 atm H₂ and 275-400 °C. The primary product was phenol and the catalysts showed no significant deactivation during 72 h time-on-stream. At 375 °C, ceria showed a 25 % yield of phenol and was found to increase upon incorporation of zirconia. A correlation was observed between the oxygen storage capacity (i.e. vacancy concentration) of the ceria-based materials and the conversion of guaiacol. The most active catalyst composition was Ce_{0.6}Zr_{0.4}O₂ which afforded 59 % yield of phenol. The authors proposed that the high-temperature reducing environment facilitated vacancy formation and that the oxophilic defects were active sites for deoxygenation. Noronha *et al.*¹⁷⁵ suggested that hydrodeoxygenation was promoted over oxophilic materials and was in agreement with the hydrodeoxygenation activity observed by Sievers. Similarly, the activity of ceria-promoted Ni/SBA-15 was tested for the hydrotreatment of anisole by Coronado *et al.*¹⁷⁶⁻¹⁷⁷ At 270 °C with hydrogen pressure of 7 bar and Ce/Si = 0.08, the hydrodeoxygenation rate to benzene increased three-fold over Ni/SBA-15. The increased rate was attributed to the formation of active sites in the interface between Ni and

CeO₂ moieties. Tomishige *et al.*¹⁷⁸ prepared heterogeneous ReO_x-Pd/CeO₂ catalysts that showed excellent performance for simultaneous hydrodeoxygenation of vicinal OH groups. High yield (>99 %), turnover frequency (300 h⁻¹), and turnover number (10⁴) were achieved for the conversion of 1,4-anhydroerythritol to tetrahydrofuran. The high catalytic performance of ReO_x-Pd/CeO₂ was assigned to rhenium species with +4 or +5 valence state, and the formation of these species was promoted by H₂/Pd and the ceria support. The catalyst was proposed to be well-suited for upgrading of cellulose-derived sugar alcohols.

The reactions of alcohols have been intensively studied over ceria and ceria-based materials often in the context of characterization probes for catalytic properties and active sites.¹⁷⁹⁻¹⁸⁸ Alcohols, polyols, and sugar-alcohols can be derived from cellulose and are valuable platform molecules that can lead to a number of industrially relevant chemicals. Ceria and ceria-based materials are able to catalyze many prototypical alcohol reactions including dehydration, dehydrogenation, transesterification, oxidation, etc.¹⁵⁶ The seminal report by Cortright *et al.*¹⁸⁹ demonstrated that hydrogen can be produced from sugars and alcohols at temperatures near 500 K in a single-reactor aqueous-phase reforming process. Since then, several studies have reported ceria-based catalytic systems active for reforming of bio-derived alcohols.¹⁹⁰⁻²⁰¹ In particular, ethanol and glycerol reforming catalysts and catalytic processes are desirable because the substrates can be currently obtained from renewable sources on an industrial scale. The desired catalytic properties are high selectivity to hydrogen and low selectivity to light hydrocarbons (e.g. methane, ethane, etc.) of lower value through Fischer-Tropsch processes. Another interesting aspect of alcohol oxidation to produce hydrogen is through *in situ* hydrotreatment reactions. For example, Rinaldi *et al.*²⁰²⁻²⁰³ reported a transfer hydrogenation method for direct phenolic dehydroxylation yielding arenes under low-severity conditions. They demonstrated that

the mild procedure was useful for the depolymerization of lignin and removal of its oxygen-containing functionalities. In relation, Ford *et al.*²⁰⁴⁻²⁰⁵ disassembled organosolv lignin via hydrogen transfer from supercritical methanol over copper supported on a basic porous metal oxide. The precedence for alcohol transformation over ceria-based materials holds promise for upgrading, reforming, and *in situ* hydrogen generation for biorefinery applications.

Hydrotreatment reactions (e.g. hydrogenation, hydrogenolysis, hydrodeoxygenation, etc.) are expected to play a large role in biorefinery plants due to the high oxygen content of biomass. Traditionally, ceria has not been associated with hydrogen activation in the sense that other transition metals (Ni, Cu, Pd, Pt, etc.) have been. However, density functional theory (DFT) simulations have shown that H₂ adsorbs dissociatively on the (111) surface with a low (0.2 eV) activation barrier and strong exothermicity (-2.82 eV).²⁰⁶⁻²⁰⁸ The potential hydrogen activation evidenced by DFT studies was only recently exploited for the selective hydrogenation of alkynes to olefins over pure ceria.²⁰⁹ Alkyne hydrogenation was found to be favored over CeO₂-(111) due to the low amount and more difficult formation of oxygen vacancies.¹⁶⁴ This contrasts to the beneficial role of oxygen vacancies for oxidation catalysis, which is favored over CeO₂-(100).²¹⁰ The result highlights the importance of structure-activity studies needed for the rational design of catalysts and the opposite facet sensitivity of ceria for hydrogenation and oxidation catalysis. The hydrogenation of alkynes to olefins is specific, as complete reduction to alkane was sparsely observed. Also, ceria is not known to activate hydrogen for reduction of other functional groups. However, ceria has been successfully used as a support for hydrogen-activating metals and can act as a promoter, stabilizer, or co-catalyst.

The utility of ceria as an active catalyst support is widely documented in the literature.²⁷⁻

^{28, 211-214} Ceria often enhances the performance of late transition metal catalysts relative to other

supports in relation to metal sintering resistance and synergistic effects.²¹⁵⁻²²¹ This is widely attributed to the strong interaction between ceria and the supported metal.²²² Campbell *et al.*²²³ showed that the adhesion energy of Ag nanoparticles to ceria was much larger than to magnesia and that the adhesion energy increases with the extent of ceria reduction. The results explain the unusual sinter resistance of late transition metal catalysts supported on ceria and suggest that defects stabilize supported metals more than terrace sites. The stability and synergism of metals supported on ceria make them promising materials for hydrotreatment reactions that are often conducted at high temperatures where metal loss and sintering can be problematic. Moreover, the inherent reducibility of ceria can impart increased hydrogen activation to metal clusters. That is, adsorption and nucleation of metals is thermodynamically preferred at oxygen vacancies and can result in electron transfer to the metal thereby promoting hydrogen activation.²²⁴⁻²²⁷ The reducibility of ceria also allows for hydrogen spillover to occur and can provide hydrogen to surface-bound substrates.²²⁸ Although largely unexplored, transition metals supported on ceria for hydrotreatment processes are promising candidates for biorefinery applications.

Concluding Remarks.

Ceria is a versatile and structurally robust rare earth oxide that has found widespread use in technological applications. This can be owed to the significant effort and progress made toward understanding the structure-property relationships of ceria. New characterization techniques and powerful theoretical methods that deepen our understanding of these materials can allow us to predict behavior, application potential, and synthetic methods leading to desired properties.

Ceria has been successfully utilized as an active support, catalyst, or co-catalyst for organic oxidative transformations, while its utility for chemical transformations under strongly

reducing conditions remains largely unexplored. The facile formation of oxophilic sites on ceria under reducing conditions makes it a promising material for deoxygenation reactions which is at the heart of biomass upgrading. Furthermore, the demonstrated ability to tune the acid-base properties can potentially lead to materials active for other important biomass upgrading reactions such as C-C coupling reactions.

References.

1. Klass, D. L., Biomass for Renewable Energy and Fuels A2 - Cleveland, Cutler J. In *Encyclopedia of Energy*; Elsevier: New York, 2004; pp 193-212.
2. Luterbacher, J. S.; Martin Alonso, D.; Dumesic, J. A. *Green Chem.* **2014**, 16, 4816-4838.
3. Serrano-Ruiz, J. C.; Luque, R.; Sepulveda-Escribano, A. *Chem. Soc. Rev.* **2011**, 40, 5266-5281.
4. Farmer, T. J.; Mascal, M., Platform Molecules. In *Introduction to Chemicals from Biomass*; John Wiley & Sons, Ltd: 2015; pp 89-155.
5. Gomiero, T.; Paoletti, M. G.; Pimentel, D. *J. Agric. Environ. Ethics* **2010**, 23, 403-434.
6. Cavani, F.; Albonetti, S.; Basile, F.; Gandini, A., *Chemicals and Fuels from Bio-Based Building Blocks*, Wiley: 2016.
7. Zakzeski, J.; Bruijninx, P. C. A.; Jongerius, A. L.; Weckhuysen, B. M. *Chem. Rev.* **2010**, 110, 3552-3599.
8. Chen, H., Chemical Composition and Structure of Natural Lignocellulose. In *Biotechnology of Lignocellulose: Theory and Practice*; Chen, H., Ed. Springer Netherlands: Dordrecht, 2014; pp 25-71.
9. Perlack, R. D.; Wright, L. L.; Turhollow, A. F.; Graham, R. L.; Stokes, B. J.; Erbach, D. C. U.S. Department of Energy, Biomass as feedstock for a bioenergy and bioproducts industry: the technical feasibility of a billion-ton annual supply, 2005.
10. Beckham, G. T.; Johnson, C. W.; Karp, E. M.; Salvachúa, D.; Vardon, D. R. *Curr. Opin. Biotech.* **2016**, 42, 40-53.
11. Holladay, J. E.; White, J. F.; Bozell, J. J.; Johnson, D. *Top Value-Added Chemicals from Biomass, Volume II: Results of Screening for Potential Candidates from Biorefinery Lignin*, Pacific Northwest National Laboratory: Richland, WA, **2007**.

12. Ralph, J.; Lundquist, K.; Brunow, G.; Lu, F.; Kim, H.; Schatz, P. F.; Marita, J. M.; Hatfield, R. D.; Ralph, S. A.; Christensen, J. H.; Boerjan, W. *Phytochem. Rev.* **2004**, 3, 29-60.
13. Neumann, G. T.; Pimentel, B. R.; Rensel, D. J.; Hicks, J. C. *Catal. Sci. Technol.* **2014**, 4, 3953-3963.
14. Forsythe, W. G.; Garrett, M. D.; Hardacre, C.; Nieuwenhuyzen, M.; Sheldrake, G. N. *Green Chem.* **2013**, 15, 3031-3038.
15. Rahimi, A.; Ulbrich, A.; Coon, J. J.; Stahl, S. S. *Nature* **2014**, 515, 249-252.
16. Ragauskas, A. J.; Beckham, G. T.; Bidy, M. J.; Chandra, R.; Chen, F.; Davis, M. F.; Davison, B. H.; Dixon, R. A.; Gilna, P.; Keller, M.; Langan, P.; Naskar, A. K.; Saddler, J. N.; Tschaplinski, T. J.; Tuskan, G. A.; Wyman, C. E. *Science* **2014**, 344.
17. Wang, Y.-Y.; Ling, L.-L.; Jiang, H. *Green Chem.* **2016**.
18. Alonso, D. M.; Wettstein, S. G.; Dumesic, J. A. *Chem. Soc. Rev.* **2012**, 41, 8075-8098.
19. Huber, G. W.; Iborra, S.; Corma, A. *Chem. Rev.* **2006**, 106, 4044-4098.
20. Alonso, D. M.; Bond, J. Q.; Dumesic, J. A. *Green Chem.* **2010**, 12, 1493-1513.
21. Li, H.; Fang, Z.; Smith Jr, R. L.; Yang, S. *Prog. Energ. Combust.* **2016**, 55, 98-194.
22. de Clippel, F.; Dusselier, M.; Van Rompaey, R.; Vanelderden, P.; Dijkmans, J.; Makshina, E.; Giebeler, L.; Oswald, S.; Baron, G. V.; Denayer, J. F. M.; Pescarmona, P. P.; Jacobs, P. A.; Sels, B. F. *J. Am. Chem. Soc.* **2012**, 134, 10089-10101.
23. Kleinert, M.; Barth, T. *Chem. Eng. Technol.* **2008**, 31, 736-745.
24. Yoshikawa, T.; Yagi, T.; Shinohara, S.; Fukunaga, T.; Nakasaka, Y.; Tago, T.; Masuda, T. *Fuel Process Technol.* **2013**, 108, 69-75.
25. Fisher, W. B.; VanPeppen, J. F., Cyclohexanol and Cyclohexanone. In *Kirk-Othmer Encyclopedia of Chemical Technology*; John Wiley & Sons, Inc.: 2000.
26. Schimming, S. M.; LaMont, O. D.; König, M.; Rogers, A. K.; D'Amico, A. D.; Yung, M. M.; Sievers, C. *ChemSusChem* **2015**, 8, 2073-2083.
27. Trovarelli, A., *Catalysis by Ceria and Related Materials*, Imperial College Press: London, 2002.
28. Trovarelli, A.; Fornasiero, P., *Catalysis by Ceria and Related Materials*, 2nd ed.; World Scientific Publ. Co. Pte. Ltd.: Singapore, 2013; Vol. 12, pp 1-888.
29. Trovarelli, A.; de Leitenburg, C.; Boaro, M.; Dolcetti, G. *Catal. Today* **1999**, 50, 353-367.

30. Montini, T.; Melchionna, M.; Monai, M.; Fornasiero, P. *Chem. Rev.* **2016**.
31. Bärnighausen, H.; Schiller, G. *J. Less Common Met.* **1985**, 110, 385-390.
32. Bevan, D. J. M.; Kordis, J. *J. Inorg. Nucl. Chem.* **1964**, 26, 1509-1523.
33. Ricken, M.; Nölting, J.; Riess, I. *J. Solid State Chem.* **1984**, 54, 89-99.
34. Kitayama, K.; Nojiri, K.; Sugihara, T.; Katsura, T. *J. Solid State Chem.* **1985**, 56, 1-11.
35. Haire, R. G.; Eyring, L., Comparisons of the Binary Oxides. In *Handbook on the Physics and Chemistry of Rare Earths*; Elsevier: New York, 1994; Volume 18, pp 413-505.
36. Campserveux, J.; Gerdanian, P. *J. Solid State Chem.* **1978**, 23, 73-92.
37. Panlener, R. J.; Blumenthal, R. N.; Garnier, J. E. *J. Phys. Chem. Solids* **1975**, 36, 1213-1222.
38. Ray, S. P.; Cox, D. E. *J. Solid State Chem.* **1975**, 15, 333-343.
39. Tsunekawa, S.; Sivamohan, R.; Ito, S.; Kasuya, A.; Fukuda, T. *Nanostruct. Mater.* **1999**, 11, 141-147.
40. Sayle, T. X. T.; Parker, S. C.; Catlow, C. R. A. *Surf. Sci.* **1994**, 316, 329-336.
41. Cordatos, H.; Ford, D.; Gorte, R. J. *J. Phys. Chem.* **1996**, 100, 18128-18132.
42. Kröger, F. A.; Vink, H. J., Relations between the Concentrations of Imperfections in Crystalline Solids. In *Solid State Physics*; Frederick, S.; David, T., Eds. Academic Press: 1956; Volume 3, pp 307-435.
43. Minervini, L.; Zacate, M. O.; Grimes, R. W. *Solid State Ionics* **1999**, 116, 339-349.
44. Mamontov, E.; Egami, T.; Brezny, R.; Koranne, M.; Tyagi, S. *J. Phys. Chem. B* **2000**, 104, 11110-11116.
45. Madier, Y.; Descorme, C.; Le Govic, A. M.; Duprez, D. *J. Phys. Chem. B* **1999**, 103, 10999-11006.
46. Chiang, H.-W.; Blumenthal, R. N.; Fournelle, R. A. *Solid State Ionics* **1993**, 66, 85-95.
47. Ray, S. P.; Nowick, A. S.; Cox, D. E. *J. Solid State Chem.* **1975**, 15, 344-351.
48. Faber Jr, J.; Seitz, M. A.; Mueller, M. H. *J. Phys. Chem. Solids* **1976**, 37, 903-907.
49. Faber Jr, J.; Seitz, M. A.; Mueller, M. H. *J. Phys. Chem. Solids* **1976**, 37, 909-915.
50. Esch, F.; Fabris, S.; Zhou, L.; Montini, T.; Africh, C.; Fornasiero, P.; Comelli, G.; Rosei, R. *Science* **2005**, 309, 752-755.

51. Fornasiero, P.; Balducci, G.; Di Monte, R.; Kašpar, J.; Sergio, V.; Gubitosa, G.; Ferrero, A.; Graziani, M. *J. Catal.* **1996**, 164, 173-183.
52. Eguchi, K.; Setoguchi, T.; Inoue, T.; Arai, H. *Solid State Ionics* **1992**, 52, 165-172.
53. Huang, W.; Shuk, P.; Greenblatt, M. *Chem. Mater.* **1997**, 9, 2240-2245.
54. Shuk, P.; Greenblatt, M.; Croft, M. *Chem. Mater.* **1999**, 11, 473-479.
55. Blumenthal, R. N.; Brugner, F. S.; Garnier, J. E. *J. Electrochem. Soc.* **1973**, 120, 1230-1237.
56. Hong, S. J.; Virkar, A. V. *J. Am. Ceram. Soc.* **1995**, 78, 433-439.
57. Steele, B. C. H. *Solid State Ionics* **2000**, 129, 95-110.
58. Lamonier, C.; Ponchel, A.; D'Huysser, A.; Jalowiecki-Duhamel, L. *Catal. Today* **1999**, 50, 247-259.
59. de Carolis, S.; Pascual, J. L.; Pettersson, L. G. M.; Baudin, M.; Wójcik, M.; Hermansson, K.; Palmqvist, A. E. C.; Muhammed, M. *J. Phys. Chem. B* **1999**, 103, 7627-7636.
60. Terribile, D.; Trovarelli, A.; de Leitenburg, C.; Primavera, A.; Dolcetti, G. *Catal. Today* **1999**, 47, 133-140.
61. Balducci, G.; Islam, M. S.; Kašpar, J.; Fornasiero, P.; Graziani, M. *Chem. Mater.* **2003**, 15, 3781-3785.
62. Steele, B. C. H.; Floyd, J. M. *Proc. British. Ceram. Trans.* **1971**, 72, 55-76.
63. Floyd, J. M. *Indian J. Technol.* **1973**, 11, 589-594.
64. Kharton, V. V.; Figueiredo, F. M.; Navarro, L.; Naumovich, E. N.; Kovalevsky, A. V.; Yaremchenko, A. A.; Viskup, A. P.; Carneiro, A.; Marques, F. M. B.; Frade, J. R. *J. Mater. Sci.* **2001**, 36, 1105-1117.
65. Li, C.; Domen, K.; Maruya, K.; Onishi, T. *J. Am. Chem. Soc.* **1989**, 111, 7683-7687.
66. Li, C.; Domen, K.; Maruya, K.-I.; Onishi, T. *J. Catal.* **1990**, 123, 436-442.
67. Pushkarev, V. V.; Kovalchuk, V. I.; d'Itri, J. L. *J. Phys. Chem. B* **2004**, 108, 5341-5348.
68. Descorme, C.; Madier, Y.; Duprez, D. *J. Catal.* **2000**, 196, 167-173.
69. Guzman, J.; Carrettin, S.; Corma, A. *J. Am. Chem. Soc.* **2005**, 127, 3286-3287.
70. Wu, Z.; Li, M.; Howe, J.; Meyer, H. M.; Overbury, S. H. *Langmuir* **2010**, 26, 16595-16606.

71. Wu, Z.; Li, M.; Overbury, S. H. *J. Catal.* **2012**, 285, 61-73.
72. Liu, X.; Zhou, K.; Wang, L.; Wang, B.; Li, Y. *J. Am. Chem. Soc.* **2009**, 131, 3140-3141.
73. Murugan, B.; Ramaswamy, A. V. *J. Am. Chem. Soc.* **2007**, 129, 3062-3063.
74. Hu, J.-d.; Li, Y.-x.; Zhou, X.-z.; Cai, M.-x. *Mater. Lett.* **2007**, 61, 4989-4992.
75. Li, L.; Chen, Y. *Mater. Sci. Eng. A* **2005**, 406, 180-185.
76. Bumajdad, A.; Eastoe, J.; Mathew, A. *Adv. Colloid Interface Sci.* **2009**, 147-148, 56-66.
77. Zhang, D.; Du, X.; Shi, L.; Gao, R. *Dalton Trans.* **2012**, 41, 14455-14475.
78. Yuan, Q.; Duan, H.-H.; Li, L.-L.; Sun, L.-D.; Zhang, Y.-W.; Yan, C.-H. *J. Colloid Interf. Sci.* **2009**, 335, 151-167.
79. Sun, C.; Li, H.; Chen, L. *Energy Environ. Sci.* **2012**, 5, 8475.
80. Lin, K.-S.; Chowdhury, S. *Int. J. Mol. Sci.* **2010**, 11.
81. Qiao, Z.-A.; Wu, Z.; Dai, S. *ChemSusChem* **2013**, 6, 1821-1833.
82. Kaneko, K.; Inoke, K.; Freitag, B.; Hungria, A. B.; Midgley, P. A.; Hansen, T. W.; Zhang, J.; Ohara, S.; Adschiri, T. *Nano Lett.* **2007**, 7, 421-425.
83. Wang, R.; Dangerfield, R. *RSC Adv.* **2014**, 4, 3615.
84. Sreeremya, T. S.; Thulasi, K. M.; Krishnan, A.; Ghosh, S. *Ind. Eng. Chem. Res.* **2012**, 51, 318-326.
85. Taniguchi, T.; Watanabe, T.; Sakamoto, N.; Matsushita, N.; Yoshimura, M. *Cryst. Growth Des.* **2008**, 8, 3725-3730.
86. Matijević, E.; Hsu, W. P. *J. Colloid Interf. Sci.* **1987**, 118, 506-523.
87. Chen, F.; Cao, Y.; Jia, D. *Appl. Surf. Sci.* **2011**, 257, 9226-9231.
88. Perrichon, V.; Laachir, A.; Abouarnadasse, S.; Touret, O.; Blanchard, G. *Appl. Catal. A-Gen* **1995**, 129, 69-82.
89. Wang, Z. L.; Feng, X. *J. Phys. Chem. B* **2003**, 107, 13563-13566.
90. Yin, L.; Wang, Y.; Pang, G.; Koltypin, Y.; Gedanken, A. *J. Colloid Interf. Sci.* **2002**, 246, 78-84.
91. Nelson, N. C.; Manzano, J. S.; Sadow, A. D.; Overbury, S. H.; Slowing, I. I. *ACS Catal.* **2015**, 5, 2051-2061.

92. Palmisano, P.; Russo, N.; Fino, P.; Fino, D.; Badini, C. *Appl. Catal., B* **2006**, 69, 85-92.
93. Narula, C. K.; Haack, L. P.; Chun, W.; Jen, H. W.; Graham, G. W. *J. Phys. Chem. B* **1999**, 103, 3634-3639.
94. Chu, X.; Chung, W.-i.; Schmidt, L. D. *J. Am. Ceram. Soc.* **1993**, 76, 2115-2118.
95. Yang, H.; Huang, C.; Tang, A.; Zhang, X.; Yang, W. *Mater. Res. Bull.* **2005**, 40, 1690-1695.
96. Nermeen, N.; Renate, S.; Ingo, L.; Emanuel, K.; Robert, F.; Stefan, K.; Clemens, K. W.; Katharina, L. *Nanotechnol.* **2011**, 22, 135606.
97. Masui, T.; Fujiwara, K.; Machida, K.-i.; Adachi, G.-y.; Sakata, T.; Mori, H. *Chem. Mater.* **1997**, 9, 2197-2204.
98. Carey, G. H.; Abdelhady, A. L.; Ning, Z.; Thon, S. M.; Bakr, O. M.; Sargent, E. H. *Chem. Rev.* **2015**, 115, 12732-12763.
99. Oh, M.-H.; Nho, J.-S.; Cho, S.-B.; Lee, J.-S.; Singh, R. K. *Mater. Chem. Phys.* **2010**, 124, 134-139.
100. Gu, H.; Soucek, M. D. *Chem. Mater.* **2007**, 19, 1103-1110.
101. Kockrick, E.; Schrage, C.; Grigas, A.; Geiger, D.; Kaskel, S. *J. Solid State Chem.* **2008**, 181, 1614-1620.
102. Lee, S. S.; Zhu, H.; Contreras, E. Q.; Prakash, A.; Puppala, H. L.; Colvin, V. L. *Chem. Mater.* **2012**, 24, 424-432.
103. Xin, Y.; Yang, X.; Jiang, P.; Zhang, Z.; Wang, Z.; Zhang, Y. *ChemCatChem* **2011**, 3, 1772-1778.
104. Corma, A.; Atienzar, P.; Garcia, H.; Chane-Ching, J.-Y. *Nat. Mater.* **2004**, 3, 394-397.
105. Wu, L.; Wiesmann, H. J.; Moodenbaugh, A. R.; Klie, R. F.; Zhu, Y.; Welch, D. O.; Suenaga, M. *Phys. Rev. B* **2004**, 69, 125415.
106. Hailstone, R. K.; DiFrancesco, A. G.; Leong, J. G.; Allston, T. D.; Reed, K. J. *J. Phys. Chem. C.* **2009**, 113, 15155-15159.
107. Deshpande, S.; Patil, S.; Kuchibhatla, S. V.; Seal, S. *Appl. Phys. Lett.* **2005**, 87, 133113.
108. Migani, A.; Vayssilov, G. N.; Bromley, S. T.; Illas, F.; Neyman, K. M. *Chem. Comm.* **2010**, 46, 5936-5938.
109. Gangopadhyay, S.; Frolov, D. D.; Masunov, A. E.; Seal, S. *J. Alloy Compds.* **2014**, 584, 199-208.

110. Tsunekawa, S.; Sahara, R.; Kawazoe, Y.; Ishikawa, K. *Appl. Surf. Sci.* **1999**, 152, 53-56.
111. Patsalas, P.; Logothetidis, S.; Sygellou, L.; Kennou, S. *Phys. Rev. B* **2003**, 68, 035104.
112. Lee, S. S.; Song, W.; Cho, M.; Puppala, H. L.; Nguyen, P.; Zhu, H.; Segatori, L.; Colvin, V. L. *ACS Nano* **2013**, 7, 9693-9703.
113. Kresge, C. T.; Leonowicz, M. E.; Roth, W. J.; Vartuli, J. C.; Beck, J. S. *Nature* **1992**, 359, 710-712.
114. Beck, J. S.; Vartuli, J. C.; Roth, W. J.; Leonowicz, M. E.; Kresge, C. T.; Schmitt, K. D.; Chu, C. T. W.; Olson, D. H.; Sheppard, E. W.; McCullen, S. B.; Higgins, J. B.; Schlenker, J. L. *J. Am. Chem. Soc.* **1992**, 114, 10834-10843.
115. Feng, X.; Ding, X.; Jiang, D. *Chem. Soc. Rev.* **2012**, 41, 6010-6022.
116. Zhou, H.-C.; Long, J. R.; Yaghi, O. M. *Chem. Rev.* **2012**, 112, 673-674.
117. Soler-Illia, G. J. d. A. A.; Sanchez, C.; Lebeau, B.; Patarin, J. *Chem. Rev.* **2002**, 102, 4093-4138.
118. Guo, Z.; Xiao, C.; Maligal-Ganesh, R. V.; Zhou, L.; Goh, T. W.; Li, X.; Tesfagaber, D.; Thiel, A.; Huang, W. *ACS Catal.* **2014**, 4, 1340-1348.
119. Li, J.-R.; Kuppler, R. J.; Zhou, H.-C. *Chem. Soc. Rev.* **2009**, 38, 1477-1504.
120. Hugo, K. C. *J. Phys. Condens. Matter.* **2001**, 13, R95.
121. Liu, D.-J.; Wang, J.; Ackerman, D. M.; Slowing, I. I.; Pruski, M.; Chen, H.-T.; Lin, V. S. Y.; Evans, J. W. *ACS Catal.* **2011**, 1, 751-763.
122. Singappuli-Arachchige, D.; Manzano, J. S.; Sherman, L. M.; Slowing, I. I. *Chemphyschem* **2016**, 17, 2982-2986.
123. Lyons, D. M.; Ryan, K. M.; Morris, M. A. *J. Mater. Chem.* **2002**, 12, 1207-1212.
124. Brezesinski, T.; Antonietti, M.; Groenewolt, M.; Pinna, N.; Smarsly, B. *New J. Chem.* **2005**, 29, 237-242.
125. Crepaldi, E. L.; de A. A. Soler-Illia, G. J.; Bouchara, A.; Grosso, D.; Durand, D.; Sanchez, C. *Angew. Chem. Int. Ed.* **2003**, 42, 347-351.
126. Yuan, Q.; Liu, Q.; Song, W.-G.; Feng, W.; Pu, W.-L.; Sun, L.-D.; Zhang, Y.-W.; Yan, C.-H. *J. Am. Chem. Soc.* **2007**, 129, 6698-6699.
127. Chane-Ching, J.-Y.; Cobo, F.; Aubert, D.; Harvey, H. G.; Airiau, M.; Corma, A. *Chem. Eur. J.* **2005**, 11, 979-987.

128. Deshpande, A. S.; Pinna, N.; Smarsly, B.; Antonietti, M.; Niederberger, M. *Small* **2005**, 1, 313-6.
129. Zhou, K.; Wang, X.; Sun, X.; Peng, Q.; Li, Y. *J. Catal.* **2005**, 229, 206-212.
130. Mai, H.-X.; Sun, L.-D.; Zhang, Y.-W.; Si, R.; Feng, W.; Zhang, H.-P.; Liu, H.-C.; Yan, C.-H. *J. Phys. Chem. B* **2005**, 109, 24380-24385.
131. Nolan, M.; Parker, S. C.; Watson, G. W. *Surf. Sci.* **2005**, 595, 223-232.
132. Sayle, D. C.; Maicaneanu, S. A.; Watson, G. W. *J. Am. Chem. Soc.* **2002**, 124, 11429-11439.
133. Dholabhai, P. P.; Adams, J. B.; Crozier, P.; Sharma, R. *J. Chem. Phys.* **2010**, 132, 094104.
134. Zhang, D.; Du, X.; Shi, L.; Gao, R. *Dalton Trans* **2012**, 41, 14455-75.
135. Vantomme, A.; Yuan, Z.-Y.; Du, G.; Su, B.-L. *Langmuir* **2005**, 21, 1132-1135.
136. Kuiry, S. C.; Patil, S. D.; Deshpande, S.; Seal, S. *J. Phys. Chem. B* **2005**, 109, 6936-6939.
137. Pan, C.; Zhang, D.; Shi, L.; Fang, J. *Eur. J. Inorg. Chem.* **2008**, 2008, 2429-2436.
138. Tang, B.; Zhuo, L.; Ge, J.; Wang, G.; Shi, Z.; Niu, J. *Chem. Comm.* **2005**, 3565-3567.
139. Wu, G. S.; Xie, T.; Yuan, X. Y.; Cheng, B. C.; Zhang, L. D. *Mater. Res. Bull.* **2004**, 39, 1023-1028.
140. Yada, M.; Sakai, S.; Torikai, T.; Watari, T.; Furuta, S.; Katsuki, H. *Adv. Mater.* **2004**, 16, 1222-1226.
141. Yang, R.; Guo, L. *J. Mater. Sci.* **2005**, 40, 1305-1307.
142. Sun, C.; Li, H.; Wang, Z.; Chen, L.; Huang, X. *Chem. Lett.* **2004**, 33, 662-663.
143. La, R.-J.; Hu, Z.-A.; Li, H.-L.; Shang, X.-L.; Yang, Y.-Y. *Mater. Sci. Eng. A* **2004**, 368, 145-148.
144. Han, W.-Q.; Wu, L.; Zhu, Y. *J. Am. Chem. Soc.* **2005**, 127, 12814-12815.
145. Fang, J.; Cao, Z.; Zhang, D.; Shen, X.; Ding, W.; Shi, L. *J. Rare Earth* **2008**, 26, 153-157.
146. Zhou, K.; Yang, Z.; Yang, S. *Chem. Mater.* **2007**, 19, 1215-1217.
147. Ahniyaz, A.; Sakamoto, Y.; Bergström, L. *Cryst. Growth Des.* **2008**, 8, 1798-1800.

148. Zhou, H.-P.; Zhang, Y.-W.; Mai, H.-X.; Sun, X.; Liu, Q.; Song, W.-G.; Yan, C.-H. *Chem. Eur. J.* **2008**, *14*, 3380-3390.
149. Karakoti, A. S.; Kuchibhatla, S. V. N. T.; Baer, D. R.; Thevuthasan, S.; Sayle, D. C.; Seal, S. *Small* **2008**, *4*, 1210-1216.
150. Kuchibhatla, S. V. N. T.; Karakoti, A. S.; Sayle, D. C.; Heinrich, H.; Seal, S. *Cryst. Growth Des.* **2009**, *9*, 1614-1620.
151. Chen, G.; Xu, C.; Song, X.; Xu, S.; Ding, Y.; Sun, S. *Cryst. Growth Des.* **2008**, *8*, 4449-4453.
152. Yang, S.; Gao, L. *J. Am. Chem. Soc.* **2006**, *128*, 9330-9331.
153. Zhang, J.; Kumagai, H.; Yamamura, K.; Ohara, S.; Takami, S.; Morikawa, A.; Shinjoh, H.; Kaneko, K.; Adschiri, T.; Suda, A. *Nano Lett.* **2011**, *11*, 361-364.
154. Wang, D.; Kang, Y.; Doan-Nguyen, V.; Chen, J.; Küngas, R.; Wieder, N. L.; Bakhtmutsky, K.; Gorte, R. J.; Murray, C. B. *Angew. Chem. Int. Ed.* **2011**, *50*, 4378-4381.
155. Lin, Y.; Wu, Z.; Wen, J.; Poepelmeier, K. R.; Marks, L. D. *Nano Lett.* **2014**, *14*, 191-196.
156. Vivier, L.; Duprez, D. *ChemSusChem* **2010**, *3*, 654-78.
157. Cutrufello, M. G.; Ferino, I.; Monaci, R.; Rombi, E.; Colon, G.; Navio, J. A. *Phys. Chem. Chem. Phys.* **2001**, *3*, 2928-2934.
158. Reddy, B. M.; Thrimurthulu, G.; Saikia, P.; Bharali, P. *J. Mol. Catal. A: Chem.* **2007**, *275*, 167-173.
159. Wang, Y.; Wang, F.; Song, Q.; Xin, Q.; Xu, S.; Xu, J. *J. Am. Chem. Soc.* **2013**, *135*, 1506-1515.
160. Iglesia, E.; Barton, D. G.; Biscardi, J. A.; Gines, M. J. L.; Soled, S. L. *Catal. Today* **1997**, *38*, 339-360.
161. Metiu, H.; Chrétien, S.; Hu, Z.; Li, B.; Sun, X. *J. Phys. Chem. C.* **2012**, *116*, 10439-10450.
162. Collins, S.; Finos, G.; Alcántara, R.; del Rio, E.; Bernal, S.; Bonivardi, A. *Appl. Catal. A-Gen* **2010**, *388*, 202-210.
163. C. I. Bezen, M.; Breitkopf, C.; El Kooli, N.; Krafft, J.-M.; Louis, C.; Lercher, J. A. *Chem. Eur. J.* **2011**, *17*, 7095-7104.
164. Vilé, G.; Colussi, S.; Krumeich, F.; Trovarelli, A.; Pérez-Ramírez, J. *Angew. Chem. Int. Ed.* **2014**, *53*, 12069-12072.

165. *Catalysis by Materials with Well-Defined Structures*, Academic Press: 2015.
166. Kunkes, E. L.; Gürbüz, E. I.; Dumesic, J. A. *J. Catal.* **2009**, 266, 236-249.
167. Gürbüz, E. I.; Kunkes, E. L.; Dumesic, J. A. *Appl. Catal., B* **2010**, 94, 134-141.
168. Kobune, M.; Sato, S.; Takahashi, R. *J. Mol. Catal. A: Chem.* **2008**, 279, 10-19.
169. Hasan, M. A.; Zaki, M. I.; Pasupulety, L. *Appl. Catal. A-Gen* **2003**, 243, 81-92.
170. Gaertner, C. A.; Serrano-Ruiz, J. C.; Braden, D. J.; Dumesic, J. A. *J. Catal.* **2009**, 266, 71-78.
171. Pham, T. N.; Sooknoi, T.; Crossley, S. P.; Resasco, D. E. *ACS Catal.* **2013**, 3, 2456-2473.
172. Snell, R. W.; Shanks, B. H. *ACS Catal.* **2014**, 4, 512-518.
173. Gaertner, C. A.; Serrano-Ruiz, J. C.; Braden, D. J.; Dumesic, J. A. *Ind. Eng. Chem. Res.* **2010**, 49, 6027-6033.
174. Kunkes, E. L.; Simonetti, D. A.; West, R. M.; Serrano-Ruiz, J. C.; Gärtner, C. A.; Dumesic, J. A. *Science* **2008**, 322, 417-421.
175. de Souza, P. M.; Rabelo-Neto, R. C.; Borges, L. E. P.; Jacobs, G.; Davis, B. H.; Sooknoi, T.; Resasco, D. E.; Noronha, F. B. *ACS Catal.* **2015**, 5, 1318-1329.
176. Yang, Y.; Ochoa-Hernández, C.; Pizarro, P.; de la Peña O'shea, V. A.; Coronado, J. M.; Serrano, D. P. *Appl. Catal., B*.
177. Yang, Y.; Ochoa-Hernández, C.; de la Peña O'Shea, V. A.; Pizarro, P.; Coronado, J. M.; Serrano, D. P. *Appl. Catal., B* **2014**, 145, 91-100.
178. Ota, N.; Tamura, M.; Nakagawa, Y.; Okumura, K.; Tomishige, K. *Angew. Chem. Int. Ed.* **2015**, 54, 1897-1900.
179. Mullins, D. R.; Robbins, M. D.; Zhou, J. *Surf. Sci.* **2006**, 600, 1547-1558.
180. Wu, Z.; Li, M.; Mullins, D. R.; Overbury, S. H. *ACS Catal.* **2012**, 2, 2224-2234.
181. Li, M.; Wu, Z.; Overbury, S. H. *J. Catal.* **2013**, 306, 164-176.
182. Mullins, D. R.; Senanayake, S. D.; Chen, T. L. *J. Phys. Chem. C.* **2010**, 114, 17112-17119.
183. Albrecht, P. M.; Mullins, D. R. *Langmuir* **2013**, 29, 4559-4567.
184. Ferrizz, R. M.; Wong, G. S.; Egami, T.; Vohs, J. M. *Langmuir* **2001**, 17, 2464-2470.

185. Matolín, V.; Libra, J.; Škoda, M.; Tsud, N.; Prince, K. C.; Skála, T. *Surf. Sci.* **2009**, 603, 1087-1092.
186. Lykhach, Y.; Neitzel, A.; Ševčíková, K.; Johánek, V.; Tsud, N.; Skála, T.; Prince, K. C.; Matolín, V.; Libuda, J. *ChemSusChem* **2014**, 7, 77-81.
187. Haider, M. H.; Dummer, N. F.; Knight, D. W.; Jenkins, R. L.; Howard, M.; Moulijn, J.; Taylor, S. H.; Hutchings, G. J. *Nat. Chem.* **2015**, 7, 1028-1032.
188. Chen, T. L.; Mullins, D. R. *J. Phys. Chem. C.* **2011**, 115, 13725-13733.
189. Cortright, R. D.; Davda, R. R.; Dumesic, J. A. *Nature* **2002**, 418, 964-967.
190. Soykal, I. I.; Sohn, H.; Singh, D.; Miller, J. T.; Ozkan, U. S. *ACS Catal.* **2014**, 4, 585-592.
191. de Lima, S. M.; Silva, A. M.; Graham, U. M.; Jacobs, G.; Davis, B. H.; Mattos, L. V.; Noronha, F. B. *Appl. Catal. A-Gen* **2009**, 352, 95-113.
192. Hou, T.; Zhang, S.; Chen, Y.; Wang, D.; Cai, W. *Renew. Sust. Energ. Rev.* **2015**, 44, 132-148.
193. Liu, Z.; Duchoň, T.; Wang, H.; Peterson, E. W.; Zhou, Y.; Luo, S.; Zhou, J.; Matolín, V.; Stacchiola, D. J.; Rodriguez, J. A.; Senanayake, S. D. *J. Phys. Chem. C.* **2015**, 119, 18248-18256.
194. Soykal, I. I.; Sohn, H.; Ozkan, U. S. *ACS Catal.* **2012**, 2, 2335-2348.
195. Kugai, J.; Subramani, V.; Song, C.; Engelhard, M. H.; Chin, Y.-H. *J. Catal.* **2006**, 238, 430-440.
196. Mattos, L. V.; Jacobs, G.; Davis, B. H.; Noronha, F. B. *Chem. Rev.* **2012**, 112, 4094-4123.
197. Zhang, B.; Tang, X.; Li, Y.; Xu, Y.; Shen, W. *Int. J. Hydrogen Energy* **2007**, 32, 2367-2373.
198. Manfro, R. L.; da Costa, A. F.; Ribeiro, N. F. P.; Souza, M. M. V. M. *Fuel Process Technol.* **2011**, 92, 330-335.
199. Deluga, G. A.; Salge, J. R.; Schmidt, L. D.; Verykios, X. E. *Science* **2004**, 303, 993-997.
200. Pirez, C.; Capron, M.; Jobic, H.; Dumeignil, F.; Jalowiecki-Duhamel, L. *Angew. Chem. Int. Ed.* **2011**, 50, 10193-10197.
201. Haider, M. H.; Dummer, N. F.; Knight, D. W.; Jenkins, R. L.; Howard, M.; Moulijn, J.; Taylor, S. H.; Hutchings, G. J. *Nat. Chem.* **2015**, 7, 1028-1032.
202. Wang, X.; Rinaldi, R. *Angew. Chem. Int. Ed.* **2013**, 52, 11499-11503.

203. Ferrini, P.; Rinaldi, R. *Angew. Chem. Int. Ed.* **2014**, 53, 8634-8639.
204. Barta, K.; Matson, T. D.; Fettig, M. L.; Scott, S. L.; Iretskii, A. V.; Ford, P. C. *Green Chem.* **2010**, 12, 1640-1647.
205. Macala, G. S.; Matson, T. D.; Johnson, C. L.; Lewis, R. S.; Iretskii, A. V.; Ford, P. C. *ChemSusChem* **2009**, 2, 215-217.
206. Sohlberg, K.; Pantelides, S. T.; Pennycook, S. J. *J. Am. Chem. Soc.* **2001**, 123, 6609-6611.
207. Vicario, G.; Balducci, G.; Fabris, S.; de Gironcoli, S.; Baroni, S. *J. Phys. Chem. B* **2006**, 110, 19380-19385.
208. Chen, H.-T.; Choi, Y. M.; Liu, M.; Lin, M. C. *ChemPhysChem* **2007**, 8, 849-855.
209. Vilé, G.; Bridier, B.; Wichert, J.; Pérez-Ramírez, J. *Angew. Chem. Int. Ed.* **2012**, 51, 8620-8623.
210. Désaunay, T.; Bonura, G.; Chiodo, V.; Freni, S.; Couzinié, J. P.; Bourgon, J.; Ringuedé, A.; Labat, F.; Adamo, C.; Cassir, M. *J. Catal.* **2013**, 297, 193-201.
211. Bunluesin, T.; Gorte, R. J.; Graham, G. W. *Appl. Catal., B* **1998**, 15, 107-114.
212. Fu, Q.; Weber, A.; Flytzani-Stephanopoulos, M. *Catal. Lett.* **2001**, 77, 87-95.
213. Trovarelli, A. *Catal. Rev.* **1996**, 38, 439-520.
214. Sepúlveda-Escribano, A.; Coloma, F.; Rodríguez-Reinoso, F. *J. Catal.* **1998**, 178, 649-657.
215. Schwartz, J. M.; Schmidt, L. D. *J. Catal.* **1992**, 138, 283-293.
216. Kundakovic, L.; Flytzani-Stephanopoulos, M. *J. Catal.* **1998**, 179, 203-221.
217. Kalakkad, D.; Datye, A. K.; Robota, H. *Appl. Catal., B* **1992**, 1, 191-219.
218. Cargnello, M.; Doan-Nguyen, V. V. T.; Gordon, T. R.; Diaz, R. E.; Stach, E. A.; Gorte, R. J.; Fornasiero, P.; Murray, C. B. *Science* **2013**, 341, 771-773.
219. Bruix, A.; Rodriguez, J. A.; Ramírez, P. J.; Senanayake, S. D.; Evans, J.; Park, J. B.; Stacchiola, D.; Liu, P.; Hrbek, J.; Illas, F. *J. Am. Chem. Soc.* **2012**, 134, 8968-8974.
220. Campbell, C. T. *Nat. Chem.* **2012**, 4, 597-598.
221. Yeung, C. M. Y.; Yu, K. M. K.; Fu, Q. J.; Thompsett, D.; Petch, M. I.; Tsang, S. C. J. *Am. Chem. Soc.* **2005**, 127, 18010-18011.

222. Bernal, S.; Calvino, J. J.; Cauqui, M. A.; Gatica, J. M.; Larese, C.; Pérez Omil, J. A.; Pintado, J. M. *Catal. Today* **1999**, 50, 175-206.
223. Farmer, J. A.; Campbell, C. T. *Science* **2010**, 329, 933-6.
224. Ševčíková, K.; Szabová, L.; Kettner, M.; Homola, P.; Tsud, N.; Fabris, S.; Matolín, V.; Nehasil, V. *J. Phys. Chem. C* **2016**, 120, 5468-5476.
225. Pacchioni, G. *Phys. Chem. Chem. Phys.* **2013**, 15, 1737-1757.
226. Mullins, D. R.; Overbury, S. H. *J. Catal.* **1999**, 188, 340-345.
227. Szabová, L.; Skála, T.; Matolínová, I.; Fabris, S.; Farnesi Camellone, M.; Matolín, V. *Appl. Surf. Sci.* **2013**, 267, 12-16.
228. Prins, R. *Chem. Rev.* **2012**, 112, 2714-2738.

CHAPTER 2**SELECTIVE HYDROGENATION OF PHENOL CATALYZED BY PALLADIUM ON HIGH SURFACE CERIA AT ROOM TEMPERATURE AND AMBIENT PRESSURE**

Reprinted with permission from *ACS Catal.* **2015**, 5, 2051-2061.

Copyright © 2015 American Chemical Society

Nicholas C. Nelson, J. Sebastián Manzano, Aaron D. Sadow, Steven H. Overbury, Igor I.

Slowing

Abstract

Palladium supported on high surface ceria effectively catalyzes the hydrogenation of phenol to cyclohexanone at atmospheric pressure and room temperature. Activation of H₂ at Pd sites and phenol at surface ceria sites were investigated by probing the redox properties of the catalyst and studying the mechanism of phenol adsorption. Temperature-programmed reduction and pulsed chemisorption were used to examine the effects of pre-reduction temperature on catalyst dispersion and reducibility. A sharp effect of pre-reduction temperature on catalytic activity was observed. This dependence is rationalized as a result of interactions between palladium and ceria, which under reducing conditions enhance palladium dispersion and create different types of environments around the Pd active sites, and of encapsulation of the catalyst caused by support sintering at high temperatures. Temperature programmed diffuse reflectance infrared Fourier transform spectroscopy revealed that phenol undergoes dissociative adsorption on ceria to yield cerium-bound phenoxy and water. Reduction of the chemisorbed phenoxy species decreases the number of proton-accepting sites on the surface of ceria and prevents further dissociative adsorption. Subsequent phenol binding proceeds through physisorption,

which is a less active binding mode for reduction by hydrogen. High activity can be restored upon regeneration of proton acceptor sites via reoxidation/reduction of the catalyst.

Introduction

Cyclohexanone is a precursor to caprolactam and adipic acid, which are key intermediates for the synthesis of nylons and polyamide resins. Cyclohexanone is commercially produced by oxidation of cyclohexane or hydrogenation of phenol.¹ The former route involves high reaction temperatures (140-180 °C), pressures (8-20 bar), and low conversion (< 10 %).¹⁻² Phenol hydrogenation is much more efficient and is catalyzed by palladium on carbon (Pd/C) in the liquid phase and catalyzed by palladium on alumina (Pd/Al₂O₃) in the vapor phase.³ Of the two hydrogenation approaches, liquid phase reduction is more selective to the ketone, but operates at high temperatures (175 °C) and under excess hydrogen pressures (13 bar).^{1, 3} Given the importance of this process, significant efforts have been devoted to the development of alternative catalysts that can further improve yields and enable conversion under milder conditions. Several research groups have now achieved remarkable results with conversion and selectivity over 90 % at either room temperature or 1 bar H₂ pressure.⁴⁻¹⁶ The most efficient processes take advantage of the fact that aromatics can be reduced under mild conditions when the activation of H₂ by heterogeneous Pd catalyst is combined with the electrophilic activation of aromatics by soluble Lewis acids.¹⁷ Liu et al. demonstrated the application of this strategy for the hydrogenation of phenol by combining Pd/Al₂O₃ with AlCl₃.⁷ Lee and co-workers significantly improved the process by combining Sc(OTf)₃ with Pd/C, achieving full conversion at 20 °C and 1 bar H₂.⁸ The Lewis acid also favors the selectivity to the cyclohexanone by forming an adduct that is more difficult to reduce to the alcohol. Li, Luque and collaborators achieved similar results with a fully heterogeneous system using Pd supported on the chromium-based MOF MIL-

101, with the chromium centers in the MOF support proposed as Lewis acidic activators for the reaction.¹¹

The strategy of using the support as an active component of the reaction rather than an inert, inactive component merely for catalyst dispersion is particularly attractive from the perspective of advanced catalyst design. In this regard, redox active supports are especially appealing as they have the potential of participating in electron transfer processes during catalysis. Cerium dioxide (ceria) is an interesting support for this purpose because of its reducibility and its interactions with noble metals.¹⁸ These interactions lead to high dispersion of catalytic metals and provide beneficial electronic effects.¹⁹ Ceria and ceria-based materials have been extensively studied as structural and electronic promoters to improve activity and selectivity of heterogeneous catalysts.²⁰ Ceria is the most industrially significant rare earth oxide catalyst mainly due to its use in three-way catalytic converters (TWC) and fluid catalytic cracking (FCC).^{19, 21} Recently, ceria-based materials have been investigated for use in soot removal from diesel engine exhausts,²² volatile organic compound (VOC) degradation,²³ fuel cell technology,²⁴ water-gas shift reaction,²⁵⁻²⁶ preferential CO oxidation (PROX),²⁷ oxidative dehydrogenation,²⁸ and selective hydrocarbon oxidations.²⁹⁻³⁰ The success of ceria and ceria-based materials in catalysis is oftentimes due to facile $\text{Ce}^{4+}/\text{Ce}^{3+}$ redox cycling without disruption of the fluorite lattice structure.²⁰ Furthermore, the redox properties of ceria-based materials can be tuned by incorporation of dopants or deposition of metals, which offer significant opportunities for modifying their activity and improving their performance.³¹

Only a few studies exist for phenol hydrogenation on ceria-based materials. The groups of Inagaki and Scire studied the reaction in the vapor phase over palladium supported on high surface ceria (Pd/CeO₂) at 180 °C (80 % conversion, 50 % selectivity) and 160 °C (40 %

conversion, 95 % selectivity) respectively.³²⁻³³ The liquid phase process was investigated by Li et al. using Ce-doped Pd nanospheres (0.43 mol % Ce) with a hollow chamber, obtaining 82 % cyclohexanone yield under 10 bar H₂ at 80 °C.³⁴ In another paper, Li and co-workers used palladium-cerium-boron supported on hydrotalcite to achieve 82 % conversion and 80 % selectivity within 4 h at 10 bar H₂ and 100 °C.³⁵ Using ceria as the support rather than as a minor component of the catalyst may be a good way to take advantage of its redox properties and its electronic effects on the metal in the liquid phase process. Furthermore, using high surface area ceria as a support should result in higher activity than a low surface area counterpart, because this could lead to increased dispersion of supported metal and larger amounts of reactive species on the surface.³⁶ Herein, we report the synthesis of palladium supported on high surface ceria (Pd/CeO₂) and its exceptional performance for the selective hydrogenation of phenol to cyclohexanone in the liquid phase at low temperature and H₂ pressure.

Experimental

Reagents. Cerium(III) nitrate hexahydrate (Ce(NO₃)₃•6H₂O), palladium(II) acetate (Pd(O₂CCH₃)₂), phenol (C₆H₅OH), tetramethylorthosilicate (TMOS), aluminum(III) isopropoxide (Al(OiPr)₃), cerium (IV) oxide (CeO₂), 10 wt. % palladium supported on carbon (Pd/C), and concentrated nitric acid were purchased from Sigma Aldrich. Pluronic P104 and Pluronic P123 were obtained from BASF. Ce(NO₃)₃•6H₂O was dried under vacuum at room temperature prior to synthesis. 100 % ethyl alcohol was used for all syntheses. All other chemicals were used without further purification.

Synthesis of high surface ceria (CeO₂). In a typical synthesis, Ce(NO₃)₃•6H₂O (8.80 g, 20.3 mmol) and nonionic block co-polymer surfactant Pluronic P104 (10.1 g, 1.71 mmol) were dissolved in ethanol (200 mL) under vigorous stirring (700 rpm) for 3 h. Once thoroughly

homogenized, the solution was cast into a large crystallization dish (diameter 185 mm) and placed into a pre-heated 65 °C oven to undergo solvent evaporation. After 12-24 h, the gel was placed into a pre-heated 150 °C oven for an additional 12 h. To remove the remaining P104 surfactant, the yellow powder was calcined in air at 450 °C for 4 h with a ramp rate of 1 °C min⁻¹. Optimal surface areas were obtained when relative humidity was kept below 60 %.

CAUTION: During thermal treatment at 150 °C combustion occurs within ~12 minutes producing flames which self-extinguish within seconds after all combustible material (i.e. block co-polymer) is burned. The thermal treatment step should be conducted in an oven, preferably in a fume hood to avoid exposure to gaseous decomposition products.

Synthesis of mesoporous silica (SiO₂). This material was prepared following our previously published method.³⁷ Pluronic P104 (7.00 g, 1.19 mmol) was dissolved in aqueous HCl (273.0 g, 1.6 M). After stirring for 1 h at 56 °C, tetramethylorthosilicate (10.6 g, 69.9 mmol) was added and stirred (500 rpm) for additional 24 h. The resulting mixture was hydrothermally treated for 24 h at 150 °C in a high-pressure reactor. Upon cooling to room temperature, the white solid was collected by filtration, washed with copious amounts of methanol, and dried in air. The MSN material was calcined in air at 550 °C for 6 h with a ramp rate of 1.5 °C min⁻¹.

Synthesis of mesoporous alumina (Al₂O₃). The synthesis of alumina was adapted from Yan and co-workers.³⁸ Briefly, non-ionic block co-polymer surfactant Pluronic P123 (0.92 g, 0.16 mmol) was dissolved in ethanol (20 mL) at room temperature. After stirring for 0.5 h, concentrated nitric acid (1.5 mL, 15.8 M) and Al(OiPr)₃ (2.04 g, 10.0 mmol) were added into the above solution with vigorous stirring (800 rpm). The mixture was capped, stirred at room temperature for 5 h, and then cast into a large crystallization dish. The dish was placed into a pre-

heated 60 °C oven to undergo solvent evaporation for 48 h. The light-yellow solid was calcined in air at 400 °C for 6 h with a ramp rate of 1.5 °C min⁻¹.

Synthesis of Pd/M_xO_y. All Pd catalysts were prepared by an impregnation method with a 1 wt. % Pd loading relative to the mass of the support. In a typical synthesis, Pd(O₂CCH₃)₂ (0.0419 g, 0.187 mmol) was dissolved in acetone (1 mL). The support (2.00 g) was placed into a mortar and impregnated with the Pd solution in 0.20 mL increments. After each impregnation step, the catalyst was mixed thoroughly with a pestle until seemingly dry. The material was calcined at 350 °C for 2 h with a 2.5 °C min⁻¹ ramp rate and then reduced under flowing hydrogen at 350 °C for 2 h with a ramp rate of 2.5 °C min⁻¹. **CAUTION:** Special precaution should be taken when preparing (i.e. reducing) Pd/Al₂O₃ as pyrophoric aluminum hydrides may form. The physicochemical properties of non-ceria-based catalysts are reported in Table S1.

Hydrogenation reactions. All reactions were conducted in batch mode under flowing hydrogen (~1 bar) using a Schlenk line. In a typical experiment, the catalyst (48 mg, 1.1 wt. % Pd loading) and phenol (or phenol derivative) solution (4 mL, 0.025 M) were added to a 10 mL round bottom flask equipped with condenser and stir bar. The palladium to substrate ratio was maintained at 5 mole % for all reactions. The flask was placed onto a Schlenk line under a headspace flow of hydrogen and allowed to stir (800 rpm) for 4 h. The reaction product was collected by centrifugation. A 50 µL aliquot of the supernatant was added to 1 mL of ethanol and analyzed in an Agilent GC-MS (7890A, 5975C) with a HP-5MS column. The run started at 60 °C for 0 minutes, then ramped to 150 °C at 5 °C min⁻¹ for 0 minutes, then ramped to 300 °C at 20 °C min⁻¹ for 3 minutes. Resorcinol was used as an internal standard. Conversion was defined as mol % and calculated as moles of converted phenol per mole of starting phenol times 100 %. Selectivity was defined as mol % and calculated as moles of cyclohexanone per moles of

products times 100 %. Yields were defined as mole percent and were calculated as moles of each product multiplied by conversion times 100 %.

TPR and chemisorption. Hydrogen temperature programmed reduction (H₂-TPR) and hydrogen chemisorption were performed in a Micromeritics AutoChem II. H₂ in Ar (H₂/Ar) (10.13 %) was used as the reducing agent or metal dispersion probe. H₂-TPR experiments were performed with a flow rate of 50 mL min⁻¹ and a ramp rate of 10 °C min⁻¹. A cold trap was used to collect water produced during the reduction. H₂-chemisorption analysis was carried out by reducing samples at specified temperatures, then heating/cooling to 250 °C under H₂/Ar, followed by flowing Ar for 15 minutes at 250 °C to remove surface bound hydrogen from Pd crystallites. The sample was then cooled under Ar to -35 °C for hydrogen pulse chemisorption measurements. The palladium dispersion of the catalysts was calculated based on the following equation:

$$D(\%) = \frac{S_f \times M \times V_{ad}}{m \times W \times V_m} \times 100$$

where S_f = stoichiometry factor (the Pd/H₂ molar ratio) = 2; M = the atomic mass of Pd (106.42 g mol⁻¹); V_{ad} = the volume of chemisorbed H₂ at standard temperature and pressure conditions (mL); m = the mass of the sample (g); W = the weight fraction of Pd in the sample as determined by ICP-OES (0.011 g Pd per g sample); V_m = the molar volume of H₂ (22414 mL mol⁻¹) at STP.

The specific surface area of palladium was calculated based on the following equation:

$$\text{Pd Surface Area (m}^2 \text{ g}^{-1} \text{ of Pd)} = \frac{S_f \times N_A \times SA_{cross} \times V_{ad}}{m \times W \times V_m}$$

where S_f = stoichiometry factor (the Pd/H₂ molar ratio) = 2; N_A = Avogadro's number (6.023×10^{23} mol⁻¹); SA_{cross} = palladium cross-sectional area (7.87×10^{-20} m²); V_{ad} = the volume of chemisorbed H₂ at standard temperature and pressure conditions (mL); m = the mass of the

sample (g); W = the weight fraction of Pd in the sample as determined by ICP-OES (0.011 g Pd per g sample); V_m = the molar volume of H_2 (22414 mL mol⁻¹) at STP. The cubic crystallite size of palladium was calculated based on the following equation:

$$\text{Pd Crystallite Size (nm)} = \frac{6 \times M}{m \times W \times d_{Pd} \times N_A \times SA_{Pd}}$$

where M = the atomic mass of Pd (106.42 g mol⁻¹); m = the mass of the sample (g); W = the weight fraction of Pd in the sample as determined by ICP-OES (0.011 g Pd per g sample); d_{Pd} = density of palladium (1.202×10^{-20} g nm⁻³); N_A = Avogadro's number (6.023×10^{23} mol⁻¹); SA_{Pd} = palladium surface area from equation above (nm² g⁻¹ of Pd). The number six is derived from assuming cubic geometry.

Powder X-ray diffraction (PXRD). Diffraction patterns were collected using Co K α 1, K α 2 split radiation (45 kV, 40 mA, $\lambda_{\text{avg}} = 1.7903 \text{ \AA}$) on a PANalytical X'Pert PRO diffractometer equipped with a theta–theta vertical mode goniometer, incident Fe filter, an air-cooled X'Celerator real time multiple strip (RTMS) detector, and spinner stage. The spectra were converted to Cu K α radiation for comparison to standard patterns. Powder XRD samples were prepared by placing powders onto a background-less polycarbonate sample holder. Crystallite sizes were calculated using Scherrer equation:

$$D_{(hkl)} = \frac{K \lambda}{\beta \cos \theta}$$

where K is the shape factor (0.9) of the average crystallite, λ is the X-ray wavelength (0.17903 nm), β is the full width at half maximum (radians), and θ is the Bragg angle (radians).

Electron microscopy/energy dispersive X-ray spectroscopy. Transmission electron microscopy (TEM) was conducted using a FEI Technai G2 F20 field emission microscope and

scanning transmission electron microscope (STEM) operating at 200 kV (point-to-point resolution <0.25 nm and a line-to-line resolution of <0.10 nm). TEM samples were prepared by placing 2–3 drops of dilute ethanol suspensions onto lacey carbon-coated copper grids. The composition of Pd/CeO₂ structures were characterized by elemental mapping and energy dispersive X-ray spectroscopy (EDS) scans in STEM mode.

Surface area and porosimetry. Textural properties of the supports and catalysts were measured by nitrogen sorption isotherms at -196 °C in a Micromeritics Tristar analyzer. The surface areas were calculated by the Brunauer-Emmett-Teller (BET) method, and the pore size distribution was calculated by the Barrett-Joyner-Halenda (BJH) method. Pretreatment of samples for surface area measurement was done by flowing N₂ for 6 h at 100 °C.

ICP-OES. Pd loadings were analyzed by a Perkin Elmer Optima 2100 DV Inductively Coupled Plasma-Optical Emission Spectroscopy (ICP-OES). Samples (5 mg) were digested for 24 h in aqueous HF and HCl solution (0.18 v/v % and 5 v/v % respectively).

Diffuse reflectance infrared Fourier transform (DRIFT). Measurements were made on a Bruker Vertex 80 FT-IR spectrometer with OPUS software and apodized spectral resolution of 0.2 cm⁻¹. The spectrometer was equipped with a HeNe laser and photovoltaic MCT detector. A Praying Mantis™ diffuse reflectance accessory and high temperature reaction chamber was used for room temperature and variable temperature measurements, respectively.

Diffuse reflectance UV/Visible absorption spectroscopy (DR UV/Vis). Measurements were made on an Ocean Optics USB2000+ fiber optic spectrometer (bandwidth = 350-1100 nm) operating in absorption mode. Samples were prepared by suspending 50 mg of ceria in 0.5 mL of

phenol dissolved in test solvents (33 mg mL⁻¹) overnight. The solid was collected by centrifugation and analyzed.

Nuclear magnetic resonance. Proton nuclear magnetic resonance (¹H-NMR) spectra were collected on a Varian VXR-300 equipped with a narrow bore 7.05 tesla/300 MHz magnet and a standard ¹H probe. Deuterated benzene and cyclohexane were used as solvent and internal standard, respectively.

X-Ray photoelectron spectroscopy (XPS). XPS analysis was done with a PHI 5500 multi-technique system using a standard Al x-ray source. The Pd/CeO₂ catalyst exposed to air was prepared by deposition onto double-sided tape sample holder. The Pd/CeO₂ catalyst exposed to hydrogen was prepared in a glove box and then transferred to the XPS chamber in an air-free sample cell. Charge correction was accomplished by shifting the O1s peak to 529.0 eV for all spectra.³⁹

Results and Discussion

Support synthesis and characterization. The ceria support was synthesized by an evaporation-induced self-assembly method (EISA) commonly used for the synthesis of high surface metal oxides.⁴⁰⁻⁴³ The physical properties of CeO₂ support and Pd/CeO₂ catalyst are summarized in Table 1. The PXRD pattern measured was indexed to the fluorite cubic structure of ceria (space group *Fm3m* (225), JCPDS 34-0394) (Figure 1a). The broad peaks indicated small ceria crystallites, and estimation of the average crystallite size using the Scherrer equation provided a value of 5.9 nm. Nitrogen sorption analysis gave a high specific surface area and displayed a hysteresis loop at high partial pressures suggesting significant textural porosity (Figure 1b). TEM imaging revealed that the material is comprised of aggregated particles with

small voids within each aggregate that likely to account for the measured pore volume (Figure 1c). HR-TEM (Figure 1d) examination indicated the presence of the most thermodynamically stable (111) planes of the cubic lattice.³¹ Given the polycrystalline nature of the material, (200) and (220) planes were also observed, although far less prevalent than the (111) planes.

Table 1. Physical properties of CeO₂ support and Pd/CeO₂ catalyst.

Sample	BET Surface Area (m ² g ⁻¹)	BJH Pore Volume (cm ³ g ⁻¹)	CeO ₂ Crystallite Size (nm) ^a	Pd Dispersion (%) ^b	Pd Crystallite Size (nm) ^b
CeO ₂	241	0.31	5.9	---	---
Pd/CeO ₂	159	0.27	7.1	64	1.5 nm

^a Obtained by PXRD analysis. ^b Obtained by H₂ chemisorption.

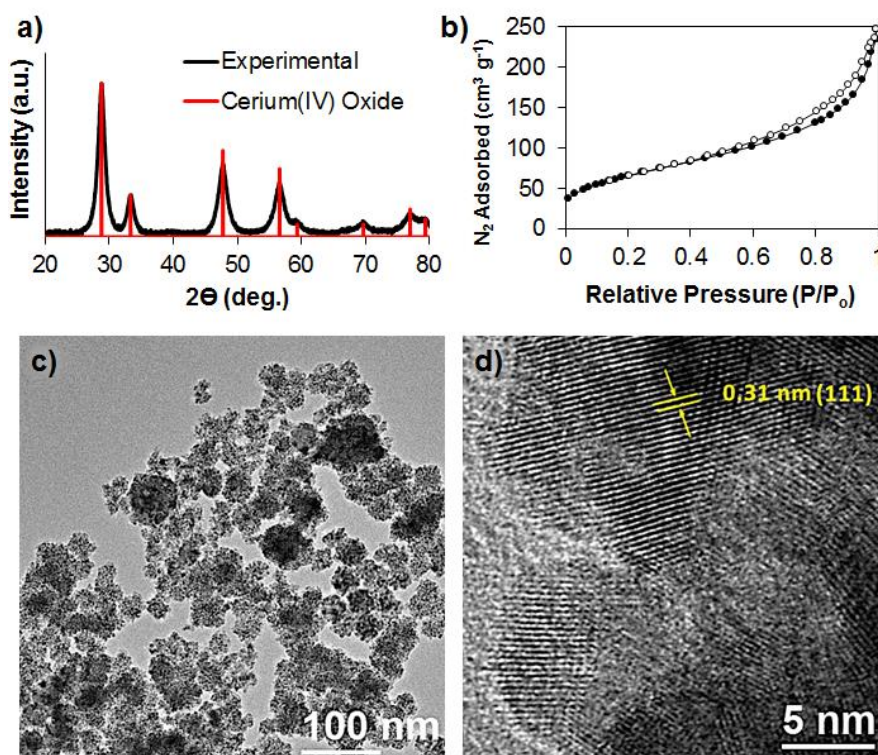


Figure 1. a) Wide-angle PXRD pattern of the synthesized CeO₂ (black) and reference cerium(IV) oxide (red); b) N₂ sorption isotherms of CeO₂; c) TEM and d) HR-TEM images of CeO₂ showing a d-spacing of 0.31 nm corresponding to the (111) planes of CeO₂.

Catalyst synthesis and characterization. The catalyst was prepared via incipient wetness impregnation. An acetone solution of palladium (II) acetate was initially added to the ceria material, the mixture was then calcined in air to produce PdO_xH_y/CeO₂ precatalyst, which was finally reduced by flowing hydrogen at 350 °C to give the Pd/CeO₂ catalyst. The PXRD pattern of Pd/CeO₂ is nearly identical to CeO₂ (Figure 2a). The ceria reflections of the catalyst are slightly narrower than the original support, suggesting sintering occurred during the additional thermal aging, which is common for ceria under reducing environments.⁴⁴ This sintering likely led to the lowered specific surface area and pore volume of Pd/CeO₂ relative to CeO₂ (Table 1). Palladium species could not be detected by XRD analysis, suggesting it was highly dispersed over the support,⁴⁵ and/or incorporated into the ceria framework.⁴⁶ The rationalization of highly dispersed palladium is consistent with the low loading of palladium (1.1 wt. % as determined by ICP-OES) and its high affinity for ceria.⁴⁷ In support of this idea, sub-ambient pressure H₂ chemisorption measurements gave a high Pd dispersion of 64 % and a calculated cubic crystallite size of 1.5 nm. The catalyst was further investigated by STEM-HAADF imaging (Figure 2b). Palladium particles could not be directly observed possibly due to high dispersion, small crystallite size, and/or low contrast between Pd and Ce. However, Energy dispersive X-ray spectroscopy (EDS) mapping confirmed the presence of Pd on the support (Figures 2c, S2). XPS analysis was also used to evaluate the oxidation state of palladium in the catalyst. The binding energy of Pd 3d_{5/2} electrons in the catalyst exposed to ambient air (336.5 eV) is close to that in PdO (336.9 eV) suggesting part of the metal, likely the atoms at the surface, is easily oxidized in air (Figure 2d, black trace).³⁹ Exposure of the catalyst to H₂ at room temperature (a more accurate description of the catalyst under catalytic conditions) shifts the

binding energy to lower values (335.2 eV) suggesting significant conversion to the metallic form (Figure 2d, red trace).

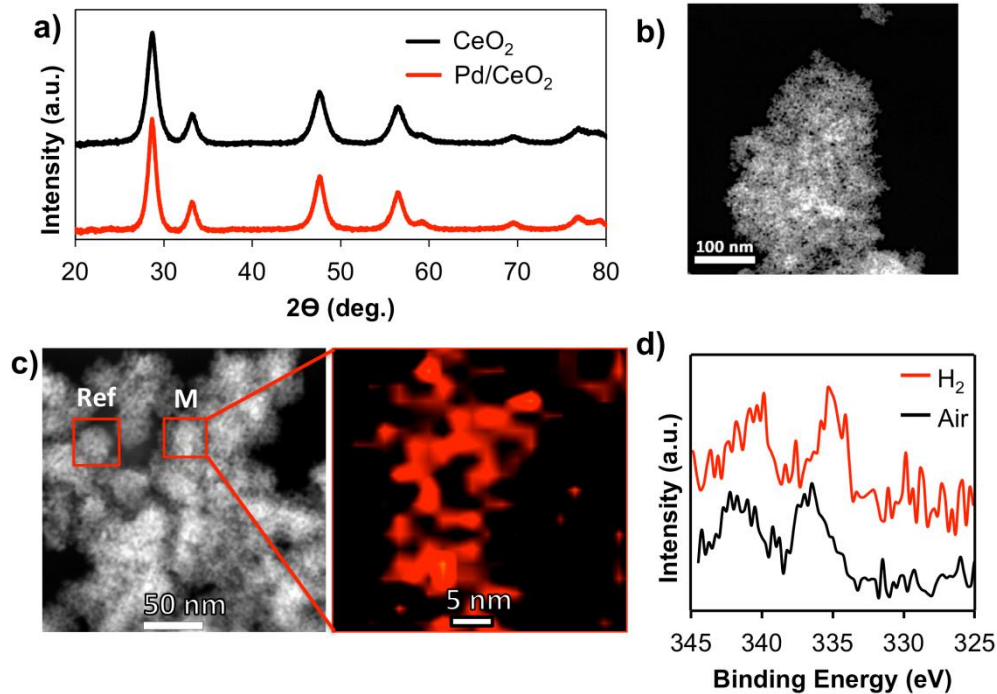


Figure 2. a) Wide-angle PXRD patterns of CeO₂ support (black) and Pd/CeO₂ catalyst (red); b) STEM-HAADF image of Pd/CeO₂; c) EDS map of Pd (red image) on a 25 x 25 square section of the support (Region M), the square labeled ‘Ref’ was taken as a reference for drift correction between scans; d) x-ray photoelectron spectra of Pd/CeO₂ exposed to air (black) and to hydrogen atmosphere (red).

H₂-TPR experiments were run on CeO₂ and the precatalyst (PdO_xH_y/CeO₂) to study the effect of Pd impregnation on the redox properties of the material (Figure 3). The results are summarized in Table 2. Upon hydrogen treatment of CeO₂, two peaks were observed corresponding to reduction of surface and bulk ceria at 473 °C (T₂) and 791 °C (T₃), respectively.⁴⁸ Overall, the amount of H₂ consumed in the pure CeO₂ sample was less than the total amount consumed by the PdO_xH_y/CeO₂ precatalyst. There was considerable hydrogen consumption by the PdO_xH_y/CeO₂ precatalyst at 95 °C (T₁) which can be attributed, in part, to

the reduction of PdO_xH_y species.⁴⁹ Interestingly, the PdO_xH_y/CeO₂ precatalyst consumed less H₂ at the higher temperatures associated with surface and bulk ceria reduction than the Pd-free CeO₂ support. Thus, the presence of Pd facilitated the reduction of surface and bulk CeO₂ as indicated by the lower reduction temperatures compared to the support alone (332 °C for T₂ and 703 °C for T₃). The total amount of hydrogen consumed by PdO_xH_y/CeO₂ was 0.40 mmol H₂ g⁻¹ greater than the amount consumed by the CeO₂ support (Table 2). Assuming that Pd is in the +2 oxidation state, this is 4 times greater than the theoretical amount of hydrogen that ought to be consumed (0.10 mmol H₂ g⁻¹) to reduce PdO to Pd based off ICP results. If all Pd atoms formed hydrides this would imply consumption of additional 0.05 mmol H₂ g⁻¹, which would leave still 0.25 mmol H₂ g⁻¹. This difference suggests hydrogen spilled over onto the support during the reduction of PdO_xH_y, which could have been either physisorbed or led to the reduction of ceria.⁵⁰ A significant decrease in the amount of hydrogen consumed by the PdO_xH_y/CeO₂ catalyst at high temperatures (Table 2) relative to the CeO₂ support suggested that some hydrogen spilled over leading to the reduction of ceria. These results are consistent with previous hydrogen adsorption studies for palladium-ceria catalysts.⁵⁰ Hydrogen spillover is common in reducible oxides serving as supports for noble metals.⁵¹

Table 2. Reducibility of CeO₂ support and PdO_xH_y/CeO₂ precatalyst.

Sample	H ₂ Consumed at T ₁ (mmol g ⁻¹)	H ₂ Consumed at T ₂ (mmol g ⁻¹)	H ₂ Consumed at T ₃ (mmol g ⁻¹)	Total H ₂ Consumed (mmol g ⁻¹)
CeO ₂	---	0.69	1.1	1.79
PdO _x H _y /CeO ₂	0.98	0.63	0.58	2.19

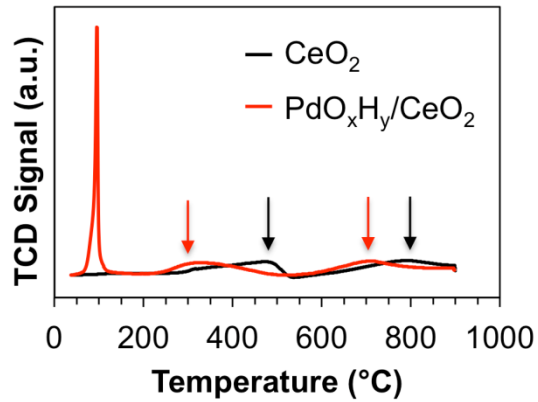


Figure 3. H₂-TPR profile of CeO₂ (black) and PdO_xH_y/CeO₂ (red).

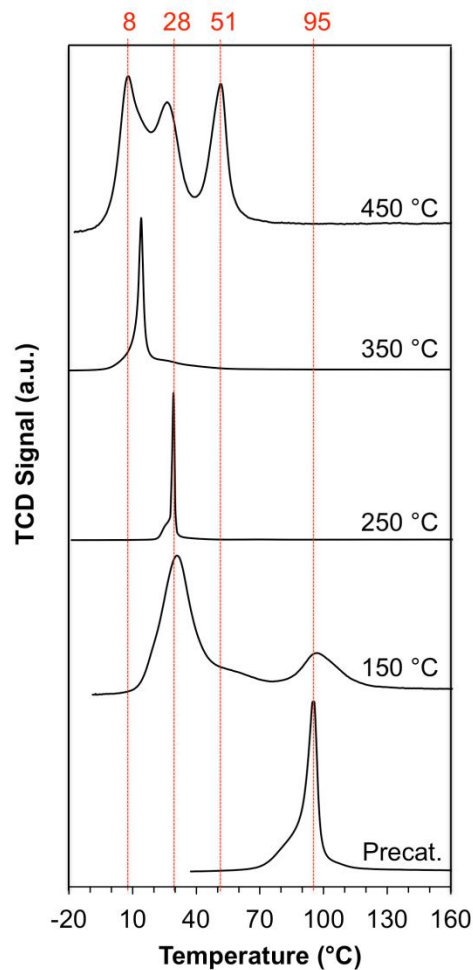


Figure 4. H₂-TPR profiles of PdO_xH_y/CeO₂ precatalyst reduced at 150 °C, 250 °C, 350 °C, and 450 °C. To measure the TPR each sample was previously re-oxidized at 350 °C. TPR of the precatalyst is included at the bottom as a reference. Temperatures of selected peaks are indicated in red at the top.

The TPR profile of the PdO_xH_y/CeO₂ precatalyst (Figure 3) suggested that complete reduction of Pd is achieved at temperatures above 125 °C. The effects of PdO_xH_y/CeO₂ reduction temperature on the redox properties of the catalyst were further evaluated on the basis of literature reports of the significant structural changes observed for noble metals supported on ceria under reducing conditions.⁴⁷ To this end, four Pd/CeO₂ samples were produced by reduction of PdO_xH_y/CeO₂ precatalyst at 150 °C, 250 °C, 350 °C and 450 °C respectively. Each sample was then re-oxidized (350 °C under O₂/He mixture for 1 h, 10 °C min⁻¹) to examine their reducibility as a function of pretreatment temperature. The TPR analysis revealed significant effects of the pre-reduction temperature on the H₂ uptake of the catalyst (Figure 4). PdO_xH_y/CeO₂ pre-reduced at 150 °C consumed hydrogen near room temperature (28 °C), but there was also considerable hydrogen uptake at the same temperature as the original precatalyst (95 °C). Pretreatment of PdO_xH_y/CeO₂ under H₂ at 250 °C or 350 °C resulted in only one peak centered at 28 °C and 14 °C, respectively. PdO_xH_y/CeO₂ pre-reduced at 450 °C showed three hydrogen consumption peaks at 8 °C, 25 °C and 51 °C. These changes could be due to interactions between Pd and CeO₂ and structural transformations undergone by CeO₂ as reduction temperature increases, which have been well documented for noble metals supported on ceria under reducing conditions.⁴⁷ Thus, increasing reduction temperatures may lead to incremental spreading of Pd over CeO₂ to give smaller particles that are reactive at lower temperatures, as indicated by the shift in the TPR peak from 95 °C to 28 °C and 14 °C. While reduction of the precatalyst at 450 °C led to further shifting of signal to 8 °C, additional peaks appeared at 25 °C and 51 °C. These higher temperature H₂ uptake peaks can be attributed to the metal existing in different types of environments that involve additional interactions with CeO₂,

such as decoration phenomena (i.e. burial of surface palladium by sintered ceria),^{47, 52} alloying of Pd-Ce,⁵³ and/or electronic-support effects.³¹

Dispersion measurements were taken on the catalysts after the initial reduction in order to further evaluate the changes in Pd surface with reduction temperature (Figure S1). Measurements were performed at -35 °C to eliminate erroneous results from hydrogen spillover.^{31, 54} The results revealed that, indeed, Pd dispersion increased as reduction temperature increased from 150 °C to 350 °C. Sanchez and Gazquez⁵² proposed a model to explain the changes in dispersion of metals in oxide supports upon reduction at high temperatures. In their model, they proposed the occupancy of oxygen ion vacancies by metal atoms; as the reduction temperature increases, more vacancies are formed which lead to migration of Pd crystallites into these high energy environments resulting in increased dispersion. Part of the hydrogen consumed by PdO_xH_y/CeO₂ pre-reduced at 150 °C was observed at the same temperature (95 °C) as the original precatalyst (Figure 4). This suggests that some Pd crystallites remained in the same environment as they were upon deposition of Pd(O₂CCH₃)₂ precursor and calcination in air, while others relocated to a different environment. As the pre-reduction temperature was increased to 250 °C, only one peak (28 °C) was observed, which coincided with part of the hydrogen uptake temperature for the catalyst pre-reduced at 150 °C (Figure 4). These data are consistent with the Pd species spreading over different sites on the surface of CeO₂. Recent studies have shown that surface oxygen vacancies promote late transition metal dispersion over ceria supports.⁵⁵⁻⁵⁶ Pre-reduction at 350 °C resulted in one peak at 14 °C (Figure 4). Interestingly, this pre-reduction temperature corresponded to the temperature for reduction of surface ceria (i.e. vacancy formation) in the PdO_xH_y/CeO₂ precatalyst (Figure 3 (red)). Pre-reduction of PdO_xH_y/CeO₂ at 450 °C led to a dramatically lower dispersion than the catalysts pre-reduced at lower temperatures. The sharp

decrease in metal surface area (from $285 \text{ m}^2\text{g}^{-1}$ to $34 \text{ m}^2\text{g}^{-1}$) supports the idea that reduction of the precatalyst at $450 \text{ }^\circ\text{C}$ led to burial of surface Pd into CeO_2 as previously suggested by the TPR measurements; this catalyst encapsulation is likely the result of support sintering (Figures 4, S1).

Catalysis. Hydrogenation reactions were carried out in batch mode by flowing hydrogen ($\sim 1 \text{ bar}$) in the headspace of a hexane solution of phenol, with a Pd to phenol mole ratio of 0.05. The results are summarized in Table 3. There was no phenol conversion when CeO_2 or $\text{PdO}_x\text{H}_y/\text{CeO}_2$ was used as the catalyst, confirming that Pd was crucial for hydrogen activation (Entry 1 and 2). The Pd/ CeO_2 catalyst hydrogenates 85.5 % of the phenol with a ketone selectivity of 96.1 % at room temperature and 1 bar hydrogen in only 4 h (Entry 3). These results show that Pd/ CeO_2 is competitive with the best performing catalysts reported for the liquid-solid interfacial hydrogenation of phenol.⁴ Catalysts prepared in the same way using other commonly employed supports (e.g. alumina, silica and carbon) gave significantly lower conversion under the same reaction conditions. This could be due to the weak interactions between the supports and Pd, which lead to low catalyst dispersion (Table S1) or due to the inability to shuttle hydrogen from Pd to non-reducible supports (i.e. spillover),⁵¹ which limits their influence on catalytic turnover. Furthermore, Pd supported on commercial ceria (surface area $55 \text{ m}^2 \text{ g}^{-1}$) was less active than Pd/ CeO_2 , showing the clear advantages of using high surface area ceria support to promote the selective hydrogenation of phenol.

Table 3. Reaction conditions and results for the hydrogenation of phenol in hexane.

Entry	Catalyst	T (°C)	t (h)	Conversion (%)	Selectivity (%)	
					C=O	OH
1	CeO ₂	25	4	0.0	---	---
2	PdO _x H _y /CeO ₂	25	4	0.0	---	---
3	Pd/CeO ₂	25	4	86.2 ± 1.8 ^c	96.3 ± 1.4	3.7 ± 1.4
4	Pd/CeO ₂	35	4	94.1 ± 0.4	90.8 ± 3.4	9.2 ± 3.4
5	Pd/Al ₂ O ₃	25	4	7.4 ± 3.4	100.0 ± 0.0	0.0
6	Pd/SiO ₂	25	4	36.6 ± 3.3	100.0 ± 0.0	0.0
7 ^a	Pd/C	25	4	42.7 ± 2.5	95.4 ± 2.6	4.6 ± 2.6
8 ^b	Pd/CeO ₂	25	4	62.5 ± 3.6	96.2 ± 2.0	3.8 ± 2.0

^aCommercial Pd/C. ^bCommercial ceria. ^cStandard deviations calculated from 3 different catalytic runs.

The reduction temperature used during the synthesis of Pd/CeO₂ catalyst greatly affected its activity for phenol hydrogenation. The catalysts reduced at 150, 250 and 450 °C gave significantly lower conversions than the catalyst reduced at 350 °C (Figure 5). The differences can be attributed to the dispersion and the nature of the active sites (Figures 4, S1). The changes in TPR profiles relative to catalyst reduction temperature must reflect the changes that occur in the interactions between the metal and support. Considering that the amount of H₂ taken up during the TPR experiments significantly exceeded the stoichiometric amount required to reduce the precatalyst, the temperatures of the TPR peaks could be taken as indicators of the capacity of the catalytic sites to activate H₂. The catalysts prepared at 250 and 350 °C gave single TPR peaks at 28 and 14 °C, and the conversion of phenol using the former as a catalyst was 76 % relative to that using the latter. The catalyst reduced at 150 °C had a TPR peak at a similar temperature (29 °C) as the sample prepared at 250 °C; however, there was a second catalytic site, identified by a

reduction peak at 95 °C, which could be responsible for lowering the conversion of phenol (42 % relative to the conversion with the catalyst prepared at 350 °C). While the catalyst prepared at 450 °C had a TPR peak at 8 °C, there were also two additional peaks at 25 and 51 °C that accounted for 75 % of the H₂ consumed. If the latter peaks correspond to sites that are, as suspected, buried within the CeO₂ matrix because of high temperature reduction, then they could be responsible for the decreased conversion (44 % relative to that of the catalyst prepared at 350 °C). Decreased hydrogenation efficiency upon high temperature reduction of metal-supported ceria catalysts has also been observed for other systems and has been attributed to catalyst burial,⁵⁷⁻⁵⁸ which could result from support sintering induced by thermal treatment under H₂.

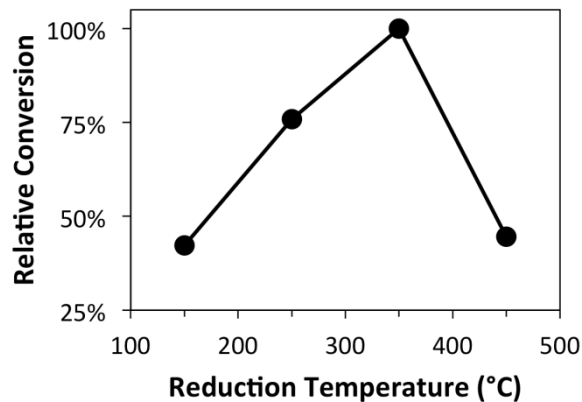


Figure 5. Relative conversion of phenol over Pd/CeO₂ as a function of PdO_xH_y/CeO₂ reduction temperature.

While H₂ adsorption and activation takes place at Pd sites, phenol is expected to adsorb to the surface of the support. The high catalytic activity of Pd/CeO₂ could result from high dispersion of Pd and H₂ spillover onto the reducible support, but also from activation of phenol upon adsorption to surface sites of CeO₂. To better understand how phenol interacts with the CeO₂ support, temperature programmed DRIFT studies were conducted. The spectrum of CeO₂

after evacuation under vacuum at 150 °C showed four distinct bands at 3710, 3689, 3660, and 3554 cm^{-1} (Figure 6a). Lavalley and coworkers assigned the bands to mono-coordinated OH (I) species (3710 cm^{-1}), doubly bridging OH (II) species (3657 cm^{-1}), triply bridging OH (III) species (3581 cm^{-1}), and surface-bound water (3687 cm^{-1}).⁵⁹⁻⁶¹ The latter was classified on the basis of the characteristic $\delta(\text{OH})$ mode at 1631 cm^{-1} and the disappearance of the band at 3687 cm^{-1} upon evacuation at 150 °C. However, our experimental data showed no $\delta(\text{OH})$ mode at 1631 cm^{-1} after evacuation at 150 °C (Figure 6b) while the band at 3689 cm^{-1} remained even after increasing the temperature to 200 °C. The band at 3689 cm^{-1} is likely due to the hydroxyl stretch of surface-bound hydrogen carbonate species.⁶² The other peaks in Figure 6b correspond to various binding modes of carbonate from contamination during the synthesis and/or calcination in air.⁶² After evacuation at 150 °C, a dilute solution of phenol in hexane was deposited onto CeO_2 at room temperature under air- and water-free conditions. The difference spectrum in the hydroxyl region clearly shows that some hydroxyl bands have disappeared indicated by the negative peaks at 3710, 3689, and 3660 cm^{-1} (Figure 6c). In addition, there was an emergence of a band at 1631 cm^{-1} attributed to newly-formed water (Figure 6d). Evacuation at 150 °C resulted in the removal of the band at 1631 cm^{-1} (Figure 6d, red). The disappearance of hydroxyl groups and the appearance of water suggest that phenol undergoes dissociative chemisorption on ceria to form phenoxy species (Scheme 1). The formation of phenoxy species is also consistent with the basic nature of cerium dioxide.³¹ The C-O stretching frequency of cerium-bound phenoxy is expected to shift relative to that of phenol,⁶³ and the O-H bands of phenol should not be observed. The peaks in Figure 6d at 1587, 1479, and 1273 cm^{-1} correspond to adsorbed phenyl species (Figure S3). For comparison, the intense C-O stretching frequency of phenol occurs at 1259 cm^{-1} (Figure S4a).⁶⁴ Figure 6d shows an intense absorption band at 1273

cm^{-1} , which is attributed to the C-O stretch of a phenoxy molecule covalently bonded to a cerium cation. The increased C-O vibrational energy relative to phenol is consistent with the formation of cerium-bound phenoxy owing to the strong interaction expected between cationic cerium and anionic oxygen.⁶³ This likely results in electron withdrawal from phenoxy towards cerium cation and shortening (i.e. strengthening) of the C-O bond. The various O-H bands of phenol are typically observed at 3623, 3350, 1343, and 1207 cm^{-1} .⁶⁴ The O-H out-of-plane (1343 cm^{-1}) and intense in-plane (1207 cm^{-1}) bends are absent upon phenol adsorption onto CeO_2 (Figure S4a). Also, Figure 6c and Figure S4b show no indication of the O-H stretch at 3623 and 3350 cm^{-1} . The only increased intensity is observed in the triply bridging hydroxyl region (3552 cm^{-1}) even after degassing the sample at 150 °C under vacuum (Figure S5), which suggests new triply bridging hydroxyl groups are formed upon adsorption of phenol (Scheme 1c).⁶⁵

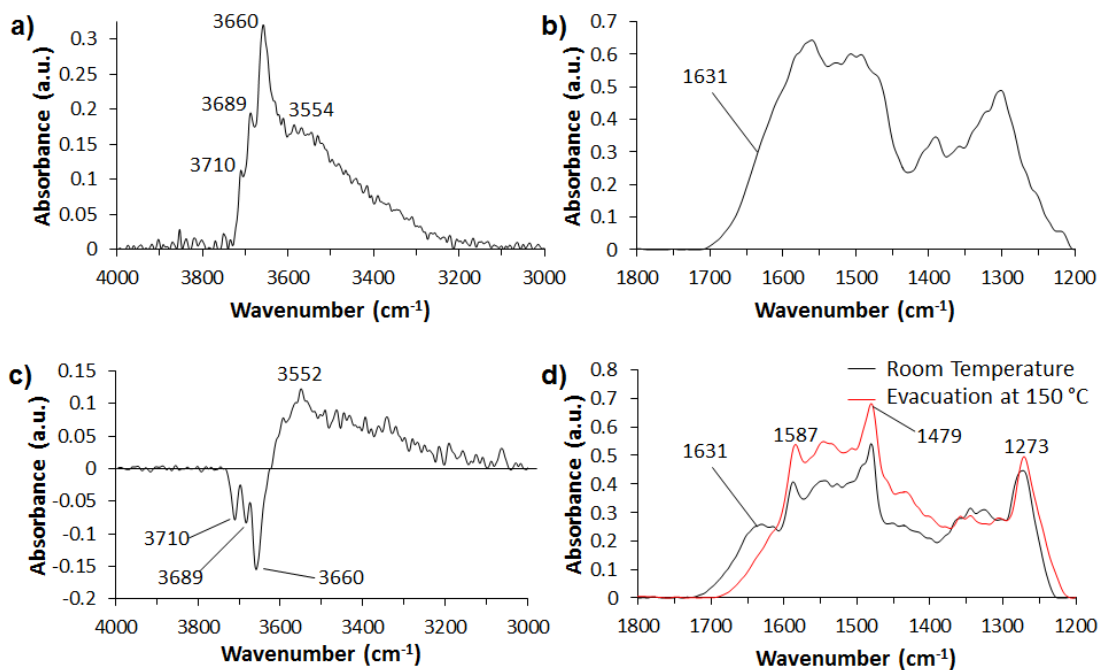
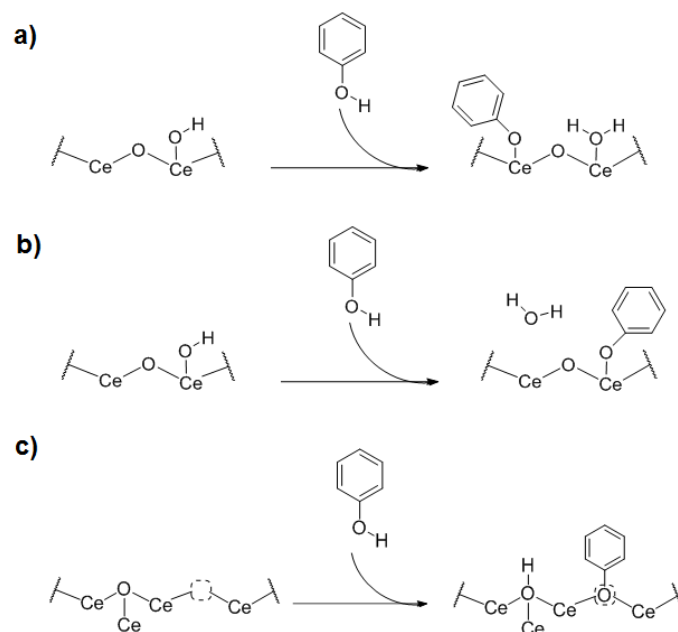


Figure 6. DRIFT spectra of CeO_2 recorded at 150 °C under evacuation from (a) 4000-3000 cm^{-1} and (b) 1800-1200 cm^{-1} , (c) DRIFT difference spectrum of CeO_2 evacuated at 150 °C and phenol adsorbed onto CeO_2 at room temperature, (d) DRIFT spectra of phenol adsorbed onto CeO_2 at room temperature and under evacuation at 150 °C.



Scheme 1. Possible phenol adsorption mechanisms on CeO₂. Phenol undergoes dissociative adsorption onto cerium cation (a) adjacent to a surface hydroxyl, (b) containing a surface hydroxyl, and (c) at an oxygen vacancy to produce triply-bridging surface hydroxyl in its neighborhood.

The phenol adsorption analysis suggests that coordinatively unsaturated cerium cations near hydroxyl groups may be active sites for the reaction. It is not entirely clear, however, whether the newly-formed water stays bound to the surface or desorbs under the reaction conditions. To address the latter, ¹H-NMR spectroscopy studies were conducted in deuterated benzene. The CeO₂ support was degassed at 150 °C under vacuum and placed into a NMR tube containing phenol dissolved in benzene-*d*₆. The ¹H-NMR spectrum showed the formation of water and decrease of phenol upon addition of CeO₂ (Figure S6). Introduction of more CeO₂ into the same NMR tube led to increased water signal and decreased phenol signal. Because the signals from phenol and water result from the liquid phase species (i.e non-surface-bound), it can be concluded that water desorbs from the surface of CeO₂ in benzene. However, when CeO₂ was introduced into an NMR tube containing phenol dissolved in hexane-*d*₁₄ phenol signals were lost

from the spectra but no water was observed in the liquid phase, even though water was detected on the solid by DRIFT analysis. Thus, the water formed upon phenol adsorption on CeO₂ remains bound to the surface of the support when the reaction is performed in hexane.

The production of water upon phenol binding suggested that performing the reaction in water should affect the binding equilibrium and consequently conversion. Indeed, the catalytic activity decreased dramatically when the reaction was run in water, requiring up to 12 h to achieve 69 % conversion at room temperature and 1 bar H₂ (Table S2). Inhibition of the reaction was likely due to adsorption of water on CeO₂ competing with phenol, thus limiting formation of phenoxy species. Dissociative and non-dissociative adsorption of water on ceria has been shown to occur at room temperature and is even more pronounced on reduced ceria.⁶⁶ The formation and relative amounts of phenoxy species could be indirectly determined by the color change of the material, which results from the charge transfer of the bound phenoxy to cerium cations.⁶⁷ The color change of CeO₂ was obvious when in contact with hexane solution of phenol, but was less apparent in an aqueous solution of phenol (Figure 7a). Diffuse reflectance UV-Vis measurements of the solids obtained by subtracting the contribution of CeO₂ clearly showed a higher absorbance (λ_{max} 480 nm) when hexane was used as solvent compared to water, an indication of higher amounts of phenoxy species present on the former (Figure 7b). These findings suggest that the increased catalytic activity in hexane relative to water may be partially due to the increased amount of phenoxy species formed on the ceria surface. The formation of a cerium-bound phenoxy group as an intermediate in the reduction can lead to a similar path of activation as the one exploited by Liu,⁷ Lee,⁸ Li and Luque,¹¹ because the direct complexation of oxygen to cerium cation results in electron withdrawal from the ring. This activation mechanism

is also consistent with the increased vibrational energy of the C-O stretch of phenol adsorbed onto CeO₂ (Figure 6d).

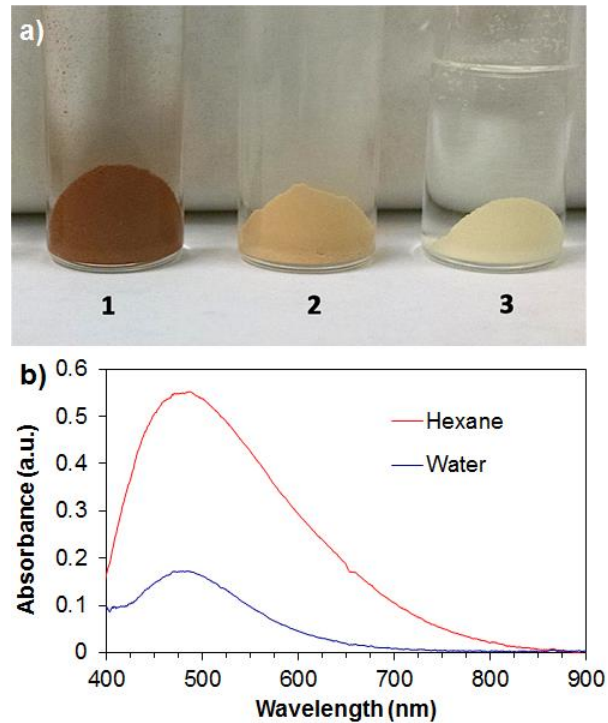


Figure 7. (a) CeO₂ samples treated with **1** hexane solution of phenol, **2** aqueous solution of phenol, and **3** water, (b) DR UV-Vis difference spectra of CeO₂ and CeO₂ after removal from different phenol solutions.

Catalyst recycling experiments performed in hexane and water provided additional insight on the system (Figure 8). In hexane, the conversion decreased by nearly 50 % after the third cycle, but then appeared to stabilize during subsequent reaction cycles. In water, the decrease in catalyst performance was much milder with successive cycles. After an initial decrease of about 10 %, the conversion became steady in the following cycles. ICP-OES analysis of both hexane and water spent solutions had no detectable metal, indicating that leaching was not the cause of the decreased activity.⁶⁸ In addition, hot filtration experiments proved the active

phase was not homogenous.⁶⁹⁻⁷⁰ Interestingly, the catalytic activity could be fully recovered for both samples by regeneration via oxidation followed by reduction of the materials.

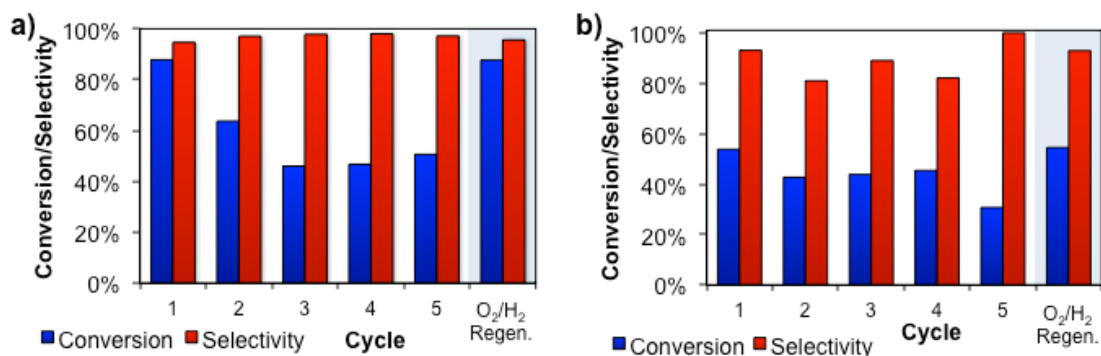


Figure 8. Cycling experiments for the hydrogenation of phenol using Pd/CeO₂ (a) in hexane at T = 25 °C, (b) in water at T = 35 °C. Reaction conditions: t = 4 h, P_{H₂} = 1 bar, Pd : Phenol = 5 mol %.

The catalysts were washed with the solvents used in the reaction, dried and analyzed by DRIFT to elucidate the types of surface species present after the conversion (Figure 9). The different possible types of surface-bound species were independently supported by DRIFT spectra of phenol, cyclohexanone, and cyclohexanol deposited onto the catalyst (Figure S3). The bands at 3070, 1596, 1482, 1263, and 1166 cm⁻¹ were assigned to adsorbed phenyl species and at 2929, 2854, 1446, 1400, and 1157 cm⁻¹ to cyclohexyl species. The bands at 3699, 3558 cm⁻¹ correspond to surface hydroxyls, and at 1654, 1544, and 1236 cm⁻¹ to H₂O, CO₂, and HCO₂⁻ on the catalyst surface, respectively (Figure S7).⁶¹⁻⁶² Phenyl and cyclohexyl compounds (cyclohexanone and/or cyclohexanol) were observed on the catalyst for the reaction run in hexane (black trace), while only cyclohexyl compounds were observed on the catalyst used in water (red trace). The absence of adsorbed phenyl species for the reaction in water, even if the reaction is incomplete, supports the idea that water competes for adsorption with phenyl or

phenoxy species, which is consistent with the visual inspection and DR UV/Vis measurements of CeO₂ treated with aqueous phenol (Figure 7). Also, the hydroxyl band at 3699 cm⁻¹ is present on the catalyst for the reaction in water, but absent for the reaction in hexane. The absence of the hydroxyl band for the reaction in hexane is consistent with DRIFT analysis of phenol adsorbed onto CeO₂ (Figure 6c) and the presence of the hydroxyl band for the reaction in water is consistent with the lower amounts of phenoxy species (formed at the expense of hydroxyl species) on CeO₂ in water (Figure 7).

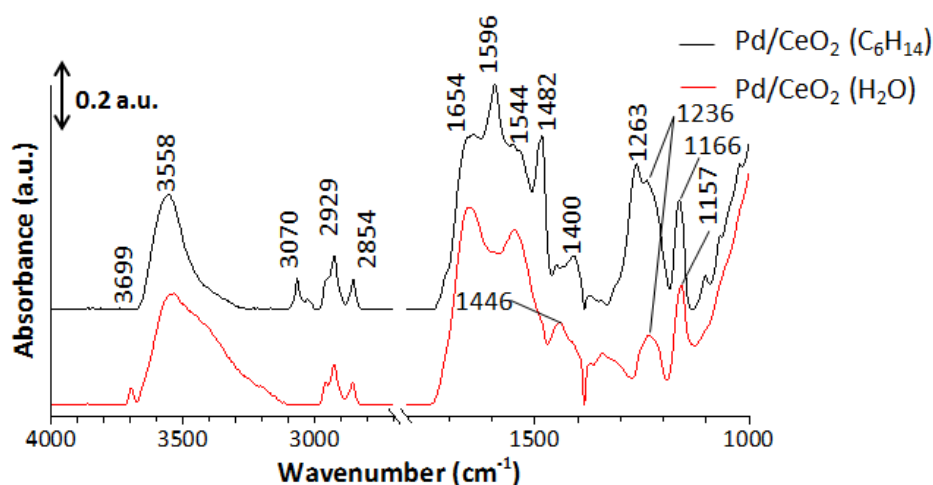
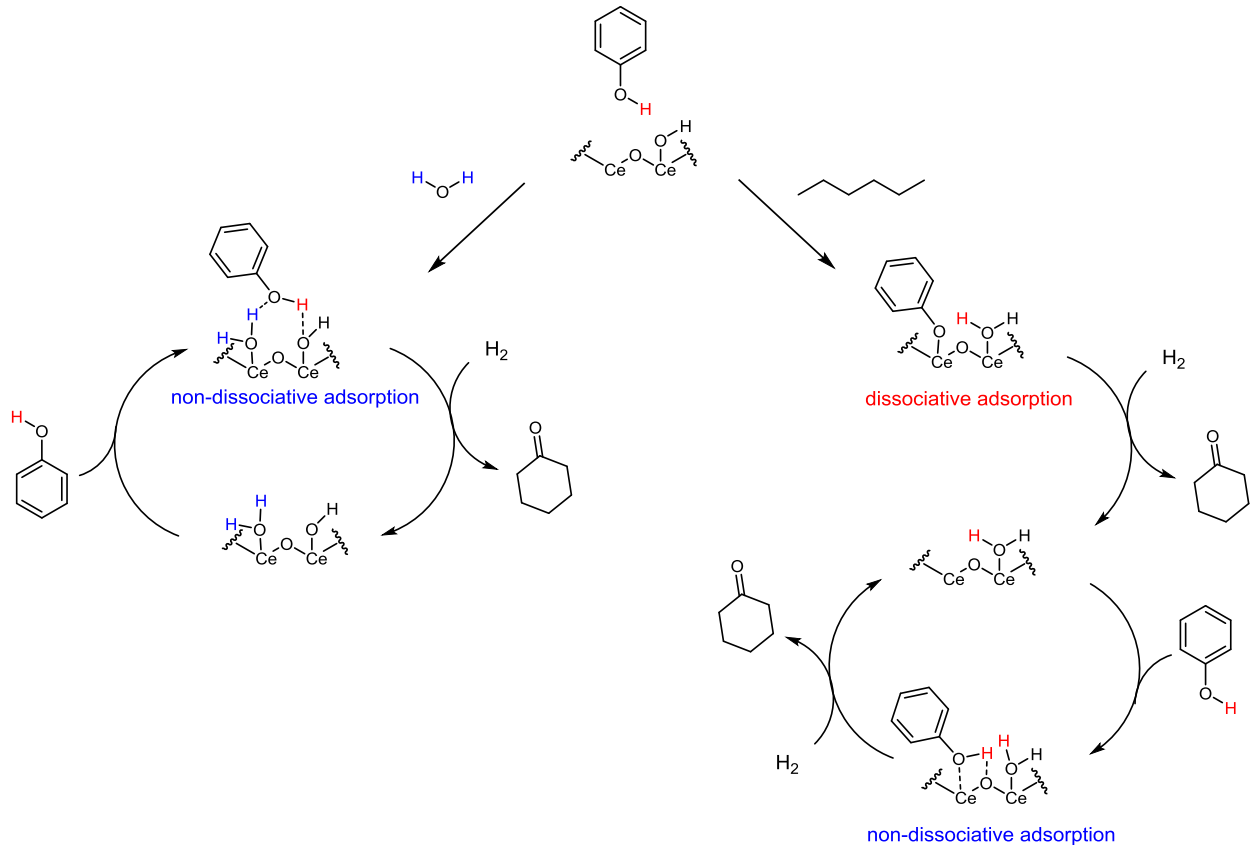


Figure 9. DRIFT spectra of Pd/CeO₂ catalysts after reaction in hexane (black) and water (red).

The transformation of ceria hydroxyl groups into water during phenol adsorption and the decreased activity upon cycling suggests that cerium cations near hydroxyls are highly effective sites for phenol activation in hexane and were not regenerated *in situ*. The data put forth suggests that the fundamental difference between catalyst activity and recyclability in water and hexane is the way in which phenol adsorbs to the CeO₂ support. While dissociative adsorption of phenol onto the support is significant in hexane, the interaction in water seems to occur mainly through physisorption, as dissociative binding is limited by competitive adsorption of water. Physisorbed

phenol is expected to be less active for reduction by dissociated H_2 than phenoxy coordinated to cerium cation. The reason being, the cerium centers are better able to activate the phenolic ring for nucleophilic attack by dissociated H_2 because they pull more electron density away from the ring, than simple hydrogen bonds with hydroxyls/water on the ceria surface. Thus, the higher activity observed in hexane should be due to the dissociative phenol adsorption and its direct binding to coordinatively unsaturated Ce cations, which is enabled by the lack of competition between substrate and solvent (Scheme 2). However, upon phenoxy formation and subsequent reduction to the ketone or alcohol, the phenoxy-forming sites were seemingly not regenerated as indicated by the decreased activity observed in the recycling experiments. In order for the active site to be retained, a hydroxyl near a coordinatively unsaturated cerium cation should be present, which is not the case after one phenol molecule adsorbs dissociatively and is reduced (Scheme 2). The proposed deactivation mechanism is supported by the red shift of the C-O band for phenol adsorbed on the fresh (1273 cm^{-1}) and recycled (1263 cm^{-1}) catalyst (Figure S8). Also, the C-O band red shift on the recycled catalyst indicates that phenol is no longer able to bind dissociatively to ceria (Figure 9). The proposed solvent-dependent adsorption mechanism is consistent with the greater amounts of phenoxy species formed in hexane relative to in water, the higher catalytic activity in hexane compared to in water, the sharp decrease in activity after the first catalytic run in hexane, and the stability of catalyst activity after cycling experiments in both solvents. Furthermore, after oxidation and reduction treatment of the cycled catalyst, the DRIFT spectrum shows the reemergence of the hydroxyl peak at 3699 cm^{-1} (Figure S9) and the activity is restored (Figure 8), further supporting the adsorption mechanism.



Scheme 2. Proposed mechanism for phenol adsorption onto ceria and reduction by hydrogen in water (left) and hexane (right), lower structures depict the binding after the first catalytic turnover.

Conclusions

High surface Pd/CeO₂ is a very active and selective catalyst for the hydrogenation of phenol to cyclohexanone at room temperature and 1 bar hydrogen in hexane. The activity of the catalyst depends on the reduction temperature used to prepare it: activity increases with increasing reduction temperature up to 350 °C but then decreases sharply at higher reduction temperatures. The enhanced activity at low to moderate temperatures is likely due to high dispersion of Pd as vacancies form on the surface of the support under reducing conditions. The decrease in activity at higher temperatures is likely due to support sintering that leads to catalyst encapsulation. During the catalytic reaction, phenol adsorbs dissociatively to the surface of ceria,

forming cerium-bound phenoxy and water. This process likely involves hydroxyl groups in the neighborhood of the Ce sites. Conversion of the hydroxyls to water prevents dissociative adsorption in later catalytic cycles and lowers the activity of Pd/CeO₂. Non-dissociative adsorption occurs when Ce sites are blocked by water and/or hydroxyls are absent in the neighborhood of the Ce sites. Chemisorbed phenoxide species are more reactive than physisorbed phenol because binding to Ce cations decreases the electron density of the aromatic ring facilitating attack by Pd-activated hydrogen. This catalytic system constitutes a simple and efficient alternative for the production of cyclohexanone under mild reaction conditions. Since the catalyst is fully heterogeneous and does not require addition of acids or homogeneous co-catalysts it may be a good candidate for application in continuous flow mode.

Acknowledgments

The authors want to thank BASF for the generous donation of Pluronics surfactant. This research is supported by the Critical Materials Institute, and Energy Innovation Hub funded by the U.S. Department of Energy, Office of Energy Efficiency and Renewable Energy, Advanced Manufacturing Office.

References

1. Fisher, W. B.; VanPeppen, J. F., Cyclohexanol and Cyclohexanone. In *Kirk-Othmer Encyclopedia of Chemical Technology [Online]*; John Wiley & Sons, Inc.: Posted December 4: 2000; pp 1-7.
2. Musser, M. T., Cyclohexanol and Cyclohexanone. In *Ullmann's Encyclopedia of Industrial Chemistry [Online]*; Wiley-VCH Verlag GmbH & Co. KGaA: Posted October 15: 2011; pp 1-12.
3. Rase, H. F., *Handbook of Commercial Catalysts: Heterogeneous Catalysts*, CRC Press: Boca Raton, FL, 2000; pp 1-488.

4. Zhong, J.; Chen, J.; Chen, L. *Catal. Sci. Technol.* **2014**, 4, 3555-3569.
5. Buil, M. L.; Esteruelas, M. A.; Niembro, S.; Oliván, M.; Orzechowski, L.; Pelayo, C.; Vallribera, A. *Organomet.* **2010**, 29, 4375-4383.
6. Tang, L.-M.; Huang, M.-Y.; Jiang, Y.-Y. *Macromolecular Rapid Communications* **1994**, 15, 527-529.
7. Liu, H.; Jiang, T.; Han, B.; Liang, S.; Zhou, Y. *Science* **2009**, 326, 1250-2.
8. Shin, J. Y.; Jung, D. J.; Lee, S.-g. *ACS Catal.* **2013**, 3, 525-528.
9. Cirtiu, C. M.; Dunlop-Brière, A. F.; Moores, A. *Green Chem.* **2011**, 13, 288.
10. Wang, Y.; Yao, J.; Li, H.; Su, D.; Antonietti, M. *J Am Chem Soc* **2011**, 133, 2362-5.
11. Liu, H.; Li, Y.; Luque, R.; Jiang, H. *Advanced Synthesis & Catalysis* **2011**, 353, 3107-3113.
12. Zhu, J.-F.; Tao, G.-H.; Liu, H.-Y.; He, L.; Sun, Q.-H.; Liu, H.-C. *Green Chem.* **2014**, 16, 2664.
13. Chen, A.; Zhao, G.; Chen, J.; Chen, L.; Yu, Y. *RSC Adv.* **2013**, 3, 4171.
14. Chen, J.; Zhang, W.; Chen, L.; Ma, L.; Gao, H.; Wang, T. *ChemPlusChem* **2013**, 78, 142-148.
15. Li, Z.; Liu, J.; Xia, C.; Li, F. *ACS Catal.* **2013**, 3, 2440-2448.
16. Cheng, L.; Dai, Q.; Li, H.; Wang, X. *Catal. Commun.* **2014**, 57, 23-28.
17. Deshmukh, R. R.; Lee, J. W.; Shin, U. S.; Lee, J. Y.; Song, C. E. *Angew. Chem. Int. Ed.* **2008**, 47, 8615-8617.
18. Panagiotopoulou, P.; Kondarides, D. I. *Catal. Today* **2006**, 112, 49-52.
19. Trovarelli, A. E., *Catalysis by Ceria and Related Materials*, Imperial College Press: London, 2002; Vol. 2.
20. Trovarelli, A. *Catal. Rev.* **1996**, 38, 439-520.
21. Trovarelli, A.; de Leitenburg, C.; Boaro, M.; Dolcetti, G. *Catal. Today* **1999**, 50, 353-367.
22. Aneggi, E.; Wiater, D.; de Leitenburg, C.; Llorca, J.; Trovarelli, A. *ACS Catal.* **2014**, 4, 172-181.
23. Li, W. B.; Wang, J. X.; Gong, H. *Catal. Today* **2009**, 148, 81-87.

24. Fan, L.; Wang, C.; Chen, M.; Zhu, B. *J. Power Sources* **2013**, 234, 154-174.
25. Ratnasamy, C.; Wagner, J. P. *Catal. Rev.* **2009**, 51, 325-440.
26. Si, R.; Flytzani-Stephanopoulos, M. *Angew. Chem. Int. Ed.* **2008**, 47, 2884-7.
27. Gamarra, D.; Belver, C.; Fernández-García, M.; Martínez-Arias, A. *J. Am. Chem. Soc.* **2007**, 129, 12064-12065.
28. Murugan, B.; Ramaswamy, A. V. *J. Am. Chem. Soc.* **2007**, 129, 3062-3063.
29. Beckers, J.; Rothenberg, G. *Green Chem.* **2010**, 12, 939.
30. Vivier, L.; Duprez, D. *ChemSusChem* **2010**, 3, 654-78.
31. Andreeva, D.; Tabakova, T.; Ilieva, L., Ceria-Based Gold Catalysts: Synthesis, Properties, and Catalytic Performance for the WGS and PROX Processes. In *Catalysis by ceria and related materials*; 2nd ed.; Trovarelli, A.; Fornasiero, P., Eds. Imperial College Press: London, 2013; 12, pp 497-564.
32. Velu, S.; Kapoor, M. P.; Inagaki, S.; Suzuki, K. *Appl. Catal. A-Gen* **2003**, 245, 317-331.
33. Scirè, S.; Minicò, S.; Crisafulli, C. *Appl. Catal. A-Gen* **2002**, 235, 21-31.
34. Li, H.; Liu, J.; Xie, S.; Qiao, M.; Dai, W.; Lu, Y.; Li, H. *Advanced Functional Materials* **2008**, 18, 3235-3241.
35. Liu, J.; Li, H.; Li, H. *Chin. J. Catal.* **2007**, 28, 312-316.
36. Davis, M. E. *Nature* **2002**, 417, 813-821.
37. Kandel, K.; Frederickson, C.; Smith, E. A.; Lee, Y.-J.; Slowing, I. I. *ACS Catalysis* **2013**, 3, 2750-2758.
38. Yuan, Q.; Yin, A.-X.; Luo, C.; Sun, L.-D.; Zhang, Y.-W.; Duan, W.-T.; Liu, H.-C.; Yan, C.-H. *J. Am. Chem. Soc.* **2008**, 130, 3465-3472.
39. Shyu, J. Z.; Otto, K.; Watkins, W. L. H.; Graham, G. W.; Belitz, R. K.; Gandhi, H. S. *J. Catal.* **1988**, 114, 23-33.
40. Brinker, C. J.; Lu, Y.; Sellinger, A.; Fan, H. *Adv. Mater.* **1999**, 11, 579-585.
41. Fan, J.; Boettcher, S. W.; Stucky, G. D. *Chem. Mater.* **2006**, 18, 6391-6396.
42. Meng, Y.; Gu, D.; Zhang, F.; Shi, Y.; Cheng, L.; Feng, D.; Wu, Z.; Chen, Z.; Wan, Y.; Stein, A.; Zhao, D. *Chem. Mater.* **2006**, 18, 4447-4464.
43. Grosso, D.; Cagnol, F.; Soler-Illia, G. J. d. A. A.; Crepaldi, E. L.; Amenitsch, H.; Brunet-Bruneau, A.; Bourgeois, A.; Sanchez, C. *Advanced Functional Materials* **2004**, 14, 309-322.

44. Perrichon, V.; Laachir, A.; Abouarnadasse, S.; Touret, O.; Blanchard, G. *Appl. Catal. A-Gen* **1995**, 129, 69-82.
45. Peterson, E. J.; DeLaRiva, A. T.; Lin, S.; Johnson, R. S.; Guo, H.; Miller, J. T.; Hun Kwak, J.; Peden, C. H. F.; Kiefer, B.; Allard, L. F.; Ribeiro, F. H.; Datye, A. K. *Nat Commun* **2014**, 5, 4885.
46. Gulyaev, R. V.; Slavinskaya, E. M.; Novopashin, S. A.; Smovzh, D. V.; Zaikovskii, A. V.; Osadchii, D. Y.; Bulavchenko, O. A.; Korenev, S. V.; Boronin, A. I. *Appl. Catal., B* **2014**, 147, 132-143.
47. Bernal, S.; Calvino, J. J.; Cauqui, M. A.; Gatica, J. M.; Larese, C.; Pérez Omil, J. A.; Pintado, J. M. *Catal. Today* **1999**, 50, 175-206.
48. Giordano, F.; Trovarelli, A.; de Leitenburg, C.; Giona, M. *J. Catal.* **2000**, 193, 273-282.
49. Luo, M.-F.; Hou, Z.-Y.; Yuan, X.-X.; Zheng, X.-M. *Catal. Lett.* **1998**, 50, 205-209.
50. Bensalem, A.; Bozon-Verduraz, F.; Perrichon, V. *J. Chem. Soc. Faraday Trans.* **1995**, 91, 2185-2189.
51. Prins, R. *Chem. Rev.* **2012**, 112, 2714-2738.
52. Sanchez, M. G.; Gazquez, J. L. *J. Catal.* **1987**, 104, 120-135.
53. Kepinski, L.; Wolcyrz, M.; Okal, J. *J. Chem. Soc. Faraday Trans.* **1995**, 91, 507-515.
54. Bernal, S.; Botana, F. J.; Calvino, J. J.; Cauqui, M. A.; Cifredo, G. A.; Jobacho, A.; Pintado, J. M.; Rodriguez-Izquierdo, J. M. *J. Phys. Chem.* **1993**, 97, 4118-4123.
55. Ta, N.; Liu, J.; Chenna, S.; Crozier, P. A.; Li, Y.; Chen, A.; Shen, W. *J. Am. Chem. Soc.* **2012**, 134, 20585-20588.
56. Farmer, J. A.; Campbell, C. T. *Science* **2010**, 329, 933-6.
57. Cunningham, J.; O'Brien, S.; Sanz, J.; Rojo, J. M.; Soria, J. A.; Fierro, J. L. G. *J. Mol. Catal.* **1990**, 57, 379-396.
58. Barrault, J.; Alouche, A.; Paul-Boncour, V.; Hilaire, L.; Percheron-Guegan, A. *Appl. Catal.* **1989**, 46, 269-279.
59. Laachir, A.; Perrichon, V.; Badri, A.; Lamotte, J.; Catherine, E.; Lavalley, J. C.; El Fallah, J.; Hilaire, L.; Le Normand, F.; Quemere, E.; Sauvion, G. N.; Touret, O. *J. Chem. Soc. Faraday Trans.* **1991**, 87, 1601-1609.
60. Badri, A.; Binet, C.; Lavalley, J.-C. *J. Chem. Soc. Faraday Trans.* **1996**, 92, 4669-4673.
61. Binet, C.; Daturi, M.; Lavalley, J.-C. *Catal. Today* **1999**, 50, 207-225.

62. Vayssilov, G. N.; Mihaylov, M.; Petkov, P. S.; Hadjiivanov, K. I.; Neyman, K. M. *J. Phys. Chem. C* **2011**, 115, 23435-23454.
63. Wu, Z.; Li, M.; Mullins, D. R.; Overbury, S. H. *ACS Catal.* **2012**, 2, 2224-2234.
64. Nguyen, M. T.; Kryachko, E. S.; Vanquickenborne, L. G., General and Theoretical Aspects of Phenols. In *The Chemistry of Phenols Part 1*; Rappoport, Z., Ed. John Wiley & Sons, Ltd: West Sussex, England, 2003; pp 31-48.
65. Hansen, H. A.; Wolverton, C. *J. Phys. Chem. C* **2014**, 118, 27402-27414.
66. Mullins, D. R.; Albrecht, P. M.; Chen, T.-L.; Calaza, F. C.; Biegalski, M. D.; Christen, H. M.; Overbury, S. H. *J. Phys. Chem. C* **2012**, 116, 19419-19428.
67. Sharpe, E.; Frasco, T.; Andreescu, D.; Andreescu, S. *Analyst* **2013**, 138, 249-262.
68. Phan, N. T. S.; Van Der Sluys, M.; Jones, C. W. *Adv. Synth. Catal.* **2006**, 348, 609-679.
69. Richardson, J. M.; Jones, C. W. *J. Catal.* **2007**, 251, 80-93.
70. Ji, Y.; Jain, S.; Davis, R. J. *J. Phys. Chem. B* **2005**, 109, 17232-17238.

Appendix of Supporting Information

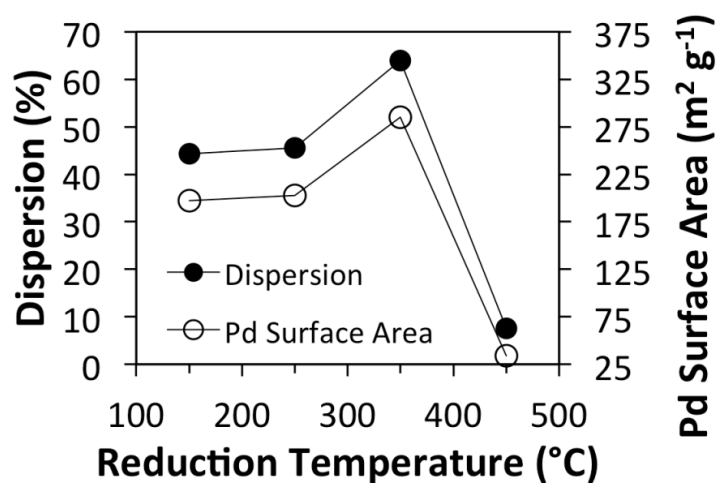
Table S1. Physical properties of Pd-based catalysts.

Sample	BET Surface Area (m ² g ⁻¹)	BJH Pore Volume (cm ³ g ⁻¹)	Pd Dispersion (%) ^a	Pd Crystallite Size (nm) ^a	Pd Loading (wt. %) ^b
Pd/SiO ₂	450	1.1	44	2.1	1.0
Pd/Al ₂ O ₃	379	0.73	18	5.1	1.1
Pd/C ^c	637	0.51	28	3.3	10.0
Pd/CeO ₂ ^d	57	0.20	19	4.9	1.0

^a Obtained by H₂ chemisorption. ^b Obtained by ICP-OES analysis. ^c Commercial Pd/C. ^d Commercial CeO₂.

Table S2. Reaction conditions and results for the hydrogenation of phenol in water.

Entry	T (°C)	t (h)	Conversion (%)	Selectivity (%)	
				C=O	OH
1	25	12	69.4	86.7	13.3
2	35	4	56.4	94.1	5.9
3	45	4	73.1	92.9	7.1
4	55	4	92.8	87.1	12.9

**Figure S1.** Pd dispersion and surface area as a function of PdO_xH_y/CeO₂ reduction temperature.

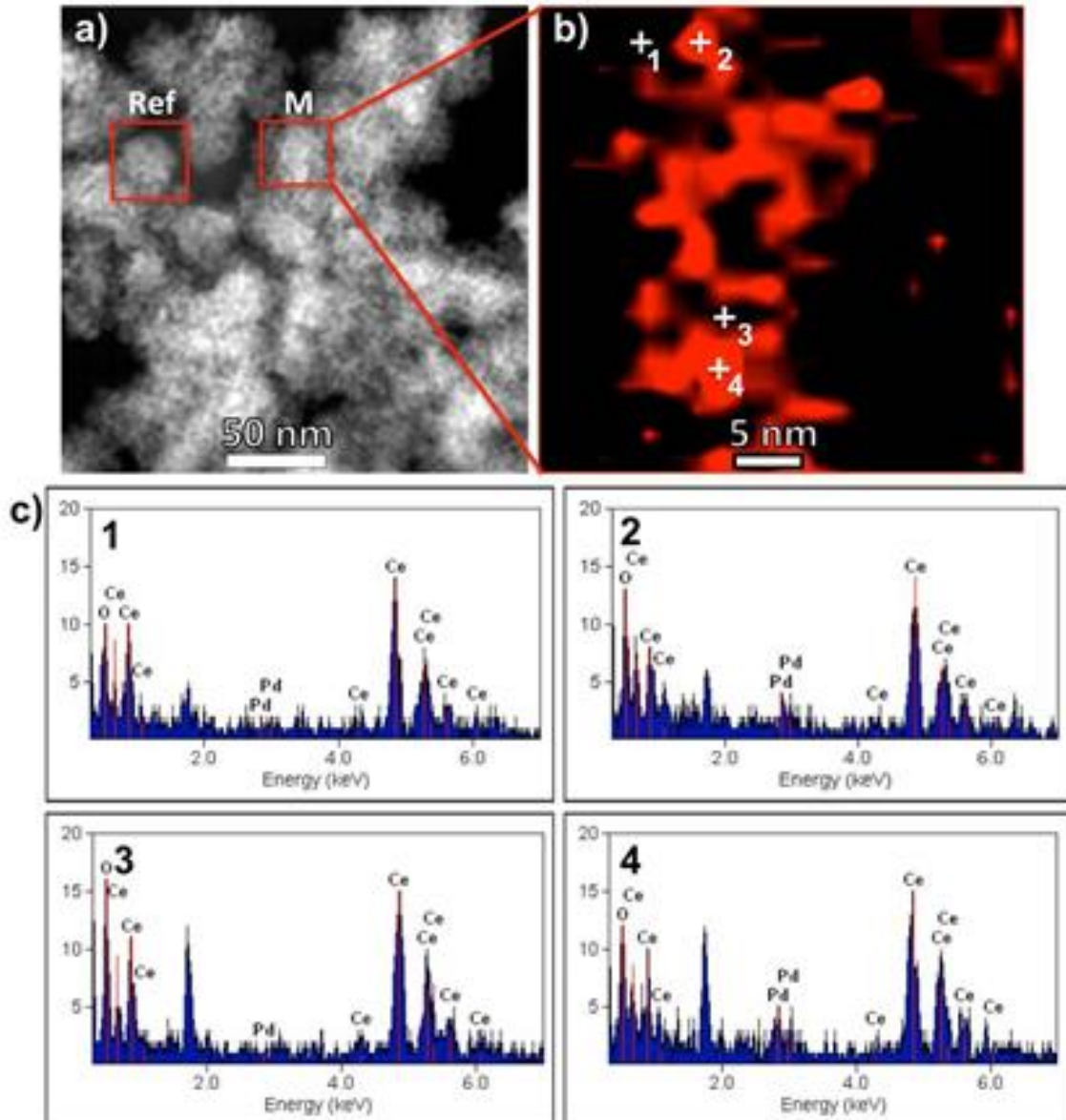


Figure S2. a) STEM image, and EDS maps of b) Ce and c) Pd in the Pd/CeO₂ catalyst. The maps correspond to the 25 x 25 nm square region of the catalyst labeled 'M', square 'Ref' was used as a reference to correct drift between scans. The four numbered EDS spectra in d) were acquired at the corresponding spots in the maps. Spots 1 and 3 that are dark in the Pd map show only noise in the Pd energy, while spots 2 and 4, which are intense red show distinct Pd L α peaks. Scale bar in a) is 50 nm, and in b) and c) is 5 nm.

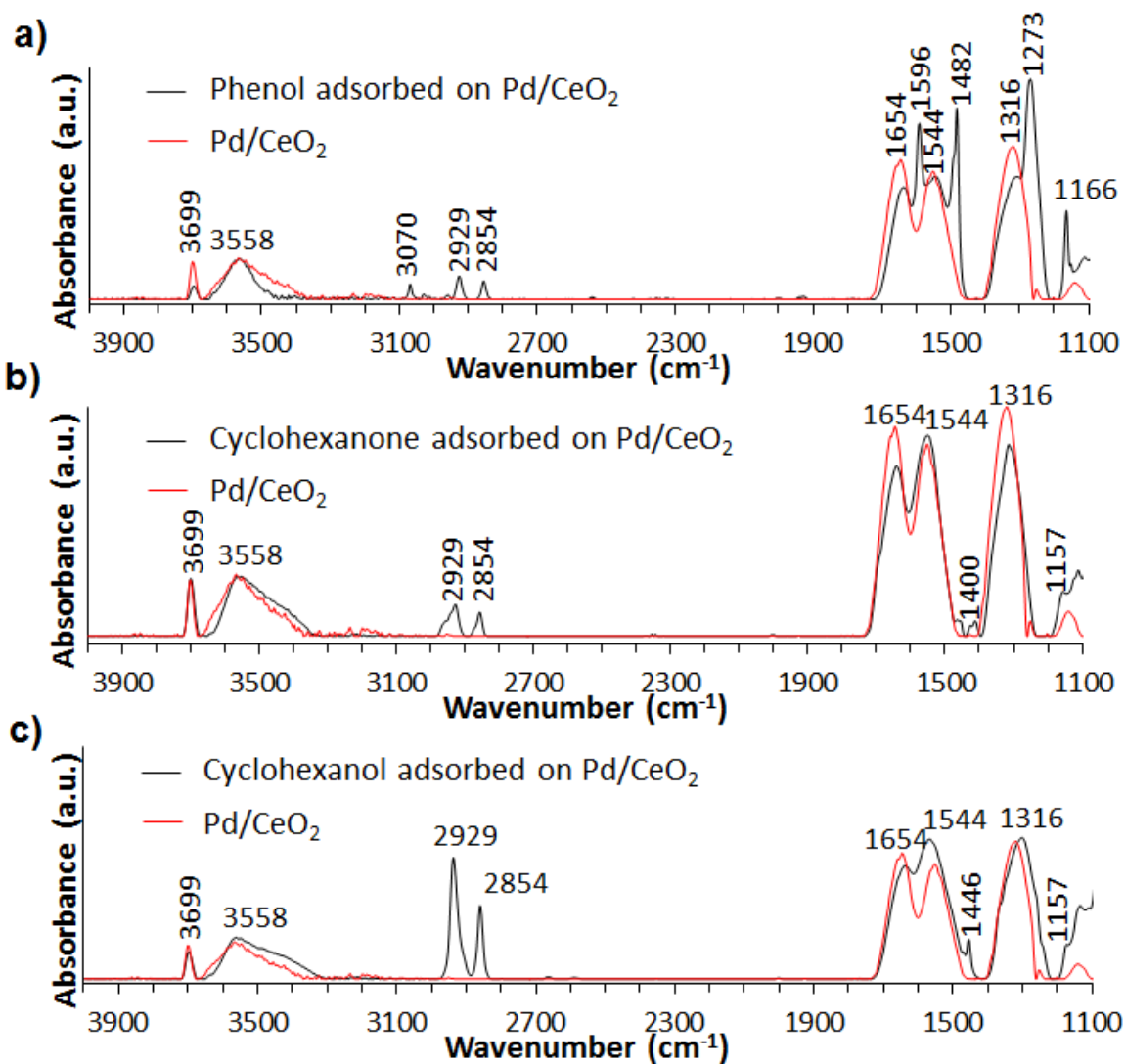


Figure S3. Room temperature DRIFT spectra of Pd/CeO₂ and Pd/CeO₂ with (a) phenol, (b) cyclohexanone, and (c) cyclohexanol adsorbed. The bands at 2929 and 2854 cm^{-1} for (a) are due to hexane which was used to dissolve the phenol.

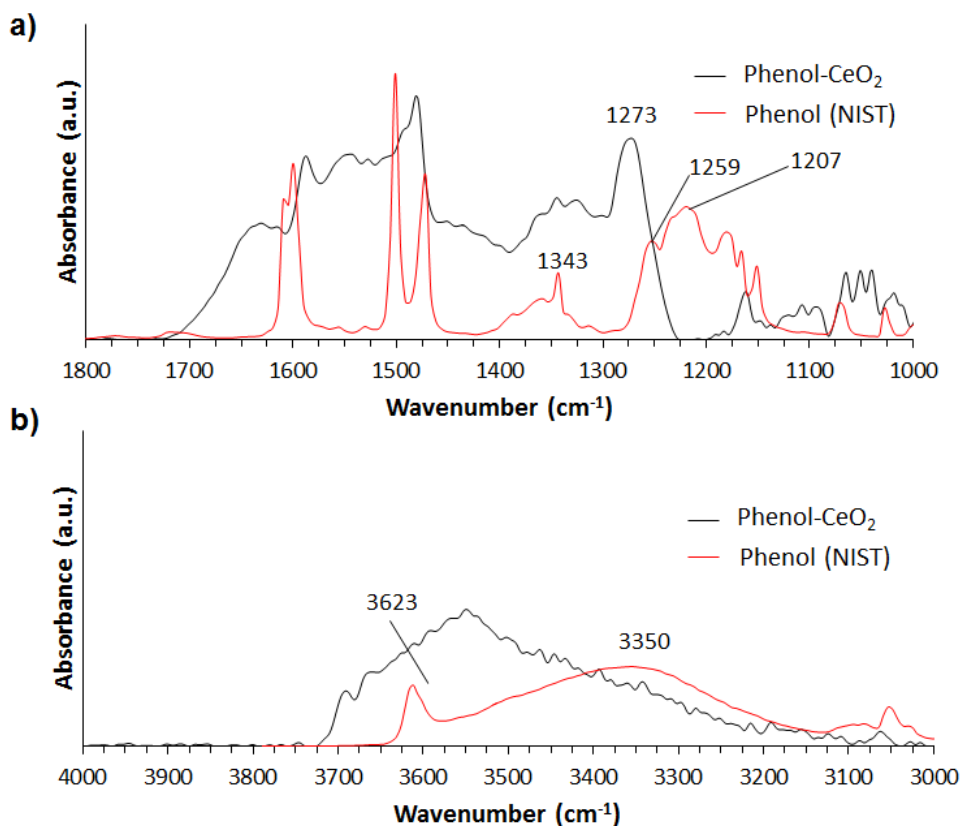
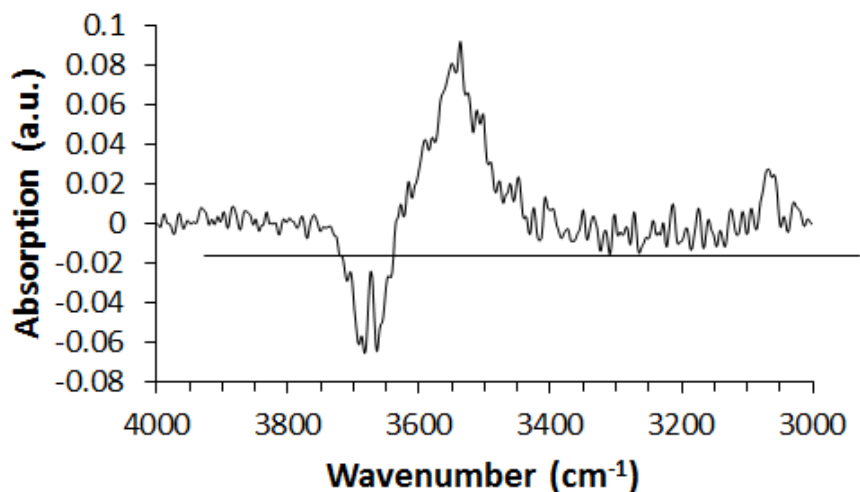
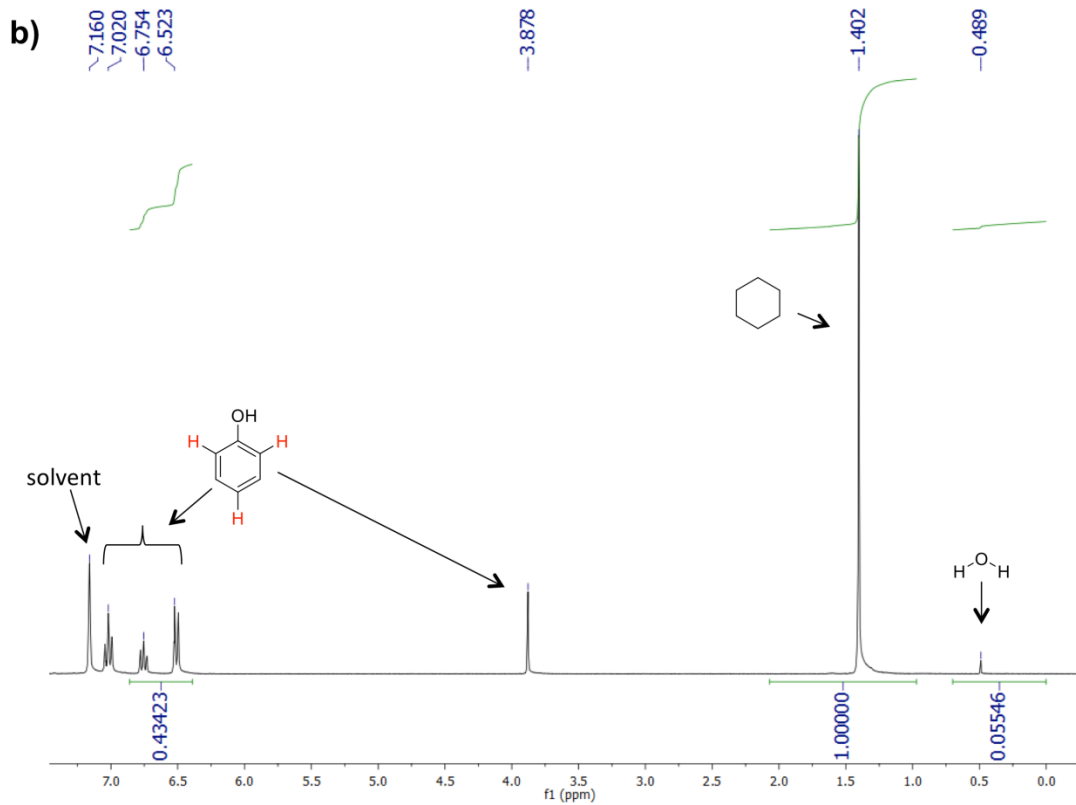
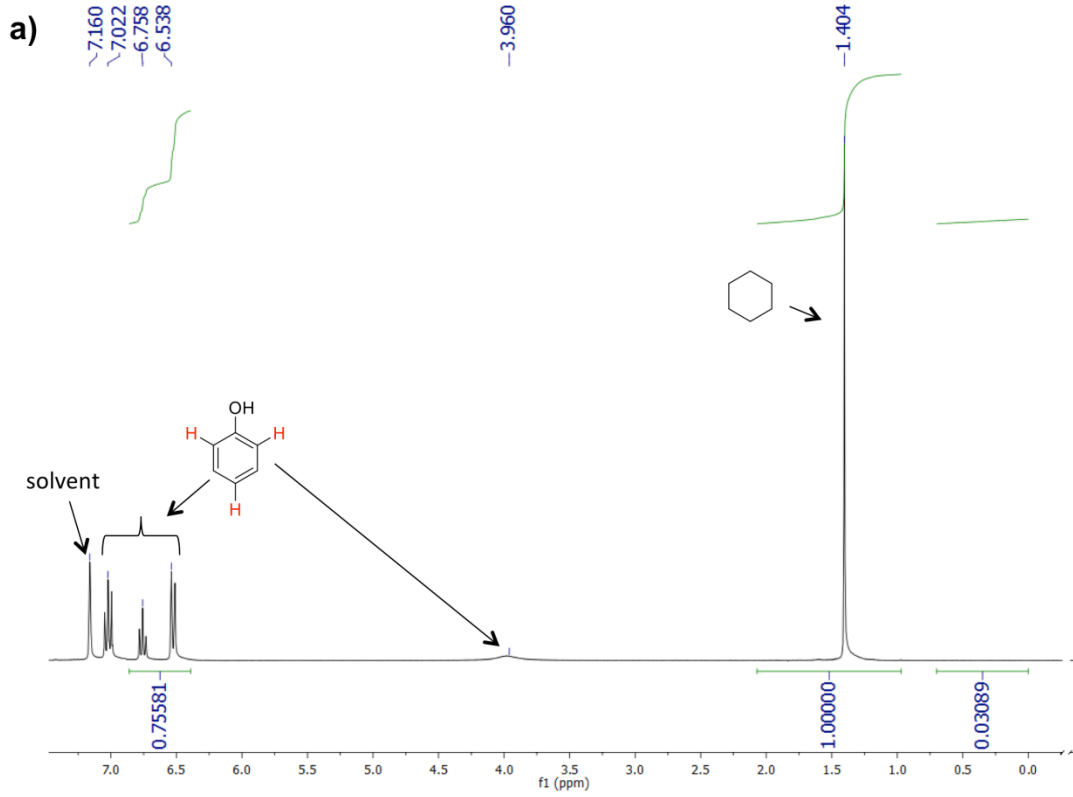


Figure S4. Room temperature IR spectra of phenol adsorbed onto CeO₂ (Phenol-CeO₂) and phenol reference (NIST) from (a) 1800-1000 cm^{-1} and (b) 4000-3000 cm^{-1} .



Figures S5. DRIFT difference spectrum between CeO₂ degassed at 150 °C and phenol adsorbed onto CeO₂ under air- and water-free conditions and then heated to 150 °C under evacuation.



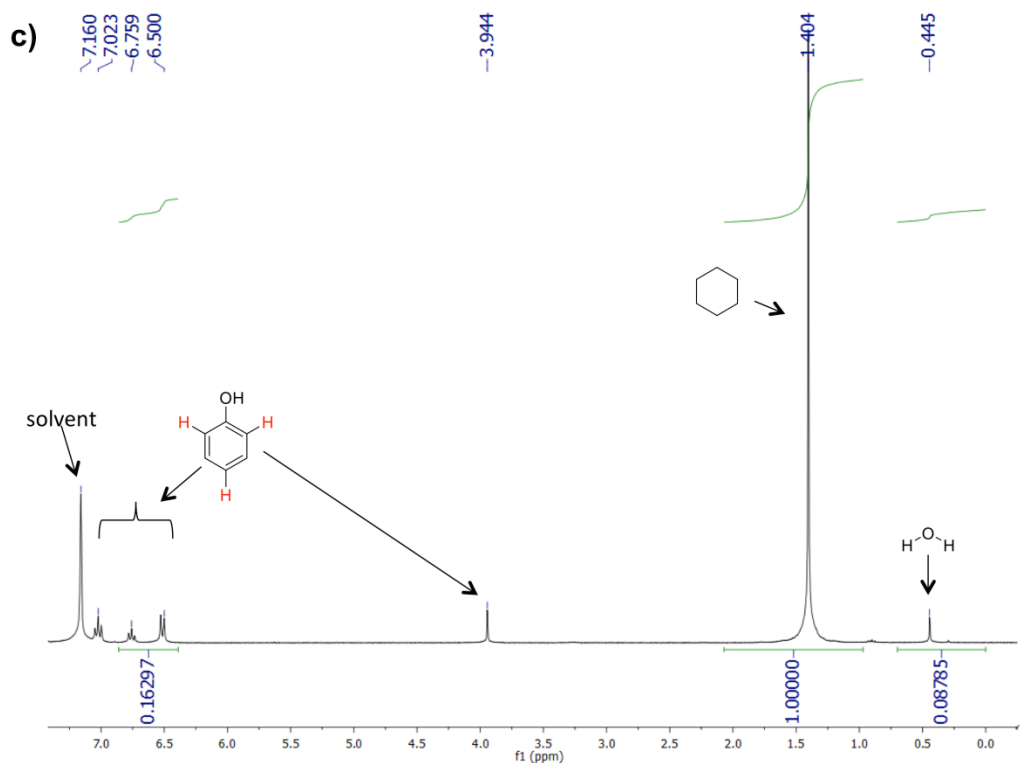


Figure S6. $^1\text{H-NMR}$ spectra taken in benzene- d_6 of (a) phenol and cyclohexane, (b) phenol, cyclohexane, and CeO_2 , (c) phenol, cyclohexane, and additional CeO_2 added to the contents of (b). The red protons of phenol correspond to the protons used for integration.

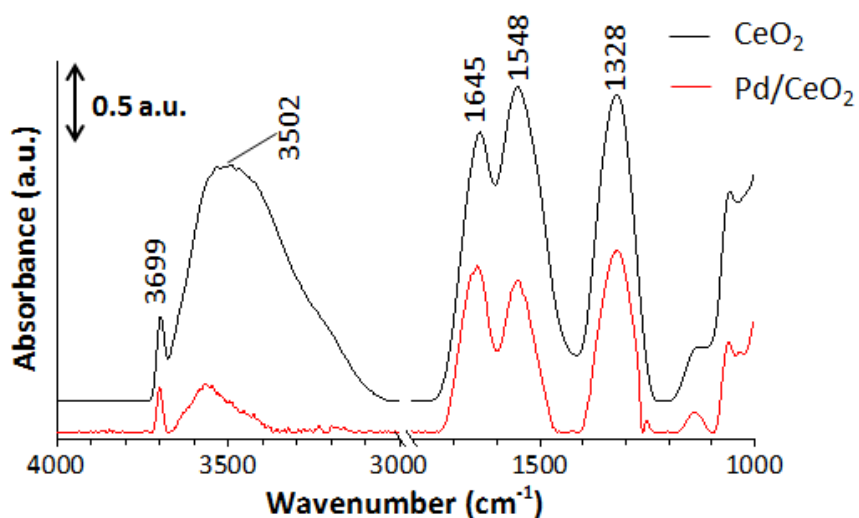


Figure S7. Room temperature DRIFT spectra of CeO_2 support and Pd/CeO_2 catalyst.

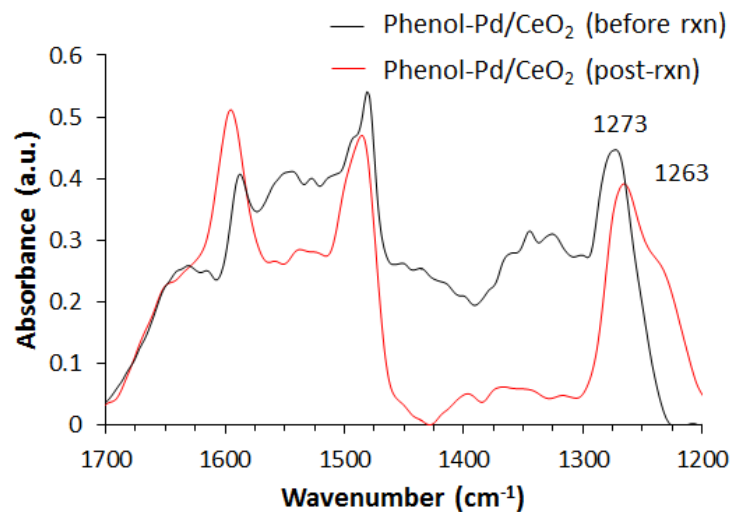


Figure S8. Room temperature DRIFT spectra of phenol adsorbed onto Pd/CeO₂ (Phenol-Pd/CeO₂) before (black) and after (red) reaction in hexane.

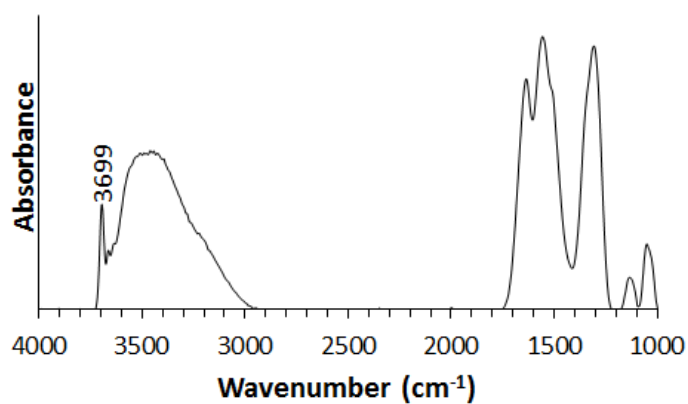


Figure S9. Room temperature DRIFT spectra of Pd/CeO₂ catalyst after regeneration by oxygen and hydrogen.

CHAPTER 3

TRANSFER HYDROGENATION OVER SODIUM-MODIFIED CERIA: ENRICHMENT OF REDOX SITES ACTIVE FOR ALCOHOL DEHYDROGENATION

Adapted from manuscript submitted to *J. Catal.*

Copyright © 2016 Elsevier

Nicholas C. Nelson, Brett W. Boote, Aaron J. Rossini, Emily A. Smith, Igor I. Slowing

Abstract

Ceria (CeO_2) and sodium-modified ceria (Ce-Na) were prepared through combustion synthesis. Palladium was deposited onto the supports (Pd/ CeO_2 and Pd/Ce-Na) and their activity for the aqueous-phase transfer hydrogenation of phenol using 2-propanol under flow conditions was studied. Pd/Ce-Na showed a marked increase (6x) in transfer hydrogenation activity over Pd/ CeO_2 , lowering the apparent activation barrier of the reaction. Material characterization indicated water-stable sodium species were not doped into the ceria lattice, but rather existed as sub-surface carbonates. Modification of ceria by sodium provided more 2-propanol adsorption sites and redox active sites (i.e. defects) for 2-propanol dehydrogenation. This effect was an intrinsic property of the C-Na support and independent of Pd. The types of redox sites active for 2-propanol dehydrogenation were thermodynamically equivalent on both supports/catalysts. The difference in apparent activation barrier over the two catalysts reflected the adsorption barrier of 2-propanol in the presence of phenol.

Introduction

The inevitable depletion of fossil fuels and the controversy that surrounds their use makes it imperative to develop sustainable, economical, and efficient alternatives to petrochemicals. Plant biomass is the most recognized alternative and is widely regarded as the most promising

renewable resource to replace petroleum feedstocks.¹ Of plant biomass, lignin is the only large-scale source of aromatics. As such, there has been a significant amount of effort devoted and progress made to efficiently harvest the aromatics in a cost-competitive manner.² The obvious and urgent needs for more sustainable chemical processes will likely lead to the development of lignin-based technologies and allow it to become a significant source of renewable aromatics.³ However, to take full advantage of renewable aromatic feedstocks, sustainable and economical downstream processes that convert the depolymerization products into high-value commodity chemicals need to be developed.⁴

Lignin is a phenolic-based polymer and therefore a significant portion of the depolymerization products are phenolics.⁵⁻⁶ Phenol finds its major use as a precursor for plastics often by reaction with other compounds or molecules. For example, phenol can be reduced to afford cyclohexanone and/or cyclohexanol. Both reduction products, either separately or in a mixture (KA oil), are predominantly used as precursors for nylon.⁷ Industrial processes that convert phenol to precursors used in nylon production rely on high pressure molecular hydrogen as the reductant.⁸ Therefore, it is advantageous to develop catalysts and catalytic systems that lower the hydrogen pressure needed for phenol reduction or eliminate the need for molecular hydrogen all together. Recently, there have been several catalytic systems developed for phenol reduction at or near atmospheric hydrogen pressures.⁹ Far fewer systems have been developed that eliminate the need for molecular hydrogen through transfer hydrogenation.¹⁰⁻¹³ Thus, there is a present and forecasted need to develop catalytic transfer hydrogenation systems that can transform biomass platform molecules into high-value commodity chemical precursors and lessen our reliance on petroleum-based feedstocks for downstream processing of biomolecules.

In recent years there has been a surge in the development of heterogeneous transfer hydrogenation catalytic systems.¹⁴ Oftentimes, these systems contain two components: one to activate the donor molecule for hydrogen liberation and the other to activate the liberated hydrogen for reduction of the unsaturated functionality. Noble metals are widely used to promote the latter, while homogenous inorganic or organic bases (e.g. NaOH, K-O^tBu) have traditionally been used for the former. From an advanced catalyst design standpoint, it is beneficial to incorporate the necessary promoters within the solid catalyst to achieve the desired activity and avoid the undesired homogeneous components. In a previous study, we showed that ceria supported palladium was active for room temperature phenol hydrogenation with molecular hydrogen at atmospheric pressure.¹⁵ Ceria is a mildly basic, redox active metal oxide and as such, a seemingly good candidate for transfer hydrogenation reactions. Considering its potential, ceria has been poorly studied for transfer hydrogenation catalysis. Catalytic systems involving iridium oxide,¹⁶ gold,¹⁷⁻¹⁸ and nickel¹⁹ supported on ceria have been reported for transfer hydrogenation of ketones and aldehydes without the use of a base promoter. Shimizu et al.¹⁹ studied the transfer hydrogenation of ketones over Ni/CeO₂ catalyst using 2-propanol as the hydrogen donor. The catalyst showed good activity for aromatic and aliphatic ketone reduction. Although a base metal was used, the catalyst was not stable in air and thermal regenerative treatments were needed between recycling experiments.

Ceria and ceria-based materials are best known for their redox properties, which are related to the number and type of oxygen vacancies within the material.²⁰⁻³¹ The significant effort and progress made to understand the role of oxygen vacancies during catalytic processes has enabled the design of defect-engineered ceria-based materials.³²⁻³⁸ Perhaps most notable are ceria materials with well-defined shapes that expose specific crystallographic planes, which dictate the

amount and type of defect sites present.³⁹⁻⁴³ The redox properties of these materials are oftentimes probed with short-chain alcohols, whose adsorption, reactions, and product distribution/desorption temperature are believed to depend on the defect sites present.⁴⁴⁻⁴⁸ Typically, the more defect-rich ceria materials give rise to higher yields of dehydrogenation products. With this in mind, the development of ceria-based materials with high concentrations of defect sites should translate into high dehydrogenation activities and therefore be excellent candidates for transfer hydrogenation reactions. Herein, we report the combustion synthesis of ceria and sodium-modified ceria using cerium nitrate and cerium/sodium nitrate precursors, respectively. Sodium modification was found to increase the number of redox active sites on the surface that lead to 2-propanol dehydrogenation. Palladium was supported on both materials and their activity for phenol transfer hydrogenation using potentially renewable 2-propanol⁴⁹ is reported. Keeping along the lines of sustainable biomass upgrading, the reactions were run in liquid flow mode, which has the added advantages of high throughput and catalyst recycling efficiency.⁵⁰

Experimental

Reagents. Cerium(III) nitrate hexahydrate, sodium(I) nitrate, palladium(II) acetate, phenol, 2,4-dinitrophenylhydrazine, 2-propanol, and malononitrile were purchased from Sigma Aldrich. Acetone, methanol, and ethanol were purchased from Fischer. Acetonitrile-d₃ and benzene-d₆ were purchased from Cambridge Isotope Laboratories. Pluronic P104 was obtained from BASF. Cerium(III) nitrate hexahydrate was dried under vacuum at room temperature for 48 h prior to all synthetic methods. All other chemicals were used without further purification. All reagents met or exceeded ACS specifications.

Synthesis of ceria (CeO₂). The method was adopted from a previous published report¹⁵. Briefly, Ce(NO₃)₃•6H₂O (8.8 g, 20.3 mmol) and Pluronic P104 (10.1 g) were dissolved in ethanol (200 mL). The contents were stirred vigorously until complete dissolution (~2 h). The solution was cast into a large crystallization dish and placed into a pre-heated 65 °C oven until the ethanol had evaporated (~8 h). The resulting gel was placed into a pre-heated 150 °C oven overnight. The yellow powder was calcined in air at 450 °C for 4 h with a ramp rate of 2 °C min⁻¹. *Caution!* During thermal treatment at 150 °C, combustion occurs within ~12 min, producing flames which self-extinguish within seconds after all combustible material (i.e., block copolymer) is burned. The thermal treatment step should be conducted in an oven, preferably in a fume hood with a closed sash to avoid exposure to gaseous decomposition products.

Synthesis of cerium-sodium composite oxide (Ce-Na). The synthetic method was analogous to the synthesis of CeO₂ with slight thermal treatment modifications. In a typical synthesis with nominal sodium loading of 20 at. %, Ce(NO₃)₃•6H₂O (7.0 g, 16.1 mmol), NaNO₃ (0.34 g, 4 mmol), and Pluronic P104 (10.1 g) were dissolved in ethanol (200 mL). The contents were stirred vigorously until complete dissolution (~2 h). The solution was cast into a large crystallization dish and placed into a pre-heated 65 °C oven until the ethanol had evaporated (~8 h). The resulting gel was gathered and placed into two crucibles. The crucibles were capped with aluminum foil (many holes were poked into the aluminum foil with a needle for venting). The crucibles were placed into a pre-heated 350 °C oven for 1 h. Then, the temperature was ramped to 500 °C for 6 h with a ramp rate of 2 °C min⁻¹. *Caution!* During thermal treatment at 350 °C, combustion occurs within ~12 min, producing flames which self-extinguish within seconds after all combustible material (i.e., block copolymer) is burned. The thermal treatment step should be

conducted in an oven, preferably in a fume hood with a closed sash to avoid exposure to gaseous decomposition products.

Synthesis of cerium-sodium composite oxide control (Na/CeO₂). A control cerium-sodium composite oxide with nominal 20 at. % sodium was synthesized by an impregnation route. NaNO₃ (0.078 g, 0.92 mmol) was dissolved in water (0.3 mL). This solution was added (in 0.1 mL increments) to CeO₂, followed by thorough mixing with an agate mortar and pestle and subsequent drying in a 60 °C oven before addition of the next sodium salt solution aliquot. The material was calcined at 500 °C for 6 h with a 2 °C min⁻¹ ramp rate.

Synthesis of catalysts (Pd/CeO₂, Pd/Ce-Na, and Pd/Na/CeO₂). Catalysts were prepared by an impregnation method with a nominal 1 wt. % Pd loading relative to the mass of the support. In a typical synthesis, Pd(O₂CCH₃)₂ (0.0419 g, 0.187 mmol) was dissolved in acetone (1 mL). The support (2.00 g) was placed into a mortar and impregnated with the Pd solution in 0.20 mL increments. After each impregnation step, the catalyst was mixed thoroughly with a pestle until seemingly dry. The material was calcined at 350 °C for 2 h with a 2.5 °C min⁻¹ ramp rate and after cooling to room temperature it was reduced under flowing hydrogen at 350 °C for 2 h with a ramp rate of 2.5 °C min⁻¹.

Transfer hydrogenation reactions. A Uniqsis FlowSynTM continuous liquid flow reactor was used for all reactions and operated in automatic mode. In a typical experiment, the catalyst (0.5 g) was packed into an Omnifit Labware column (PEEK, 10 mm diameter). The catalyst was secured by placing an adjustable endpiece equipped with a 10 µm PTFE filter into the inlet and outlet of the column. The volume of the catalyst bed was 0.4 mL (for 0.5 g of catalyst). Water was passed through the system (0.1 mL min⁻¹) at room temperature for ~2h to

remove soluble species before beginning reaction with fresh catalyst. The column was then heated to the desired temperature (instrument $T_{\max} = 140\text{ }^{\circ}\text{C}$) under continuous water flow. At this point, an automated system switched from water feed to reagent feed. Typically, the reagent feed (0.1 mL min^{-1}) was an aqueous solution of 2-propanol (90 v/v %) and phenol, with varying concentration of phenol depending on reaction conditions. The outlet feed was segmented in 4 mL increments by a Gilson FC 203B fraction collector. A typical reaction was conducted for 24 h (144 mL). Six 4 mL solution vials were taken to make a composite sample (24 mL, six data points over 24 h). A 50 μL aliquot from each 24 mL composite sample was added to 1 mL of resorcinol internal standard solution (0.3 mM) used to construct quantitative calibration curves and analyzed in an Agilent GC-MS (7890A, 5975C) with a HP-5MS column. Mass balances were $100 \pm 8\%$. The GC-MS run started at $60\text{ }^{\circ}\text{C}$ for 0 minutes, then ramped to $150\text{ }^{\circ}\text{C}$ at $5\text{ }^{\circ}\text{C min}^{-1}$ for 0 minutes, then ramped to $300\text{ }^{\circ}\text{C}$ at $20\text{ }^{\circ}\text{C min}^{-1}$ for 3 minutes. Conversion was defined as mol % and calculated as moles of converted phenol per mole of starting phenol times 100 %. Yields were defined as mol % and were calculated as moles of each product divided by moles of starting phenol times 100 %. Conversion rates were calculated from conversion, catalyst mass (g), initial phenol concentration (μM), and flow rate (L h^{-1}). Calibrated flow rates were used for conversion rate. For simplicity, the calibrated flow rate was rounded to one significant figure when discussing flow rate in the text.

$$\frac{(\text{Conversion}) \times (\text{Flow Rate}) \times [\text{Phenol}]_0}{(\text{Catalyst Mass})}$$

H₂ chemisorption. Hydrogen chemisorption was performed in a Micromeritics AutoChem II equipped with TCD detector. H₂-Ar (10 % H₂) was used as the metal dispersion probe. H₂-chemisorption analysis was carried out by reducing samples at $150\text{ }^{\circ}\text{C}$ under H₂/Ar

flow, followed by flowing Ar for 15 minutes at 150 °C to remove surface bound hydrogen from Pd crystallites. The sample was then cooled under Ar to -25 °C for hydrogen pulse chemisorption measurements. The palladium dispersion of the catalysts was calculated based on the following equation:

$$D(\%) = \frac{S_f \times M \times V_{ad}}{m \times W \times V_m} \times 100$$

where S_f = stoichiometry factor (the Pd/H₂ molar ratio) = 2; M = the atomic mass of Pd (106.42 g mol⁻¹); V_{ad} = the volume of chemisorbed H₂ at standard temperature and pressure conditions (mL); m = the mass of the sample (g); W = the weight fraction of Pd in the sample as determined by ICP-OES; V_m = the molar volume of H₂ (22414 mL mol⁻¹) at STP.

Powder X-ray diffraction (PXRD). Diffraction patterns were collected using Co K α 1, K α 2 split radiation (45 kV, 40 mA, λ_{avg} = 1.7903 Å) on a PANalytical X'Pert PRO diffractometer equipped with a theta-theta vertical mode goniometer, incident Fe filter, an air-cooled X'Celerator real time multiple strip (RTMS) detector, and spinner stage. The patterns were converted to Cu K α radiation for comparison to standard patterns using Bragg's law. PXRD samples were prepared by placing powders onto a background-less sample holder. Crystallite sizes were calculated using Scherrer equation:

$$D_{(hkl)} = \frac{K\lambda}{\beta \cos \theta}$$

where K is the shape factor (0.9) of the average crystallite, λ is the X-ray wavelength (0.17903 nm), β is the full width at half maximum (radians), and θ is the Bragg angle (radians). HighScore was used for Rietveld Refinement.

Raman spectroscopy. Raman spectroscopy was performed on the CeO₂ and Ce-Na powder samples using the 488-nm line of an argon ion laser (Cyonics Uniphase, Santa Clara, CA) illuminating a DM IRBE inverted light microscope (Leica Microsystems, Buffalo Grove, IL) fitted with a 10× (0.25 NA) objective. A line filter was used to isolate the 488-nm line from the multiple wavelength output of the laser. The backscattered Raman signal was passed into a HoloSpec spectrometer (Kaiser Optical Systems, Ann Arbor, MI) equipped with a Newton 940 CCD camera (Andor Technology, Belfast, United Kingdom). Single acquisition Raman spectra of the powders were acquired with the laser set to 6 mW (2.5×10^6 W/cm²), and the acquisition times were 60 seconds. Gaussian fits of the peaks were used to calculate peak area ratios and were performed in IGOR (Wavemetrics, Portland, OR). The data were plotted using Excel, and spectra were normalized at the maximum intensity for the F_{2g} mode.

²³Na-SSNMR. All solid-state NMR experiments were performed on a Bruker Avance III 9.4 T (400 MHz) widebore NMR spectrometer. Experiments were performed with a Bruker broadband 4 mm HXY E-free probe configured in double resonance mode. ¹H chemical shifts were referenced to neat tetramethylsilane via an external secondary standard of adamantane ($\delta_{\text{iso}} = 1.82$ ppm). ²³Na chemical shifts were referenced with respect to proton chemical shifts by the recommended relative frequency scale.⁵¹

All ²³Na MAS experiments were performed with an MAS frequency of 8 kHz. Central transition selective $\pi/2$ and π pulses of 5.81 μs and 11.62 μs (21.5 kHz rf field), respectively, were used for ²³Na spin echo and REDOR experiments. ²³Na{¹H} REDOR experiments⁵² were performed with the direct excitation of ²³Na and rotor synchronized ¹H REDOR π -pulses were applied with an XY-8 phase cycle.⁵³ The MAS frequency was 8000 Hz, with 4096 scans per data point, a 0.25 s recycle delay. The total echo (dephasing) time was varied from 125 μs to 6125 μs

in steps of 250 μs with acquisition of 48 total data points (24 individual reference and dephased spectra). The $^{23}\text{Na}\{^1\text{H}\}$ REDOR curves were calculated with the previously described analytical Bessel functions.⁵⁴ In order to account for a distribution of $^{23}\text{Na}\text{-}^1\text{H}$ inter-nuclear distances, individual REDOR curves were calculated for $^{23}\text{Na}\text{-}^1\text{H}$ inter-nuclear distances of 2 \AA (this was the minimum allowed distance) to 30 \AA in steps 0.1 \AA .⁵⁵ The intensity of each individual REDOR curve was then multiplied by a normalized Gaussian weighting function with a center of 2.25 \AA and a width of 2.75 \AA . The weighted curves were then summed to obtain a curve modeling the distribution. This simple model likely under-estimates the average distance (i.e., the true distances are larger) since multi-spin systems tend to show faster signal dephasing than isolated spin systems. Triple quantum multiple quantum magic angle spinning (3Q-MQMAS)⁵⁶ experiments on Ce-Na were performed with the previously described phase-modulated split- t_1 pulse sequence.⁵⁷ The spectrum was acquired with 40320 scans per increment, a Δt_1 increment of 62.5 μs (spectral width of twice the spinning frequency) and 20 t_1 increments were acquired (ca. 22.4 hours total experiment time). 4.10 μs and 1.35 μs pulses with an rf field of ca. 61 kHz were applied for generation of triple quantum coherence and reconversion to single quantum coherence, respectively. The indirect dimension spectral width was divided by a factor 2.125 to illustrate the distribution in isotropic chemical shift.⁵⁸

Electron microscopy/energy dispersive X-ray spectroscopy. Transmission electron microscopy (TEM) was conducted using a FEI Tecnai G2 F20 field emission microscope and scanning transmission electron microscope (STEM) operating at 200 kV (point-to-point resolution <0.25 nm and a line-to-line resolution of <0.10 nm). TEM samples were prepared by placing 2–3 drops of dilute ethanol suspensions onto carbon-coated copper grids. The

composition of Ce-Na structures were characterized by energy dispersive X-ray spectroscopy (EDX) scans in STEM mode.

Surface area and porosimetry. Textural properties of the supports and catalysts were measured by nitrogen sorption isotherms at $-196\text{ }^{\circ}\text{C}$ in a Micromeritics Tristar analyzer. The surface areas were calculated by the Brunauer-Emmett-Teller (BET) method. Sample pretreatment for surface area measurement was done by flowing N_2 for 6 h at $100\text{ }^{\circ}\text{C}$.

ICP-OES. Ce, Na, and Pd loadings were analyzed by a Perkin Elmer Optima 2100 DV Inductively Coupled Plasma-Optical Emission Spectroscopy (ICP-OES). Samples ($\sim 10\text{ mg}$) were digested in 5 mL of 4 M HCl, 1 mL of concentrated HNO_3 , and 2 mL of 30 v/v % H_2O_2 . The samples were sonicated for ten minutes. Then they were placed into a $50\text{ }^{\circ}\text{C}$ water bath for ~ 12 h. Each sample was then diluted to 10 mL of total solution.

Diffuse reflectance infrared Fourier transform (DRIFT). Measurements were made on a Bruker Vertex 80 FT-IR spectrometer with OPUS software and apodized spectral resolution of 0.2 cm^{-1} . The spectrometer was equipped with a HeNe laser and photovoltaic MCT detector. A Praying MantisTM diffuse reflectance accessory and high temperature reaction chamber was used for room temperature and variable temperature measurements, respectively. 32 scans were collected for each measurement in absorbance mode with 4 cm^{-1} resolution. The samples were heated to $400\text{ }^{\circ}\text{C}$ in O_2 -He (10 % O_2) flow (50 mL min^{-1}) for 30 minutes prior to DRIFT analysis of probe molecule (i.e. acetonitrile- d_6 , chloroform, acetone, 2-propanol) adsorption. The samples were cooled to room temperature under O_2 -He flow and then switched to He flow (50 mL min^{-1}). Blank spectra were recorded at this time. Then, the He flow was redirected through a saturator containing the probe molecule at room temperature. Spectra were taken at 1 min intervals under

probe molecule exposure until the formation of liquid-like bands was observed (~1-5 min). At this time, the He flow was redirected away from the saturator. Spectra were taken at 10 min intervals until no changes were observed between subsequent spectra (~20-30 min). For 2-propanol adsorption, the sample was heated to 60 °C for 30 min and cooled back down to room temperature before taking spectra.

X-ray photoelectron spectroscopy (XPS). XPS analysis was done with a PHI 5500 multitechnique system using a standard Al X-ray source. Samples were analyzed at room temperature with no special preparation. Charge correction was accomplished by shifting the Ce 3d v-peak to 882.6 eV for all spectra.⁵⁹⁻⁶⁰ All spectra were normalized within each spectral region by setting the maximum intensity equal to one. Spectral deconvolution was done using OriginPro[®] with Shirley background subtraction. The peaks were modelled using Gaussian functions.

Temperature programmed desorption (TPD). CO₂-TPD experiments were carried out using a Micromeritics AutoChem II equipped with TCD detector and dry ice/acetone bath. The samples (~300 mg) were placed into a quartz U-tube and degassed at 500 °C for 60 minutes (10 °C min⁻¹) under O₂-He (10 % O₂) flow (50 mL min⁻¹). The samples were cooled to 100 °C under O₂-He and the gas flow switched to CO₂-He (10 % CO₂). After 15 minute exposure, the gas flow was switched to He and held at 100 °C for 15 minutes before cooling to 40 °C. The temperature was then ramped at 10 °C min⁻¹ while monitoring the TCD signal. Trapping experiments with dry ice/acetone mixture (-78 °C) and liquid nitrogen (-196 °C) indicated that the species evolved during desorption were CO₂.

Temperature programmed surface reaction (TPSR). For 2-propanol TPD, a Netzsch STA 449 F1 Jupiter[®] TGA/DSC/MS/IR instrument was used. The mass spectrometer is a Netzsch quadrupole mass spectrometer 403 D Aeolos equipped with electron impact ion source and Channeltron SEM detector with 0.5 amu resolution. The data was collected in multiple ion detection (MID) mode while monitoring $m/z = 41$ (propylene), $m/z = 43, 58$ (acetone), and $m/z = 45$ (2-propanol). The samples were prepared by heating to 250 °C under O₂ flow for 60 minutes in a round bottom flask with septum. After cooling to room temperature and still under O₂ flow, 2-propanol (~1 mL) was added via syringe and needle to saturate the sample. The excess 2-propanol was allowed to evaporate at room temperature under O₂ flow (~4 h). The samples were placed into the Netzsch instrument during which time they were exposed to atmospheric conditions. The temperature was ramped from 40 °C to 400 °C at 10 °C min⁻¹ under 60 mL min⁻¹ Ar flow while monitoring the mass signals. For DSC-MS experiment the sample was placed into the analysis chamber with no prior treatment and heated from 40 °C to 1200 °C at 10 °C min⁻¹ under 60 mL min⁻¹ Ar flow while monitoring the mass signal ($m/z = 44$).

Acetone formation rate. The formation rate of acetone was monitored by reaction of evolved acetone during liquid flow catalysis with 2,4-dinitrophenylhydrazine (DNPH) to form acetone-2,4-dinitrophenylhydrazone (Ac-DNPH). The fresh catalysts were allowed to equilibrate under reaction conditions (i.e. 0.15 M phenol in 90 v/v % aqueous 2-propanol, T = 140 °C, 0.1 mL min⁻¹) for 48 h prior to acetone formation rate determination. The acetone formation rate under various reaction conditions was then determined after 1 h time-on-stream (TOS). The proceeding method was validated by reacting DNPH (1.2, 2.4, and 3.7 equiv) with a known amount of acetone. The average relative error over four trials was ± 9.9 %. In a typical run, the product feed (1.5-2.0 mL, 15-20 min) was directed into a solution containing DNPH (0.4 g, 2

mmol), methanol (14.4 mL), water (4 mL), and concentrated sulfuric acid (1.6 mL). Precipitates were formed immediately. Ac-DNPH was extracted with benzene and the solvent was removed by rotary evaporation to give an orange-yellow solid. The solid was redissolved in a known volume (2-3 mL) of acetonitrile- d_3 . A 1 mL aliquot was placed into a NMR tube along with internal standard 1,4-dioxane (5 μ L, 58 μ mol). Proton nuclear magnetic resonance ($^1\text{H-NMR}$) spectra were collected on a Varian VXR-300 equipped with a narrow bore 7.05T/300 MHz magnet and a standard ^1H probe. $^1\text{H-NMR}$ (acetonitrile- d_3 , 300 MHz, 25 $^\circ\text{C}$): δ , ppm: 2.08 (3H, s); 2.16 (3H, s); 7.81 (1H, d); 8.26 (1H, d); 8.92 (1H, s); 10.80 (1H, s).

Knoevenagel condensation. Reactions were performed in screw-cap vials. Benzaldehyde (1 mmol) and active methylene compound (1 mmol) were dissolved in ethanol (2 mL). The catalyst (6 mg) was then added to the solution which was heated to 60 $^\circ\text{C}$ for 0.5 h. The catalysts were separated by centrifugation and the supernatant concentrated under reduced pressure. Reaction yields were monitored by $^1\text{H-NMR}$ using dimethyl sulfone as internal standard. Mass balances were 100 ± 5 %. $^1\text{H-NMR}$ (chloroform- d_1 , 300 MHz, 25 $^\circ\text{C}$): δ , ppm: 7.53 (2H, t); 7.63 (1H, t); 7.79 (1H, s); 7.90 (2H, d).

Phenol adsorption isotherms. Phenol adsorption curves were constructed by measuring sample absorbances (A) at 278 nm and 290 nm. The A_{278} corresponds to phenol absorbance and the A_{290} was used to correct for anomalous scattering. Two cuvettes were prepared each with hexane (2 mL). One cuvette was designated as the blank. The UV/VIS spectrum for the other cuvette (sample) was recorded at A_{278} and A_{290} to correct for differences in absorbance between the two cuvettes. The sample (~10 mg) was placed into the sample cuvette containing hexane. A known amount of phenol in hexane was then added to the sample cuvette, capped, and allowed to

equilibrate under static conditions for 24 h. At this time the measurement was recorded and the A_{278} value corrected. This process was repeated 4-5 times.

Results and Discussion

Catalysis. Ceria (CeO_2) and the cerium-sodium oxide material (Ce-Na) with nominal 20 at. % Na loading were prepared using a modified solution combustion synthesis (SCS) with Pluronic polymer as fuel and metal nitrate salts. The SCS method was chosen due to its precedence for forming homogeneous multi-metal oxide composites.⁶¹ Palladium was deposited onto Ce-Na (Pd/Ce-Na) and CeO_2 (Pd/ CeO_2) through impregnation with palladium(II) acetate, followed by oxidative and reductive thermal treatments at 350 °C. The physicochemical properties of the supports and catalyst are summarized in Table S1.

The liquid flow transfer hydrogenation of phenol using 2-propanol as the sacrificial hydrogen donor with Pd/Ce-Na and Pd/ CeO_2 catalysts proceeded through the formation of cyclohexanone and cyclohexanol in various proportions depending on reaction conditions (Table 1). Both catalysts displayed outstanding stability during 7-day continuous catalytic runs (Figure 1a). However, Pd/Ce-Na showed a marked increase in transfer hydrogenation activity over Pd/ CeO_2 . For instance, under the conditions given in Table 1 for Entries 2 and 7, the rate of phenol conversion was nearly five times higher over Pd/Ce-Na than Pd/ CeO_2 and about six times as high for Entries 5 and 10. As evident from Table 1, Pd/Ce-Na showed higher phenol conversion rates under all the reaction conditions tested. For Pd/Ce-Na, the ketone to alcohol yield ratio (K:A) varied from about 10:90 to 40:60 through control of the flow rate and phenol concentration (Table 1, Entries 1-5). The ketone yield was more or less constant when varying these parameters, while the alcohol yield was more sensitive to these variations (Table 1, Entries 1-5). For Pd/ CeO_2 , the K:A ratio was larger than for Pd/Ce-Na, giving almost exclusively the

ketone (Table 1, Entries 6-10). Both catalysts showed a higher conversion rate as the 2-propanol-water ratio was increased. Interestingly, neat 2-propanol resulted in a monotonic, yet significant decrease of conversion rate as a function of time over both catalysts which was not observed in the presence of water (Figure S1). Washing the catalysts with water overnight at 140 °C after the reaction in neat 2-propanol resulted in regeneration of the original activity. This suggests the decreased activity may be related to hydroxyl disproportionation, which results in the removal of lattice oxygen through water formation.⁶²⁻⁶⁵ In absence of water, the hydroxyl disproportionation equilibrium lies to the right in Scheme S1, giving oxygen deficient ceria, which is a poor oxidation catalyst.⁶² The regeneration data implies that water is able to dissociatively adsorb on partially reduced ceria,⁶⁵⁻⁶⁷ and shift the equilibrium in Scheme S1 to the left. Thus, water appears to be a necessary component to maintain hydroxyl disproportionation equilibrium in a way that favors the redox process. Arrhenius plots were constructed and the apparent activation barriers for phenol conversion over Pd/CeO₂ and Pd/Ce-Na were 115 ± 3 kJ mol⁻¹ and 48 ± 2 kJ mol⁻¹, respectively (Figure 1b).

Table 1. Reaction conditions and catalytic results for transfer hydrogenation of phenol with 2-propanol.^a

Entry	Catalyst	Phenol (M)	Flow Rate (μL min ⁻¹)	Conversion Rate (μmol g ⁻¹ h ⁻¹)	Yield (%)		K:A
					C=O	C-OH	
1	Pd/Ce-Na	0.150	44.1 ^b	759 ± 6	13 ± 1	82 ± 1	14:86
2	Pd/Ce-Na	0.150	95.6 ^c	1390 ± 40	26 ± 1	54 ± 2	33:67
3	Pd/Ce-Na	0.150	191 ^d	1410 ± 20	16 ± 1	25 ± 1	40:60
4	Pd/Ce-Na	0.200	44.1	905 ± 16	19 ± 1	67 ± 2	22:78
5	Pd/Ce-Na	0.200	95.6	1360 ± 60	18 ± 1	41 ± 3	30:70
6	Pd/CeO ₂	0.150	44.1	266 ± 9	31 ± 4	2 ± 1	93:7
7	Pd/CeO ₂	0.150	95.6	287 ± 8	16 ± 1	<1	96:4
8	Pd/CeO ₂	0.150	191	279 ± 3	8 ± 1	0	100:0
9	Pd/CeO ₂	0.200	44.1	215 ± 4	20 ± 2	<1	97:3
10	Pd/CeO ₂	0.200	95.6	217 ± 5	10 ± 2	0	100:0

^a0.5g of catalyst was used for all reactions. Water was flowed over the catalyst at room temperature for 2 h before beginning the initial run (Entries 1, 6). After that, the reactions were

run sequentially (Entries 2-5, 7-10). 90 v/v % aqueous 2-propanol was used for all reactions. Column temperature was 140 °C. Catalyst bed volume (V_{bed}) was 0.4 mL. Errors are reported as one standard deviation away from the mean. ^bFor a flow rate of $\sim 0.05 \text{ mL min}^{-1}$, 72 mL of reagent was used with 12 mL sample composite intervals generating 6 data points over 24 h. ^cFor a flow rate of $\sim 0.10 \text{ mL min}^{-1}$, 144 mL of reagent was used with 24 mL sample composite intervals generating 6 data points over 24 h. ^dFor a flow rate of $\sim 0.20 \text{ mL min}^{-1}$, 168 mL of reagent was used with 24 mL sample composite intervals generating 7 data points over 14 h.

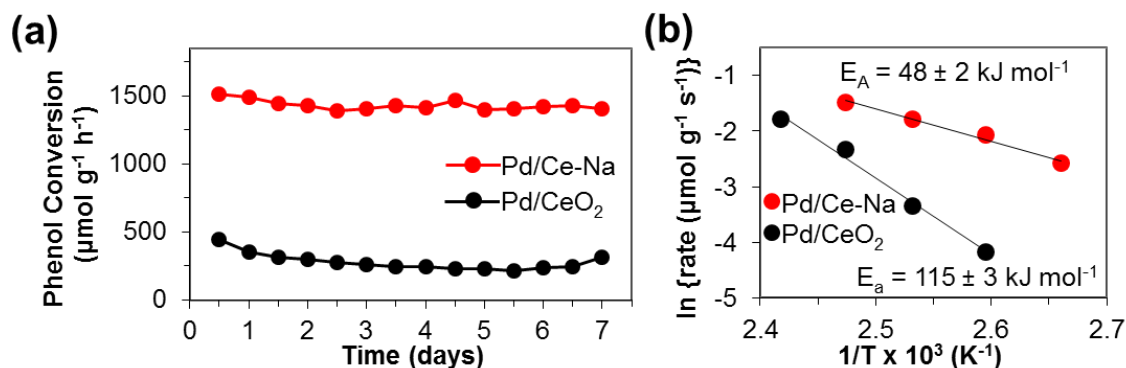


Figure 1. (a) Phenol conversion rate for Pd/CeO₂ and Pd/Ce-Na during 7 day time-on-stream (TOS) study. Conditions: 0.15 M phenol in 90 v/v % aqueous 2-propanol, 0.5 g catalyst, $\sim 0.1 \text{ mL min}^{-1}$, $T = 140 \text{ }^\circ\text{C}$, $V_{\text{bed}} = 0.4 \text{ mL}$. Each data point corresponds to 72 mL product stream composite. (b) Arrhenius plots of phenol conversion over Pd/CeO₂ ($E_A = 115 \text{ kJ mol}^{-1}$) and Pd/Ce-Na ($E_A = 48 \text{ kJ mol}^{-1}$). Conditions: 0.1 M phenol in 90 v/v % aqueous 2-propanol, 0.5 g catalyst, $\sim 0.1 \text{ mL min}^{-1}$, $V_{\text{bed}} = 0.4 \text{ mL}$. Each data point (at each temperature) corresponds to the average of 6 rate measurements collected at 4 h sampling intervals (24 mL composite) over 24 h.

Physicochemical properties are often invoked to explain differences in activity and were found to be similar for both catalysts after the reaction (Table S2). That is, the specific surface area of Pd/CeO₂ decreased by an order of magnitude over the course of the reaction, which made it comparable to Pd/Ce-Na. Likewise, the Pd dispersion value on both catalysts decreased to about 10 % during time-on-stream, suggesting Na does not enhance Pd dispersion.⁶⁸⁻⁶⁹ Both catalysts showed the same Pd loadings before and after reaction, which is consistent with the long-term catalyst stability. The similar post-reaction physicochemical properties between the catalysts suggest that sodium modification was able to promote transfer hydrogenation activity.

In order to understand the role of sodium promotion more clearly, preferential attention was given to support characterization. The role of palladium was studied where deemed relevant.

Materials characterization. Elemental analysis of as-synthesized Ce-Na support confirmed sodium was present at 18 at. % and agreed well with nominal loading of 20 at. % (Table 2, Entry 1). DRIFT (Figure S2-S4) and XPS (Figure S5) analysis showed sodium was present as a carbonate. ICP analysis of Ce-Na after continuous-flow aqueous treatment at room temperature for twelve hours showed a drastic reduction of sodium content from 18 to 4.0 at. % (Table 2, Entries 1, 3), with most soluble sodium species removed after two hours during washing (Figure S6). The data presented in Figure S6 was obtained after washing the material at catalytic temperatures (i.e. 140 °C) and showed a further decrease in sodium loading to 2.6 at. % (Table 2, Entry 4). Quite surprisingly, sodium was retained even after 7 days on stream (Table 2, Entry 5). While ICP analysis confirmed the presence of sodium after washing, XPS (Figure S5g) indicated that there were minimal amounts of sodium on the surface, suggesting that sodium species are contained within the material. Bearing in mind the aqueous conditions used during catalysis, all Ce-Na and Pd/Ce-Na characterization was performed after aqueous washing at room temperature (Table 2, Entry 3).

Table 2. Physicochemical properties of supports and catalysts under varying conditions.

Entry	Sample	Surface Area (m ² g ⁻¹) ^a	Na Loading (at. %) ^b	Lattice Constant (Å) ^c
1	Ce-Na	29	18 ± 1 ^d	5.412
2	CeO ₂	210	0	5.412
3	Ce-Na ^e	42	4.0 ± 0.2 ^f	5.412
4	Ce-Na ^g	40	2.6 ± 0.1 ^h	---
5	Pd/Ce-Na ⁱ	20	2.7 ± 0.2 ^j	---

^aDetermined by nitrogen physisorption using BET approximation. ^bDetermined by ICP-OES and is relative to Ce. ^cDetermined using HighScore software. ^dMeasured across three batches. ^eWashed with flowing water (0.1 mL min⁻¹) for 12 h at room temperature. ^fMeasured across two

batches with two sample preps in duplicate (i.e. 8 data points). ^gWashed with flowing water (0.1 mL min⁻¹) for 12 h at 140 °C. ^hMeasured for one batch with two sample preparations in duplicate (i.e. 4 data points). ⁱResults after 7 d reaction. ^jMeasured in duplicate with two sample preparations (i.e. 4 data points).

The PXRD pattern of the supports (Figure 2a) and catalysts (Figure S7) exhibited diffraction peaks that could be indexed to the fluorite structure of ceria, with no other reflections observed. The absence of sodium-containing reflections (e.g. Na₂O, Na₂CO₃, etc.) in the diffraction pattern suggests sodium species could be amorphous or have a crystallite size below the detection limit of the instrument. Since XPS analysis indicated that sodium was not present on or near the surface, it is also possible that sodium was doped into the ceria matrix. Rietveld analysis showed no significant difference in lattice constant between Ce-Na and CeO₂ (Table 2, Entries 1-3). The identical lattice constants between Ce-Na and CeO₂ could be an indication that residual sodium species were not contained within the bulk ceria lattice. Alternatively, it could reflect the similar sizes of Ce⁴⁺ (0.97 Å)⁷⁰ and Na⁺ (0.99 Å)⁷⁰, which has been observed for Pr-(0.99 Å)⁷⁰ doped ceria.⁷¹⁻⁷² The identical lattice parameters from PXRD analysis were also supported by HR-TEM imaging for several crystallites of Ce-Na that gave an average d-spacing of 0.31 ± 0.03 nm (Figure S8). This value corresponds to the (111) surface termination and is also the predominant facet observed for CeO₂ (Figure S9).¹⁵ The result rules out structural promotion (i.e. surface termination) for the higher rate of phenol turnover and lower activation barrier for conversion.

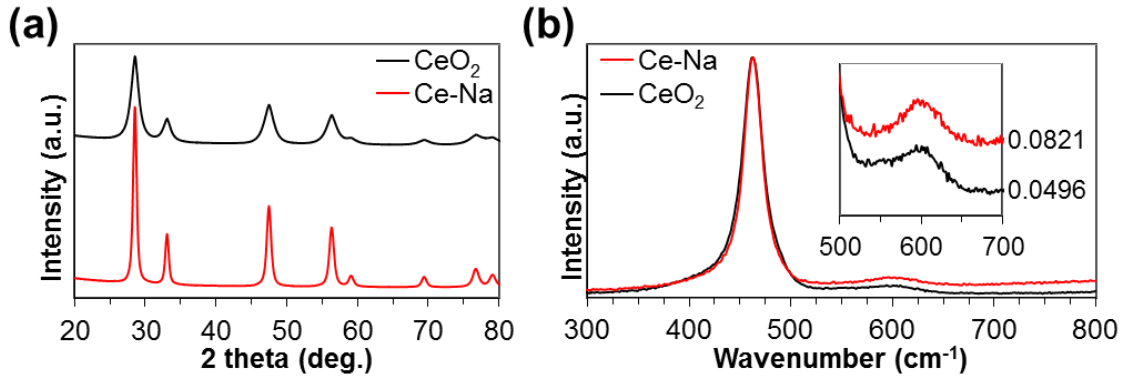


Figure 2. (a) PXRD patterns for CeO₂ and Ce-Na showing cubic fluorite phase. (b) Raman spectra using 488 nm excitation for CeO₂ and Ce-Na. Inset shows band associated with intrinsic defects (D-band). The numbers represent the ratio ($A_D:A_{F_{2g}}$) of the peak areas for the D-band (600 cm⁻¹) and the F_{2g}-band (462 cm⁻¹).

Given the comparable size of sodium and cerium (IV) cations, PXRD may not be suitable for determining whether sodium was doped into the ceria lattice. In direct contrast to PXRD, which primarily gives information related to the cationic sublattice, Raman spectra of fluorite-type oxides are sensitive to bulk oxygen lattice vibrations, which are related to M-O bond symmetry and defects. The Raman spectra for CeO₂ and Ce-Na are shown in Figure 2b. Both samples exhibited Raman bands around 462 cm⁻¹ and were attributed to the F_{2g} triply degenerate Raman-active phonon of the cubic CeO₂-fluorite phase.^{41, 73-74} This band can be viewed as a symmetrical stretching vibration of the oxygen atoms surrounding a cerium cation (i.e. CeO₈). Thus, the location of the absorption band is sensitive to the M-O bond lengths and symmetry present in ceria-based materials.^{72, 74} The band positions for the two materials were identical suggesting similar bond lengths in accordance with the lattice constants obtained from PXRD analysis. Both samples also exhibited bands around 600 cm⁻¹ that have been suggested to result from the presence of intrinsic oxygen defects.⁴¹ The ratio between the defect band (D-band) and the F_{2g} band (i.e. $A_D:A_{F_{2g}}$) is used to compare the amounts of intrinsic defects between different ceria-based materials.^{41, 75} Ce-Na showed a higher $A_D:A_{F_{2g}}$ ratio (1.7×) indicating more defects

compared to CeO₂ even with the former having a larger crystallite size.⁷⁴ However, the exact nature of these defects, either vacancy-interstitial (Frenkel) or Ce³⁺ substitutional in an octahedral environment, is still debated.^{41, 73} Another defect band around 570 cm⁻¹ has been observed for ceria during thermal treatment under reducing environments and is attributed to oxygen vacancies formed during reduction (i.e. extrinsic oxygen vacancies).⁴⁴ The same band has also been observed upon substitutional doping of cerium cations with aliovalent metals and is thought to result from charge compensation and is thus associated with extrinsic oxygen vacancies.⁷² The absence of this band in Ce-Na suggests sodium is not acting as a substitutional dopant that exhibits charge-compensation. Charge compensation through formation of Na⁺-Ce³⁺ cationic pairs could also be possible and would not involve formation of oxygen vacancies. However, this motif would be expected to result in differences of lattice constant between the two materials due to the larger ionic radius of Ce³⁺, which was not observed in PXRD analysis. Thus, the PXRD and Raman data together suggest sodium was not acting as a dopant.

Structural analysis of the Ce-Na support indicated that sodium was not contained within the ceria lattice, but it was shown through chemical analysis that sodium species are still present even after washing with water at elevated temperatures for extended periods of time (Table 2). Considering that the predominant sodium species before washing were carbonates, the residual sodium may be in the form of carbonates that are trapped at the grain boundaries within the bulk of the particles (Table S1, Figure S8). Figure S10 shows the CO₂-TPD profile while monitoring the heat flow and weight loss for the Ce-Na support. The TGA-DSC-MS analysis showed two high temperature CO₂ desorption peaks around 700-800 °C and 900-1100 °C. The former CO₂ desorption peak was exothermic while the latter was endothermic. The exothermic transition with evolution of CO₂ suggests carbonate decomposition and likely arises from sodium

carbonate decay. Anhydrous sodium carbonate is known to decompose at temperatures higher than 800 °C, but metal oxide additives have been shown to lower the decomposition temperature.⁷⁶ Furthermore, the decomposition of sodium carbonate is an exothermic process in agreement with the thermal data and is expected to result in the formation of sodium oxide. The endothermic CO₂ evolution peak could be due to CO₂ desorbing from sodium oxide. The total weight loss from the onset of the exothermic transition to the end of the endothermic transition (i.e. 700-1100 °C), assuming sodium carbonate decomposition, allowed an estimation of residual sodium to be 3.8 at. %. This result is in excellent agreement with that obtained from elemental analysis (Table 2, Entry 3). Furthermore, XPS depth-profiling experiments showed the Na 1s binding energy was characteristic of sodium carbonate (Figure S11).⁷⁷ Thus, it appears that the insoluble sodium fraction was sodium carbonate and that it was largely inaccessible to water (Table 2).

²³Na solid-state NMR (SSNMR) spectroscopy was also performed on the Ce-Na support. ²³Na is a 100% naturally abundant $I = 3/2$ quadrupolar nucleus which normally gives rise to relatively narrow solid-state NMR spectra. The ²³Na spin echo SSNMR spectrum of Ce-Na support possessed a relatively broad, featureless resonance (Figure S12A). A 2D triple quantum multiple quantum magic angle spinning (MQMAS) experiment suggested that the broadening of the ²³Na SSNMR spectrum was primarily due to a distribution of isotropic ²³Na chemical shifts in the range of 10 to -10 ppm; broadening from the second order quadrupolar interaction was minimal (Figure S12A). This suggests that there are many distinct sodium sites/environments, and within these sites the sodium ions must reside at sites of relatively high spherical symmetry (i.e., pseudo-octahedral coordination environments). A ²³Na{¹H} rotational echo double resonance (REDOR) experiment was performed to assess the spatial proximity of the Na ions to

protons. The REDOR experiment indicates that ca. 60% of the Na ions are proximate (within 5 Å) of ^1H nuclei (Figure S12B and Figure S12C). This would suggest that the majority of the sodium carbonate is present as a hydrated phase or nearby to sorbed water. This is perhaps to be expected since the Ce-Na support was thoroughly washed to remove excess Na. Several distinct crystalline anhydrous and hydrated sodium carbonate phases have previously been reported.⁷⁸⁻⁷⁹ Therefore, the range of isotropic ^{23}Na chemical shifts most likely arises from the presence of a variety of hydrated and anhydrous sodium carbonate phases/environments. Keeping the XPS results in mind, these sodium carbonate phases are likely trapped in between the ceria grains.

The role of residual sodium carbonate during catalysis remains unclear. The insolubility under aqueous conditions at elevated temperatures for 7 days suggests that it is not accessible to the environment and thus should not participate directly in the catalysis. To better understand the role of sodium carbonate a control sample was prepared through impregnation of CeO_2 with aqueous NaNO_3 (20 at. %) followed by calcination at 450 °C (Na/CeO_2). Pd was then deposited on the support (Pd/Na/CeO_2). It is expected that decomposition of the sodium precursor should yield surface sodium carbonate species that are easily removed with water and thus clarify the role of sodium carbonate. Quite remarkably, the control catalyst was slightly more active than Pd/Ce-Na (Figure S13). ICP analysis revealed that Pd/Na/CeO_2 contained 1.1 Na-at. % after reaction, which is about a 60 % decrease of Na content compared to Pd/Ce-Na (Table 2, Entry 5). XPS depth profiling experiments showed the Na 1s binding energy for Na/CeO_2 (washed with water at room temperature) was consistent with sodium carbonate (Figure S14). The result suggests that the physical amount of sodium carbonate during catalysis does not affect activity, at least from about 1-3 Na-at. %. Although the results provide some insight into the role of sodium carbonate, they are not conclusive.

Considering that bulk characterization techniques did not support the formation of sodium-doped ceria and that the physical amount of sodium carbonate doesn't appear to correlate with activity, it is possible that sodium modification affects the surface properties of the material. XPS analysis was conducted on both supports to probe possible electronic structure differences that could provide insight into the different catalytic activity. The Ce 3d spectral region (Figure S15a) showed characteristic peaks attributed to Ce(IV),^{59-60, 80-81} with no obvious difference between the two supports. The O 1s spectral region shown in Figure S15b displayed subtle differences between CeO₂ and Ce-Na. The O 1s spectrum peak maximum, assigned to lattice oxygen, shifted from 529.5 eV (CeO₂) to 529.3 eV (Ce-Na). The shift signifies, on average, a more electron-rich environment of lattice oxygens. Since sodium is present it would seem plausible that the apparent increased oxygen electron density for Ce-Na could be due to higher material basicity, which has been observed for other metal oxides modified with sodium⁸²⁻⁸³ and could explain the different reaction rates observed. However, the basic properties and C-H activating ability⁸⁴ of the two materials were found to be identical by testing with basicity probes and base-catalyzed reactions (Figure S16-S18, Table S3-S4). For completeness, the acidic properties were also found to be unmodified (Figure S19-20). This data indicates that the acid-base properties for Ce-Na were unaltered relative to CeO₂ and that these reactivity descriptors are not relevant for the activity difference observed during phenol transfer hydrogenation.

Redox properties and kinetic analysis. The most notable reactivity descriptor for ceria-based materials is the redox property. The redox property of ceria correlates to the number of defects within the material, especially as they relate to oxygen vacancies.^{20, 35, 41-42, 44, 85} Since 2-propanol oxidation is a prerequisite for phenol turnover, the 2-propanol reactivity over both CeO₂ and Ce-Na were studied. The temperature programmed surface reaction (TPSR) of 2-

propanol was used to determine the relationship between acetone formation and the transfer hydrogenation activity of the two materials. At this point it should be noted that 2-propanol was adsorbed dissociatively^{62, 86-88} on both materials as evidenced by two $\nu(\text{C-O})$ stretching bands at 1162 and 1132 cm^{-1} corresponding to end-on and bridging coordination of isopropoxide to cerium cations, respectively (Figure S21). The materials were saturated *ex situ* with 2-propanol and heated under Ar while monitoring evolved 2-propanol ($m/z = 45$), acetone ($m/z = 43, 58$), and propylene ($m/z = 41$). The characteristic acetone signal at $m/z = 58$, whose intensity is weak relative to the somewhat uncharacteristic signal at $m/z = 43$, was monitored to ensure the signal at $m/z = 43$ is primarily due to acetone desorption. The identical profiles observed for all samples at $m/z = 43$ and $m/z = 58$ indicates that the intensity of the $m/z = 43$ signal is primarily due to evolved acetone (Figure S22). Figure 3a, b shows the 2-propanol, acetone, and propylene signal intensity profile versus temperature for CeO_2 and Ce-Na, respectively. For CeO_2 , acetone desorption occurred over a broad temperature range. Onset desorption occurred around 50 °C and continued to about 320 °C. There were two major desorption maxima centered at 133 °C and 237 °C, with a significant shoulder around 300 °C. Unreacted 2-propanol also desorbed over a broad temperature range spanning 50-275 °C, with two maxima observed at 105 °C and 208 °C slightly below the acetone maxima. A small propylene desorption was found at 307 °C. For Ce-Na, onset desorption also occurred around 50 °C with a dominant acetone desorption maximum at 150 °C and a significant shoulder at 228 °C. Unreacted 2-propanol desorbed over 50-250 °C with single maximum at 120 °C. There were negligible amounts of propylene observed.

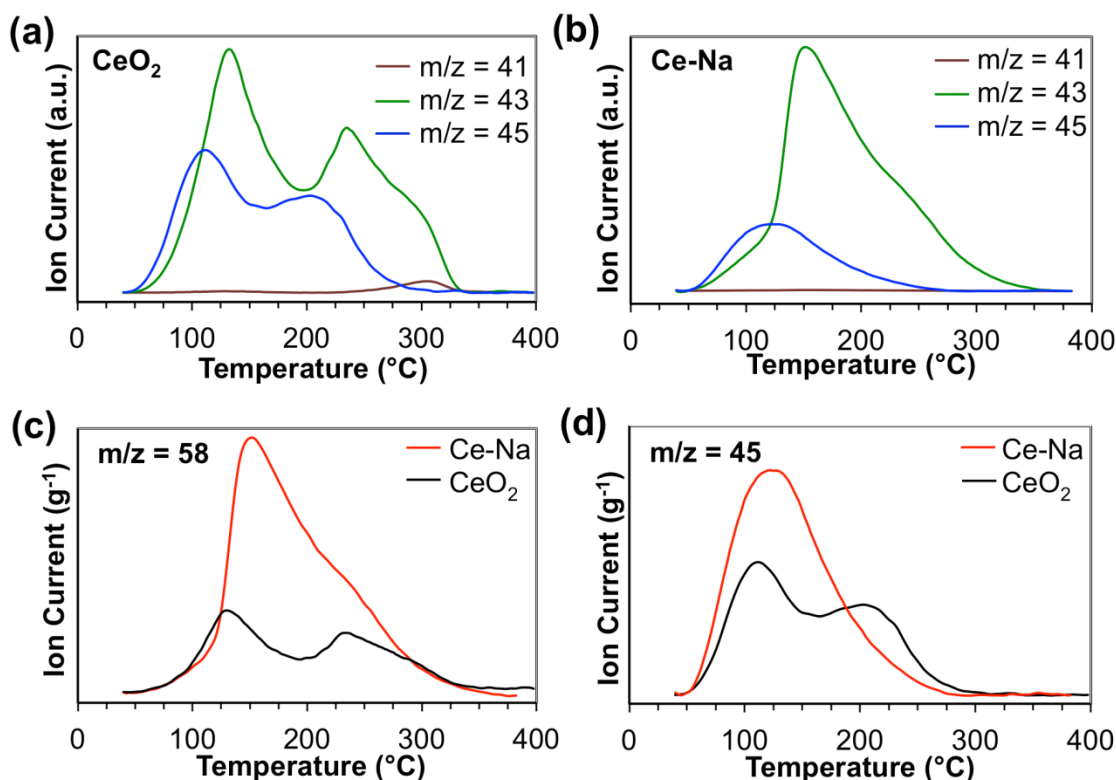


Figure 3. TPD-MS profile for TPSR of adsorbed 2-propanol on (a) CeO_2 and (b) Ce-Na. The $m/z = 41$, 43, and 45 signals correspond to propylene, acetone, and 2-propanol, respectively. Mass normalized TPD-MS profile for TPSR of adsorbed 2-propanol on Ce-Na and CeO_2 while monitoring (c) $m/z = 58$ and (d) $m/z = 45$ which correspond to acetone and 2-propanol, respectively.

The signal corresponding to acetone ($m/z = 58$) for Ce-Na and CeO_2 were normalized to the material mass and are shown in Figure 3c. The formation rate of acetone is clearly higher on Ce-Na indicated by the increased slope before the first maximum. Curiously, the temperature at maximum acetone desorption were similar for Ce-Na and CeO_2 . In addition, both materials showed an acetone desorption shoulder around 240 °C. Typically, the desorption maximum is proportional to the activation energy for the rate limiting step. This implies that the higher rate of acetone formation observed for TPSR of 2-propanol on Ce-Na was not due to a reduced activation barrier during an elementary reaction step. This result also indicates that the higher rate can be attributed to more active sites present on the surface of Ce-Na in spite of the large

difference in surface area between the two materials. According to Redhead,⁸⁹⁻⁹⁰ the activation energy of acetone formation on the two materials using the first desorption maximum was $106 \pm 21 \text{ kJ mol}^{-1}$ and $101 \pm 20 \text{ kJ mol}^{-1}$ for Ce-Na and CeO₂, respectively. Considering that formation of adsorbed isopropoxide occurs at room temperature (Figure S21) and that acetone shows little affinity for the surface of ceria above room temperature,⁶² it seems likely the observed activation barrier is due to C-H scission of adsorbed isopropoxide to form acetone. This elementary reaction step is a redox process implying that there are more redox active centers on Ce-Na and that these redox centers are equivalent. The relative areas of the mass-normalized acetone TPD-MS profiles on the two supports showed 2.9× more acetone evolving from Ce-Na, suggesting this support had about three times more 2-propanol dehydrogenation sites than CeO₂. Additionally, the 2-propanol desorption profile for the two supports indicated a higher amount of desorbed 2-propanol on Ce-Na (Figure 3d).

TPSR of adsorbed 2-propanol clearly showed the rate of acetone formation is higher for Ce-Na than for CeO₂, but the actual catalytic conditions are quite different and the reactant-limited TPSR results of the supports may not be representative during catalysis. Therefore, the rate of acetone formation under catalytic conditions was monitored by trapping with 2,4-dinitrophenylhydrazine and quantified using ¹H-NMR. The acetone formation rate was monitored at 140 °C under liquid flow conditions with 90 v/v % aqueous 2-propanol. For CeO₂ and Ce-Na the rates were $7 \mu\text{mol g}^{-1} \text{ h}^{-1}$ and $13 \mu\text{mol g}^{-1} \text{ h}^{-1}$, respectively. For Pd/CeO₂ and Pd/Ce-Na, the average acetone formation rate observed over three trials was $2920 \pm 80 \mu\text{mol g}^{-1} \text{ h}^{-1}$ and $6270 \pm 40 \mu\text{mol g}^{-1} \text{ h}^{-1}$, respectively (Table 3, Entries 1-2). The TPSR study of adsorbed 2-propanol over the supports indicated the average acetone formation rate (i.e. from 40-400 °C) was about three times higher over Ce-Na, which was more than observed with the catalysts under

catalytic conditions (2.1x). However, the TPSR study spanned a much broader temperature range than the catalytic study and is an average over each temperature within that range. Comparing the two y-maxima (130-150 °C) from the TPSR TPD-MS curve for evolved acetone (Figure 3c) should indicate the relative dynamic acetone formation rate under reaction conditions (Table 3, Entries 1-2). The relative maxima for evolved acetone between the two materials from TPSR of 2-propanol (2.4x) was in good agreement for the relative rates under dynamic liquid conditions using the catalysts (2.1x). Thus, given the acetone formation rates for the supports, it appears that palladium increases the acetone formation rate over both catalysts more or less equally, but the support largely dictates the difference in the observed acetone formation rate.

Table 3. Acetone formation over catalysts in the absence and presence of phenol.^a

Entry	Catalyst	[Phenol] (M)	Acetone Rate ($\mu\text{mol g}^{-1} \text{h}^{-1}$)	C=O Rate ($\mu\text{mol g}^{-1} \text{h}^{-1}$) ^b	C-OH Rate ($\mu\text{mol g}^{-1} \text{h}^{-1}$) ^b	Expected Acetone Rate ($\mu\text{mol g}^{-1} \text{h}^{-1}$) ^c
1	Pd/CeO ₂	0	2920 \pm 80 ^d	---	---	---
2	Pd/Ce-Na	0	6270 \pm 40 ^d	---	---	---
3	Pd/CeO ₂	0.15	576 \pm 58 ^e	288	12	612
4	Pd/Ce-Na	0.15	3680 \pm 368 ^e	476	974	3874

^aConditions: 90 v/v % aqueous 2-propanol, 0.5g of catalyst, 0.1 mL min⁻¹, T = 140 °C, V_{bed} = 0.4 mL. ^bRates obtained from data found in Table 1, Entries 2, 7. ^cCalculated assuming 2 moles of acetone per mole of cyclohexanone and 3 moles of acetone per mole of cyclohexanol. ^dAverage rate from three separate reactions. Errors represent one standard deviation from the mean. ^eRate from one reaction. Errors represent average relative error determined during method validation (see experimental).

Although there was a clear enhancement in the rate of evolved acetone for Pd/Ce-Na, it did not represent the difference in phenol transfer hydrogenation rates observed (3-6x), which should correlate to the amount of acetone formed. To ensure that our assumption of a one-to-one acetone to molecular hydrogen stoichiometric relationship was valid, the amount of acetone formed during phenol transfer hydrogenation was measured under the conditions found in Table

1, Entries 2, 7. The evolved acetone for Pd/Ce-Na and Pd/CeO₂ were 3680 $\mu\text{mol g}^{-1} \text{h}^{-1}$ and 576 $\mu\text{mol g}^{-1} \text{h}^{-1}$, respectively (Table 3, Entries 3-4). These results agree well with the expected amount of acetone that should be formed considering the yield of products (Table 3).

A series of kinetic experiments were run to understand the cause of the lower activation barrier for Pd/Ce-Na (Figure 1b) since 2-propanol TPSR suggests there should be no difference. The experimental data showed that the acetone formation rate over both catalysts decreased in presence of phenol, likely due to their affinity for the same adsorption sites.^{15, 62} However, the relative percent decrease was much more severe over Pd/CeO₂ (80 %) than over Pd/Ce-Na (33 %) (Table 3). In addition, the difference between phenol conversion rates for the two catalysts increased with phenol concentration (Table 1). These results suggest the apparent activation barrier may be related to the barrier for 2-propanol adsorption in the presence of phenol. Here, we are assuming that the surface kinetics follow Langmuir-Hinshelwood mechanism for competitive binding. That is, increasing the phenol concentration should lead to higher binding site occupancy, which would hinder 2-propanol adsorption and limit turnover. Evidence for this type of behavior was obtained by monitoring the phenol conversion rate as a function of phenol concentration (Figure 4). Both materials showed a non-linear dependence of rate versus phenol concentration at conversions less than unity. The reaction rate profiles are characteristic for competitive adsorption.⁹⁰ The rate data also suggests there are more 2-propanol/phenol adsorption sites that lead to phenol turnover on Pd/Ce-Na shown by the up and rightward shift of the rate profile relative to Pd/CeO₂. That is, if the amount of 2-propanol/phenol adsorption sites were equal, the curve would be expected to shift straight up due to the increased number of redox active sites previously shown. This was supported through phenol adsorption isotherms that showed there were more phenol/2-propanol adsorption sites on the Ce-Na support even with the

surface area of CeO₂ being five times greater (Figure 5a). The y-intercept of the linear region was taken as the approximate monolayer coverage and gave 77 $\mu\text{mol g}^{-1}$ and 36 $\mu\text{mol g}^{-1}$ for Ce-Na and CeO₂, respectively. This ratio (2.1) agrees well with the mass normalized area summation of all monitored reactants and products from the TPSR-MS profiles for Ce-Na and CeO₂ (2.4) (Figure 3c, d). Furthermore, the ratio is identical to the ratio of acetone formation rates observed over the two catalysts in the absence of phenol (Table 3, Entries 1-2). Although the latter comparison is made between the supports and catalysts, it does suggest that the phenol adsorption sites are the same as 2-propanol and that these adsorption sites are active for 2-propanol dehydrogenation.

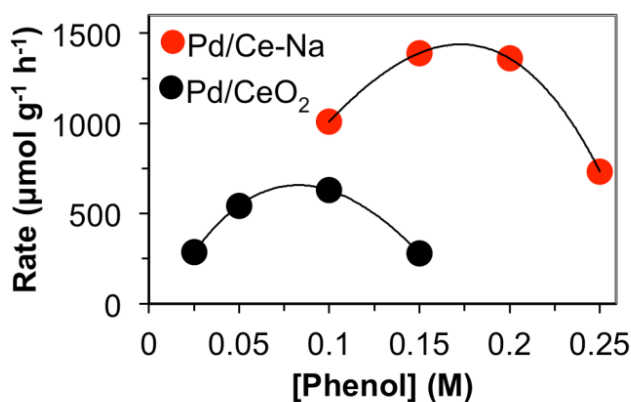


Figure 4. Phenol conversion rate versus phenol concentration over Pd/CeO₂ and Pd/Ce-Na. Conditions: 90 v/v % aqueous 2-propanol, 0.5 g catalyst, $\sim 0.1 \text{ mL min}^{-1}$, $T = 140 \text{ }^\circ\text{C}$, $V_{\text{bed}} = 0.4 \text{ mL}$.

Further evidence for the apparent activation barrier arising from the barrier for 2-propanol adsorption in presence of phenol was obtained by monitoring the phenol conversion rate as a function of aqueous 2-propanol concentration. Under the reaction conditions shown in Figure S23, the apparent order for 2-propanol during the transfer hydrogenation of phenol over

Pd/CeO₂ and Pd/Ce-Na were 3.7 and 0.9, respectively. The dependence of phenol conversion rate on the 2-propanol concentration over both catalysts indicates that water competes for the same binding sites as 2-propanol/phenol. The higher dependence of conversion rate on 2-propanol concentration for Pd/CeO₂ is consistent with phenol blocking a larger percentage of 2-propanol adsorption sites (i.e. Langmuir-Hinshelwood competitive binding) since all other conditions are equal. This was also made apparent by the drastic color change of CeO₂ in the presence of a 2-propanol/phenol solution (Figure S24).¹⁵ If the observed activation barrier for phenol transfer hydrogenation reflects the adsorption barrier for 2-propanol, the apparent activation energy should be a function of phenol concentration. Thus, Arrhenius plots were constructed to determine the variation of activation energy as a function of phenol (Figure 5b). Indeed, at high concentrations of phenol, Pd/Ce-Na showed an apparent activation barrier of 110 kJ mol⁻¹ while at low concentrations Pd/CeO₂ gave 54 kJ mol⁻¹. The transition from high to low activation barrier is dictated by phenol concentration and is consistent with Ce-Na having more binding sites than CeO₂. The higher amount of phenol/2-propanol adsorption sites and redox sites is likely related to the higher amount of O-vacancies observed from Raman studies.^{46-47, 64}

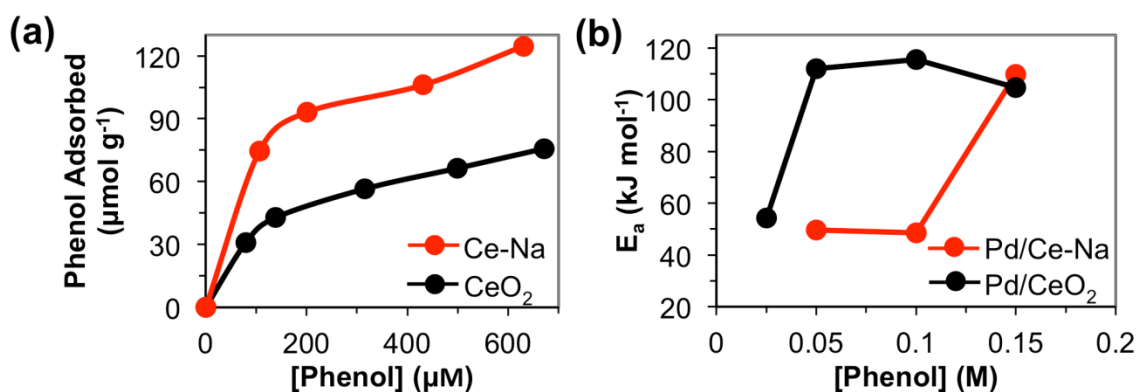


Figure 5. (a) Phenol adsorption isotherms for Ce-Na and CeO₂. (b) Plot showing the apparent activation energy for the transfer hydrogenation of phenol as a function of phenol concentration.

Conclusions

The 2-propanol dehydrogenation activity of ceria is enhanced through modification with sodium by increasing the number of adsorption and redox active sites. This effect was an intrinsic property of the Ce-Na support and independent of Pd. Sodium is neither on the surface of the active material nor is it doped into ceria, but exists likely as a subsurface carbonate species of varying degrees of hydration. Deposition of palladium onto ceria and sodium-modified ceria provides catalysts active for the transfer hydrogenation of phenol using 2-propanol. The catalytic transfer hydrogenation of phenol was conducted in flow mode and required water for stability. The higher activity of the sodium-modified catalyst was attributed to the higher amount of 2-propanol/phenol adsorption sites and redox sites active for 2-propanol dehydrogenation. The difference in apparent activation barriers between the two catalysts reflects the barrier for 2-propanol adsorption in the presence of phenol. Additional studies are in progress to determine the precise location of Na in the catalyst and the mechanism by which it increases the number of adsorption and redox-active sites on ceria.

Acknowledgements

This research is supported by the U.S. Department of Energy, Office of Basic Energy Sciences, Division of Chemical Sciences, Geosciences, and Biosciences, through the Ames Laboratory Catalysis Science program. The Ames Laboratory is operated for the U.S. Department of Energy by Iowa State University under Contract No. DE-AC02-07CH11358.

References

1. Klass, D. L., Biomass for Renewable Energy and Fuels A2 - Cleveland, Cutler J. In *Encyclopedia of Energy*; Elsevier: New York, 2004; pp 193-212.

2. Zakzeski, J.; Bruijninx, P. C. A.; Jongerius, A. L.; Weckhuysen, B. M. *Chem. Rev.* **2010**, 110, 3552-3599.
3. Xu, C.; Arancon, R. A. D.; Labidi, J.; Luque, R. *Chem. Soc. Rev.* **2014**, 43, 7485-7500.
4. Vardon, D. R.; Franden, M. A.; Johnson, C. W.; Karp, E. M.; Guarnieri, M. T.; Linger, J. G.; Salm, M. J.; Strathmann, T. J.; Beckham, G. T. *Energy Environ. Sci.* **2015**, 8, 617-628.
5. Kleinert, M.; Barth, T. *Chem. Eng. Technol.* **2008**, 31, 736-745.
6. Fu, D.; Farag, S.; Chaouki, J.; Jessop, P. G. *Bioresource Technol.* **2014**, 154, 101-108.
7. Fisher, W. B.; VanPeppen, J. F., Cyclohexanol and Cyclohexanone. In *Kirk-Othmer Encyclopedia of Chemical Technology*; John Wiley & Sons, Inc.: 2000.
8. Rase, H. F., *Handbook of Commercial Catalysts: Heterogeneous Catalysts*, CRC Press: Boca Raton, FL, 2000; pp 128-130.
9. Zhong, J.; Chen, J.; Chen, L. *Catal. Sci. Technol.* **2014**, 4, 3555-3569.
10. Chen, A.; Li, Y.; Chen, J.; Zhao, G.; Ma, L.; Yu, Y. *ChemPlusChem* **2013**, 78, 1370-1378.
11. Patil, R. D.; Sasson, Y. *Appl. Catal. A-Gen* **2015**, 499, 227-231.
12. Zhang, D.; Ye, F.; Xue, T.; Guan, Y.; Wang, Y. M. *Catal. Today* **2014**, 234, 133-138.
13. Nagasawa, Y.; Nanao, H.; Sato, O.; Yamaguchi, A.; Shirai, M. *Chem. Lett.* **2016**, 45, 643-645.
14. Wang, D.; Astruc, D. *Chem. Rev.* **2015**, 115, 6621-6686.
15. Nelson, N. C.; Manzano, J. S.; Sadow, A. D.; Overbury, S. H.; Slowing, I. I. *ACS Catal.* **2015**, 5, 2051-2061.
16. Hammond, C.; Schümperli, M. T.; Conrad, S.; Hermans, I. *ChemCatChem* **2013**, 5, 2983-2990.
17. He, L.; Ni, J.; Wang, L.-C.; Yu, F.-J.; Cao, Y.; He, H.-Y.; Fan, K.-N. *Chem. Eur. J.* **2009**, 15, 11833-11836.
18. Wang, M.-M.; He, L.; Liu, Y.-M.; Cao, Y.; He, H.-Y.; Fan, K.-N. *Green Chem.* **2011**, 13, 602-607.
19. Shimura, K.; Shimizu, K.-i. *Green Chem.* **2012**, 14, 2983-2985.
20. Trovarelli, A., *Catalysis by Ceria and Related Materials*, Imperial College Press: London, 2002.

21. Mamontov, E.; Egami, T.; Brezny, R.; Koranne, M.; Tyagi, S. *J. Phys. Chem. B* **2000**, 104, 11110-11116.
22. Esch, F.; Fabris, S.; Zhou, L.; Montini, T.; Africh, C.; Fornasiero, P.; Comelli, G.; Rosei, R. *Science* **2005**, 309, 752-755.
23. Madier, Y.; Descorme, C.; Le Govic, A. M.; Duprez, D. *J. Phys. Chem. B* **1999**, 103, 10999-11006.
24. Rossignol, S.; Gerard, F.; Duprez, D. *J. Mater. Chem.* **1999**, 9, 1615-1620.
25. Descorme, C.; Madier, Y.; Duprez, D. *J. Catal.* **2000**, 196, 167-173.
26. Guzman, J.; Carrettin, S.; Corma, A. *J. Am. Chem. Soc.* **2005**, 127, 3286-3287.
27. Li, C.; Domen, K.; Maruya, K.; Onishi, T. *J. Am. Chem. Soc.* **1989**, 111, 7683-7687.
28. Pushkarev, V. V.; Kovalchuk, V. I.; d'Itri, J. L. *J. Phys. Chem. B* **2004**, 108, 5341-5348.
29. Gorte, R. *J. AIChE J.* **2010**, 56, 1126-1135.
30. Rodriguez, J. A.; Wang, X.; Liu, P.; Wen, W.; Hanson, J. C.; Hrbek, J.; Pérez, M.; Evans, J. *Top. Catal.* **2007**, 44, 73-81.
31. Trovarelli, A. *Catal. Rev.* **1996**, 38, 439-520.
32. Paier, J.; Penschke, C.; Sauer, J. *Chem. Rev.* **2013**, 113, 3949-3985.
33. Murugan, B.; Ramaswamy, A. V. *J. Am. Chem. Soc.* **2007**, 129, 3062-3063.
34. Lawrence, N. J.; Brewer, J. R.; Wang, L.; Wu, T. S.; Wells-Kingsbury, J.; Ihrig, M. M.; Wang, G.; Soo, Y. L.; Mei, W. N.; Cheung, C. L. *Nano Lett* **2011**, 11, 2666-71.
35. Liu, X.; Zhou, K.; Wang, L.; Wang, B.; Li, Y. *J. Am. Chem. Soc.* **2009**, 131, 3140-3141.
36. Peng, D.-Z.; Chen, S.-Y.; Chen, C.-L.; Gloter, A.; Huang, F.-T.; Dong, C.-L.; Chan, T.-S.; Chen, J.-M.; Lee, J.-F.; Lin, H.-J.; Chen, C.-T.; Chen, Y.-Y. *Langmuir* **2014**, 30, 10430-10439.
37. Chen, L.; Fleming, P.; Morris, V.; Holmes, J. D.; Morris, M. A. *J. Phys. Chem. C* **2010**, 114, 12909-12919.
38. Senanayake, S. D.; Stacchiola, D.; Rodriguez, J. A. *Acc. Chem. Res.* **2013**, 46, 1702-1711.
39. Lin, Y.; Wu, Z.; Wen, J.; Poeppelmeier, K. R.; Marks, L. D. *Nano Lett* **2014**, 14, 191-6.
40. Mai, H.-X.; Sun, L.-D.; Zhang, Y.-W.; Si, R.; Feng, W.; Zhang, H.-P.; Liu, H.-C.; Yan, C.-H. *J. Phys. Chem. B* **2005**, 109, 24380-24385.

41. Wu, Z.; Li, M.; Howe, J.; Meyer, H. M.; Overbury, S. H. *Langmuir* **2010**, 26, 16595-16606.
42. Wu, Z.; Li, M.; Overbury, S. H. *J. Catal.* **2012**, 285, 61-73.
43. Aneggi, E.; Wiater, D.; de Leitenburg, C.; Llorca, J.; Trovarelli, A. *ACS Catal.* **2014**, 4, 172-181.
44. Wu, Z.; Li, M.; Mullins, D. R.; Overbury, S. H. *ACS Catal.* **2012**, 2, 2224-2234.
45. Li, M.; Wu, Z.; Overbury, S. H. *J. Catal.* **2013**, 306, 164-176.
46. Ferrizz, R. M.; Wong, G. S.; Egami, T.; Vohs, J. M. *Langmuir* **2001**, 17, 2464-2470.
47. Mullins, D. R.; Robbins, M. D.; Zhou, J. *Surf. Sci.* **2006**, 600, 1547-1558.
48. Siokou, A.; Nix, R. M. *J. Phys. Chem. B* **1999**, 103, 6984-6997.
49. Torella, J. P.; Gagliardi, C. J.; Chen, J. S.; Bediako, D. K.; Colón, B.; Way, J. C.; Silver, P. A.; Nocera, D. G. *Proc. Natl. Acad. Sci.* **2015**, 112, 2337-2342.
50. Vaccaro, L.; Lanari, D.; Marrocchi, A.; Strappaveccia, G. *Green Chem.* **2014**, 16, 3680-3704.
51. Harris, R. K.; Becker, E. D.; De Menezes, S. M. C.; Goodfellow, R.; Granger, P. *Pure Appl. Chem.* **2001**, 73, 1795-1818.
52. Gullion, T.; Schaefer, J. *J. Magn. Reson.* **1989**, 81, 196-200.
53. Gullion, T.; Baker, D. B.; Conradi, M. S. *J. Magn. Reson.* **1990**, 89, 479-484.
54. Mueller, K. T. *J. Magn. Reson., Series A* **1995**, 113, 81-93.
55. Sangodkar, R. P.; Smith, B. J.; Gajan, D.; Rossini, A. J.; Roberts, L. R.; Funkhouser, G. P.; Lesage, A.; Emsley, L.; Chmelka, B. F. *J. Am. Chem. Soc.* **2015**, 137, 8096-8112.
56. Frydman, L.; Harwood, J. S. *J. Am. Chem. Soc.* **1995**, 117, 5367-5368.
57. Brown, S. P.; Wimperis, S. *J. Magn. Reson.* **1997**, 128, 42-61.
58. Amoureux, J. P.; Huguenard, C.; Engelke, F.; Taulelle, F. *Chem. Phys. Lett.* **2002**, 356, 497-504.
59. Hardacre, C.; Roe, G. M.; Lambert, R. M. *Surf. Sci.* **1995**, 326, 1-10.
60. Romeo, M.; Bak, K.; El Fallah, J.; Le Normand, F.; Hilaire, L. *Surf. Interf. Anal.* **1993**, 20, 508-512.
61. Li, F.-t.; Ran, J.; Jaroniec, M.; Qiao, S. Z. *Nanoscale* **2015**, 7, 17590-17610.

62. Mullins, D. R.; Senanayake, S. D.; Chen, T. L. *J. Phys. Chem. C* **2010**, 114, 17112-17119.
63. Mullins, D. R.; Albrecht, P. M.; Calaza, F. *Top. Catal.* **2013**, 56, 1345-1362.
64. Mullins, D. R. *Surf. Sci. Rep.* **2015**, 70, 42-85.
65. Mullins, D. R.; Albrecht, P. M.; Chen, T.-L.; Calaza, F. C.; Biegalski, M. D.; Christen, H. M.; Overbury, S. H. *J. Phys. Chem. C* **2012**, 116, 19419-19428.
66. Chen, B.; Ma, Y.; Ding, L.; Xu, L.; Wu, Z.; Yuan, Q.; Huang, W. *J. Phys. Chem. C* **2013**, 117, 5800-5810.
67. Molinari, M.; Parker, S. C.; Sayle, D. C.; Islam, M. S. *J. Phys. Chem. C* **2012**, 116, 7073-7082.
68. Yang, M.; Liu, J.; Lee, S.; Zugic, B.; Huang, J.; Allard, L. F.; Flytzani-Stephanopoulos, M. *J. Am. Chem. Soc.* **2015**, 137, 3470-3473.
69. Zhai, Y.; Pierre, D.; Si, R.; Deng, W.; Ferrin, P.; Nilekar, A. U.; Peng, G.; Herron, J. A.; Bell, D. C.; Saltsburg, H.; Mavrikakis, M.; Flytzani-Stephanopoulos, M. *Science* **2010**, 329, 1633-1636.
70. Shannon, R. *Acta. Cryst.* **1976**, 32, 751-767.
71. Luo, M.-F.; Yan, Z.-L.; Jin, L.-Y.; He, M. *J. Phys. Chem. B* **2006**, 110, 13068-13071.
72. McBride, J. R.; Hass, K. C.; Poindexter, B. D.; Weber, W. H. *J. Appl. Phys.* **1994**, 76, 2435-2441.
73. Taniguchi, T.; Watanabe, T.; Sugiyama, N.; Subramani, A. K.; Wagata, H.; Matsushita, N.; Yoshimura, M. *J. Phys. Chem. C* **2009**, 113, 19789-19793.
74. Spanier, J. E.; Robinson, R. D.; Zhang, F.; Chan, S.-W.; Herman, I. P. *Phys. Rev. B* **2001**, 64, 245407.
75. Li, M.; Tumuluri, U.; Wu, Z.; Dai, S. *ChemSusChem* **2015**, 8, 3651-3660.
76. Siriwardane, R. V.; Poston, J. A.; Robinson, C.; Simonyi, T. *Energy Fuels* **2011**, 25, 1284-1293.
77. Hammond, J. S.; Holubka, J. W.; deVries, J. E.; Dickie, R. A. *Corros. Sci.* **1981**, 21, 239-253.
78. Dunsmore, H. S.; Speakman, J. C. *Acta Crystallogr.* **1963**, 16, 573-574.
79. Dusek, M.; Chapuis, G.; Meyer, M.; Petricek, V. *Acta Crystallogr. Sect. B* **2003**, 59, 337-352.

80. Pfau, A.; Schierbaum, K. D. *Surf. Sci.* **1994**, 321, 71-80.
81. Senanayake, S. D.; Mullins, D. R. *J. Phys. Chem. C.* **2008**, 112, 9744-9752.
82. Chen, L.; Zhao, J.; Yin, S.-F.; Au, C.-T. *RSC Adv.* **2013**, 3, 3799-3814.
83. Hattori, H. *Chem. Rev.* **1995**, 95, 537-558.
84. Evin, H. N.; Jacobs, G.; Ruiz-Martinez, J.; Graham, U. M.; Dozier, A.; Thomas, G.; Davis, B. H. *Catal. Lett.* **2008**, 122, 9-19.
85. Lawrence, N. J.; Brewer, J. R.; Wang, L.; Wu, T.-S.; Wells-Kingsbury, J.; Ihrig, M. M.; Wang, G.; Soo, Y.-L.; Mei, W.-N.; Cheung, C. L. *Nano Lett.* **2011**, 11, 2666-2671.
86. Zaki, M. I.; Sheppard, N. *J. Catal.* **1983**, 80, 114-122.
87. Mazdiyasi, K. S.; Brown, L. M. *Inorg. Chem.* **1970**, 9, 2783-2786.
88. Zaki, M. I.; Hussein, G. A. M.; El-Ammawy, H. A.; Mansour, S. A. A.; Polz, J.; Knözinger, H. *J. Mol. Catal.* **1990**, 57, 367-378.
89. Redhead, P. A. *Vacuum* **1962**, 12, 203-211.
90. Masel, R., *Principles of Adsorption and Reaction on Solid Surfaces*, Wiley-Interscience: 1996.

Appendix of Supporting Information

Table S1. Physicochemical properties of supports and catalysts.

Sample	Surface Area (m ² g ⁻¹) ^a	Crystallite Size (nm) ^b	Na Loading (at. %) ^c	Pd Loading (at. %) ^c	Pd Dispersion (%) ^d
Ce-Na	29	14	18 ± 1 ^e	0	---
CeO ₂	210	6	0	0	---
Pd/Ce-Na	17	26	18 ± 1 ^e	1.9 ± 0.1 ^f	42
Pd/CeO ₂	121	10	0	1.7 ± 0.1 ^f	64

^aDetermined by nitrogen physisorption using BET approximation. ^bDetermined by PXRD.

^cDetermined by ICP-OES and is relative to Ce. ^dDetermined by H₂ pulse chemisorption at -25

°C. ^eMeasured across three batches in singlet (i.e. 3 data points). ^fMeasured across one batch with two separate sample preps in duplicate (i.e. 4 data points).

Table S2. Post reaction (7 d TOS) physicochemical properties shared by both catalysts.

Sample	Surface Area (m ² g ⁻¹) ^a	Ce Crystallite Size (nm) ^b	Pd Loading (at. %) ^c	Pd Dispersion (%) ^d
Pd/Ce-Na	20	26	1.8 ± 0.1	7

Pd/CeO₂ 38 14 1.8 ± 0.1 11

^aDetermined by nitrogen physisorption using BET approximation. ^bDetermined by PXRD.

^cDetermined by ICP-OES and is relative to Ce Measured in duplicate with two sample preps (i.e. 4 data points). ^dDetermined by H₂ pulse chemisorption at -25 °C.

Table S3. Physicochemical properties and CO₂ desorption data for CeO₂ and Ce-Na.

Entry	Sample ^a	Surface Area (m ² g ⁻¹) ^b	CO ₂ Desorbed (mmol g ⁻¹) ^c	Site Density (μmol CO ₂ m ⁻²)	Sites (nm ⁻²)
1	Ce-Na ^d	42	0.10-0.13 ^e	2.6-3.2	1.5-1.9
2	CeO ₂	210	0.38	1.8	1.1
3	CeO ₂ -550	139	0.23	1.7	1.0
4	CeO ₂ -650	39	0.10	2.6	1.5
5	CeO ₂ -750	14	0.05	3.6	2.2

^aThe number designation indicates the calcination temperature. ^bDetermined by nitrogen physisorption using BET approximation. ^cDetermined by CO₂-TPD. ^dPeaks attributed to carbonate decomposition are excluded. ^eThe lower and upper limits were calculated by excluding and including the deconvoluted peak centered around 600 °C, respectively (Figure S16).

Temperature programmed desorption of carbon dioxide (CO₂-TPD) was used to probe the changes of material basicity upon introduction of sodium. There were four significant desorption maxima observed for CeO₂ upon CO₂-TPD profile deconvolution (Figure S15a). Low temperature desorption maxima occurred at 120 °C and 200 °C which were attributed to adsorption by weak basic sites. Higher temperature desorption maxima were found at 400 and 600 °C and were attributed to adsorption by intermediate strength basic sites. The results are consistent with the well-documented mild basicity of ceria.¹ CO₂-TPD profile deconvolution for Ce-Na showed a similar low-to-mid temperature desorption behavior (Figure S15b). Two desorption maxima were present at 110 °C and 300 °C, coinciding with adsorption by weak basic sites and another at 640 °C attributed to intermediate strength basic sites. Excluding the high temperature CO₂ desorption peaks (>600 °C) from Ce-Na that were suggested to arise from sodium carbonate decomposition allowed quantification of apparent basic site density. For CeO₂, the apparent basic site density was 1.8 μmol CO₂ m⁻² (Table S3, Entry 2), which was lower than the estimated amount for Ce-Na, 2.6-3.2 μmol CO₂ m⁻² (Table S3, Entry 1). However, it is

unclear how surface area changes the basic site density and a better comparison would be with two samples of similar surface area. Therefore, several control samples of CeO₂ were prepared with different surface areas obtained by calcination of CeO₂ at different temperatures (Table S3, Entries 2-5). Plotting the amount of CO₂ desorbed versus the surface area showed a direct linear dependence that allowed us to relate the changes in basic site density to the surface area of CeO₂ (Figure S12). In general, as the surface area decreased the basic site density increased (Table S3, Entries 2-5). Comparison between Ce-Na and CeO₂ that had similar surface area (Table S3, Entries 1, 4) showed the apparent basic site density to be more or less the same. Thus, from CO₂-TPD there doesn't appear to be a significant difference in the basic site strength or density upon modification of ceria with sodium.

Table S4. Knoevenagel reaction conditions and results.^a

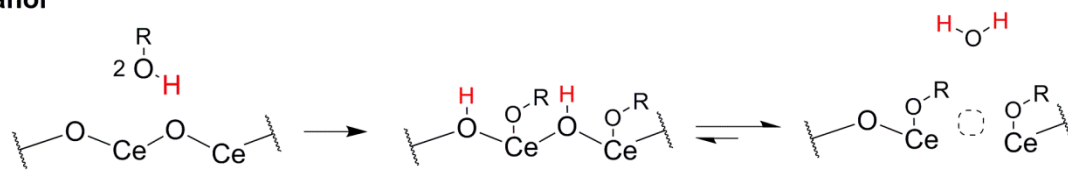
Entry	Catalyst	Substrate	TOF ^b (min ⁻¹)
1	CeO ₂	Malononitrile	0.76
2	Ce-Na	Malononitrile	0.73

^aReactions were run with ~6 mg of catalyst in ethanol (2 mL) using benzaldehyde (1 mmol) and activated methylene substrate (1 mmol) at 60 °C for 30 min. ^bMoles of converted reactant per moles of catalyst per reaction time. The molecular weight of Ce-Na was taken to be that of CeO₂.

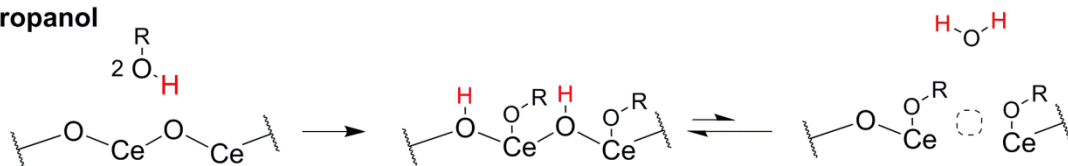
The basicity was also assessed for both materials using the Knoevenagel reaction. The Knoevenagel condensation reaction is a base-catalyzed reaction between benzaldehyde and compounds containing an activated methylene group and is often used as a test reaction to compare the relative basicity between different materials.² For a given aldehyde, the rate of reaction is directly affected by the ease of proton abstraction from the active methylene group (i.e. it's pK_a) and thus reflects the basic strength of the catalyst. The reaction between benzaldehyde and malononitrile (pK_a = 11.0) in ethanol showed similar activity with both catalysts (Table S4). Considering the three basicity characterization methods together (Figure

S16-18, Table S3-S4), there appears to be no significant difference in basic site density or strength upon modification of ceria with sodium. This suggests that the different rates of reaction and activation barriers observed during phenol transfer hydrogenation catalysis are not related to changes in basicity.

neat 2-propanol



aqueous 2-propanol



Scheme S1. Proposed hydroxyl disproportionation equilibrium in neat 2-propanol (top) and aqueous 2-propanol (bottom).

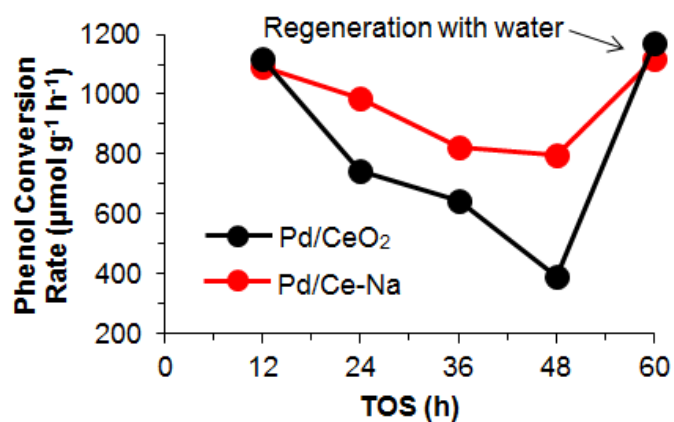


Figure S1. Phenol conversion rate versus time on stream (TOS) over Pd/CeO₂ and Pd/Ce-Na. Conditions: 0.1 M phenol in 2-propanol, 0.5 g catalyst, 0.1 mL min⁻¹, T = 140 °C, V_{bed} = 0.4 mL. Each data point corresponds to a 72 mL product stream composite. After 48 h, the reagent feed was switched to water for 12 h and then switched back to 0.1 M phenol in 2-propanol for an additional 12 h (last data point).

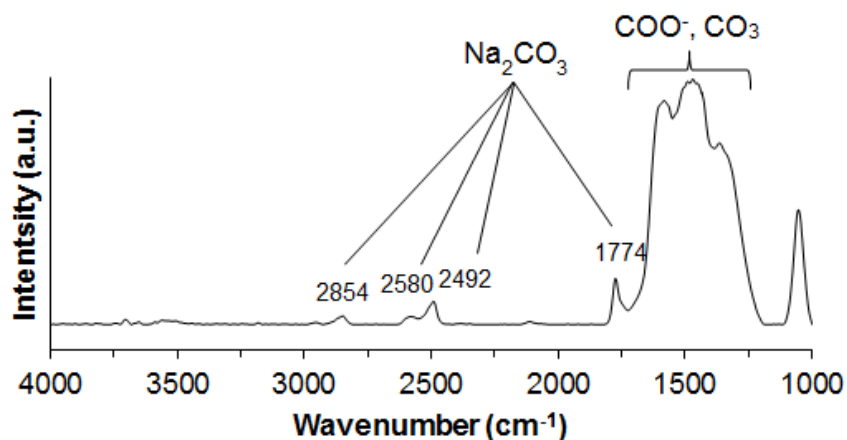


Figure S2. DRIFT spectrum of unwashed Ce-Na taken at room temperature after outgassing at 200 °C under He. The spectrum shows the presence of carbonates and carbonate overtones characteristic of sodium carbonate.³

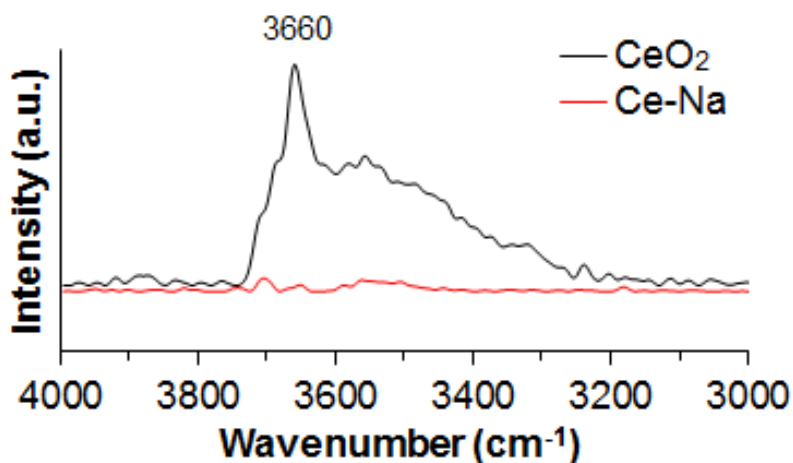


Figure S3. DRIFT spectrum of CeO₂ and unwashed Ce-Na after outgassing at 200 °C under He. The hydroxyl region for unwashed Ce-Na showed minimal band intensity, in direct contrast to the hydroxyl band intensity observed for CeO₂. The band at 3660 cm⁻¹ is attributed to type II ceria hydroxyl groups.⁴ The low hydroxyl group band intensity of unwashed Ce-Na agreed well with the IR spectrum of sodium carbonate and suggested that the surface was dominated by sodium carbonate species.

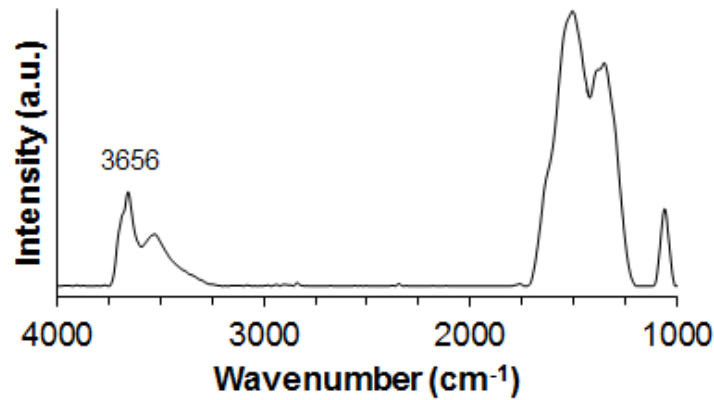
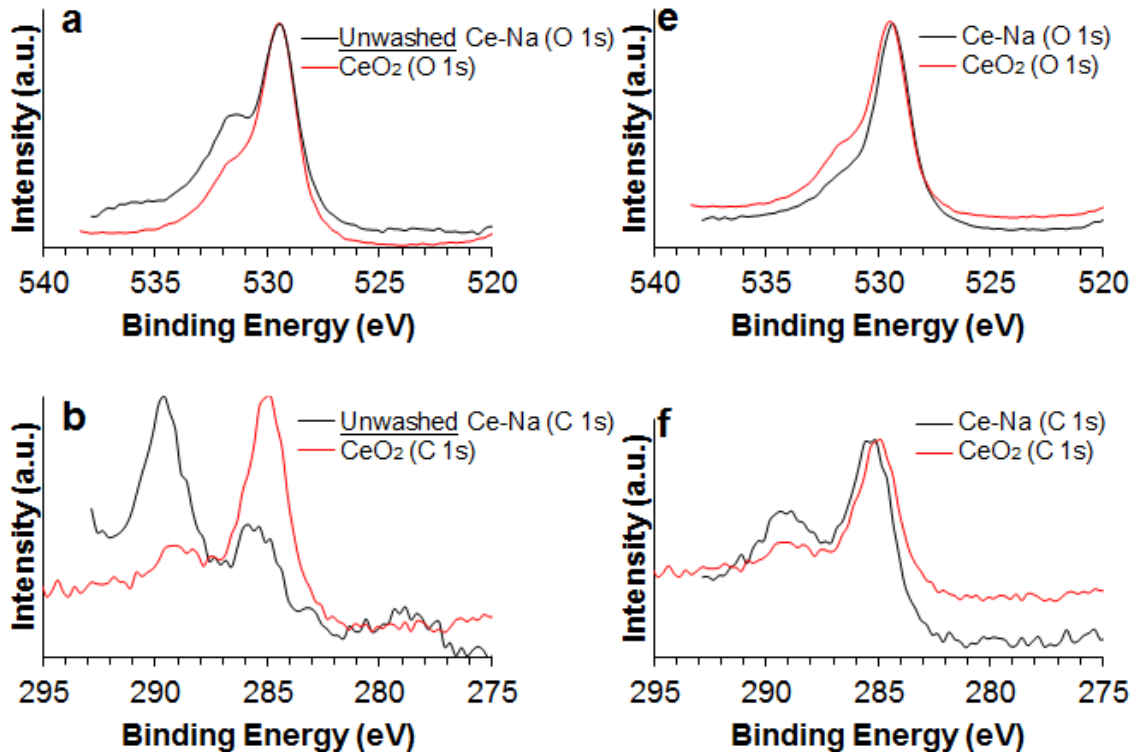


Figure S4. DRIFT spectrum of Ce-Na after washing with water at room temperature for 12 h in a liquid flow reactor. The spectrum was taken after *ex situ* thermal treatment at 125 °C to remove adsorbed water. The DRIFT spectrum showed no indication of surface sodium carbonates clearly evidenced by the absence of bands from 1750-2900 cm^{-1} . In addition, there was an emergence of characteristic type II ceria hydroxyl groups ($\sim 3653 \text{ cm}^{-1}$)⁴ and carbonates ($1700\text{-}1000 \text{ cm}^{-1}$)⁴ indicating surface sodium carbonates do not persist when Ce-Na is subjected to water. Furthermore, the specific surface area of the washed sample increased likely due to pore re-accessibility associated with sodium carbonate dissolution (Table 2, Entries 1,3).



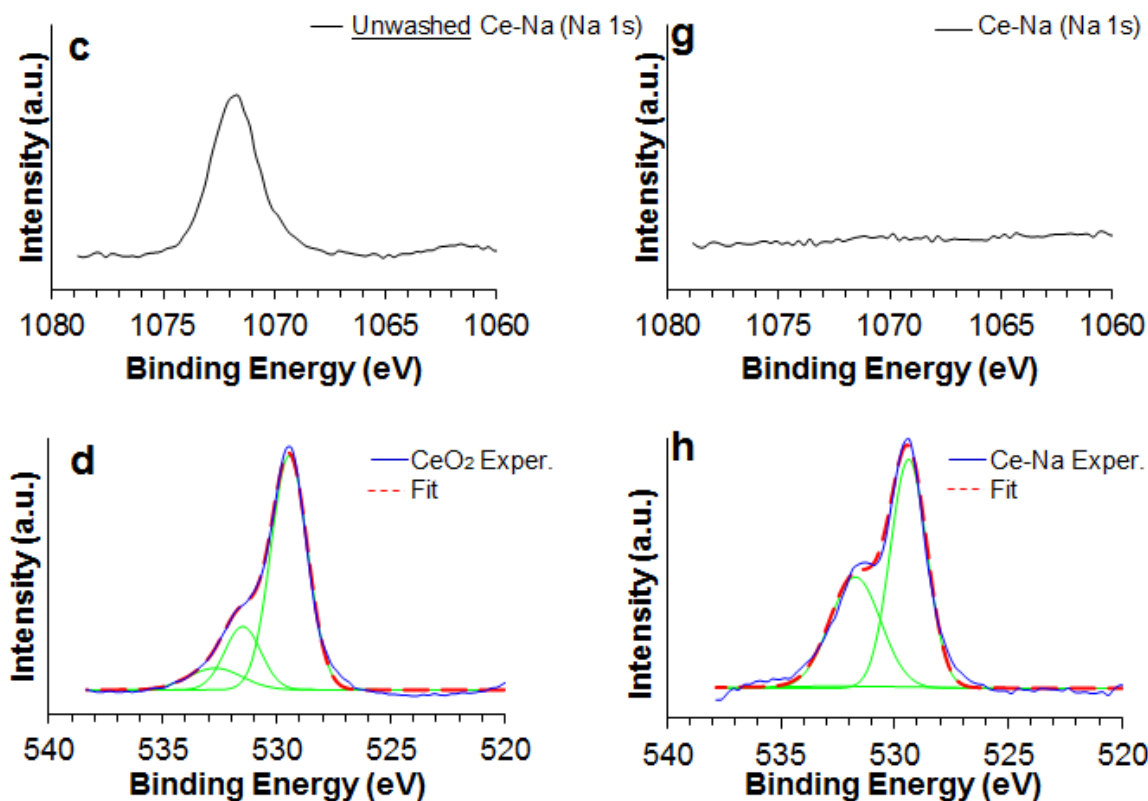


Figure S5. XPS spectra of (a-c) unwashed Ce-Na and (e-g) Ce-Na plotted with the XPS spectrum for CeO₂. (a, e), (b, f), and (c, g), corresponding to O 1s, C 1s, and Na 1s spectral regions, respectively. Deconvoluted XPS spectra of O 1s region for (d) CeO₂ and (h) unwashed Ce-Na. See text below for further explanation of XPS spectra.

Previous studies have shown the ceria O 1s spectrum can be described by three types of oxygen species: lattice oxygen⁵ (529.6 eV), adsorbed carbonates⁶⁻⁷(531.2 eV), and surface hydroxyls⁵ (532.7 eV). The O 1s spectrum of CeO₂ was deconvoluted into three peaks with maxima found at 529.5 eV, 531.5 eV, and 532.7 eV assigned to lattice oxygen, adsorbed carbonates, and surface hydroxyls, respectively (Figure S5d). Similarly, deconvolution of the O 1s spectral region for unwashed Ce-Na showed two maxima centered at 529.4 eV and 531.7 eV assigned to lattice oxygen and adsorbed carbonates, respectively (Figure S5h). The peak assigned to hydroxyl groups (532.7 eV) only accounted for 3 % of the total area and is therefore not visible. The O1s carbonate peak for unwashed Ce-Na (531.7 eV) was slightly shifted to higher

binding energies than for adsorbed carbonates on CeO₂ (531.5 eV) and corresponds very well to the O 1s binding energy in sodium carbonate.⁸ The relative peak area of O1s carbonate groups for unwashed Ce-Na was 39 % compared to only 19 % for CeO₂ (Figure S5d, h). The higher amount of carbonates and lower amount of hydroxyls on unwashed Ce-Na evidenced by XPS peak-fitting analysis is consistent with DRIFT analysis for unwashed Ce-Na, further indicating that the surface was saturated with sodium carbonate species. In addition, the C 1s spectral region for unwashed Ce-Na (Figure S5b) showed a signal centered around 289.6 eV, that was not present in CeO₂, and is consistent with the C 1s binding energy in sodium carbonate.⁸ Finally, the Na 1s region for unwashed Ce-Na (Figure S5c) showed a single peak centered around 1071.8 eV and was attributed to sodium carbonate.⁸ Quantitative XPS analysis showed the sodium content of Ce-Na was 25 at. % and is in agreement with ICP analysis (Table 2, Entry 1). These results indicate sodium is mostly present on unwashed Ce-Na as a carbonate and is preferentially located near the surface of the material. XPS analysis of Ce-Na showed a severely diminished Na 1s spectrum that did not provide insight into the electronic or chemical environment of residual sodium species due to the low S/N (Figure S5g). The decrease of the Na 1s signal coincided with the attenuation of the O 1s peak at 531.7 eV (Figure S5a, e) and the C 1s peak at 289.6 eV (Figure S5b, f) which were attributed to sodium carbonates.

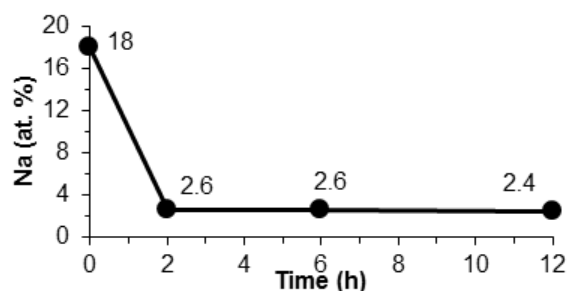


Figure S6. Na at. % versus time under water flow (0.1 mL min⁻¹) at 140 °C.

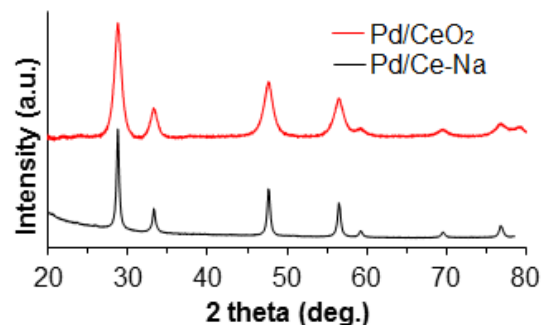


Figure S7. PXRD patterns for Pd/CeO₂ and Pd/Ce-Na.

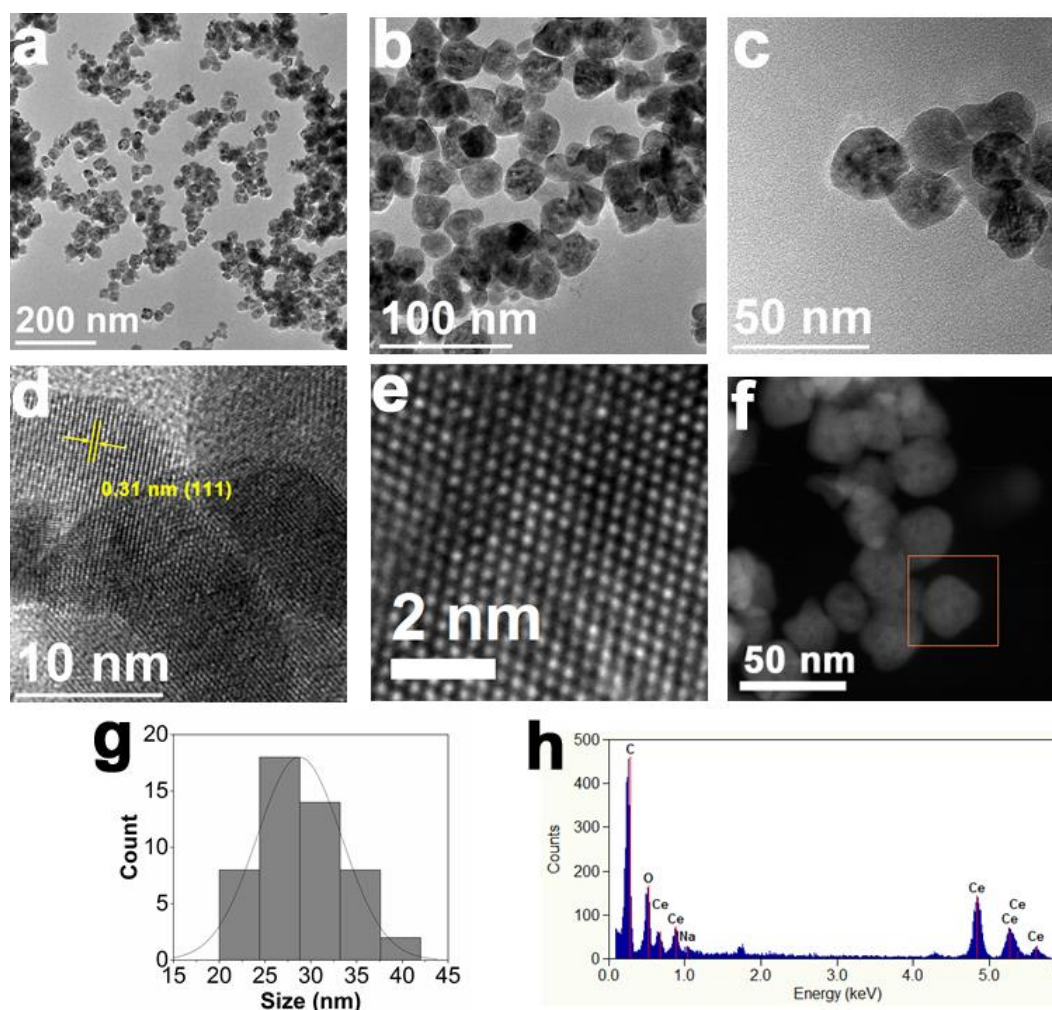


Figure S8. (a-c) TEM images of Ce-Na displaying spherical particle morphology. (d-e) HR-TEM images of Ce-Na showing (111) surface termination and hexagonal array of atoms consistent with (111) surface. (f) STEM image and corresponding EDX spectrum (h) of Ce-Na showing marginal amounts of surface sodium consistent with XPS analysis. (g) Particle size histogram giving an average particle size of 29 ± 5 nm.

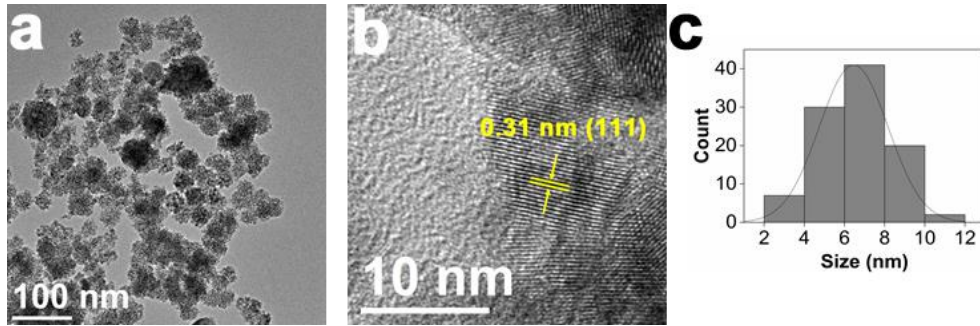


Figure S9. (a) TEM image of CeO₂ displaying aggregated particle morphology. (b) HR-TEM image of CeO₂ showing (111) surface termination. (c) Particle size histogram giving an average particle size of 6.5 ± 1.7 nm.

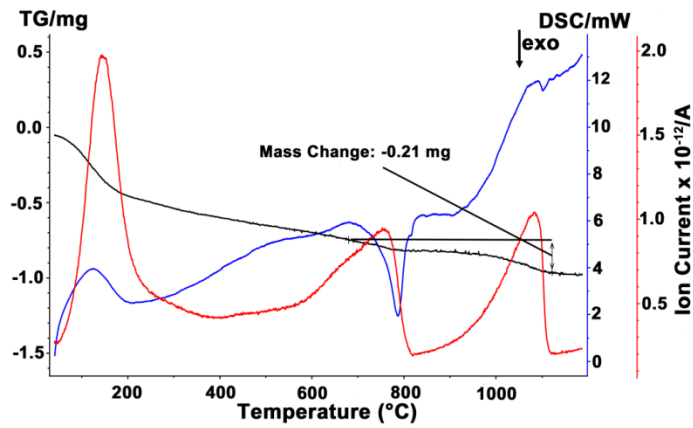


Figure S10. TGA-DSC-MS profile for Ce-Na. MS signal corresponds to $m/z = 44$ (CO₂).

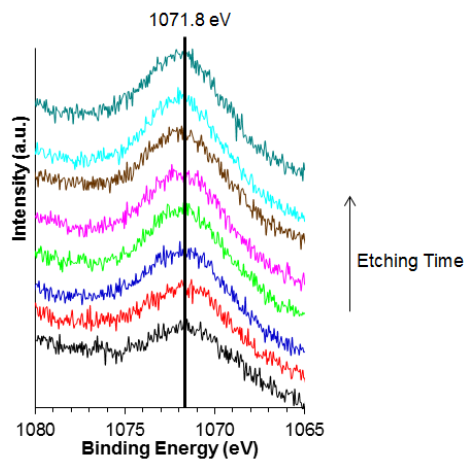


Figure S11. XPS depth-profiling Na 1s spectra for Ce-Na. Na 1s binding energy for Na₂O is 1072.5 eV.

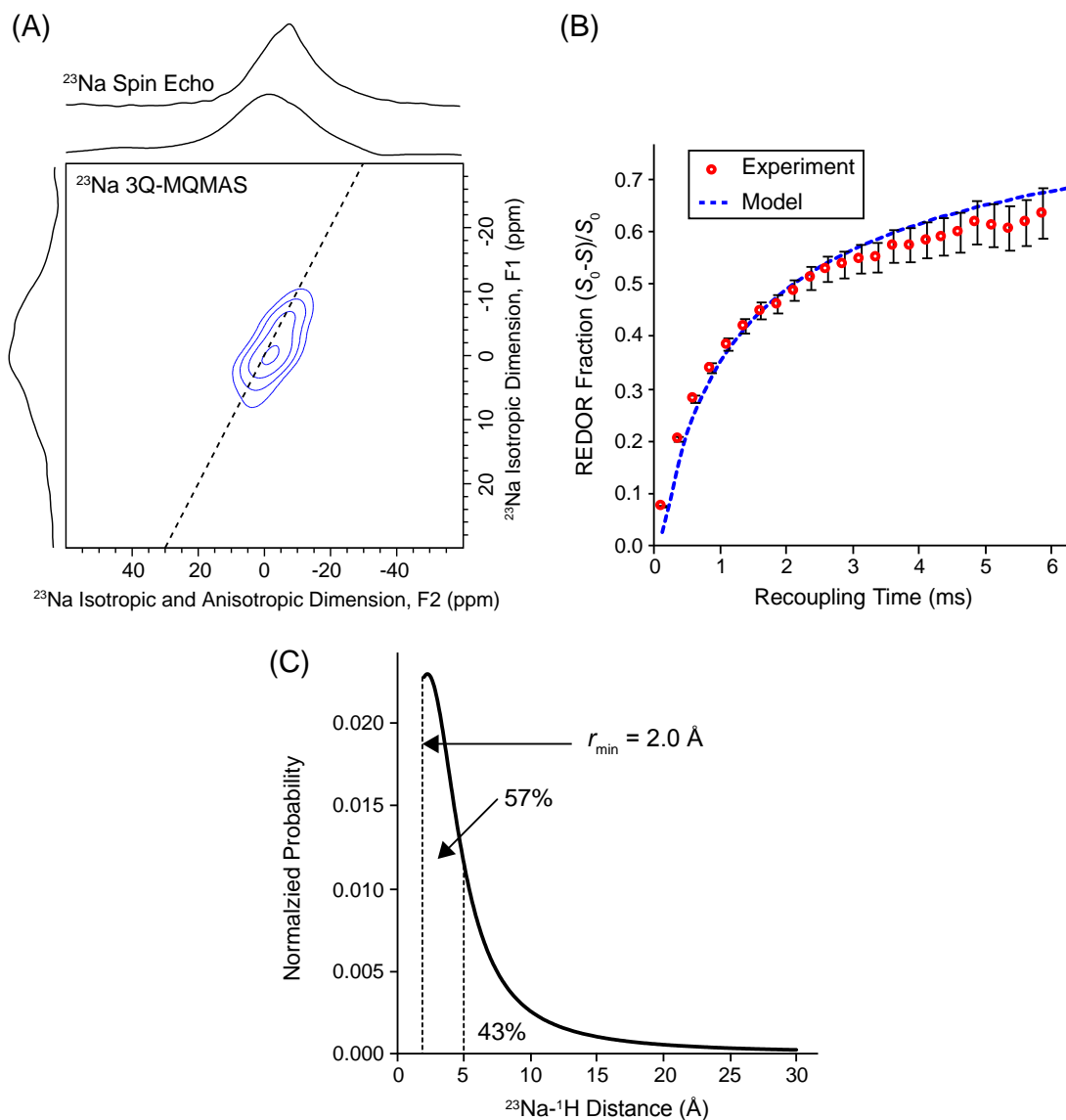


Figure S12. Summary of ^{23}Na solid-state NMR experiments on Ce-Na support. (A) 1D ^{23}Na spin echo (upper trace) and 2D ^{23}Na MQMAS solid-state NMR spectra. The MQMAS spectrum shows that the broadening of the ^{23}Na NMR spectrum primarily arises from a distribution of isotropic ^{23}Na chemical shifts. (B) Results of $^{23}\text{Na}\{^1\text{H}\}$ REDOR experiments. Experimental points are shown as open red circles and model resulting from a distribution of ^{23}Na - ^1H inter-nuclear distances is shown as the blue dashed line. (C) Distribution of ^{23}Na - ^1H distances resulting from the model of the experimental REDOR dephasing curve.

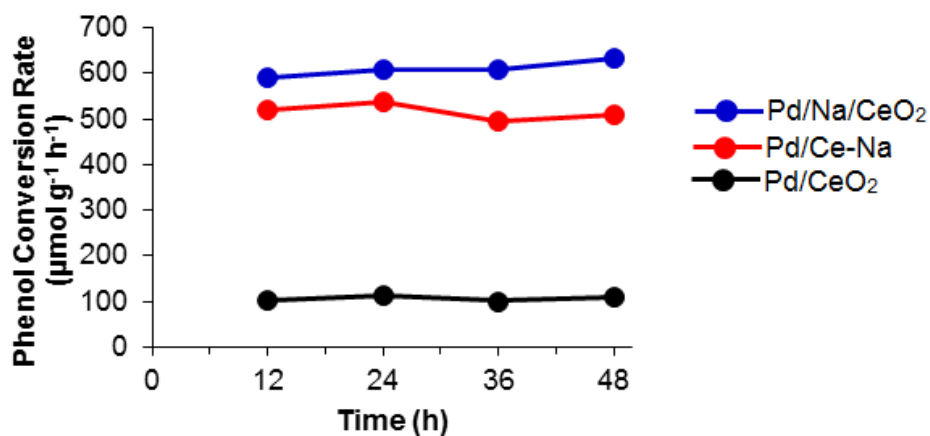


Figure S13. Phenol conversion rate over 48 h using different catalysts. Conditions: 0.025 M phenol in 30 v/v % aqueous 2-propanol, 0.2 g catalyst, $\sim 0.1 \text{ mL min}^{-1}$, $T = 130 \text{ }^\circ\text{C}$, $V_{\text{bed}} = 0.2 \text{ mL}$.

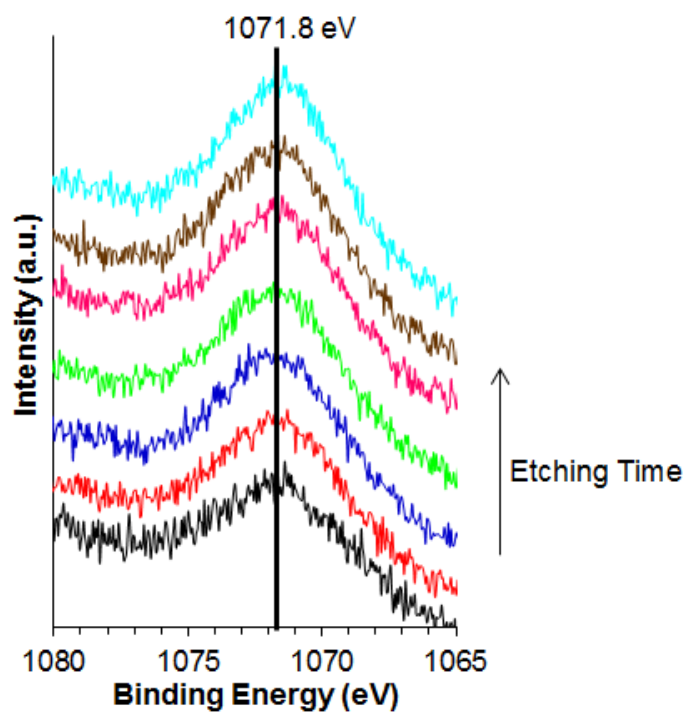


Figure S14. XPS depth-profiling Na 1s spectra for Na/CeO₂ (washed with water). Na 1s binding energy for Na₂O is 1072.5 eV.

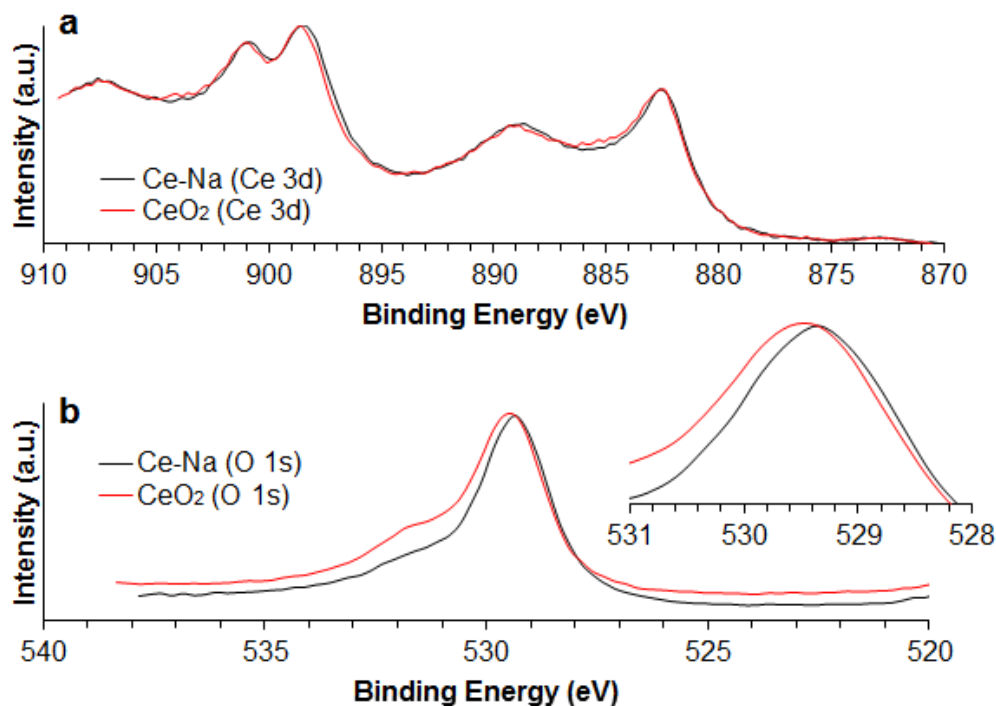


Figure S15. XPS spectra for Ce-Na and CeO₂ within in the (a) Ce 3d and (b) O 1s spectral regions. Inset shows zoomed in O 1s region.

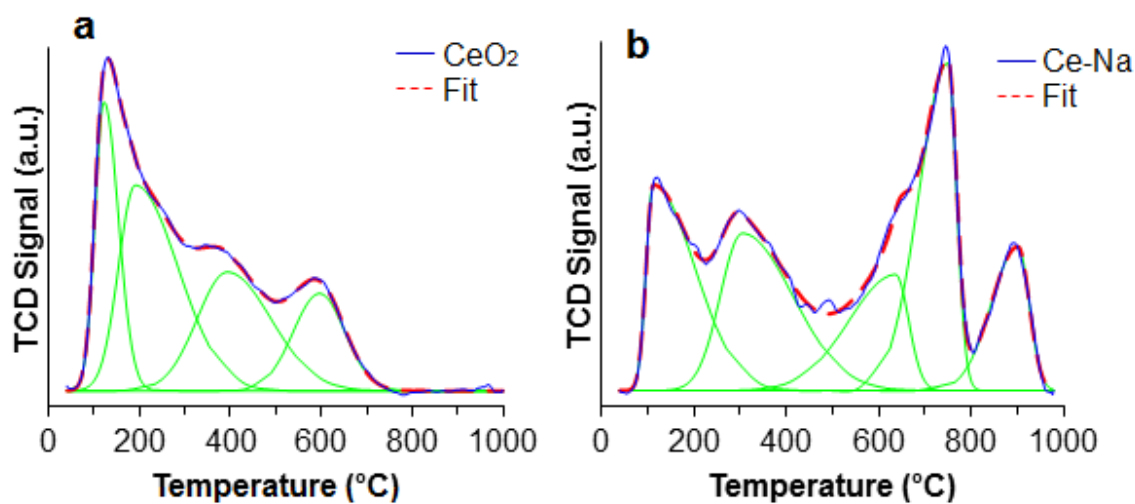


Figure S16. Deconvoluted CO₂-TPD profiles for (a) CeO₂, and (b) Ce-Na.

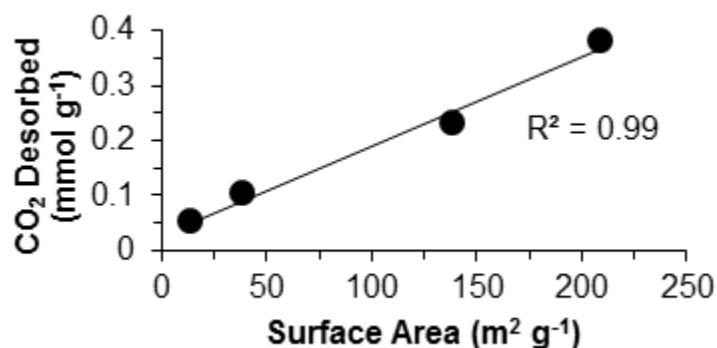


Figure S17. Plot showing the amount of CO₂ desorbed versus specific surface area for CeO₂ calcined at different temperatures.

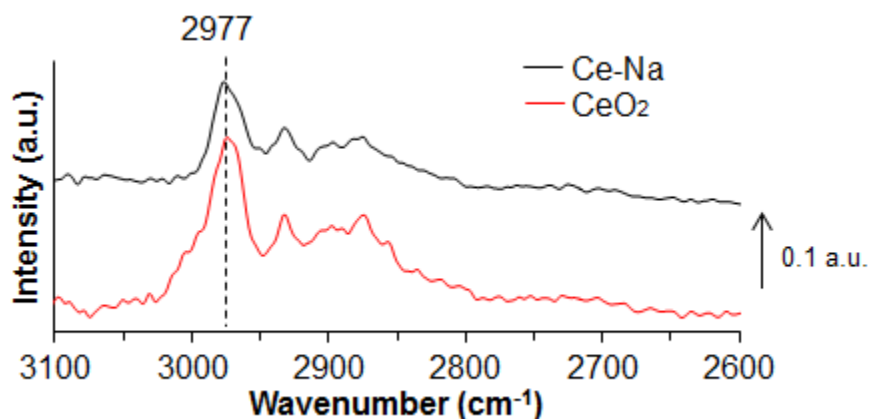


Figure S18. DRIFT spectrum of adsorbed CHCl₃ on Ce-Na and CeO₂.

The results from CO₂-TPD experiments are somewhat inconclusive due to the overlap of signals around 600 °C ascribed to either CO₂ desorbed or decomposed. Therefore, the basic properties of the materials were also compared using CHCl₃ as a basicity probe through adsorption at room temperature. CHCl₃ has been shown to interact with the surface of metal oxides via end-on mode (H to lattice O), bridging mode (Cl to metal cation and H to lattice O) and/or end-on mode (Cl to metal cation).^{1,9-11} The first two adsorption modes result in a red shift of the ν(C-H) stretching mode (ν(C-H)_{liq} = 3019 cm⁻¹) with the end-on adsorption giving larger

shifts, while the Cl to metal cation end-on interaction leads to a blue shift. Figure S16 shows the DRIFT spectra for adsorbed CHCl_3 on degassed CeO_2 and Ce-Na . For both materials, the $\nu(\text{C-H})$ stretching mode was found at 2977 cm^{-1} indicating there was a significant, yet identical interaction of CHCl_3 with both surfaces, consistent with previous studies.^{1, 10} Given the large red shift of the $\nu(\text{C-H})$ stretching mode the interaction is believed to be primarily end-on adsorption and thus should reflect the basicity of lattice oxygen. The identical spectra implied there are no substantial differences in basicity between the two materials and is in agreement with the results obtained from CO_2 -TPD data. Furthermore, previous studies have suggested that alkali modified ceria catalysts promote water gas shift and methanol steam reforming reactions through weakening (IR red-shift) of C-H bonds. The weakening was proposed to promote dehydrogenation of reactive intermediates. However, the catalysts used in the aforementioned study were not washed with water and contained a significant amount of alkali metal on the surface. The results here indicate there is no C-H weakening upon sodium modification and is consistent with the absence of surface sodium.

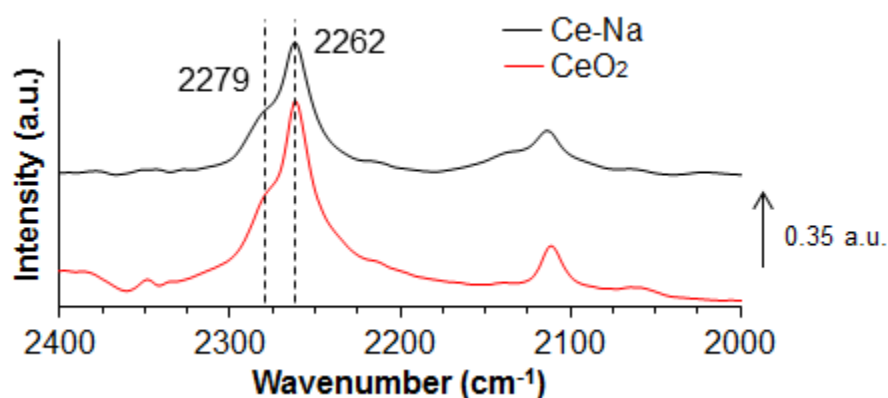


Figure S19. DRIFT spectrum of adsorbed CD_3CN on Ce-Na (top) and CeO_2 (bottom).

Ceria is known to contain weak Lewis acid sites that have been shown to be relevant for catalytic transformations by themselves¹² or through acid-base pair cooperativity.¹³ Although it seems unlikely, changes in the surface acidity between the materials was compared using two different probe molecules. The acidic sites of degassed Ce-Na and CeO₂ were probed by adsorption of deuterated acetonitrile (CD₃CN) at room temperature while monitoring the $\nu(\text{CN})$ stretch. CD₃CN is a relatively weak base and as such, more sensitive to changes in Lewis acidity than stronger bases.¹⁴⁻¹⁵ CD₃CN interacts with acid sites via coordination through the nitrogen and a blue shift is observed that depends on the type and strength of acid.^{14, 16} The magnitude of the nitrile band shift relative to the liquid phase ($\sim 2259 \text{ cm}^{-1}$)¹⁵ can be correlated to the strength of a particular acid site, with higher shifts indicating stronger acidic sites.¹⁴ Figure S17 shows the spectra obtained after room temperature adsorption of CD₃CN on CeO₂ and Ce-Na. Both materials exhibited $\nu(\text{CN})$ adsorption bands at 2262 cm^{-1} and 2279 cm^{-1} . The different bands suggest there are at least two types of different interactions occurring between CD₃CN and the support surfaces, but both interactions are common to the two materials. The low energy band (2262 cm^{-1}) can be attributed to interaction of CD₃CN via hydrogen bonding with surface hydroxyls and/or via van der Waals forces.^{14, 17} The high energy band (2279 cm^{-1}) is attributed to Lewis acid binding and reflects weak acidity, as blue shifts of up to 70 cm^{-1} have been observed on other materials.^{14, 17} These results are consistent with previous studies of adsorbed acetonitrile on ceria.^{1, 10} The identical spectra obtained for each material suggests that the Lewis acidity has not changed upon introduction of sodium. Since the $\nu(\text{CN})$ blue shift is a result of coordination to a specific element within a specific environment,^{16, 18} it seems likely that both materials show the same $\nu(\text{CN})$ blue shift since only cerium cations are present on the surface. That is, if sodium

were present on the surface we would expect a $\nu(\text{CN})$ shift contribution from coordination to a sodium atom.

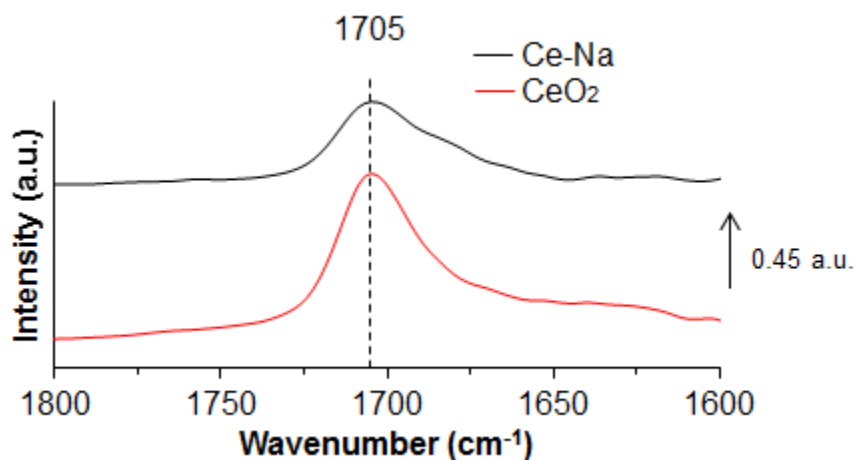


Figure S20. DRIFT spectrum of adsorbed $(\text{CH}_3)_2\text{CO}$ on Ce-Na and CeO_2 .

A less basic probe, such as acetone, should in theory be better suited to distinguish differences in acidity between the two materials.¹⁹ Acetone can interact with acids through the oxygen atom of the carbonyl. Stronger interactions between the carbonyl oxygen and the acid results in a red shift of the carbonyl stretch.^{14, 20-21} Figure S18 shows the DRIFT spectra obtained for degassed CeO_2 and Ce-Na after room temperature adsorption of acetone. Both materials showed the carbonyl stretch at 1705 cm^{-1} indicating a red shift from the gas phase value (1740 cm^{-1}). Again, there is no difference between the IR spectra for both samples. This agrees well with the CD_3CN adsorption spectra and suggests there is no large difference in surface acidity upon ceria modification with sodium. These results, in conjunction with data obtained from the basicity probes and TEM, suggest there are no significant modification to surface acidity, basicity, and structure (i.e. surface termination) upon introduction of sodium implying these reactivity descriptors are irrelevant for the observed increase of rate and lowering of activation energy observed for the phenol transfer hydrogenation on the two different catalysts.

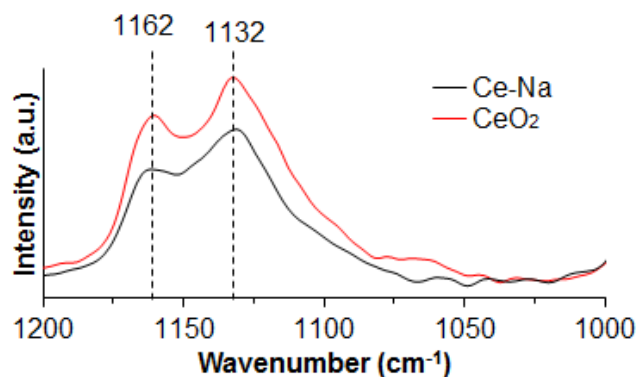


Figure S21. DRIFT spectrum of adsorbed 2-propanol on CeO₂ and Ce-Na. Highlighted bands correspond to adsorbed isopropoxide species.

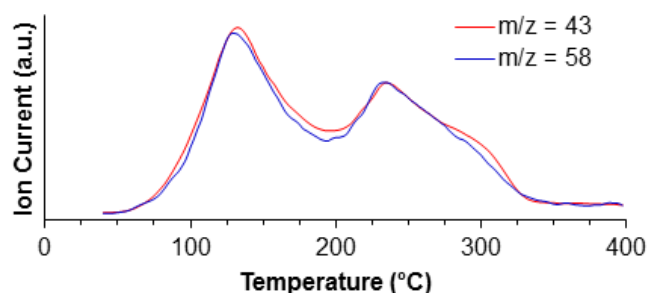


Figure S22. TPD-MS profile for TPSR of adsorbed 2-propanol on CeO₂ while monitoring $m/z = 43, 58$ (acetone).

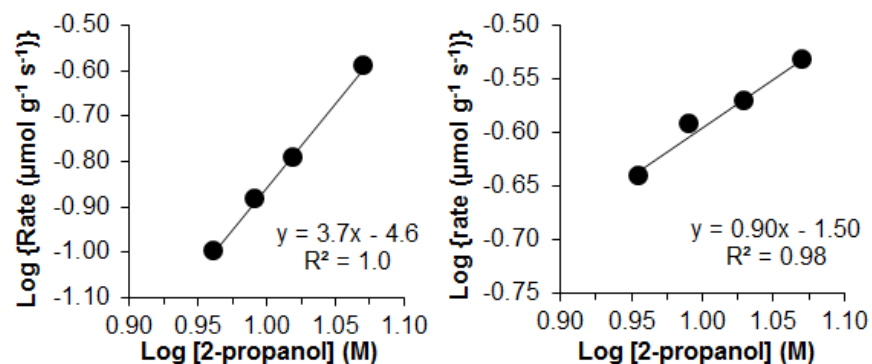


Figure S23. Log of phenol conversion rate versus log of 2-propanol concentration for (a) Pd/CeO₂ and (b) Pd/Ce-Na. Conditions: 0.1 M phenol in aqueous 2-propanol (data spans 70-90 v/v % 2-propanol), 0.5 g catalyst, 0.1 mL min⁻¹, T = 140 °C, V_{bed} = 0.4 mL. Each data point corresponds to the average rate over 24 h with a 4 h sampling interval for a total of 6 data points.

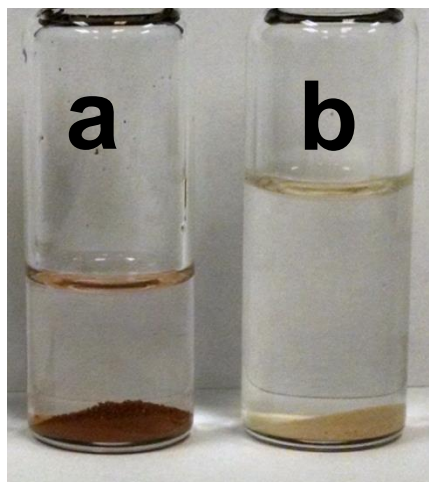


Figure S24. Digital image showing CeO_2 dissolved in (a) 0.05 g mL^{-1} 2-propanol solution of phenol and (b) 0.05 g mL^{-1} aqueous solution of phenol. The red color signifies dissociative adsorption of phenol and indicates that phenol has a higher affinity for the surface of ceria than 2-propanol. The yellow color signifies non-dissociative adsorption of phenol and indicates water has a higher affinity for the surface of ceria than phenol.²²

References

1. Wu, Z.; Mann, A. K. P.; Li, M.; Overbury, S. H. *J. Phys. Chem. C* **2015**, 119, 7340-7350.
2. Ono, Y.; Hattori, H., *Solid Base Catalysis*, Springer-Verlag: Berlin, Heidelberg, 2011.
3. Miller, F. A.; Wilkins, C. H. *Anal. Chem.* **1952**, 24, 1253-1294.
4. Binet, C.; Daturi, M.; Lavalley, J.-C. *Catal. Today* **1999**, 50, 207-225.
5. Praline, G.; Koel, B. E.; Hance, R. L.; Lee, H. I.; White, J. M. *J. Electron Spectrosc. Relat. Phenom.* **1980**, 21, 17-30.
6. Senanayake, S. D.; Mullins, D. R. *J. Phys. Chem. C* **2008**, 112, 9744-9752.
7. Perry, D.; Tsao, L.; Brittain, H. *J. Mater. Sci. Lett.* **1984**, 3, 1017-1019.
8. Hammond, J. S.; Holubka, J. W.; deVries, J. E.; Dickie, R. A. *Corros. Sci.* **1981**, 21, 239-253.
9. Lavalley, J. C. *Catal. Today* **1996**, 27, 377-401.
10. Tamura, M.; Shimizu, K.-i.; Satsuma, A. *Appl. Catal. A-Gen* **2012**, 433-434, 135-145.
11. Huber, S.; Knözinger, H. *J. Mol. Catal. A: Chem.* **1999**, 141, 117-127.

12. Wang, Y.; Wang, F.; Song, Q.; Xin, Q.; Xu, S.; Xu, J. *J. Am. Chem. Soc.* **2013**, 135, 1506-1515.
13. Vivier, L.; Duprez, D. *ChemSusChem* **2010**, 3, 654-78.
14. Lercher, J. A.; Gründling, C.; Eder-Mirth, G. *Catal. Today* **1996**, 27, 353-376.
15. Knoezinger, H.; Krietenbrink, H. *J. Chem. Soc. Faraday Trans.* **1975**, 71, 2421-2430.
16. Pelmeshnikov, A. G.; van Santen, R. A.; Janchen, J.; Meijer, E. *J. Phys. Chem.* **1993**, 97, 11071-11074.
17. Scokart, P. O.; Declerck, F. D.; Sempels, R. E.; Rouxhet, P. G. *J. Chem. Soc. Faraday Trans.* **1977**, 73, 359-371.
18. Scokart, P. O.; Rouxhet, P. G. *J. Colloid Interf. Sci.* **1982**, 86, 96-104.
19. Morterra, C.; Magnacca, G. *Catal. Today* **1996**, 27, 497-532.
20. Panov, A.; Fripiat, J. J. *Langmuir* **1998**, 14, 3788-3796.
21. Corma, A.; Domine, M. E.; Valencia, S. *J. Catal.* **2003**, 215, 294-304.
22. Nelson, N. C.; Manzano, J. S.; Sadow, A. D.; Overbury, S. H.; Slowing, I. I. *ACS Catal.* **2015**, 5, 2051-2061.

CHAPTER 4**STABILITY OF Pd/CeO₂ CATALYST DURING TRANSFER HYDROGENATION:
PRIMARY VS. SECONDARY ALCOHOLS**

Adapted from manuscript submitted to *J. Phys. Chem. C*.

Copyright © 2016 American Chemical Society

Nicholas C. Nelson, Igor I. Slowing

Abstract

The stability of palladium supported on ceria (Pd/CeO₂) was studied during liquid flow transfer hydrogenation using primary and secondary alcohols as hydrogen donors. For primary alcohols, the ceria support was reduced to cerium hydroxy carbonate during the reaction and was a contributing factor toward catalyst deactivation. For secondary alcohols, cerium hydroxy carbonate was not observed and the catalyst was stable upon prolonged reaction. Regeneration through oxidation/reduction does not restore initial activity likely due to irreversible catalyst restructuring. A deactivation mechanism involving C-C scission of acyl and carboxylate intermediates to form CO is proposed.

Introduction

Ceria is ubiquitous in catalysis science due to its inherent redox properties. The rare earth oxide is most known for its oxidizing properties owed to the facile release and storage of oxygen. The oxygen storage properties of ceria rely on the cerium redox cycle which is closely related to the concentration and type of lattice defects.¹ Oxygen vacancies are the most common defect and are often correlated to catalytic activity. The vacancies facilitate Ce³⁺/Ce⁴⁺ redox cycling²⁻³ and can also activate molecules through adsorption at the defect site.⁴⁻⁵ This is most recognized during chemical transformations involving molecular oxygen and organic oxygenates.⁶⁻⁷ For

example, methanol has been observed to adsorb dissociatively at defect sites forming methoxy,⁸ and is calculated to be more stable than adsorption on a defect-free site.⁹ Analogously, longer chain alcohols (i.e. ethanol, propanol) can also dissociatively adsorb on ceria. The resulting alkoxy species are activated toward further chemical reaction, which at low temperature, proceeds almost exclusively through dehydrogenation.

The alcohol dehydrogenation activity over ceria makes it a promising metal support for heterogeneous transfer hydrogenation. However, only a limited number of ceria-based transfer hydrogenation systems have been developed¹⁰ and even fewer involved the use of alcohols.¹¹⁻¹³ Shimizu *et al.*¹¹ studied the transfer hydrogenation of ketones over Ni/CeO₂ catalyst using 2-propanol hydrogen donor. The catalyst was initially active, but upon cycling became deactivated; the reason for deactivation was not discussed. In a recent report,¹³ the transfer hydrogenation activity over palladium supported on ceria was studied using 2-propanol in liquid flow mode. The catalyst was stable for at least 7 days and showed promising space-time-yields around 0.15 h⁻¹ at 140 °C. The previous account demonstrated that the transfer hydrogenation activity correlates to the alcohol dehydrogenation (i.e. redox properties) activity of the support. However, the aforementioned transfer hydrogenation studies have been limited to only 2-propanol as a hydrogen source. Primary alcohols, such as ethanol, are currently derived commercially from renewable resources and therefore more desirable for transfer hydrogenation reactions. Herein, the transfer hydrogenation activity and catalyst stability of palladium supported on ceria (Pd/CeO₂) using primary and secondary alcohols as hydrogen sources is reported. Reduction of the ceria support to cerium hydroxy carbonate occurred through C-C cleavage reactions for the primary alcohols. However, 2-propanol did not readily undergo C-C cleavage and the hydroxy carbonate phase was not observed.

Experimental

Reagents. Cerium (IV) oxide (CeO_2) nanopowder < 25 nm particle size (BET), palladium(II) acetate, phenol, 2,4-dinitrophenylhydrazine, acetaldehyde, and 2-propanol were purchased from Sigma Aldrich. Methanol and ethanol were purchased from Fischer. All chemicals were used without further purification and met or exceeded ACS specifications.

Synthesis of Pd/CeO₂. Pd catalysts were prepared by an impregnation method with a 1 wt. % Pd loading relative to the mass of the support. In a typical synthesis, $\text{Pd}(\text{O}_2\text{CCH}_3)_2$ (0.0419 g, 0.187 mmol) was dissolved in acetone (1 mL). The support (2.00 g) was placed into a mortar and impregnated with the Pd solution in 0.20 mL increments. After each impregnation step, the catalyst was mixed thoroughly with a pestle until seemingly dry. The material was calcined at 350 °C for 2 h with a 2.5 °C min⁻¹ ramp rate and after cooling to room temperature it was reduced under flowing hydrogen at 350 °C for 2 h with a ramp rate of 2.5 °C min⁻¹.

Transfer hydrogenation reactions. A Uniqsis FlowSynTM continuous liquid flow reactor was used for all reactions and operated in automatic mode. In a typical experiment, the catalyst (1.0 g) was packed into an Omnifit Labware column (PEEK, 10 mm diameter). The catalyst was secured by placing an adjustable endpiece equipped with a 10 μm PTFE filter into the inlet and outlet of the column. The volume of the catalyst bed was 0.8 mL (for 1.0 g of catalyst). Water was passed through the system (0.1 mL min⁻¹) at room temperature until equilibrium flow was reached (~0.5 h). The column was then heated to the desired temperature (typically 130 °C) under continuous water flow. At this point, an automated system switched from water feed to reagent feed. Typically, the reagent feed was an aqueous solution of alcohol (30 v/v %) and phenol (0.05 M). The outlet feed was segmented in 4 mL increments by a Gilson FC 203B fraction collector. A 50 μL aliquot from selected 4 mL fractions were added to 1 mL of

resorcinol internal standard solution (0.3 mM) used to construct quantitative calibration curves and analyzed in an Agilent GC-MS (7890A, 5975C) with a HP-5MS column. The GC-MS run started at 60 °C for 0 min, then ramped to 150 °C at 5 °C min⁻¹ and held for 0 min, then ramped to 300 °C at 20 °C min⁻¹ and held for 3 min. Conversion was defined as mol % and calculated as moles of converted phenol per mole of starting phenol times 100 %. Conversion rates were calculated from conversion, catalyst mass (g), initial phenol concentration (μM), and flow rate (L h⁻¹).

$$\frac{(\text{Conversion}) \times (\text{Flow Rate}) \times [\text{Phenol}]_0}{(\text{Catalyst Mass})}$$

H₂ chemisorption. Hydrogen chemisorption was performed in a Micromeritics AutoChem II equipped with TCD detector. H₂-Ar (10 % H₂) was used as the metal dispersion probe. H₂-chemisorption analysis was carried out by reducing samples at 150 °C under H₂/Ar flow, followed by flowing Ar for 15 min at 150 °C to remove surface bound hydrogen from Pd crystallites. The sample was then cooled under Ar to -25 °C for hydrogen pulse chemisorption measurements. The palladium dispersion of the catalysts was calculated based on the following equation:

$$D(\%) = \frac{S_f \times M \times V_{ad}}{m \times W \times V_m} \times 100$$

where S_f = stoichiometry factor (the Pd/H₂ molar ratio) = 2; M = the atomic mass of Pd (106.42 g mol⁻¹); V_{ad} = the volume of chemisorbed H₂ at standard temperature and pressure conditions (mL); m = the mass of the sample (g); W = the weight fraction of Pd in the sample as determined by ICP-OES; V_m = the molar volume of H₂ (22414 mL mol⁻¹) at STP.

Temperature programmed reduction (TPR). Hydrogen temperature programmed reduction (H₂-TPR) chemisorption was performed in a Micromeritics AutoChem II equipped with TCD detector. H₂-Ar (10 % H₂) was used as the reducing agent. The experiment was performed with a flow rate of 50 mL min⁻¹ and a ramp rate of 10 °C min⁻¹. A dry ice/acetone cold trap was used to collect water produced during the reduction.

Diffuse reflectance Fourier transform spectroscopy (DRIFTS). Measurements were made on a Bruker Vertex 80 FT-IR spectrometer with OPUS software and apodized spectral resolution of 0.2 cm⁻¹. The spectrometer was equipped with a HeNe laser and photovoltaic MCT detector. A Praying Mantis™ high temperature reaction chamber was used for variable temperature measurements. 32 scans were collected for each measurement in absorbance mode with 4 cm⁻¹ resolution. The sample was heated to 150 °C in He flow (25 mL min⁻¹) for 60 minutes prior to DRIFT analysis. The sample was cooled to room temperature under He flow. The blank spectrum was recorded at this time. Then, the He flow was redirected through a saturator containing ethanol at room temperature. Spectra were taken at 1 min intervals under probe molecule exposure until the formation of liquid-like bands was observed (~5 min). At this time, the He flow was redirected away from the saturator. The sample was allowed to sit at room temperature for 30 min before increasing the temperature. The temperature was increased to the desired value and held for 30 min. The sample was cooled back down to room temperature and held for 30 min before taking the spectrum. This process was repeated for all the temperature-dependent spectra reported.

Temperature programmed desorption (TPD). For ethanol and 2-propanol TPD, a Netzsch STA 449 F1 Jupiter® TGA/DSC/MS/IR instrument was used. The mass spectrometer is a Netzsch quadrupole mass spectrometer 403 D Aeolos equipped with electron impact ion source

and Channeltron SEM detector with 0.5 amu resolution. The data was collected in multiple ion detection (MID) mode. The samples were prepared by heating the catalyst to 200 °C under He flow for 60 min in a round bottom flask with septum. After cooling to room temperature and still under He flow, ethanol or 2-propanol (~1 mL) was added via syringe and needle to saturate the sample. The excess alcohol was allowed to evaporate at room temperature under He flow (~4 h). The samples were placed into the Netzsch instrument during which time they were exposed to atmospheric conditions. The temperature was ramped from 40 °C to 600 °C at 10 °C min⁻¹ under 40 mL min⁻¹ Ar flow while monitoring the mass signals.

Powder X-ray diffraction (PXRD). Diffraction patterns were collected using Co K α 1, K α 2 split radiation (45 kV, 40 mA, $\lambda_{\text{avg}} = 1.7903 \text{ \AA}$) on a PANalytical X'Pert PRO diffractometer equipped with a theta–theta vertical mode goniometer, incident Fe filter, an air-cooled X'Celerator real time multiple strip (RTMS) detector, and spinner stage. The spectra were converted to Cu K α radiation for comparison to standard patterns using Bragg's law. Powder XRD samples were prepared by placing powders onto a background-less polycarbonate sample holder. Crystallite sizes were calculated using Scherrer equation:

$$D_{(hkl)} = \frac{K\lambda}{\beta \cos \theta}$$

where K is the shape factor (0.9) of the average crystallite, λ is the X-ray wavelength (0.17903 nm), β is the full width at half maximum (radians), and θ is the Bragg angle (radians). HighScore was used for Rietveld Refinement.

Electron microscopy/energy dispersive X-ray spectroscopy. Transmission electron microscopy (TEM) was conducted using a FEI Tecnai G2 F20 field emission microscope operating at 200 kV (point-to-point resolution <0.25 nm and a line-to-line resolution of <0.10

nm). TEM samples were prepared by placing 2–3 drops of dilute ethanol suspensions onto lacey carbon-coated copper grids.

Surface area and porosimetry. Textural properties of the supports and catalysts were measured by nitrogen sorption isotherms at $-196\text{ }^{\circ}\text{C}$ in a Micromeritics Tristar analyzer. The surface areas were calculated by the Brunauer-Emmett-Teller (BET) method. Pretreatment of samples for surface area measurement was done by flowing N_2 for 6 h at $100\text{ }^{\circ}\text{C}$.

ICP-OES. Pd loadings were analyzed by a Perkin Elmer Optima 2100 DV Inductively Coupled Plasma-Optical Emission Spectroscopy (ICP-OES). Samples (5 mg) were digested in 5 mL of 4 M HCl, 1 mL of concentrated HNO_3 , and 2 mL of 30 v/v % H_2O_2 . The samples were sonicated for ten minutes. Then they were placed into a $50\text{ }^{\circ}\text{C}$ water bath for ~ 12 h. Each sample was then diluted to 10 mL of total solution.

X-ray photoelectron spectroscopy (XPS). XPS analysis was done with a PHI 5500 multitechnique system using a standard Al X-ray source. Samples were analyzed at room temperature with no special preparation. Charge correction was accomplished by shifting the Ce 3d v'-peak to 882.6 eV for Pd/CeO₂ before reaction and Ce 3d v'-peak to 885.5 eV for Pd/CeO₂ after reaction (ref). All spectra were normalized within each spectral region by setting the maximum intensity equal to one.

Results

Commercially obtained ceria nanopowder (Sigma) was chosen as Pd support for phenol transfer hydrogenation using primary and secondary alcohols as sacrificial hydrogen donors. The textural properties of the support (CeO₂) and catalyst (Pd/CeO₂) are summarized in Table S1. The PXRD of the support and catalyst exhibited peaks that could be indexed to the cubic fluorite

phase of ceria with no other reflections observed (Figure S1). TEM analysis of Pd/CeO₂ showed multifaceted, polyhedral particles with ill-defined morphology (Figure S2). The (111) and (200) surface terminations were the predominant facets of the CeO₂ support. Palladium particles were not detected during TEM analysis possibly owing to the high dispersion (Table S1) and/or low contrast.

Figure 1a shows the phenol conversion rate as a function of time-on-stream (TOS) using primary (methanol, ethanol, 1-propanol) and secondary (2-propanol) alcohols. Under the current reaction conditions, cyclohexanone was the major product observed (>90 % selectivity). The phenol conversion rates were similar using methanol and ethanol as hydrogen donors. For 1-propanol, the conversion rate dropped to about half the value of the other primary alcohols. 2-propanol gave a higher rate than 1-propanol, but lower than methanol and ethanol. Because of the higher rate, ethanol was chosen for an 8 day stability study (Figure 1b). There was a monotonic, yet significant decrease in phenol conversion rate for the duration of the experiment.

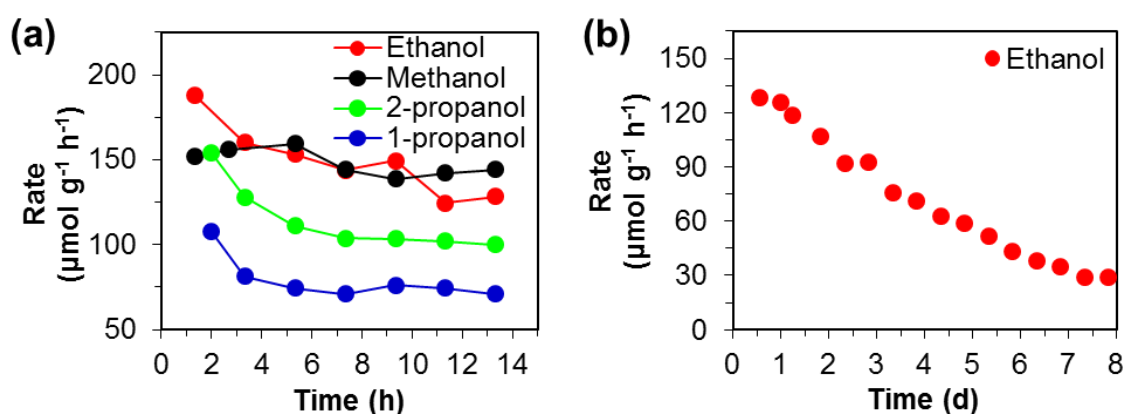


Figure 1. Phenol conversion rate as a function of time-on-stream (TOS) over Pd/CeO₂ using (a) primary and secondary alcohols and (b) ethanol. Reaction conditions: 50 mM phenol, 30 v/v % aqueous alcohol, T = 130 °C, 0.1 mL min⁻¹, V_{bed} = 0.8 mL, 1.0 g Pd/CeO₂.

Post-reaction PXRD analysis of Pd/CeO₂ after the 8 day reaction provided evidence for the formation of cerium hydroxy carbonate (Ce(CO₃)(OH)) polymorphs (Figure 2a).¹⁴⁻¹⁵ The hydroxy carbonate phase was observed after 14 h TOS for all primary alcohols, but was not observed for 2-propanol (Figure 2b). Furthermore, transfer hydrogenation of phenol using 2-propanol showed the catalyst was stable for at least 7 days.¹³ Figure 3a shows the Ce 3d spectral region of Pd/CeO₂ before (fresh) and after (aged) the 8 day reaction with ethanol. The Ce 3d spectral region for the fresh catalyst showed characteristic peaks attributed to Ce(IV).¹⁶⁻¹⁸ After reaction, the Ce 3d spectral region exhibited bands that can be attributed to Ce(III).^{17, 19-21} The reduction of cerium cations was consistent with the cerium hydroxy carbonate phase observed from PXRD. The O 1s spectral region of the fresh and aged catalyst showed a band shift from 529.6 eV to 531.4 eV (Figure 3b). The oxygen binding energies are consistent with O 1s of cerium(IV) oxide²² and cerium(III) carbonate,^{21, 23} respectively. Furthermore, temperature programmed desorption (TPD) analysis of Pd/CeO₂ after 14 h TOS presented a large evolution of CO₂ at about 400 °C (Figure S3). The evolved CO₂ was likely a decomposition product of cerium hydroxy carbonate.²⁴⁻²⁵ The PXRD pattern of Pd/CeO₂ after the thermal desorption experiment showed attenuation of the peaks attributed to the hydroxy carbonate phase (Figure S4). The results indicate that the transfer hydrogenation of phenol with ethanol over Pd/CeO₂ reduces ceria to cerium hydroxy carbonate polymorphs.

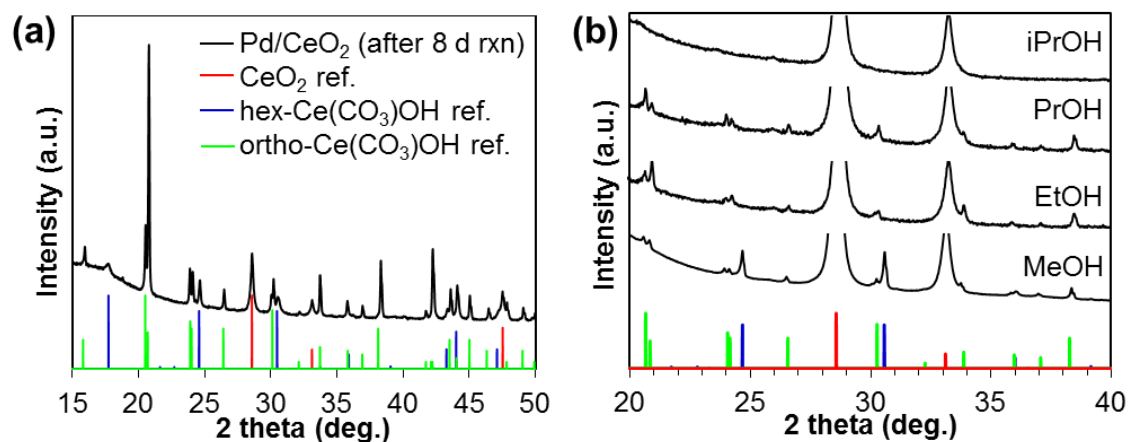


Figure 2. PXRD pattern of Pd/CeO₂ after transfer hydrogenation with (a) ethanol for 8 days and (b) primary and secondary alcohols for 14 h. The reference patterns for (a) are color coded the same as in (b).

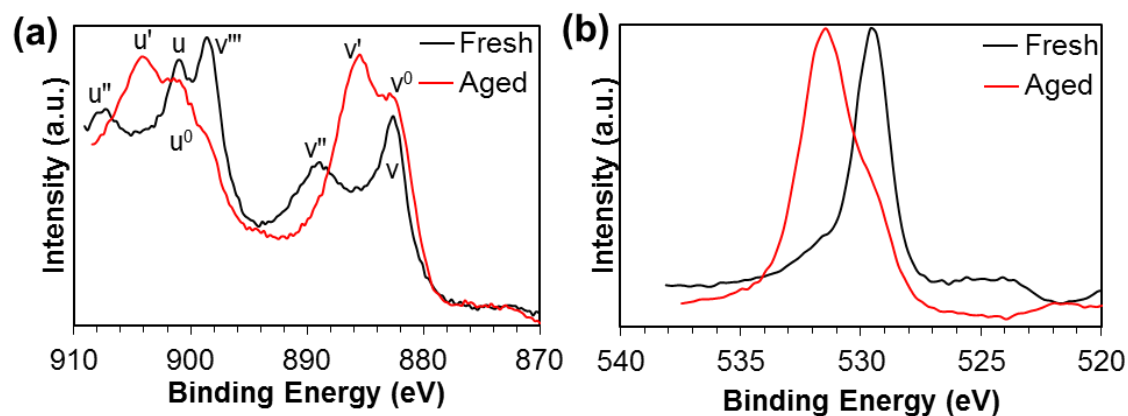


Figure 3. XPS spectra of Pd/CeO₂ before and after 8 day phenol transfer hydrogenation with ethanol in the (a) Ce 3d and (b) O 1s spectral region.

The increasing concentration of the hydroxy carbonate phase (Figure 2) corresponded to the decreasing activity (Figure 1b) upon prolonged TOS. Thus, the catalyst deactivation can be attributed to the formation of cerium(III) hydroxy carbonate and/or changes in properties upon catalyst restructuring. In a recent publication, it was demonstrated that the redox properties of ceria influence the turnover rate during phenol transfer hydrogenation using 2-propanol.¹³ Hence, the reduction of redox-active ceria to redox-inactive cerium hydroxy carbonate should decrease

phenol turnover. However, the transformation of ceria to cerium hydroxy carbonate is a reversible process and its deactivating effect could be mitigated through reoxidation. The pure ceria phase for the aged catalyst was regenerated by thermal treatment under O_2 (450 °C) and H_2 (350 °C) (Figure S5). Figure S6 indicates that oxidation of cerium hydroxy carbonate to cerium oxide did not restore the initial activity of Pd/CeO₂. The regenerated catalyst was further analyzed through H_2 chemisorption and temperature programmed reduction with hydrogen (H_2 -TPR). The textural properties are summarized in Table S2. There was a decrease in the Pd dispersion from 20 % to 4 % between the fresh and regenerated catalyst which indicated catalyst restructuring. The restructuring of the catalyst with TOS was also evident through its ability to activate hydrogen. The H_2 -TPR profile for the fresh catalyst showed a large hydrogen uptake around 10 °C (Figure S7). This peak was essentially absent for the regenerated catalyst and indicated the catalyst has decreased hydrogen activation ability. Thus, it appears that the Pd/CeO₂ catalyst is irreversibly deactivated during phenol transfer hydrogenation with ethanol through support phase transformation.

A likely intermediate during transfer hydrogenation using primary alcohols are aldehydes. A control experiment was run by replacing ethanol with acetaldehyde and did not result in phenol conversion. This indicated that acetaldehyde did not undergo further decomposition to yield hydrogen. It also indicated that the hydrogen necessary to reduce phenol was obtained from alcohol dehydrogenation. However, the PXRD pattern of the catalyst after treatment with acetaldehyde showed the cerium hydroxy carbonate phase (Figure S8). Acetaldehyde trapping experiments with 2,4-dinitrophenylhydrazine (DNPH) during transfer hydrogenation with ethanol did not produce the expected hydrazone. Considering acetaldehyde resulted in hydroxy carbonate formation and the hydrazone product was not detected in the

trapping experiment, it appears that most acetaldehyde evolved from ethanol dehydrogenation undergoes further reaction with the ceria surface. In contrast, when the reaction was performed using 2-propanol, the catalyst was stable and formation of the hydrazone product was observed.¹³ From these results, Pd/CeO₂ becomes deactivated during transfer hydrogenation with primary alcohols due to aldehyde reaction with the ceria support, but Pd/CeO₂ is stable using secondary alcohols (i.e. ketone formation).

The formation of carbonates during transfer hydrogenation indicated C-C cleavage precedes catalyst deactivation. Ethanol TPD reactions over Pd/CeO₂ confirmed C-C scission reactions through the evolution of CO, CO₂, and CH₄. (Figure 4a). Evolution of H₂ was not observed which could be due to reduction of the ceria support and result in water formation (Figure S9). Desorbed ethanol (m/z = 31) was also not observed, while a peak around 350 °C corresponding to m/z = 29 was evident (Figure S9). This could be attributed to acetaldehyde or alternatively to crotyl alcohol/crotonaldehyde. However, at the temperature used during transfer hydrogenation, acetaldehyde was not observed (Figure S13) and was in agreement with DNPH trapping experiments. Methane (m/z = 15) desorbed around 100 °C and 400 °C (Figure 4a). There was one CO (m/z = 28) desorption around 400 °C (Figure 4a). CO₂ desorption began at 100 °C, with maxima centered around 200 °C and 325 °C (Figure 4a).

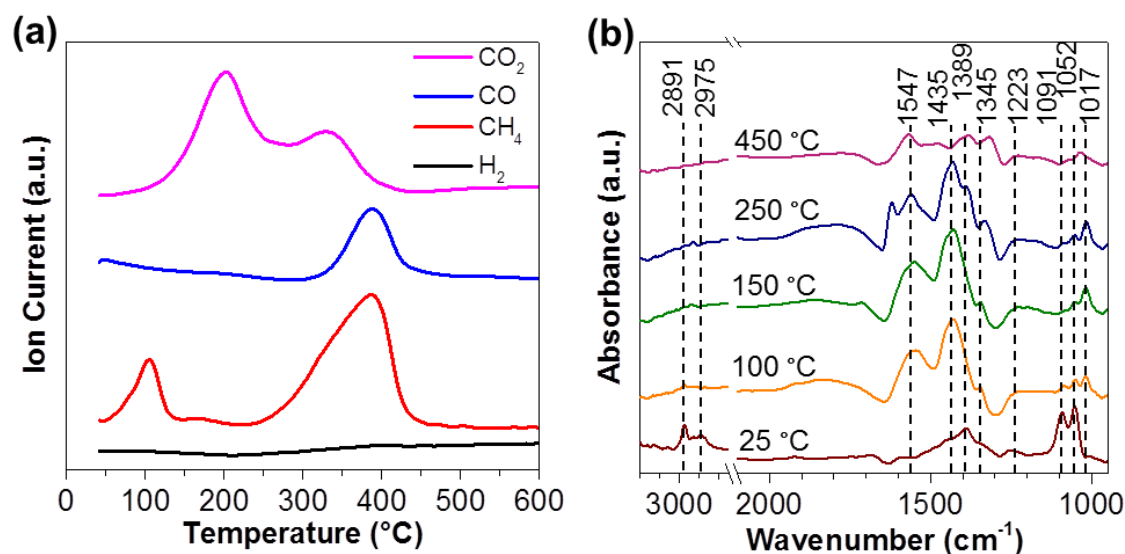


Figure 4. (a) TPD of ethanol adsorbed onto Pd/CeO₂ under He flow (40 mL min⁻¹) at 10 °C min⁻¹. The H₂, CH₄, CO, and CO₂ signals correspond to $m/z = 2, 15, 28,$ and $44,$ respectively (b) DRIFTS of ethanol adsorbed onto Pd/CeO₂ under He flow (30 mL min⁻¹) after heating to the indicated temperature and cooling to room temperature.

Temperature programmed DRIFTS analysis of adsorbed ethanol on ceria was used to identify surface intermediates during TPD experiments (Figure 3b). The room temperature spectrum indicated adsorbed ethoxy species identified by the $\nu(\text{CO})$ bands at 1052 cm⁻¹ and 1091 cm⁻¹ corresponding to bidentate and monodentate coordinated ethoxy.²⁶ The band at 1389 cm⁻¹ was attributed to $\delta_{\text{sym}}(\text{CH}_3)$ of ethoxy.²⁷ The bands at 2891 cm⁻¹, 2927 cm⁻¹, and 2975 cm⁻¹ are recognized as the $\nu_{\text{sym}}(\text{CH}_3)$, $\nu_{\text{asym}}(\text{CH}_2)$, and $\nu_{\text{asym}}(\text{CH}_3)$ of ethoxy species, respectively.²⁸ Increasing the temperature to 100 °C resulted in significant decrease of ethoxy species and formation of acetate. The bands around 1017 cm⁻¹, 1345 cm⁻¹, 1435 cm⁻¹, and 1547 cm⁻¹ can be assigned to the $\nu_{\text{sym}}(\text{CH}_3)$, $\delta_{\text{sym}}(\text{CH}_3)$, $\nu_{\text{sym}}(\text{OCO})$, and $\nu_{\text{asym}}(\text{OCO})$ modes of acetate, respectively.^{26, 29} Due to the similar vibrational signature between acetates and carbonates,³⁰⁻³¹ it is possible that underlying carbonate bands are present.³² The C-H stretch region showed low intensity, which can be explained by the weak acetate C-H stretching.²⁹ Heating to 150 °C

resulted in growth of a carbonate band^{26, 31} at 1223 cm^{-1} and the acetate band at 1017 cm^{-1} , while the ethoxy bands at 1052 cm^{-1} and 1091 cm^{-1} continued to decrease. The emergence of the band at 1704 cm^{-1} could indicate the $\nu(\text{C}=\text{O})$ mode of acetaldehyde.³³⁻³⁵ Upon increasing the temperature to 250 °C, acetate species were still present while formation of two bands at 1389 cm^{-1} and 1620 cm^{-1} appeared. These bands can be attributed to hydrogen carbonates.³⁰ At 450 °C, acetate species were largely removed, clearly shown by the disappearance of the band at 1017 cm^{-1} assigned to the $\nu_{\text{sym}}(\text{CH}_3)$ mode of acetate. The remaining bands can be attributed to carbonates.³⁰⁻³¹

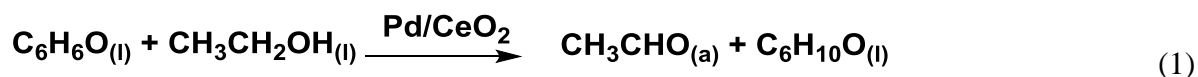
Discussion

The reaction of primary alcohols over ceria-based materials has been studied extensively in the context of material property probes,³⁶⁻⁴² partial oxidation,^{26, 43-45} and steam reforming processes.⁴⁶⁻⁵¹ It is generally accepted that the pathway for ethanol steam reforming or partial oxidation over ceria-supported platinum group metals (PGM/CeO₂) begins with dissociative adsorption to form cerium-coordinated ethoxy.^{44-45, 52-55} The dominant reaction pathway for ethoxy over PGM/CeO₂ is through dehydrogenation to acetaldehyde.^{45, 50, 53} The acetaldehyde intermediate has been observed to follow several different reaction pathways over PGM/CeO₂ that can be broadly classified as reduction, oxidation, C-C coupling, and C-C cleavage reactions.^{34, 56} The C-C cleavage reaction is proposed to proceed through acetaldehyde dehydrogenation to adsorbed acetyl species.^{34, 43-44, 52, 55, 57-58} The acetyl species can be decomposed to CH₄, CO, CO₂, and H₂ through various pathways (e.g. water-gas-shift, methane reforming, etc.).^{43, 46, 52, 59} Alternatively, the acetyl species can be oxidized by lattice oxygen forming adsorbed acetate species which decompose to CH₄, CO, CO₂, and H₂ through various

pathways.^{34, 43-46, 52, 55} Acetyl/acetate decomposition is promoted by PGM⁴⁶ and has been observed to yield surface carbonates.^{46, 58}

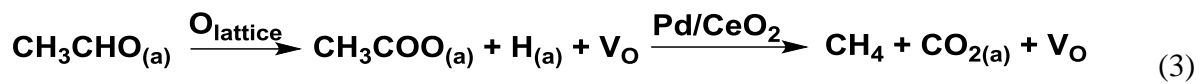
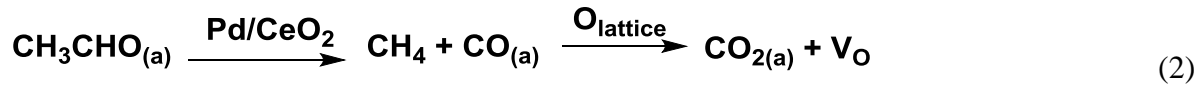
The TPD results for ethanol adsorbed on Pd/CeO₂ indicated that ethanol was primarily decomposed to CH₄ and CO₂ in the low temperature regime (< 200 °C). Evolution of CO₂ suggested loss of ceria lattice oxygen and reduction of cerium. From DRIFTS, acetate formation was clearly observed at 100 °C and coincided with methane evolution from ethanol TPD. This suggests the precursor for low temperature decomposition was acetate. Evolution of CO₂ lagged behind methane formation in the low temperature regime and could relate to the desorption barrier. At room temperature, DRIFTS provided evidence for acetyl and bridging CO species shown by the band at 1680 cm⁻¹ (ν(C=O)) and 1923 cm⁻¹, respectively (Figure S10).³⁴ The species were likely formed over Pd, which is known to decompose ethanol to H₂, CO, and CH₄ at room temperature through acetyl intermediates.⁶⁰⁻⁶¹ Furthermore, IR spectra of the Pd/CeO₂ catalyst after reaction (Figure S11) clearly showed linear CO (2141 cm⁻¹) adsorbed onto Pd.³³ This suggests that decomposition through acetyl species was a relevant reaction pathway in this system. From these results, ethanol decomposition through acetate and acetyl intermediates seemed to occur.

Based on the data obtained for the phenol transfer hydrogenation system and literature results for ethanol decomposition over PGM/CeO₂, the following deactivation pathway is proposed. Ethanol adsorbs dissociatively to yield adsorbed acetaldehyde with evolution of hydrogen and phenol turnover (1).

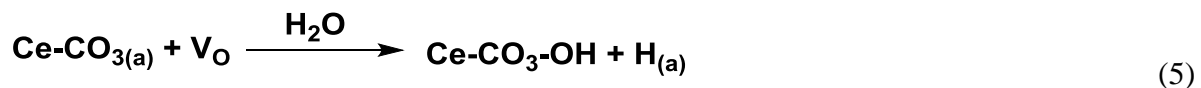
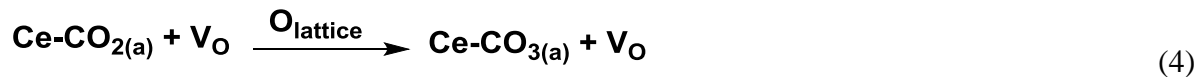


The inability for acetaldehyde to provide phenol turnover suggests any subsequent reaction pathways involving hydrogen evolution are not relevant. The acetaldehyde/acetyl

intermediate can undergo C-C scission to yield methane and carbon monoxide (2). The adsorbed CO can then be oxidized by lattice oxygen which results in reduction of cerium and oxygen vacancy (V_O) formation (2). Similarly, the acetaldehyde/acetyl intermediate can first be oxidized to acetate, again resulting in cerium reduction and oxygen vacancy formation, followed by C-C scission to yield methane and carbon dioxide (3).



The reaction pathways for methane over Pd and PGM/CeO₂ involve desorption, reforming (yielding CO_x, H₂, or H₂O), or dehydrogenation (yielding C and H₂). The low temperatures used during transfer hydrogenation make reforming unlikely. The dehydrogenation route is also not a predominant reaction pathway since phenol turnover was not observed using acetaldehyde. Thus, methane likely desorbs. The adsorbed CO₂ from (2) and (3) can desorb or exist on the surface as a carbonate. The pathway resulting in cerium hydroxy carbonate formation necessitates CO₂ to remain adsorbed on the surface in the form of carbonate (4). Hydroxyl formation likely resulted from dissociation of water at the oxygen vacancy (5).⁶²⁻⁶³



The deactivation mechanism proposed is analogous for the other primary alcohols studied. For 2-propanol TPD over Pd/CeO₂, the dehydrogenation product (acetone) was observed (Figure S12). This suggests that acetone (or ketone) is less prone to surface reaction than acetaldehyde (or aldehyde) at low temperature since the latter was not observed during ethanol

TPD. For the deactivation pathway proposed, decarbonylation must occur. Aldehyde and ketone decarbonylation is generally thought to occur through C-H and C-C activation, respectively.⁶⁴⁻⁶⁶ Cleavage of C-C bonds (C-C activation) are usually more difficult than C-H cleavage (C-H activation) for kinetic and thermodynamic reasons.⁶⁵⁻⁶⁶ Upon C-H cleavage of aldehydes (Eq. 2), acyl intermediates are formed which are activated towards C-C cleavage.⁵⁷ Thus, the catalytic stability¹³ and absence of cerium hydroxy carbonate phase for 2-propanol was likely related to the less relevant, non-activated C-C cleavage pathway that would lead to decarbonylation. The reductive deactivation with primary alcohols suggests an oxidant or aldehyde scavenger within the system could hinder catalyst deactivation. Alternatively, a non-reducible support could block the deactivation pathway. It should be noted that hydroxy carbonate formation during water-gas-shift reaction has been observed over AuCe(La)O_x catalyst under low temperature (120 °C)⁶⁷ and was associated with catalyst deactivation.

Conclusion

Pd/CeO₂ was unstable during transfer hydrogenation with primary alcohols. The ceria support was reduced to cerium hydroxy carbonate and led to irreversible restructuring of the catalyst. C-C scission of primary alcohols, mediated through acyl and carboxylate intermediates, resulted in CO formation. The adsorbed CO reacted with the ceria support forming carbonates. This led to cerium reduction and oxygen vacancy formation. The latter provided dissociation sites for water and completed cerium hydroxy carbonate formation. Pd/CeO₂ was stable during transfer hydrogenation with 2-propanol. This was attributed to the higher barrier for C-C activation of ketones, compared to C-H activation for aldehydes, both of which are proposed to precede decarbonylation. Understanding of the deactivation pathway is expected to guide the

design of more stable catalysts for transfer hydrogenation and low-temperature dehydrogenation of primary alcohols.

Acknowledgments

This research is supported by the U.S. Department of Energy, Office of Science, Basic Energy Sciences, Division of Chemical Sciences, Geosciences, and Biosciences, through the Ames Laboratory Catalysis Science program. The Ames Laboratory is operated for the U.S. Department of Energy by Iowa State University under Contract No. DE-AC02-07CH11358.

References

1. Trovarelli, A., *Catalysis by Ceria and Related Materials*, Imperial College Press: London, 2002.
2. Liyanage, A. D.; Perera, S. D.; Tan, K.; Chabal, Y.; Balkus, K. J. *ACS Catal.* **2014**, *4*, 577-584.
3. Khan, M. M.; Ansari, S. A.; Pradhan, D.; Han, D. H.; Lee, J.; Cho, M. H. *Ind. Eng. Chem. Res.* **2014**, *53*, 9754-9763.
4. Li, C.; Domen, K.; Maruya, K.; Onishi, T. *J. Am. Chem. Soc.* **1989**, *111*, 7683-7687.
5. Pushkarev, V. V.; Kovalchuk, V. I.; d'Itri, J. L. *J. Phys. Chem. B* **2004**, *108*, 5341-5348.
6. Paier, J.; Penschke, C.; Sauer, J. *Chem. Rev.* **2013**, *113*, 3949-3985.
7. Mullins, D. R. *Surf. Sci. Rep.* **2015**, *70*, 42-85.
8. Yoshimichi, N.; Ken-ichi, F.; Yasuhiro, I. *Nanotechnol.* **2004**, *15*, S49.
9. Beste, A.; Mullins, D. R.; Overbury, S. H.; Harrison, R. J. *Surf. Sci.* **2008**, *602*, 162-175.
10. He, L.; Ni, J.; Wang, L.-C.; Yu, F.-J.; Cao, Y.; He, H.-Y.; Fan, K.-N. *Chem. Eur. J.* **2009**, *15*, 11833-11836.
11. Shimura, K.; Shimizu, K.-i. *Green Chem.* **2012**, *14*, 2983-2985.
12. Hammond, C.; Schümperli, M. T.; Conrad, S.; Hermans, I. *ChemCatChem* **2013**, *5*, 2983-2990.
13. Nelson, N. C.; Boote, B. W.; Rossini, A. J.; Smith, E. A.; Slowing, I. I. *Submitted* **2016**.

14. Li, G.; Feng, S.; Li, L. *J. Solid State Chem.* **1996**, 126, 74-79.
15. Akinc, M.; Sordelet, D. *Adv. Ceram. Mater.* **1987**, 2, 232-238.
16. Pfau, A.; Schierbaum, K. D. *Surf. Sci.* **1994**, 321, 71-80.
17. Romeo, M.; Bak, K.; El Fallah, J.; Le Normand, F.; Hilaire, L. *Surf. Interf. Anal.* **1993**, 20, 508-512.
18. Hardacre, C.; Roe, G. M.; Lambert, R. M. *Surf. Sci.* **1995**, 326, 1-10.
19. Mullins, D. R.; Overbury, S. H.; Huntley, D. R. *Surf. Sci.* **1998**, 409, 307-319.
20. Henderson, M. A.; Perkins, C. L.; Engelhard, M. H.; Thevuthasan, S.; Peden, C. H. F. *Surf. Sci.* **2003**, 526, 1-18.
21. Perry, D.; Tsao, L.; Brittain, H. *J. Mater. Sci. Lett.* **1984**, 3, 1017-1019.
22. Praline, G.; Koel, B. E.; Hance, R. L.; Lee, H. I.; White, J. M. *J. Electron Spectrosc. Relat. Phenom.* **1980**, 21, 17-30.
23. Senanayake, S. D.; Mullins, D. R. *J. Phys. Chem. C.* **2008**, 112, 9744-9752.
24. Hrizi, F.; Dhaouadi, H.; Touati, F. *Ceramics International* **2014**, 40, 25-30.
25. Lu, C.-H.; Wang, H.-C. *Materials Science and Engineering: B* **2002**, 90, 138-141.
26. Li, M.; Wu, Z.; Overbury, S. H. *J. Catal.* **2013**, 306, 164-176.
27. Sheng, P. Y.; Bowmaker, G. A.; Idriss, H. *Appl. Catal. A-Gen* **2004**, 261, 171-181.
28. Song, H.; Bao, X.; Hadad, C. M.; Ozkan, U. S. *Catal. Lett.* **2011**, 141, 43-54.
29. Finocchio, E.; Busca, G.; Lorenzelli, V.; Willey, R. J. *J. Chem. Soc. Faraday Trans.* **1994**, 90, 3347-3356.
30. Binet, C.; Daturi, M.; Lavalley, J.-C. *Catal. Today* **1999**, 50, 207-225.
31. Li, C.; Sakata, Y.; Arai, T.; Domen, K.; Maruya, K.-i.; Onishi, T. *J. Chem. Soc. Faraday Trans.* **1989**, 85, 929-943.
32. Resini, C.; Cavallaro, S.; Frusteri, F.; Freni, S.; Busca, G. *React. Kinet. Catal. Lett.* **2007**, 90, 117-126.
33. Yee, A.; Morrison, S. J.; Idriss, H. *J. Catal.* **1999**, 186, 279-295.
34. Idriss, H.; Diagne, C.; Hindermann, J. P.; Kiennemann, A.; Barteau, M. A. *J. Catal.* **1995**, 155, 219-237.

35. Calaza, F. C.; Xu, Y.; Mullins, D. R.; Overbury, S. H. *J. Am. Chem. Soc.* **2012**, 134, 18034-18045.
36. Wu, Z.; Li, M.; Mullins, D. R.; Overbury, S. H. *ACS Catal.* **2012**, 2, 2224-2234.
37. Mullins, D. R.; Senanayake, S. D.; Chen, T. L. *J. Phys. Chem. C* **2010**, 114, 17112-17119.
38. Capdevila-Cortada, M.; García-Melchor, M.; López, N. *J. Catal.* **2015**, 327, 58-64.
39. Mašek, K.; Škoda, M.; Beran, J.; Cabala, M.; Prince, K. C.; Skála, T.; Tsud, N.; Matolín, V. *Catal. Lett.* **2015**, 145, 1474-1482.
40. Badri, A.; Binet, C.; Lavalley, J.-C. *J. Chem. Soc. Faraday Trans.* **1997**, 93, 1159-1168.
41. Binet, C.; Daturi, M. *Catal. Today* **2001**, 70, 155-167.
42. Ferrizz, R. M.; Wong, G. S.; Egami, T.; Vohs, J. M. *Langmuir* **2001**, 17, 2464-2470.
43. Costa, L. O. O.; Silva, A. M.; Borges, L. E. P.; Mattos, L. V.; Noronha, F. B. *Catal. Today* **2008**, 138, 147-151.
44. Tóth, M.; Varga, E.; Oszkó, A.; Baán, K.; Kiss, J.; Erdőhelyi, A. *J. Mol. Catal. A: Chem.* **2016**, 411, 377-387.
45. Mattos, L. V.; Noronha, F. B. *J. Catal.* **2005**, 233, 453-463.
46. de Lima, S. M.; Silva, A. M.; Graham, U. M.; Jacobs, G.; Davis, B. H.; Mattos, L. V.; Noronha, F. B. *Appl. Catal. A* **2009**, 352, 95-113.
47. Ciambelli, P.; Palma, V.; Ruggiero, A. *Appl. Catal., B* **2010**, 96, 190-197.
48. Sun, J.; Wang, Y. *ACS Catal.* **2014**, 4, 1078-1090.
49. Ni, M.; Leung, D. Y. C.; Leung, M. K. H. *Int. J. Hydrogen Energy* **2007**, 32, 3238-3247.
50. Zhang, B.; Tang, X.; Li, Y.; Xu, Y.; Shen, W. *Int. J. Hydrogen Energy* **2007**, 32, 2367-2373.
51. Liu, Z.; Duchoň, T.; Wang, H.; Peterson, E. W.; Zhou, Y.; Luo, S.; Zhou, J.; Matolín, V.; Stacchiola, D. J.; Rodriguez, J. A.; Senanayake, S. D. *J. Phys. Chem. C* **2015**, 119, 18248-18256.
52. Silva, A. M.; Costa, L. O. O.; Barandas, A. P. M. G.; Borges, L. E. P.; Mattos, L. V.; Noronha, F. B. *Catal. Today* **2008**, 133-135, 755-761.
53. Mavrikakis, M.; Barteau, M. A. *J. Mol. Catal. A: Chem.* **1998**, 131, 135-147.
54. Yee, A.; Morrison, S. J.; Idriss, H. *Catal. Today* **2000**, 63, 327-335.

55. Erdöhelyi, A.; Raskó, J.; Kecskés, T.; Tóth, M.; Dömök, M.; Baán, K. *Catal. Today* **2006**, 116, 367-376.
56. Raskó, J.; Kiss, J. *Appl. Catal. A-Gen* **2005**, 287, 252-260.
57. Gürbüz, E. I.; Hibbitts, D. D.; Iglesia, E. *J. Am. Chem. Soc.* **2015**, 137, 11984-11995.
58. Yee, A.; Morrison, S. J.; Idriss, H. *J. Catal.* **2000**, 191, 30-45.
59. Salge, J. R.; Deluga, G. A.; Schmidt, L. D. *J. Catal.* **2005**, 235, 69-78.
60. Davis, J. L.; Barteau, M. A. *Surf. Sci.* **1987**, 187, 387-406.
61. Li, M.; Guo, W.; Jiang, R.; Zhao, L.; Shan, H. *Langmuir* **2010**, 26, 1879-1888.
62. Mullins, D. R.; Albrecht, P. M.; Chen, T.-L.; Calaza, F. C.; Biegalski, M. D.; Christen, H. M.; Overbury, S. H. *J. Phys. Chem. C* **2012**, 116, 19419-19428.
63. Molinari, M.; Parker, S. C.; Sayle, D. C.; Islam, M. S. *J. Phys. Chem. C* **2012**, 116, 7073-7082.
64. Fristrup, P.; Kreis, M.; Palmelund, A.; Norrby, P.-O.; Madsen, R. *J. Am. Chem. Soc.* **2008**, 130, 5206-5215.
65. Daugulis, O.; Brookhart, M. *Organometallics* **2004**, 23, 527-534.
66. Rybtchinski, B.; Milstein, D. *Angew. Chem. Int. Ed.* **1999**, 38, 870-883.
67. Deng, W.; Flytzani-Stephanopoulos, M. *Angew. Chem. Int. Ed.* **2006**, 45, 2285-2289.

Appendix of Supporting Information

Table S1. Textural properties of support and catalyst.

Sample	Ce Crystallite Size (nm) ^a	Surface Area (m ² g ⁻¹) ^b	Dispersion (%) ^c
CeO ₂	19	57	---
Pd/CeO ₂	25	53	20 ± 3

^aObtained from PXRD data. ^bCalculated using the BET approximation. ^cDetermined from H₂ chemisorption at -25 °C. Error represents standard deviation from three separate measurements.

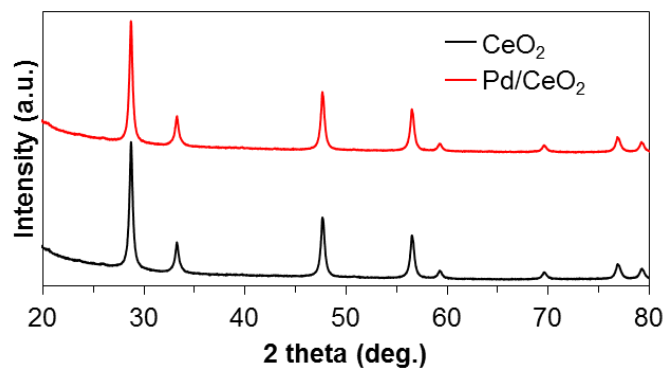


Figure S1. PXRD pattern for CeO₂ and Pd/CeO₂.

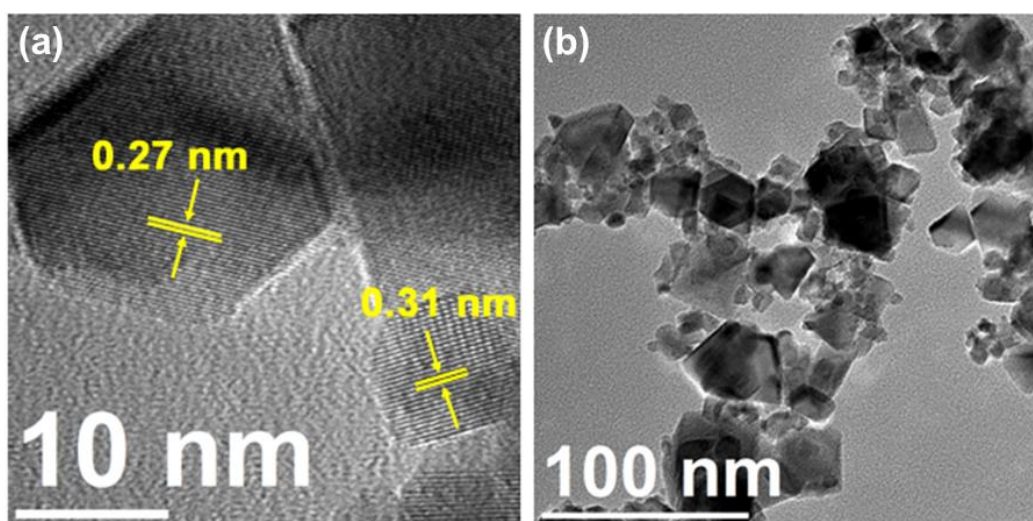


Figure S2. (a) HR-TEM image of Pd/CeO₂ showing lattice fringes corresponding to (200) and (111) surface termination. (b) TEM image of Pd/CeO₂ showing particle morphology.

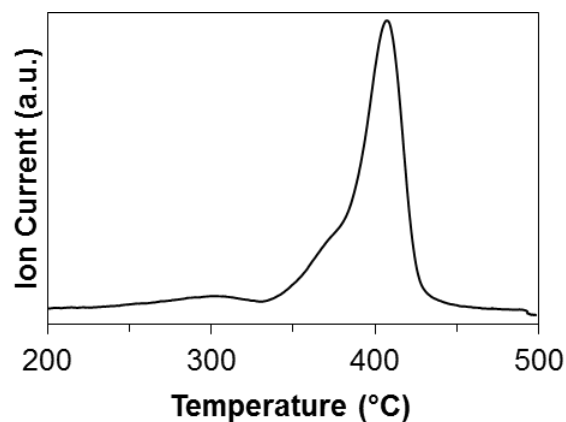


Figure S3. TPD profile (He flow) of Pd/CeO₂ after 14 h phenol transfer hydrogenation reaction with ethanol. The signal corresponds to $m/z = 44$ (CO₂). Heating rate was 10 °C min⁻¹.

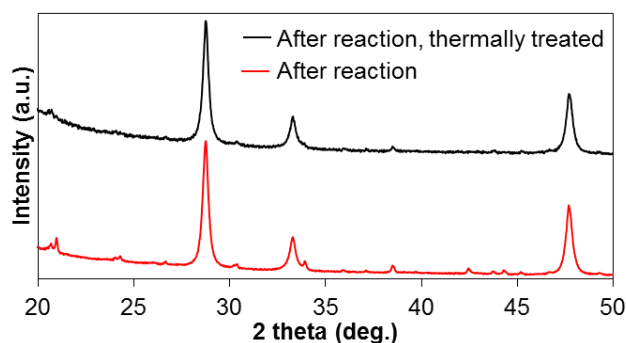


Figure S4. PXR D pattern of Pd/CeO₂ after 14 h phenol transfer hydrogenation reaction with ethanol. The patterns correspond to the catalyst after reaction (bottom) and after reaction followed by TPD under He (top).

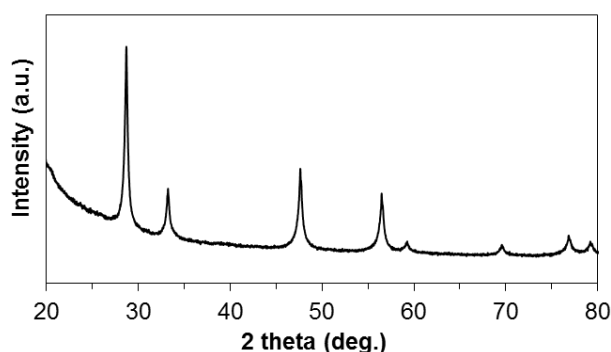


Figure S5. PXR D pattern of Pd/CeO₂ after 8 d reaction followed by calcination at 450 °C for 4 h at 2 °C min⁻¹.

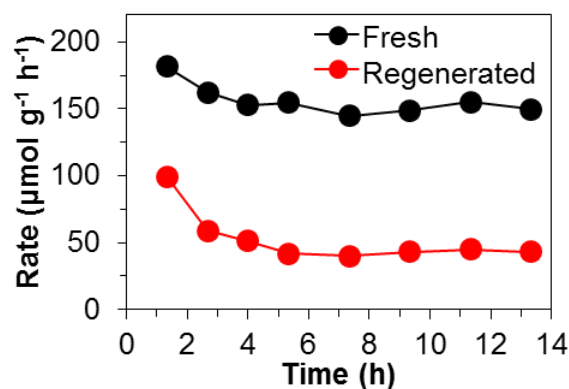


Figure S6. Phenol conversion rate as a function of time over fresh Pd/CeO₂ (top) and Pd/CeO₂ after 8 d reaction followed by O₂/H₂ regeneration (bottom). Reaction conditions: 12.5 mM phenol, 30 v/v % aqueous ethanol, T = 130 °C, 0.1 mL min⁻¹, V_{bed} = 0.2 mL, 0.25 g Pd/CeO₂.

Table 2. Textural properties of catalysts.^a

Sample	Ce crystallite Size (nm) ^b	Surface Area (m ² g ⁻¹) ^c	Dispersion (%) ^d
Pd/CeO ₂ -fresh	25	53	20 ± 3
Pd/CeO ₂ -regen	25	76	4 ± 1

^aProperties in the table correspond to the as-synthesized Pd/CeO₂ catalyst (fresh) and the catalyst after 8 day reaction followed by regeneration under O₂/H₂ (regen). ^bObtained from PXRD data by measuring the full width-half maximum for the (111) reflection of ceria. ^cCalculated using the BET approximation. ^dDetermined from H₂ pulse chemisorption at -25 °C. Errors represent standard deviation from three separate measurements.

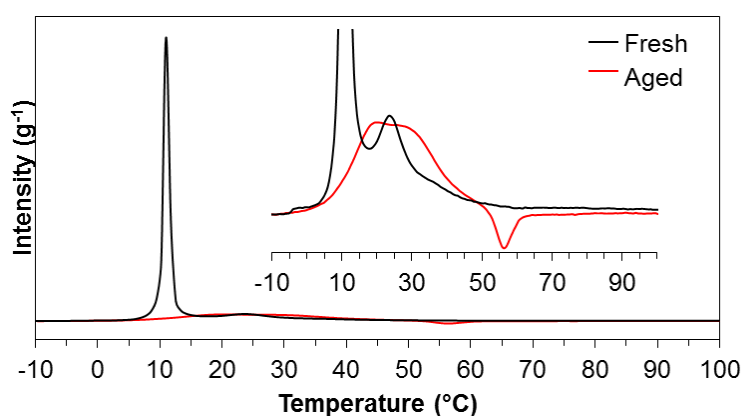


Figure S7. H₂-TPR profile for Pd/CeO₂. The catalyst was pre-oxidized in O₂/He flow at 350 °C for 0.5 h before beginning the reduction profile.

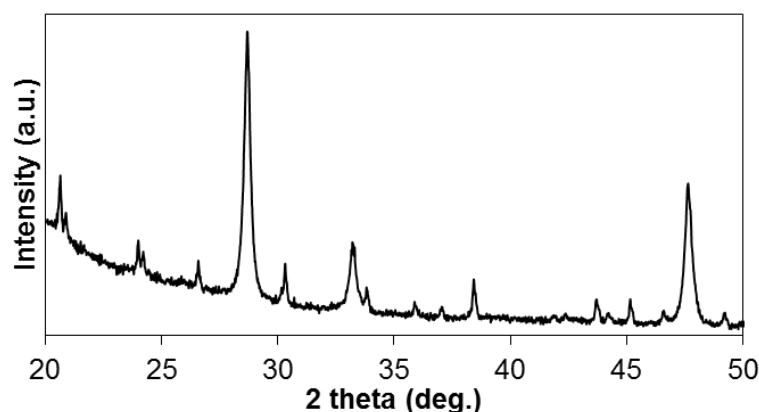


Figure S8. PXRD pattern for Pd/CeO₂ after 7 h TOS using acetaldehyde as hydrogen donor. Reaction conditions are the same as in Figure 1a, but replacing ethanol with acetaldehyde.

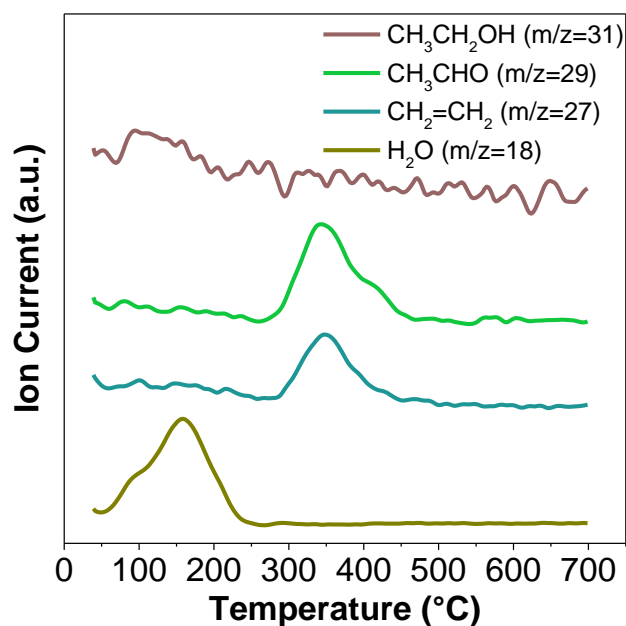


Figure S9. TPD of ethanol adsorbed onto Pd/CeO₂ under He flow (40 mL min⁻¹) at 10 °C min⁻¹.

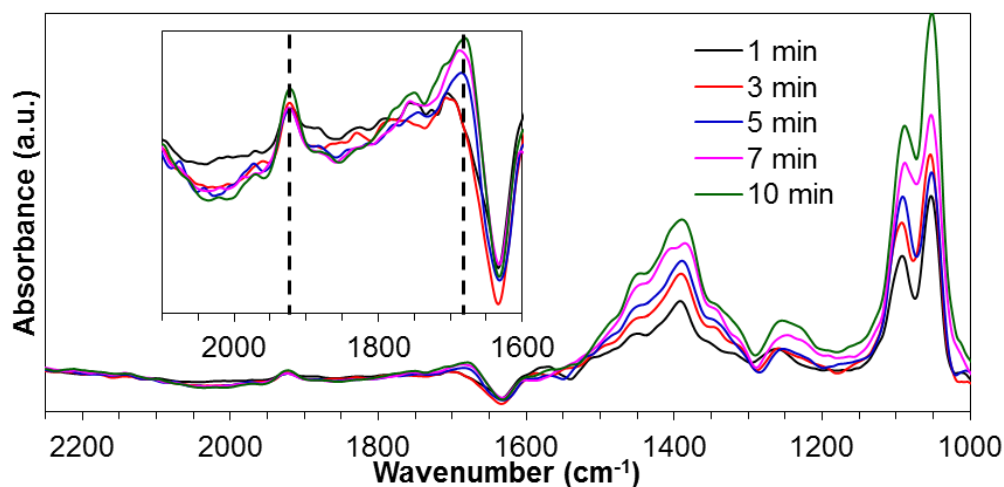


Figure S10. DRIFTS of Pd/CeO₂ during helium/ethanol flow (30 mL min⁻¹). Dashed lines of inset show bands at 1680 cm⁻¹ and 1923 cm⁻¹ attributed to acetyl and bridging CO species, respectively.

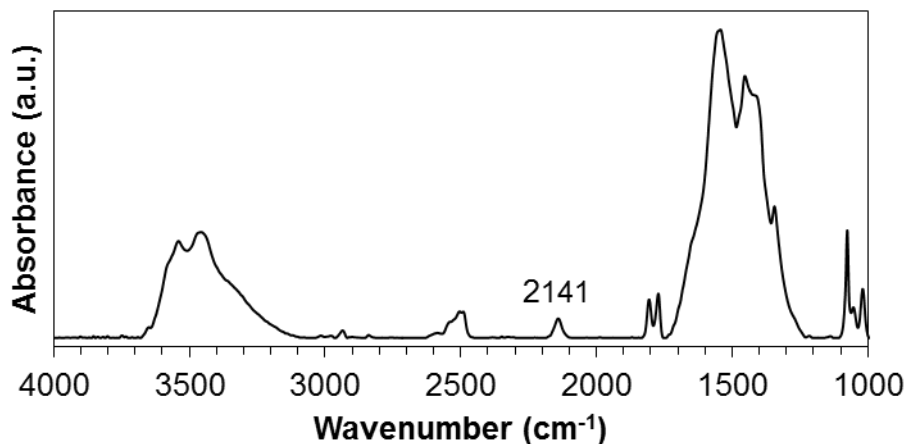


Figure S11. DRIFTS of Pd/CeO₂ after phenol transfer hydrogenation with ethanol. Conditions are the same as in the caption of Figure 1a.

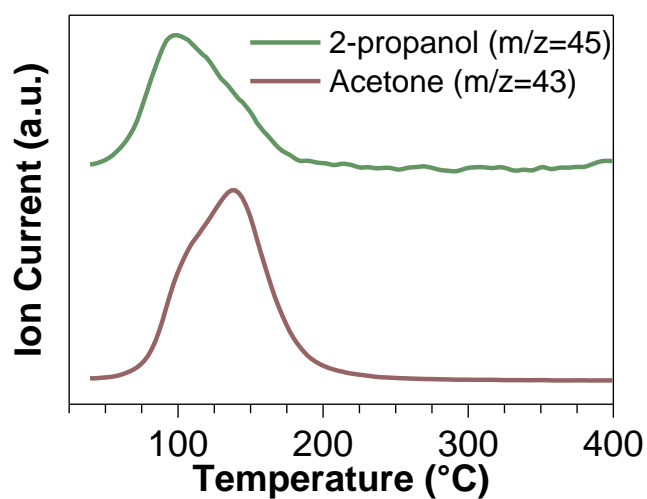


Figure S12. TPD of 2-propanol adsorbed onto Pd/CeO₂ under He flow (40 mL min⁻¹) at 10 °C min⁻¹.

CHAPTER 5**PHOSPHATE-MODIFIED CERIA AS A BRØNSTED ACIDIC/REDOX
MULTIFUNCTIONAL CATALYST**

Adapted from manuscript submitted to *J. Mater. Chem. A*

Copyright © 2016 Royal Society of Chemistry

Nicholas C. Nelson, Zhuoran Wang, Marek Pruski, Igor I. Slowing

Abstract

Deposition of trimethylphosphate onto ceria followed by thermal treatment resulted in formation of surface phosphates with retention of redox activity. The structural and chemical properties of phosphate-functionalized ceria were studied using ^{31}P solid-state NMR, XPS, zeta titration, ammonia thermal desorption, pyridine adsorption, and model reactions. The introduction of phosphates generated Brønsted acidic sites and decreased the number of Lewis acidic sites on the surface. The relative amount of Lewis and Brønsted acids can be controlled by the amount of trimethylphosphate used in the synthesis. Upon deposition of Pd, the multifunctional material showed enhanced activity for the hydrogenolysis of eugenol compared to Pd on the unmodified ceria support. This was attributed to the cooperativity between the Lewis acid sites, which activate eugenol for dearomatization, and the redox/acid property, which catalyzes hydrogenolysis.

Introduction

Ceria (CeO_2) is a unique material in catalysis science due to its inherent redox properties.¹⁻² Many ceria-based technological applications rely on the facile $\text{Ce}^{3+}/\text{Ce}^{4+}$ redox cycle, which supplies reactive oxygen species to substrates.³ Perhaps the most notable is three-way catalysis, but other uses (reforming processes, water-gas shift reaction, solid oxide fuel

cells, etc.) are emerging and are expected to be industrialized soon.⁴ Fundamental research and continued atomistic understanding of the structure and formation of ceria redox-active sites has led to the development of complex ceria-based materials with enhanced redox capability.⁵⁻¹⁴ In the past decade, synthetic procedures have been developed that allow strict geometric control over ceria particle morphology resulting in materials that selectively expose specific sets of lattice planes.¹⁵⁻¹⁸ These materials and their enhanced defect-mediated redox capabilities have led to the development of ceria-based catalytic systems for organic transformations, especially as they relate to redox processes.¹⁹⁻²²

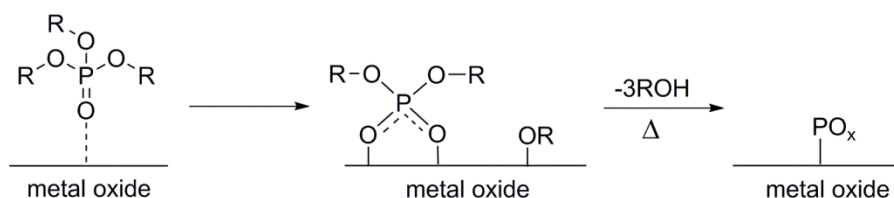
In contrast to the extensive progress made towards understanding and engineering redox sites in ceria-based materials,¹⁴ limited efforts have been devoted to incorporate additional functionalities to their surface.²³ Yet, developing methods to add surface functionalities while retaining redox activity could provide multipurpose materials capable of performing specialized tasks and tandem processes. Furthermore, incorporation of surface functionalities may offer precise control over activity and selectivity in catalytic conversions.²³⁻²⁴ One simple, yet important functionality that can be added to ceria is Brønsted acidity. Ceria exhibits weak Lewis acidity and its surface hydroxyl groups show little to no Brønsted acid character.²⁵⁻²⁸ Brønsted acidic sites have been introduced through impregnation of ceria with tungsten and vanadium precursors followed by calcination to yield supported oxides.²⁹⁻³² Ceria-supported tungsten oxides and their analogs are perhaps the most widely known ceria-based materials exhibiting Brønsted acidity due to their activity in the selective catalytic reduction of NO_x with NH_3 .³³⁻³⁵ Another class of ceria-based materials exhibiting Brønsted acidity has been developed through sulfonation of ceria-zirconia mixed metal oxide.³⁶⁻³⁸

An attractive alternative option for introducing Brønsted acidity to the surface is through organophosphate precursors. Organophosphates represent a versatile class of compounds that can be specifically tailored with desired organic functional groups for target applications.³⁹⁻⁴⁰ Immobilization of organophosphates with varying organic components on ceria may allow material properties to be tuned⁴¹ and enable cooperativity with the intrinsically active sites of the supporting material to control catalytic activity and/or product selectivity.⁴²⁻⁴⁴ For example, hydrogenolysis reactions relevant to biomass processing can be catalyzed by acid and redox-active sites.⁴⁵⁻⁵⁰ Under typical reaction conditions, oxygen substituents can be activated towards C-O bond cleavage through protonation by the acid component or binding to oxophilic vacancies in the redox-active component. Therefore, the introduction of acidic sites to a redox-active material could lead to a higher hydrogenolysis activity. In this context, this work explores the structure and catalytic properties of phosphate-functionalized ceria.

Previous studies have indicated that the thermal decomposition of organophosphates and closely related organophosphonates on metal oxides produces surface-adsorbed alkoxides and surface-bound phosphates.⁵¹⁻⁵⁷ It is thought that the first step occurs via coordination of the phosphoryl oxygen with a metal cation (Scheme 1). Cleavage of an alkoxide follows shortly thereafter, and can occur at low temperature. Upon subsequent heating, the organophosphate ester is completely decomposed into surface-bound phosphates. High temperature (600 °C) treatment of phosphorous-containing compounds deposited onto ceria can lead to formation of subsurface CePO₄ (monazite) crystals.⁵⁸⁻⁶⁰ This process involves the reduction of cerium(IV) to cerium(III), with the extent of reduction depending on the phosphorus loading.⁵⁹⁻⁶⁰ This leads to the undesirable inhibition of redox properties. A potential approach to prevent over reduction and monazite formation may be through the use of high-surface area ceria and lower calcination

temperatures. For a given phosphorus loading, a high-surface-area support would minimize the formation of bulk phosphate phases due to the larger amount of surface Ce-atoms that coordinate to the phosphoryl group. Similarly, lower calcination temperatures could prevent sintering that likely contributes to bulk phosphate formation. Confining phosphate groups to the ceria surface could lead to unique properties not previously observed (e.g. Brønsted acidity). In the present study, deposition of trimethylphosphate onto high-surface-area ceria, followed by low-temperature calcination, led to a bifunctional (redox and acid) material. Upon deposition of palladium, the multifunctional material showed higher eugenol hydrogenolysis activity than palladium on unmodified ceria.

Scheme 1. Proposed adsorption and decomposition of trimethylphosphate.⁵¹



Experimental

Reagents. Cerium(III) nitrate hexahydrate, trimethylphosphate, propylene oxide, deuterium oxide, 1,4-dioxane, indigo carmine, and pyridine were purchased from Sigma Aldrich. Potassium nitrate, sodium hydroxide, ammonium acetate, nitric acid, hydrogen peroxide, acetic acid, and hydrochloric acid were purchased from Fisher. Pluronic P104 was obtained from BASF. Cerium(III) nitrate hexahydrate was dried under vacuum at room temperature for 48 h prior to all synthetic methods. All other chemicals were used without further purification. All reagents met or exceeded ACS specifications.

Synthesis of ceria (CeO₂). The method was adopted from a previously published report.⁶¹ Briefly, Ce(NO₃)₃•6H₂O (8.8 g, 20.3 mmol) and Pluronic P104 (10.1 g) were dissolved in ethanol (200 mL). The contents were stirred vigorously until complete dissolution (~2 h). The solution was cast into a large crystallization dish and placed in a pre-heated 65 °C oven until the ethanol had evaporated (~8 h). The resulting gel was placed in a pre-heated 150 °C oven overnight. The yellow powder was subsequently calcined in air at 450 °C for 4 h with a ramp rate of 2 °C min⁻¹. *Caution!* During thermal treatment at 150 °C, combustion occurs within ~12 min, producing flames which self-extinguish within seconds after all combustible material (i.e., block copolymer) is burned. The thermal treatment step should be conducted in an oven, preferably in a fume hood with a closed sash to avoid exposure to gaseous decomposition products.

Synthesis of phosphate-modified ceria (CeO₂-PO_x). The synthesis of phosphate-modified ceria was accomplished through an impregnation route. In a typical procedure, the desired amount of trimethylphosphate (TMP) was deposited onto the CeO₂ support in five increments. That is, five cycles of TMP impregnation, followed by thorough mixing with a mortar and pestle, were performed until the total desired amount of TMP was added to the CeO₂ support. The material was calcined at 450 °C for 4 h with a 10 °C min⁻¹ ramp rate.

Synthesis of Pd/CeO₂ and Pd/CeO₂-PO_x. In a typical procedure, palladium (II) acetate (1 wt. % Pd) was dissolved in acetone and impregnated onto the support. The precatalysts were heated in air to 350 °C at 2.5 °C min⁻¹ and held for 2 h. After cooling to room temperature, the catalysts were heated under flowing H₂ (50 mL min⁻¹) using the same temperature program.

Powder X-ray diffraction (PXRD). Diffraction patterns were collected using Co K α 1, K α 2 split radiation (45 kV, 40 mA, $\lambda_{\text{avg}} = 1.7903 \text{ \AA}$) on a PANalytical X'Pert PRO diffractometer equipped with a theta–theta vertical mode goniometer, incident Fe filter, an air-cooled X'Celerator real time multiple strip (RTMS) detector, and spinner stage. The patterns were converted to Cu K α radiation for comparison to standard patterns using Bragg's law. PXRD samples were prepared by placing powders onto a background-less sample holder. Crystallite sizes were calculated using Scherrer equation.

Surface area and porosimetry. Textural properties of the supports and catalysts were measured by nitrogen sorption isotherms at $-196 \text{ }^\circ\text{C}$ in a Micromeritics Tristar analyzer. The surface areas were calculated by the Brunauer-Emmett-Teller (BET) method. Sample pretreatment for surface area measurement was done by flowing N₂ for 6 h at $100 \text{ }^\circ\text{C}$.

ICP-OES. Ce, P, and Pd loadings were analyzed by a Perkin Elmer Optima 2100 DV Inductively Coupled Plasma-Optical Emission Spectroscopy (ICP-OES). Samples (*ca.* 10 mg) were digested in 5 mL of 4 M HCl, 1 mL of concentrated HNO₃, and 2 mL of 30 v/v % H₂O₂. The samples were sonicated for ten minutes. Then they were placed into a $50 \text{ }^\circ\text{C}$ water bath for ~ 12 h. Each sample was then diluted to 10 mL of total solution.

Diffuse reflectance infrared Fourier transform spectroscopy (DRIFTS). Measurements were made on a Bruker Vertex 80 FT-IR spectrometer with OPUS software and apodized spectral resolution of 0.2 cm^{-1} . The spectrometer was equipped with a HeNe laser and photovoltaic MCT detector. A Praying Mantis™ diffuse reflectance accessory and high temperature reaction chamber was used for room temperature and variable temperature measurements, respectively. 32 scans were collected for each measurement in absorbance mode with 8 cm^{-1} resolution. For pyridine adsorption experiments, the samples were heated to $100 \text{ }^\circ\text{C}$

in He flow (50 mL min^{-1}) for 60 minutes and the samples were subsequently cooled to room temperature under He flow. Blank spectra were recorded at this time. Then, the He flow was redirected through a saturator containing pyridine at room temperature. Spectra were taken at 1 min intervals under probe molecule exposure until the formation of liquid-like bands was observed ($\sim 1\text{-}5 \text{ min}$). At this time, the He flow was redirected away from the saturator. Spectra were taken at 10 min intervals until no changes were observed between subsequent spectra ($\sim 20\text{-}30 \text{ min}$).

X-ray photoelectron spectroscopy (XPS). XPS analysis was done with a PHI 5500 multitechnique system using a standard Al X-ray source. Samples were analyzed at room temperature with no special preparation. Charge correction was accomplished by shifting the Ce 3d v-peak to 882.6 eV for all spectra.⁶²⁻⁶³ All spectra were normalized so that the most intense peak had a value of 1.

SSNMR. The SSNMR measurements were performed on a 400 MHz Agilent DD2 spectrometer equipped with a 3.2-mm Chemagnetics double resonance magic angle spinning (MAS) probe, and on a 600 MHz Varian DD1 spectrometer equipped with a 1.6-mm FastMASTM T3-type probe. Samples were directly packed into zirconia rotors without any further treatment. The ^1H background-free MAS spectra of all samples were obtained by subtracting the signal measured with an empty probe. The ^1H Hahn echo spectra were obtained using pulse sequence ($90^\circ - \tau - 180^\circ - \tau$) with various echo delays synchronized with MAS period. The 1D ^{31}P spectra were obtained under MAS using direct polarization (DPMAS) and a $^{31}\text{P}\{^1\text{H}\}$ tangent-ramped cross polarization scheme (CPMAS). The same CP scheme was used to generate the 2D $^{31}\text{P}\{^1\text{H}\}$ heteronuclear correlation (Hetcor) spectra. The ^1H chemical shifts are reported relative to tetramethylsilane (TMS), and the ^{31}P chemical shifts are reported relative to phosphoric acid

(H_3PO_4 , 85% in D_2O). The detailed experimental parameters are given in the corresponding figure captions using the following symbols: ν_R denotes the MAS rate; $\nu_{\text{RF}}(\text{X})$, the magnitude of the RF field applied to X nuclei; τ_{CP} , the cross-polarization contact time; τ_{rd} , the recycle delay and Δt_1 , the increment of t_1 in 2D experiments.

Temperature programmed desorption (TPD). NH_3 -TPD experiments were carried out using a Micromeritics AutoChem II equipped with TCD detector. The samples (*ca.* 300 mg) were placed into a quartz U-tube and degassed at 500 °C for 60 minutes (10 °C min^{-1}) under O_2 -He (10 % O_2) flow (50 mL min^{-1}). The samples were cooled to 100 °C under O_2 -He and the gas flow switched to NH_3 -He (10 % NH_3). After 15 minute exposure, the gas flow was switched to He and held at 100 °C for 15 minutes before cooling to 40 °C. The temperature was then ramped at 10 °C min^{-1} while monitoring the TCD signal.

Zeta potential measurements. Zeta potential measurements were made on a Zetasizer Nano ZS90 instrument with a standard 633 nm He-Ne laser using the Smoluchowski approximation. Samples were prepared by suspending the solid (~ 10 mg) in aqueous KNO_3 (0.01M, 10 mL). The pH of the suspension was adjusted with dilute NaOH and HCl solutions. Afterwards, the samples were sonicated for 30 minutes and then allowed to sit for varying amounts of time in order to obtain reliable data.

Cationic exchange. Two samples with different masses (*ca.* 10 and 100 mg) for each material were weighed into 20 mL scintillation vials. The solids were suspended in aqueous ammonium acetate (0.1 M, 10.0 mL, pH = 6.99). After 24h, with periodic agitation, the pH of the suspension was measured. The measured pH was related to the exchangeable H^+ on the materials through a calibration curve. The calibration curve was constructed by adding a known amount of

standardized acetic acid solution (0.0984 ± 0.003 M) to ammonium acetate solution (0.1 M, 10.0 mL, pH = 6.99) and measuring the pH after each addition (20-40 μ L). The curve was fit to a third order polynomial with a correlation coefficient of 0.9991 within the pH range of 6.99-6.01.

Hydrolysis of propylene oxide. In a typical reaction, ~10 mg of catalyst, 1 mL of D₂O, and a stir bar were placed into 4 mL glass vial. The vial was then placed into an OptiBlock parallel synthesis reaction block (OP500 series) equipped with thermocouple, locking base, locking plate, and PTFE faced silicone septa pad. Once the vials were sealed, propylene oxide (40 μ L, 0.6 mmol) was added via syringe. The reactor assembly was heated to the desired temperature for the desired time with stirring (200 rpm). Afterwards, the reactor assembly was allowed to cool to room temperature, at which time the catalyst was separated by centrifugation. The supernatant (1 mL) was analyzed by ¹H-NMR using 1,4-dioxane (5 μ L, 58 μ mol) as internal standard. The ¹H-NMR spectra were collected on a Bruker DRX 500 equipped with a narrow bore 11.7T/500 MHz magnet and a standard ¹H probe. ¹H-NMR (deuterium oxide, 500 MHz, 25 °C): δ , ppm: 1.07 (3H, s, CH₃); 3.37 (1H, dd, CH_a); 3.47 (1H, dd, CH_b); 3.81 (1H, sext, CH). Mass balances were 94-100 %.

Photodegradation of indigo carmine. A 2.0 mL aliquot of an aqueous indigo carmine stock solution (18.3 mg L⁻¹) was added to 4.1 mg of catalyst in a 4 mL glass vial. The suspension was allowed to pre-equilibrate in the dark for 0.5 h. Afterward the vials were placed into a Rayonet RPR-200 photoreactor with a 350 nm light source under stirring for 1.5 h. The photodegradation activity was monitored by comparing the absorbance of indigo carmine solution before and after the reaction using a UV/VIS spectrometer.

Eugenol hydrotreatment. Eugenol hydrogenation reactions were carried out using a high pressure reactor. The Pd/CeO₂ or Pd/CeO₂-PO_x catalyst (*ca.* 50 mg) was placed into the reactor along with water (25 mL) and eugenol (15 μ L, 97 μ mol). The reactor was purged with nitrogen and then pressurized with H₂ (10 bar). The contents were heated to 100 °C (10 °C min⁻¹) and held for 4 h under mechanical stirring (800 rpm). The reactor was allowed to cool to room temperature (~0.5 h). The products were extracted with ethyl acetate (25 mL) and analyzed by GCMS (7890A, 5975C with HP-5MS column). Mass balances were between 90 and 100 %.

Results and Discussion

Phosphate-functionalized ceria (CeO₂-PO_x) was prepared by impregnation of CeO₂ with trimethylphosphate (TMP) followed by calcination at 450 °C for 4 h. The maximum loading of P-containing compounds on the CeO₂ support was about 0.23 moles of P per mole of Ce (i.e. P:Ce = 0.23) (Figure S1). This loading corresponds to about 7.4 P-atoms nm⁻² and essentially represents surface saturation as the theoretical amount of Ce atoms on the (111) surface is about 7.9 Ce-atoms nm⁻².⁶⁴ The physical and chemical properties of two samples with P:Ce loadings of 0.1 and 0.2, denoted as CeO₂-0.1PO_x and CeO₂-0.2PO_x, are listed in Table 1. The specific surface areas of the P-containing materials were lower than that of the unmodified CeO₂ support. The PXRD pattern for all materials could be indexed to the fluorite structure of ceria with no other reflections observed (Figure 1). This indicates that crystalline phosphate phases were not formed as in previous reports with identical P:Ce loadings.⁵⁹⁻⁶⁰ The difference can be attributed to the significantly lower surface area (13 m² g⁻¹) and higher calcination temperature (600 °C) used in the previous studies. That is, for the same P:Ce loading, a lower-surface-area material would result in fewer surface phosphates, with the excess penetrating into the bulk. High calcination temperatures would induce sintering and contribute to bulk phosphate formation.

Here, the PXRD analysis showed that the CeO₂ crystallite size and lattice parameters increased only slightly upon phosphorus modification (Table 1). The elongation of the ceria lattice has previously been attributed to higher concentrations of Ce(III) due to phosphate binding (i.e. CePO₄).⁵⁹⁻⁶⁰ The presence of surface phosphates was confirmed through DRIFT analysis as indicated by the appearance of bands between 1200-900 cm⁻¹ which are characteristic for the $\nu(\text{P-O})$ of phosphates (Figure S2a).^{51-53, 56, 65-67} Considering the significant overlap between the various $\nu(\text{P-O})$ values for phosphates (e.g. ortho-, pyro-, polyphosphates, etc.) within this region it was difficult to distinguish the type of phosphate(s) present. There was also a band present around 2400 cm⁻¹ for the phosphate-containing samples that was not present for CeO₂ (Figure S2b). This band is consistent with P-OH through comparison with the IR spectrum for monobasic sodium phosphate.⁶⁸

Table 1. Physical properties of the materials.

Sample	P Loading ^a		Surface Area (m ² g ⁻¹) ^c	Crystallite Size (nm) ^d	Lattice Parameter (Å) ^e
	(mmol g ⁻¹) ^b	(nm ⁻²)			
CeO ₂	0	0	213	6	5.413
CeO ₂ -0.1PO _x	0.64±0.05	3.5	110	8	5.417
CeO ₂ -0.2PO _x	1.1±0.1	5.8	115	9	5.421

^aLoadings obtained from ICP analysis. ^bCalculated using CeO₂ molecular weight. ^cSurface areas calculated using BET approximation. ^dObtained from PXRD data using Scherrer equation. ^eObtained from Rietveld refinement of PXRD data.

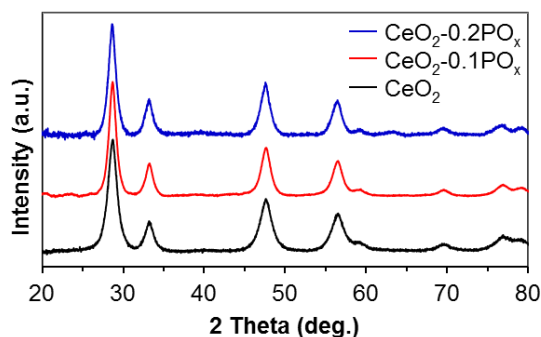


Figure 1. PXRD patterns of the ceria and phosphate-modified ceria materials.

The electronic structure of the materials was probed via XPS to determine the nature and valency of surface species (Figure 2). The Ce 3d spectral region for both P-containing materials and CeO₂ displayed bands consistent with those reported for fully oxidized ceria.^{62-63, 69} A slight increase in intensity was observed around 885 and 904 eV for the P-containing materials, possibly due to the v' and u' bands of Ce(III), respectively.⁶⁹⁻⁷² This was consistent with results from XRD analysis. The O 1s spectrum for all three materials showed a band centered around 529.5 eV. Additional intensity for the phosphate-impregnated materials was observed at higher binding energies, suggesting oxygen species different from those observed for CeO₂. Previous studies have shown the ceria O 1s spectrum can be described by three types of oxygen species: lattice oxygen (529.6 eV),⁷³ adsorbed carbonates (531.2 eV),⁷⁴⁻⁷⁵ and surface hydroxyls (532.7 eV).⁷³ The O 1s spectrum for CeO₂ was deconvoluted into three peaks with maxima found at 529.5 eV, 531.5 eV, and 532.7 eV, assigned to lattice oxygen, adsorbed carbonates, and surface hydroxyls, respectively (Figure S3a). For the phosphate-functionalized materials, the O 1s spectrum was also deconvoluted into three peaks with maxima at 529.5 eV, 531.1 eV, and 532.7 eV, assigned to lattice oxygen, phosphate, and hydroxyls, respectively. The O 1s band assigned to surface phosphates is consistent with the O 1s binding energy for cerium(III) phosphate (531.0 eV).⁷⁶ It is also expected that different types of phosphates (e.g. pyro-, meta-, polyphosphate, etc.) would have similar O 1s binding energies.⁷⁷ The relative deconvoluted peak area for the band at 531.1 eV increased from about 13 % for CeO₂-0.1PO_x to about 27 % for CeO₂-0.2PO_x indicating that the band correlates with P-loading. The P 2p spectrum for CeO₂-0.1PO_x and CeO₂-0.2PO_x showed one band centered around 133.1 eV, which is also consistent with phosphates (Figure S3d).

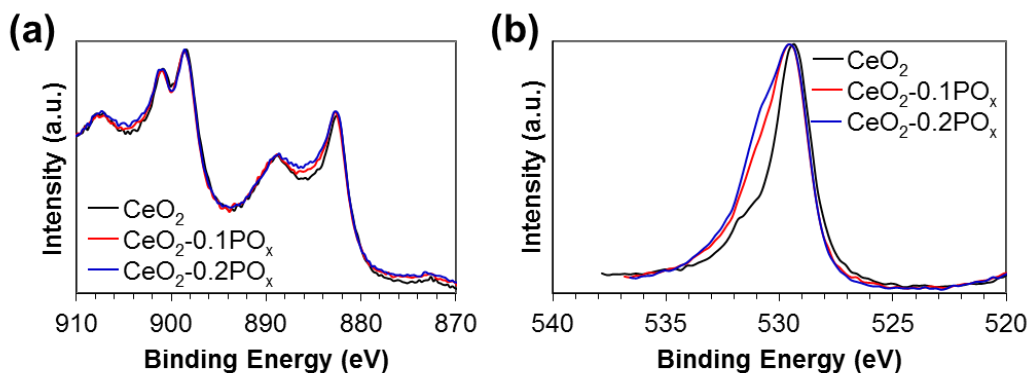


Figure 2. XPS spectra for CeO₂ and phosphate-functionalized CeO₂ in the (a) Ce 3d spectral and (b) O 1s spectral region.

The ³¹P DPMAS spectra of CeO₂-0.1PO_x and CeO₂-0.2PO_x contain a strong peak centered at around -5 ppm with the line width at half height of roughly 10 ppm (Figure 3), which is flanked by a pair of spinning sidebands, marked with asterisks. Additionally, the spectrum of CeO₂-0.2PO_x features a less intense and broader peak centered at around 0 ppm. Identical line shapes were observed in the ³¹P{¹H} CPMAS spectra (Figure S4). By comparing the total integrated spectral intensity of DPMAS spectra with that of a reference sample measured under identical conditions (ammonium dihydrogen phosphate, NH₄H₂PO₄), the phosphorus loading was estimated at 0.42 (±0.04) mmol g⁻¹ for CeO₂-0.1PO_x and 0.73 (±0.07) mmol g⁻¹ for CeO₂-0.2PO_x. These estimates are lower, by about one-third, than those obtained by the ICP analysis (Table 1), which may be attributable, at least in part, to paramagnetic broadening. The presence of paramagnetic species in both samples was also suggested by the short T₁ relaxation times of phosphorous, which were about 1 and 2 seconds for these two samples, respectively. We note, however, that while these ³¹P relaxation times are much shorter than those typically encountered in diamagnetic solids,⁷⁸ T₁ values on the order of 10 ms were reported in heavily paramagnetic CePO₄ nanoparticles.⁷⁹ The ratios between phosphorus loadings in CeO₂-0.1PO_x and CeO₂-

0.2PO_x obtained by SSNMR and ICP are almost identical (1 : 1.74 and 1: 1.72, respectively), and are reasonably close to the targeted proportion of 1 : 2.

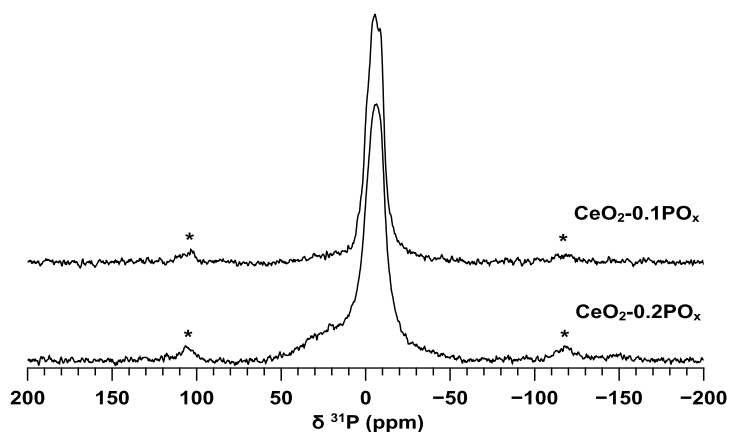


Figure 3. ³¹P DPMAS spectra of CeO₂-0.1PO_x and CeO₂-0.2PO_x. The spectra were obtained using $\nu_R = 18$ kHz, $\nu_{RF}(^{31}\text{P } 90^\circ) = 83.3$ kHz, $\nu_{RF}(^1\text{H SPINAL-64}) = 100$ kHz, and 128 scans with $\square\square\square_{rd} = 10$ s for CeO₂-0.1PO_x and $\square_{rd} = 6$ s for CeO₂-0.2PO_x.

To assign the ³¹P resonance(s), we also measured the 2D ³¹P{¹H} Hetero spectra of CeO₂-0.1PO_x and CeO₂-0.2PO_x, using the through-space CP scheme for ¹H → ³¹P magnetization transfer (Figure 4). In both samples, the ³¹P sites are correlated to two types of protons, resonating at 5.2 ppm and ~8.2 ppm. The upfield ¹H peak at 5.2 ppm coincides with the single resonance observed in an unmodified CeO₂ support (spectrum not shown), and is thus assigned to water, which is hydrogen-bound to ceria. The ¹H peak at 8.2 ppm is attributed to P-OH groups of the surface attached phosphates, as it only appears in phosphate-impregnated materials and its chemical shift falls into the range typical for P-OH species (between 7.0–16.8 ppm).⁸⁰ These assignments are further supported by the long T₂^ρ relaxation times associated with both resonances (Figure S5). Based on these 1D and 2D spectra, the dominant ³¹P peak can be assigned to orthophosphate- and/or pyrophosphate-type functionalities bound to the CeO₂ support. The orthophosphate species in inorganic phosphates are known to resonate near 0 ppm

(typically between -5–10 ppm), whereas pyrophosphates are typically observed only a few ppm upfield from this range.⁸⁰⁻⁸¹

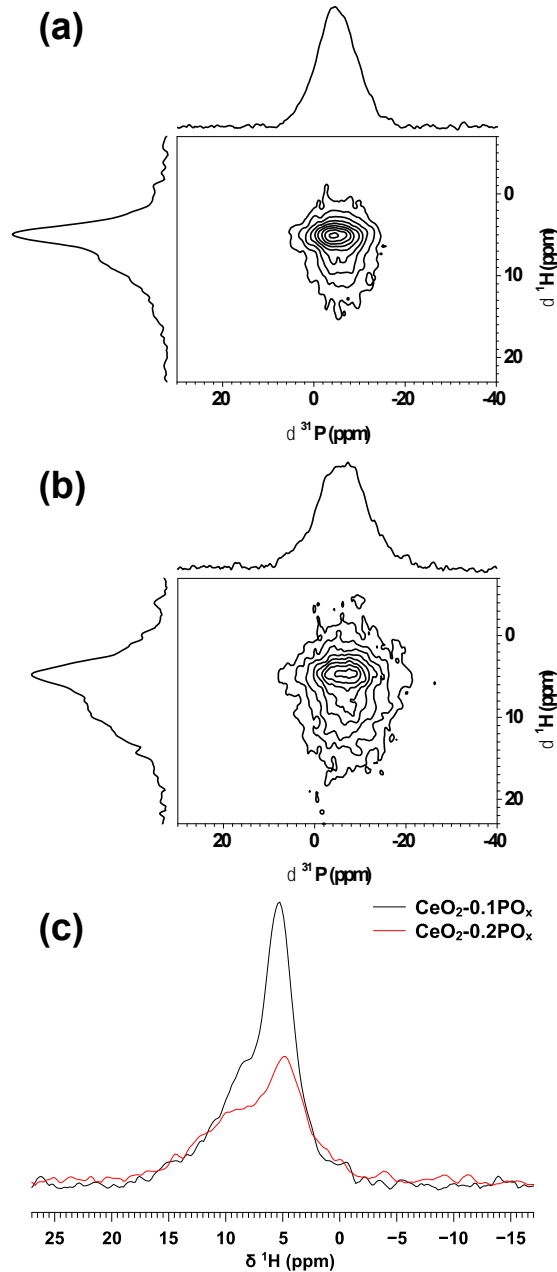
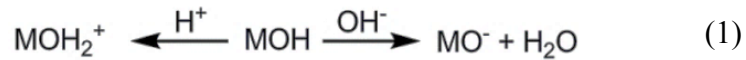


Figure 4. 2D $^{31}\text{P}\{^1\text{H}\}$ Hetcor spectra of (a) $\text{CeO}_2\text{-}0.1\text{PO}_x$ and (b) $\text{CeO}_2\text{-}0.2\text{PO}_x$. The spectra were obtained using $\nu_R = 18$ kHz, $\square_{\text{CP}} = 2.1$ ms, $\nu_{\text{RF}}(^1\text{H CP}) = 96$ kHz, $\nu_{\text{RF}}(^{31}\text{P CP}) = 78$ kHz, $\nu_{\text{RF}}(^1\text{H SPINAL-64}) = 96$ kHz, $\Delta t_1 = 55$ μs , 128 (a) or 256 (b) scans per row, and $\square_{\text{rd}} = 1$ s. (c) Comparison of the ^1H projections of $\text{CeO}_2\text{-}0.1\text{PO}_x$ (black line) and $\text{CeO}_2\text{-}0.2\text{PO}_x$ (red line).

Zeta potential titrations were carried out to evaluate how phosphate modification affected the acid-base properties of the material. The zeta potential represents the average potential difference between the diffuse layer (i.e. surface of shear or shear plane) of counter ions surrounding a charged particle and the bulk solution.⁸² Thus, the sign and magnitude of the zeta potential reflect the charge distribution on the surface of metal oxides. The charge on the surface of solid oxides in aqueous solutions can be described by equation (1):⁸³



It follows from equation (1) that H^+ and OH^- are the fundamental potential-determining ions in solution. Thus, the pH at the zero point of charge (ZPC) or isoelectric point is a measure of the acidity or basicity of a material. In general, a low ZPC (i.e. low pH) indicates that the metal oxide surface has low affinity for protons and is therefore acidic. In contrast, a higher ZPC represents a more basic surface. The zeta titration curves for the materials are shown in Figure 5. The ZPC for CeO_2 was around $\text{pH} = 7$ and is in general agreement with reported literature values.⁸⁴⁻⁸⁵ For both P-containing materials, the ZPC was around $\text{pH} = 2$ suggesting that their surfaces were more acidic than that of unmodified CeO_2 . This result is consistent with the presence of P-O-H groups suggested by SS NMR and DRIFTS measurements.

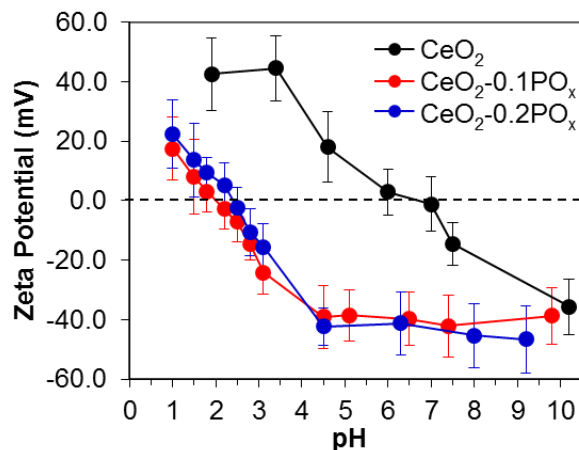


Figure 5. Zeta titration measurements for the three materials in 0.01 M $\text{KNO}_3(\text{aq})$. The error bars represent the zeta standard deviation.

The zeta titration measurements indicated that phosphate modification altered the acid-base properties of CeO_2 . To further understand these changes, surface acidity was probed via thermal desorption of ammonia (NH_3 -TPD). In general, the amount of ammonia desorbed is proportional to the total number of acidic sites while the temperature of desorption is proportional to their acidic strength.⁸⁶ The samples were pretreated in O_2 -He flow at 500 °C before cooling down to 100 °C for ammonia adsorption. The NH_3 -TPD profiles for the two materials are shown in Figure 6a. CeO_2 showed significant desorption below 200 °C indicating weak interaction with the support possibly through hydrogen bonding with lattice oxygen (i.e. physisorbed). Ammonia desorption continued to about 700 °C with desorption maxima occurring between 200-400 °C and around 600 °C. These results are in agreement with the mild acidity of ceria.^{25, 27-28} The NH_3 -TPD integrated value was corrected for multilayer/physisorbed species through profile deconvolution (Figure S6). After correcting for physisorption, the acid site density for CeO_2 was 2.0 $\mu\text{mol m}^{-2}$. This value agrees well with prior studies using NH_3 adsorption microcalorimetry ($1.9 \pm 0.3 \mu\text{mol m}^{-2}$).⁸⁷⁻⁹⁰ The NH_3 -TPD profile for the phosphate-modified materials showed significant differences compared to CeO_2 . Most notable was a higher

amount of desorbed ammonia between 100-300 °C and very little desorption between 300-400 °C. There was also a broad desorption from 400-700 °C. The profile indicates that the surface acidity was altered, in agreement with zeta titration data, and that there seems to be a larger fraction of physisorbed (< 200 °C) or weak acidic sites (200-300 °C) for the P-containing materials. Interestingly, integration showed that the number of acidic sites per mass was relatively constant among the three materials (0.44, 0.41, 0.44 mmol g⁻¹ for CeO₂, CeO₂-0.1PO_x, and CeO₂-0.2PO_x, respectively).

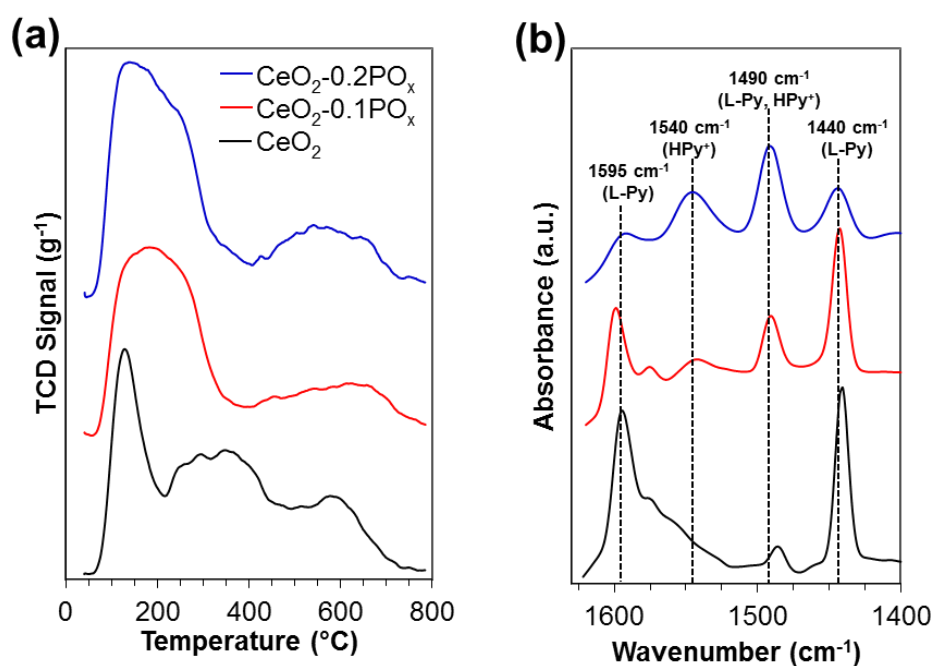


Figure 6. (a) NH₃-TPD profiles for the three materials. The profiles are shifted for clarity. (b) DRIFT spectra for the three materials after adsorption of pyridine. The legend is the same as in (a) and the profiles are shifted for clarity.

Pyridine adsorption was used to probe the strength and type (Lewis vs. Brønsted) of acidic sites by monitoring with IR spectroscopy. Coordination of pyridine molecule to a Lewis acid (L-Py) results in IR bands around 1590-1630 cm⁻¹ and 1440 cm⁻¹, attributable to the ν_{8a} and ν_{19b} pyridine vibrational modes, respectively.⁹¹⁻⁹² Pyridine interaction with Brønsted acidic sites

(HPy⁺) results in formation of the pyridinium cation and its characteristic ν_{19b} vibrational mode at 1540-1545 cm⁻¹.⁹¹⁻⁹² For pyridine adsorbed on CeO₂ (Figure 6b), the ν_{8a} and ν_{19b} bands were found at 1595 cm⁻¹ and 1440 cm⁻¹, respectively, and were attributed to coordination to Lewis acid sites (i.e. Ce cation). There was a shoulder band around 1575 cm⁻¹ and it was assigned to the ν_{8b} mode of pyridine bound to cerium cation.⁹¹ The shoulder slowly decreased in intensity to baseline value and could be caused by perturbation by adsorbed carbonates.²⁶ The band at 1487 cm⁻¹ arose due to the ν_{19a} vibrational mode of Lewis-bound pyridine and pyridinium cation.⁹² Since there was no significant pyridinium band at 1540 cm⁻¹, the 1487 cm⁻¹ band was attributed to cerium-coordinated pyridine. These results indicated that CeO₂ contains only weak Lewis acids and is in agreement with previous studies.²⁵⁻²⁸

Similar spectral features were observed for pyridine adsorbed on CeO₂-0.1PO_x. The ν_{8a} and ν_{19b} bands for cerium-coordinated pyridine were found at 1599 cm⁻¹ and 1443 cm⁻¹, respectively. The similar absorption band frequency for Lewis acid-coordinated pyridine (ν_{8a}) on CeO₂ and CeO₂-0.1PO_x materials suggested most of the adsorbed pyridine was interacting with cerium cations and that the Lewis acid strength was basically unchanged.⁹¹⁻⁹⁴ There was also a small band at 1542 cm⁻¹ attributable to the ν_{19b} vibrational mode of the pyridinium cation, suggesting the presence of Brønsted acidic sites not observed in CeO₂. Further support for the formation of pyridinium is indicated by the larger relative intensity of the overlap band at 1490 cm⁻¹ (HPy⁺, L-Py) and the band at 1440 cm⁻¹ (L-Py), which would be expected upon formation of adsorbed pyridinium. The formation of Brønsted acidic sites was also confirmed on CeO₂-0.2PO_x. The pyridinium band was clearly observed at 1540 cm⁻¹ along with a pronounced increase in intensity of the overlap band at 1490 cm⁻¹ relative to the band at 1440 cm⁻¹. It is worth noting that the band integral at 1440 cm⁻¹ decreased as the phosphorus loading increased.

This indicates that the formation of Brønsted sites comes at the expense of Lewis acidic sites and is consistent with the adsorption mechanism shown in Scheme 1.

The Brønsted acidic sites were quantified through cation exchange with an aqueous ammonium acetate (pH = 6.99) solution.⁹⁵ The number of acidic protons displaced by ammonium cations (24 h exchange) was determined by pH measurement of the resulting suspension (Table 2). To this effect, a calibration curve was prepared based on the pH of an aqueous ammonium acetate solution after addition of known amounts of standardized acetic acid solution. For CeO₂, the pH of the suspension was higher than the ammonium acetate solution, which is consistent with the mild basicity of ceria. In agreement with the zeta potential measurements, this result suggests there are no exchangeable protons for CeO₂ at pH = 7. The result is also consistent with the pyridine adsorption experiments, and indicates that cerium cations do not have sufficient Lewis acidity to dissociate water, which would result in a decreased pH value. Therefore, any observed decrease in the pH of the phosphated ceria suspensions can be solely attributed to cationic exchange of H⁺ for NH₄⁺. For CeO₂-0.1PO_x and CeO₂-0.2PO_x the concentrations of Brønsted acidic sites were 0.18 and 0.31 mmol g⁻¹, respectively. The relative increase of exchangeable H⁺ between CeO₂-0.1PO_x and CeO₂-0.2PO_x was identical to the relative increase of P at. % (0.7) and suggests that the number of Brønsted acid sites is directly proportional to the phosphorous loading. The cationic exchange experiments also indicated that the ratio between Brønsted acidic protons and phosphorous (mmol g⁻¹ basis) was about 0.3 for both materials. The number of Lewis acidic sites for the materials was estimated by subtracting the quantities of physisorbed ammonia (Figure S6) and Brønsted acid sites from the NH₃-TPD integrated value. The number of Lewis acidic sites decreased as the number of Brønsted acid sites increased with increasing P content (Table 2). These results are

consistent with the changes in relative intensities of HPy⁺ and L-Py bands observed in the pyridine adsorption experiments. The fraction of Brønsted sites determined from cationic exchange relative to the total acidic sites from NH₃-TPD agrees well with the theoretical phosphorous surface coverage (Table 2).

Table 2. Brønsted and Lewis acidic site distribution and quantification.

Material	Brønsted Acid (mmol g ⁻¹) ^a	Lewis Acid (mmol g ⁻¹) ^b	P _{surf} /Ce _{surf} ^c
CeO ₂	0	0.44	0
CeO ₂ -0.1PO _x	0.18 ± 0.01	0.23	0.44
CeO ₂ -0.2PO _x	0.31 ± 0.04	0.13	0.73

^aCalculated from cationic exchange with ammonium acetate. ^bObtained from NH₃-TPD integration after subtracting Brønsted acid sites and correcting for physisorption (see Figure S6). ^cCalculated assuming that all P-species reside on the surface and a cerium surface density of 7.9 Ce-atom nm⁻².⁶⁴

The catalytic activities of the three materials were assessed through the hydrolysis of propylene oxide to yield propylene glycol. The hydrolysis reaction can be catalyzed by acids and bases, but it has been shown that the active site for hydrolysis using ceria is the water-tolerant Lewis-acidic cerium cation.⁹⁶ The catalytic results are summarized in Table 3. For CeO₂, the propylene glycol yield was 12 % after 3 h reaction time. This corresponds to a turnover frequency (TOF) of 5.8 h⁻¹ calculated using the total concentration of acid sites (Brønsted and Lewis) from Table 2. Hydrolysis carried out using CeO₂-0.1PO_x resulted in a TOF of 44 h⁻¹, while the TOF for CeO₂-0.2PO_x increased to 100 h⁻¹. The results indicate that the difference in activity between the three materials can be attributed to the presence and amount of Brønsted acidic sites. ICP analysis of the supernatant from the reaction catalyzed by CeO₂-0.2PO_x showed only traces of P (less than 0.2% of the original P), indicating that the catalyst was stable to hydrolysis. Recycling experiments also supported these results (Figure S7).

Table 3. Results for the hydrolysis of propylene oxide to propylene glycol (PG).^a

Catalyst	Time (h)	Conversion (%)	PG Yield (%)	TOF ^b (h ⁻¹)
CeO ₂	3	12	12	5.8
CeO ₂ -0.1PO _x	1	32	32	44
CeO ₂ -0.2PO _x	1	74	74	100

^aConditions: ~10 mg of catalyst, T = 60 °C, D₂O (1 mL), propylene oxide = 0.6 mmol. ^bTOF defined as moles of converted substrate per mole of total acidic sites per reaction time.

Previous oxygen isotopic exchange studies have indicated that the amount of labile surface and bulk oxygen in ceria are significantly reduced upon contamination with phosphorous.⁵⁸⁻⁶⁰ This leads to suppression of redox activity over ceria catalysts (e.g. CO oxidation). It was suggested that the suppression could be caused by surface phosphates blocking coordinatively unsaturated cerium sites (*cus*-Ce) and/or P(V) cations inhibiting the diffusion of oxygen species within the subsurface region due to lower oxygen vacancy concentrations.⁵⁹⁻⁶⁰ In this study, the influence of phosphate loading on the redox properties of the materials was probed through the photocatalytic decomposition of indigo carmine. When ceria is irradiated, electrons from the O_{2p} valence band are excited to the Ce_{4f} conduction band to form electron-hole pairs (i.e. redox pairs).⁹⁷ Oxygen vacancies can act as electron capture centers and inhibit electron-hole recombination events thereby improving photocatalytic activity.⁹⁸⁻¹⁰³ Thus, the photocatalytic activity of ceria is directly related to defect concentration, which in turn is known to correlate to the ease and occurrence of Ce³⁺/Ce⁴⁺ redox cycling.^{8, 104} The indigo carmine photodegradation activity over the three supports is shown in Table 4. There was almost no redox activity over CeO₂-0.2PO_x as it gave similar conversion to the blank (i.e. no catalyst), while CeO₂-0.1PO_x and CeO₂ were redox active. Clearly, an inverse correlation exists between the phosphate loading and the photocatalytic activity (i.e. redox ability). In addition, there was a direct correlation between redox activity and the number of *cus*-Ce (i.e. Lewis acidity). This

suggests that *cus*-Ce and redox activity are directly related to one another. This is consistent with many redox processes of oxygenates over ceria-based materials that require substrate binding or activation through coordination to cerium cations.¹⁰⁵ The results shown here demonstrate that ceria can be functionalized with Brønsted acids while maintaining the desired redox properties.

Table 4. Results for the photodegradation ($\lambda_{\text{ex}} = 350$ nm) of indigo carmine.^a

Catalyst	Time (h)	Conversion (%)
Blank	1.5	1.8
CeO ₂	1.5	58
CeO ₂ -0.1PO _x	1.5	28
CeO ₂ -0.2PO _x	1.5	4.1

^aConditions: 18.3 ppm indigo carmine ($A_{\text{max}} = 610$ nm), 2.0 mL water, 4.1 mg of catalyst.

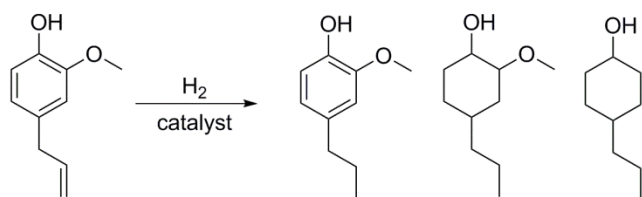
The introduction of Brønsted acidic sites while maintaining the redox-active ceria fluorite structure could lead to catalysts useful for biomass upgrading technology. An important target in biomass processing is the selective deconstruction of lignin via reductive cleavage of C-O bonds (i.e. hydrogenolysis),¹⁰⁶ which can be achieved by the combined action of redox and acid-base catalysts. Lee *et al.* studied the role of noble metal and acidic alumina-based supports in the hydrodeoxygenation of the lignin model guaiacol to cyclohexane.¹⁰⁷ Their data indicated that noble metals catalyzed the hydrogenation of the aromatic ring while the presence and quantity of acidic sites on the support had a positive effect on the deoxygenation activity. Ceria-based materials are also active for hydrogenolysis of bio-derived compounds even though ceria is considered a mildly basic oxide. The activity has been attributed to the redox capacity of the catalyst components. For example, Schimming *et al.* studied the hydrogenolysis of guaiacol to phenol over ceria-zirconia catalysts and observed a direct correlation between hydrogenolysis activity and catalyst redox properties.¹⁰⁸ Ring saturation products were not observed due to the

absence of metals that are active for aromatic hydrogenation. Furthermore, Ota *et al.* studied the hydrogenolysis of vicinal OH groups over a rhenium catalyst promoted by palladium and ceria support.¹⁰⁹ The rhenium component was active for the hydrogenolysis reaction mediated through a Re redox cycle whereas the palladium and ceria components were active for hydrogenation of the alkene intermediate. The results from these studies indicate that both acidity and redox ability promote hydrogenolysis activity, while noble metals are needed to provide saturated products.

Catalysts were prepared by deposition of palladium onto the three supports. The physicochemical properties of all three catalysts are summarized in Table S1 and the PXRD patterns are shown in Figure S8. Their reactivity trends and hydrogenolysis activity towards a lignin model compound (eugenol) were assessed by monitoring product yields (Scheme 2). Pd/CeO₂ was most selective for the fully hydrogenated product (4-propyl-2-methoxycyclohexanol, 59 % yield) (Figure S9). The result is consistent with previous studies that demonstrated phenolics can be activated towards dearomatization over ceria-based catalysts by forming cerium-coordinated phenoxy species.⁶¹ Since Pd/CeO₂ contained the most *cus*-Ce (Table 2), this catalyst should have the largest concentration of activated phenoxy species, which explains the high yield of dearomatized product. In contrast to Pd/CeO₂, Pd/CeO₂-0.2PO_x showed a lower dearomatization yield (27 %) and a higher yield for the allyl hydrogenation product (4-propyl-2-methoxyphenol, 37 %) (Figure S9). The lower yield of dearomatization product is likely due to the low concentration of *cus*-Ce sites in the Pd/CeO₂-0.2PO_x catalyst (Table 2). With this catalyst, phosphate binding limited the availability of *cus*-Ce sites, which decreased the number of phenolic molecules that could be activated for dearomatization shifting the selectivity to the allyl hydrogenation product. Pd/CeO₂-0.1PO_x showed intermediate dearomatization yields (36 %) between Pd/CeO₂ and Pd/CeO₂-0.2PO_x. (Figure S9). The

intermediate yield correlated well with the intermediate amount of *cus*-Ce (Table 2). Both phosphate-modified catalysts (Pd/CeO₂-PO_x) showed increased hydrogenolysis activity relative to palladium supported on unmodified ceria (Pd/CeO₂) (Figure 7b). The hydrogenolysis activity of Pd/CeO₂ (25 % yield of 4-propylcyclohexanol) likely arises from redox active sites (*cus*-Ce and/or Pd) since the support does not contain Brønsted acid sites. The hydrogenolysis activity of Pd/CeO₂-0.1PO_x catalyst was higher than that of Pd/CeO₂-0.2PO_x (55 % versus 36 % yields, respectively) even though the CeO₂-0.2PO_x support had more Brønsted acidic sites, which should promote C-O cleavage. The Pd/CeO₂-0.1PO_x catalyst appears to be the most active for hydrogenolysis of eugenol due to its optimized bifunctionality (*cus*-Ce/redox and Brønsted acidity) (Figure 7a). That is, the dissociation of phenolics on ceria to form adsorbed phenoxy species requires *cus*-Ce (or Lewis acid) sites that are active for phenolic dearomatization. The dearomatized product is more prone to acid-catalyzed methoxy cleavage than the aromatic methoxy due to the weaker C-O bonds of the former.^{46, 110-113} Thus, the *cus*-Ce sites appear to be necessary for efficient eugenol dearomatization, whereas the redox active *cus*-Ce sites and Brønsted acid group facilitate methoxy removal of the saturated intermediate.

Scheme 2. Products from the hydrotreatment of eugenol.



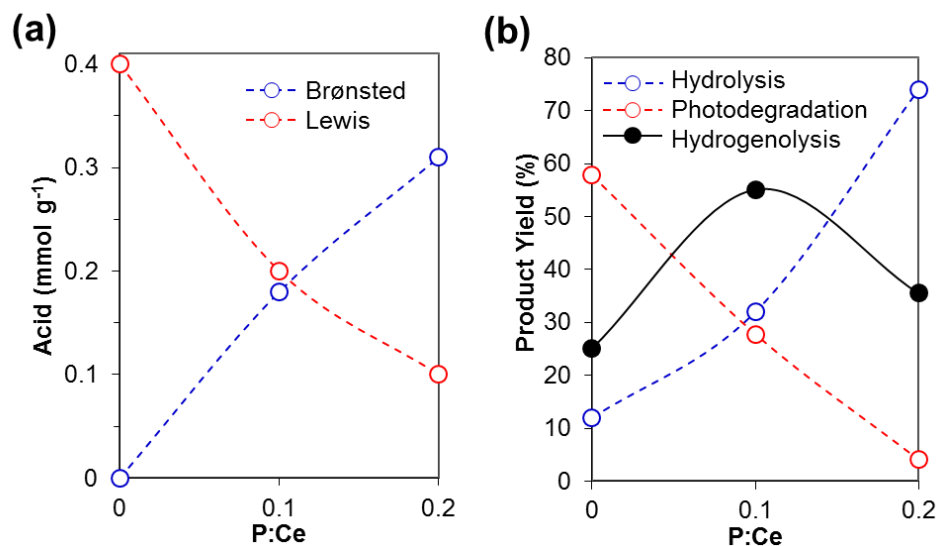


Figure 7. (a) Brønsted and Lewis acid surface concentrations as a function of P:Ce. (b) Product yields for hydrolysis of propylene oxide, photodegradation of indigo carmine, and hydrogenolysis of eugenol as a function of P:Ce. Conditions for hydrolysis and photodegradation reactions are found in Tables 3 and 4, respectively. Conditions for eugenol (4-allyl-2-methoxyphenol) hydrogenolysis: T = 100 °C, t = 4 h, P_{H₂} = 10 bar, Pd:Eugenol = 5 mol. %, 25 mL H₂O.

Conclusion

Deposition of trimethylphosphate onto ceria followed by thermal treatment leads to the formation of surface phosphates while retaining the cubic fluorite structure of ceria. The phosphates introduce Brønsted acidity to the ceria surface at the expense of Lewis acidic sites. The relative amounts of the two types of acidic sites can be controlled by varying the amount of trimethylphosphate deposited onto the ceria. This work demonstrates that ceria can be functionalized with Brønsted acids while retaining its desired redox properties. Furthermore, the redox-to-Brønsted acid ratios can be tuned to achieve the desired activity and selectivity, as demonstrated by the eugenol hydrogenolysis activity. The decomposition of trimethylphosphate to form Brønsted acidic surface phosphates is an important first step in developing redox active ceria-based materials with tailorable functionalities. Further studies exploring derivatized

organophosphates and organophosphonates will likely uncover new possibilities for introducing other functionalities to the surface of ceria.¹¹⁴

Acknowledgments

This research is supported by the U.S. Department of Energy, Office of Science, Basic Energy Sciences, Division of Chemical Sciences, Geosciences, and Biosciences, through the Ames Laboratory Catalysis Science program. The Ames Laboratory is operated for the U.S. Department of Energy by Iowa State University under Contract No. DE-AC02-07CH11358.

References

1. Trovarelli, A., *Catalysis by Ceria and Related Materials*, Imperial College Press: London, 2002.
2. Trovarelli, A. *Catal. Rev.* **1996**, 38, 439-520.
3. Trovarelli, A.; de Leitenburg, C.; Boaro, M.; Dolcetti, G. *Catal. Today* **1999**, 50, 353-367.
4. Montini, T.; Melchionna, M.; Monai, M.; Fornasiero, P. *Chem. Rev.* **2016**.
5. Campbell, C. T.; Peden, C. H. *Science* **2005**, 309, 713-4.
6. Esch, F.; Fabris, S.; Zhou, L.; Montini, T.; Africh, C.; Fornasiero, P.; Comelli, G.; Rosei, R. *Science* **2005**, 309, 752-755.
7. Lin, Y.; Wu, Z.; Wen, J.; Poeppelmeier, K. R.; Marks, L. D. *Nano Lett* **2014**, 14, 191-6.
8. Mamontov, E.; Egami, T.; Brezny, R.; Koranne, M.; Tyagi, S. *J. Phys. Chem. B* **2000**, 104, 11110-11116.
9. Cargnello, M.; Doan-Nguyen, V. V. T.; Gordon, T. R.; Diaz, R. E.; Stach, E. A.; Gorte, R. J.; Fornasiero, P.; Murray, C. B. *Science* **2013**, 341, 771-773.
10. Nolan, M. *J. Mater. Chem.* **2011**, 21, 9160-9168.
11. Paier, J.; Penschke, C.; Sauer, J. *Chem. Rev.* **2013**, 113, 3949-3985.
12. Nolan, M.; Parker, S. C.; Watson, G. W. *Surf. Sci.* **2005**, 595, 223-232.

13. Wu, Z.; Li, M.; Howe, J.; Meyer, H. M.; Overbury, S. H. *Langmuir* **2010**, 26, 16595-16606.
14. Nelson, N. C.; Boote, B. W.; Rossini, A. J.; Smith, E. A.; Slowing, I. I. *Submitted* **2016**.
15. Mai, H.-X.; Sun, L.-D.; Zhang, Y.-W.; Si, R.; Feng, W.; Zhang, H.-P.; Liu, H.-C.; Yan, C.-H. *J. Phys. Chem. B* **2005**, 109, 24380-24385.
16. Wang, D.; Kang, Y.; Doan-Nguyen, V.; Chen, J.; Kungas, R.; Wieder, N. L.; Bakhmutsky, K.; Gorte, R. J.; Murray, C. B. *Angew. Chem. Int. Ed.* **2011**, 50, 4378-4381.
17. Yang, S.; Gao, L. *J. Am. Chem. Soc.* **2006**, 128, 9330-9331.
18. Agarwal, S.; Lefferts, L.; Mojet, B. L.; Ligthart, D. A.; Hensen, E. J.; Mitchell, D. R.; Erasmus, W. J.; Anderson, B. G.; Olivier, E. J.; Neethling, J. H.; Datye, A. K. *ChemSusChem* **2013**, 6, 1898-906.
19. Zhang, Y.; Hou, F.; Tan, Y. *Chem. Comm.* **2012**, 48, 2391-2393.
20. Zhu, H.-Z.; Lu, Y.-M.; Fan, F.-J.; Yu, S.-H. *Nanoscale* **2013**, 5, 7219-7223.
21. Wang, S.; Zhao, L.; Wang, W.; Zhao, Y.; Zhang, G.; Ma, X.; Gong, J. *Nanoscale* **2013**, 5, 5582-5588.
22. Lv, J.; Shen, Y.; Peng, L.; Guo, X.; Ding, W. *Chem. Comm.* **2010**, 46, 5909-5911.
23. Tamura, M.; Kishi, R.; Nakagawa, Y.; Tomishige, K. *Nat. Commun.* **2015**, 6.
24. Kandel, K.; Frederickson, C.; Smith, E. A.; Lee, Y.-J.; Slowing, I. I. *ACS Catal.* **2013**, 3, 2750-2758.
25. Zaki, M. I.; Hussein, G. A. M.; Mansour, S. A. A.; El-Ammawy, H. A. *J. Mol. Catal.* **1989**, 51, 209-220.
26. Wu, Z.; Mann, A. K. P.; Li, M.; Overbury, S. H. *J. Phys. Chem. C.* **2015**, 119, 7340-7350.
27. Tamura, M.; Shimizu, K.-i.; Satsuma, A. *Appl. Catal. A-Gen* **2012**, 433-434, 135-145.
28. Binet, C.; Daturi, M.; Lavalley, J.-C. *Catal. Today* **1999**, 50, 207-225.
29. Peng, Y.; Li, J.; Chen, L.; Chen, J.; Han, J.; Zhang, H.; Han, W. *Environ. Sci. Technol.* **2012**, 46, 2864-2869.
30. Ma, Z.; Weng, D.; Wu, X.; Si, Z. *J. Environ. Sci.* **2012**, 24, 1305-1316.
31. Natile, M. M.; Tomaello, F.; Glisenti, A. *Chem. Mater.* **2006**, 18, 3270-3280.

32. Li, Y.; Wei, Z.; Sun, J.; Gao, F.; Peden, C. H. F.; Wang, Y. *J. Phys. Chem. C* **2013**, 117, 5722-5729.
33. Li, Y.; Cheng, H.; Li, D.; Qin, Y.; Xie, Y.; Wang, S. *Chem. Comm.* **2008**, 1470-1472.
34. Shan, W.; Liu, F.; He, H.; Shi, X.; Zhang, C. *Chem. Comm.* **2011**, 47, 8046-8048.
35. Chen, L.; Weng, D.; Si, Z.; Wu, X. *Prog. Nat. Sci. Mater. Int.* **2012**, 22, 265-272.
36. Azambre, B.; Zenboury, L.; Weber, J. V.; Burg, P. *Appl. Surf. Sci.* **2010**, 256, 4570-4581.
37. Gao, S.; Chen, X.; Wang, H.; Mo, J.; Wu, Z.; Liu, Y.; Weng, X. *J. Colloid Interf. Sci.* **2013**, 394, 515-521.
38. Reddy, B. M.; Sreekanth, P. M.; Lakshmanan, P.; Khan, A. *J. Mol. Catal. A: Chem.* **2006**, 244, 1-7.
39. Goura, J.; Chandrasekhar, V. *Chem. Rev.* **2015**, 115, 6854-6965.
40. Chambers, J. E.; Levi, P. E., *Organophosphates Chemistry, Fate, and Effects: Chemistry, Fate, and Effects*, Elsevier Science: 2013.
41. Timpel, M.; Nardi, M. V.; Krause, S.; Ligorio, G.; Christodoulou, C.; Pasquali, L.; Giglia, A.; Frisch, J.; Wegner, B.; Moras, P.; Koch, N. *Chem. Mater.* **2014**, 26, 5042-5050.
42. Pang, S. H.; Schoenbaum, C. A.; Schwartz, D. K.; Medlin, J. W. *Nat. Commun.* **2013**, 4.
43. Schoenbaum, C. A.; Schwartz, D. K.; Medlin, J. W. *Acc. Chem. Res.* **2014**, 47, 1438-1445.
44. Kandel, K.; Frederickson, C.; Smith, E. A.; Lee, Y.-J.; Slowing, I. I. *ACS Catalysis* **2013**, 3, 2750-2758.
45. Yan, N.; Yuan, Y.; Dykeman, R.; Kou, Y.; Dyson, P. J. *Angew. Chem. Int. Ed.* **2010**, 49, 5549-5553.
46. Zhao, C.; He, J.; Lemonidou, A. A.; Li, X.; Lercher, J. A. *J. Catal.* **2011**, 280, 8-16.
47. Shetty, M.; Murugappan, K.; Prasomsri, T.; Green, W. H.; Román-Leshkov, Y. *J. Catal.* **2015**, 331, 86-97.
48. Thibodeau, T. J.; Canney, A. S.; DeSisto, W. J.; Wheeler, M. C.; Amar, F. G.; Frederick, B. G. *Appl. Catal. A-Gen* **2010**, 388, 86-95.
49. Moberg, D. R.; Thibodeau, T. J.; Amar, F. G.; Frederick, B. G. *J. Phys. Chem. C* **2010**, 114, 13782-13795.
50. Kandel, K.; Anderegg, J. W.; Nelson, N. C.; Chaudhary, U.; Slowing, I. I. *J. Catal.* **2014**, 314, 142-148.

51. Chen, D. A.; Ratliff, J. S.; Hu, X.; Gordon, W. O.; Senanayake, S. D.; Mullins, D. R. *Surf. Sci.* **2010**, 604, 574-587.
52. Mäkie, P.; Persson, P.; Österlund, L. *J. Phys. Chem. C* **2012**, 116, 14917-14929.
53. Mäkie, P.; Westin, G.; Persson, P.; Österlund, L. *J. Phys. Chem. A* **2011**, 115, 8948-8959.
54. Henderson, M. A. *J. Phys. Chem. C* **2011**, 115, 23527-23534.
55. Lin, S. T.; Klabunde, K. J. *Langmuir* **1985**, 1, 600-605.
56. Štengl, V.; Henych, J.; Grygar, T.; Pérez, R. *Mater. Res. Bull.* **2015**, 61, 259-269.
57. Mitchell, M. B.; Sheinker, V. N.; Cox, W. W.; Gatimu, E. N.; Tesfamichael, A. B. *J. Phys. Chem. B* **2004**, 108, 1634-1645.
58. Xu, L.; Guo, G.; Uy, D.; O'Neill, A. E.; Weber, W. H.; Rokosz, M. J.; McCabe, R. W. *Appl. Catal., B* **2004**, 50, 113-125.
59. Larese, C.; Cabello Galisteo, F.; Lopez Granados, M.; Mariscal, R.; Fierro, J. L. G.; Lambrou, P. S.; Efstathiou, A. M. *J. Catal.* **2004**, 226, 443-456.
60. Lopez Granados, M.; Cabello Galisteo, F.; Lambrou, P. S.; Mariscal, R.; Sanz, J.; Sobrados, I.; Fierro, J. L. G.; Efstathiou, A. M. *J. Catal.* **2006**, 239, 410-421.
61. Nelson, N. C.; Manzano, J. S.; Sadow, A. D.; Overbury, S. H.; Slowing, I. I. *ACS Catal.* **2015**, 5, 2051-2061.
62. Hardacre, C.; Roe, G. M.; Lambert, R. M. *Surf. Sci.* **1995**, 326, 1-10.
63. Romeo, M.; Bak, K.; El Fallah, J.; Le Normand, F.; Hilaire, L. *Surf. Interf. Anal.* **1993**, 20, 508-512.
64. Madier, Y.; Descorme, C.; Le Govic, A. M.; Duprez, D. *J. Phys. Chem. B* **1999**, 103, 10999-11006.
65. Miller, F. A.; Wilkins, C. H. *Anal. Chem.* **1952**, 24, 1253-1294.
66. Masui, T.; Hirai, H.; Imanaka, N.; Adachi, G. *Phys. Status Solidi A - Appl. Res.* **2003**, 198, 364-368.
67. Hezel, A.; Ross, S. D. *Spectrochim. Acta* **1966**, 22, 1949-1961.
68. Stein, S. E. "Infrared Spectra" in **NIST Chemistry WebBook**, Eds. Linstrom, P. J.; Mallard, W. G. National Institute of Standards and Technology, Gaithersburg MD, 20899, <http://webbook.nist.gov>, (accessed June 29, 2016).
69. Pfau, A.; Schierbaum, K. D. *Surf. Sci.* **1994**, 321, 71-80.

70. Henderson, M. A.; Perkins, C. L.; Engelhard, M. H.; Thevuthasan, S.; Peden, C. H. F. *Surf. Sci.* **2003**, 526, 1-18.
71. Mullins, D. R.; Overbury, S. H.; Huntley, D. R. *Surf. Sci.* **1998**, 409, 307-319.
72. Shahed, S. M. F.; Hasegawa, T.; Sainoo, Y.; Watanabe, Y.; Isomura, N.; Beniya, A.; Hirata, H.; Komeda, T. *Surf. Sci.* **2014**, 628, 30-35.
73. Praline, G.; Koel, B. E.; Hance, R. L.; Lee, H. I.; White, J. M. *J. Electron Spectrosc. Relat. Phenom.* **1980**, 21, 17-30.
74. Senanayake, S. D.; Mullins, D. R. *J. Phys. Chem. C.* **2008**, 112, 9744-9752.
75. Perry, D.; Tsao, L.; Brittain, H. *J. Mater. Sci. Lett.* **1984**, 3, 1017-1019.
76. Pemba-Mabiala, J. M.; Lenzi, M.; Lenzi, J.; Lebugle, A. *Surf. Interf. Anal.* **1990**, 15, 663-667.
77. Ma, J. N.; Rea, A. C.; An, H. Y.; Ma, C. S.; Guan, X. G.; Li, M. D.; Su, T.; Yeung, C. S.; Harris, K. T.; Zhu, Y.; Nganga, J. L.; Fedoryak, O. D.; Dore, T. M.; Phillips, D. L. *Chem.—Eur. J.* **2012**, 18, 6854.
78. Wiench, J. W.; Pruski, M.; Tischendorf, B.; Otaigbe, J. U.; Sales, B. C. *Journal of Non-Crystalline Solids* **2000**, 263–264, 101-110.
79. Karpowich, L.; Wilcke, S.; Yu, R.; Harley, G.; Reimer, J. A.; De Jonghe, L. C. *J. Solid State Chem.* **2007**, 180, 840-846.
80. Xue, X.; Kanzaki, M. *J. Am. Ceram. Soc.* **2009**, 92, 2803-2830.
81. Cheetham, A. K.; Clayden, N. J.; Dobson, C. M.; Jakeman, R. J. B. *Journal of the Chemical Society, Chemical Communications* **1986**, 195-197.
82. Hunter, R. J., Introduction. In *Zeta Potential in Colloid Science*; Academic Press: New York, 1981; pp 1-10.
83. Parks, G. A. *Chem. Rev.* **1965**, 65, 177-198.
84. Suphantharida, P.; Osseo-Asare, K. *J. Electrochem. Soc.* **2004**, 151, G658-G662.
85. Kosmulski, M., *Chemical Properties of Material Surfaces*, CRC Press: 2001.
86. Determination of Acidic and Basic Properties on Solid Surfaces. In *Studies in Surface Science and Catalysis*; Tanabe, K.; Misono, M.; Ono, Y.; Hattori, H., Eds. Elsevier: Tokyo, 1989; Vol. 51, pp 5-25.
87. Stošić, D.; Bennici, S.; Rakić, V.; Auroux, A. *Catal. Today* **2012**, 192, 160-168.

88. Cutrufello, M. G.; Ferino, I.; Monaci, R.; Rombi, E.; Solinas, V. *Top. Catal.* **2002**, 19, 225-240.
89. Bonnetot, B.; Rakic, V.; Yuzhakova, T.; Guimon, C.; Auroux, A. *Chem. Mater.* **2008**, 20, 1585-1596.
90. Ge, X.; Hu, S.; Sun, Q.; Shen, J. *J. Nat. Gas Chem.* **2003**, 12, 119-122.
91. Kline, C. H.; Turkevich, J. *J. Chem. Phys.* **1944**, 12, 300-309.
92. Parry, E. P. *J. Catal.* **1963**, 2, 371-379.
93. Morterra, C.; Magnacca, G. *Catal. Today* **1996**, 27, 497-532.
94. Lercher, J. A.; Gründling, C.; Eder-Mirth, G. *Catal. Today* **1996**, 27, 353-376.
95. Holm, V. C. F.; Bailey, G. C.; Clark, A. *J. Phys. Chem.* **1959**, 63, 129-133.
96. Wang, Y.; Wang, F.; Song, Q.; Xin, Q.; Xu, S.; Xu, J. *J. Am. Chem. Soc.* **2013**, 135, 1506-1515.
97. Patsalas, P.; Logothetidis, S.; Sygellou, L.; Kennou, S. *Phys. Rev. B* **2003**, 68, 035104.
98. Liyanage, A. D.; Perera, S. D.; Tan, K.; Chabal, Y.; Balkus, K. J. *ACS Catal.* **2014**, 4, 577-584.
99. Wang, J.; Liu, P.; Fu, X.; Li, Z.; Han, W.; Wang, X. *Langmuir* **2009**, 25, 1218-1223.
100. Zhang, Z.; Wang, W.; Gao, E.; Shang, M.; Xu, J. *J. Hazard. Mater.* **2011**, 196, 255-262.
101. Tachikawa, T.; Majima, T. *J. Am. Chem. Soc.* **2009**, 131, 8485-8495.
102. Hernández-Alonso, M. a. D.; Hungria, A. B.; Martínez-Arias, A.; Fernández-García, M.; Coronado, J. M.; Conesa, J. C.; Soria, J. *Appl. Catal., B* **2004**, 50, 167-175.
103. Li, Y.; Sun, Q.; Kong, M.; Shi, W.; Huang, J.; Tang, J.; Zhao, X. *J. Phys. Chem. C* **2011**, 115, 14050-14057.
104. Mogensen, M.; Sammes, N. M.; Tompsett, G. A. *Solid State Ionics* **2000**, 129, 63-94.
105. Mullins, D. R. *Surf. Sci. Rep.* **2015**, 70, 42-85.
106. Pandey, M. P.; Kim, C. S. *Chem. Eng. Technol.* **2011**, 34, 29-41.
107. Lee, C. R.; Yoon, J. S.; Suh, Y.-W.; Choi, J.-W.; Ha, J.-M.; Suh, D. J.; Park, Y.-K. *Catal. Commun.* **2012**, 17, 54-58.
108. Schimming, S. M.; LaMont, O. D.; König, M.; Rogers, A. K.; D'Amico, A. D.; Yung, M. M.; Sievers, C. *ChemSusChem* **2015**, 8, 2073-2083.

109. Ota, N.; Tamura, M.; Nakagawa, Y.; Okumura, K.; Tomishige, K. *Angew. Chem. Int. Ed.* **2015**, *54*, 1897-1900.
110. Benson, S. W., *Thermochemical Kinetics: Methods for the estimation of thermochemical data and rate parameters*, John Wiley & Sons, Inc.: New York, 1976.
111. Blanksby, S. J.; Ellison, G. B. *Acc. Chem. Res.* **2003**, *36*, 255-263.
112. Mortensen, P. M.; Grunwaldt, J. D.; Jensen, P. A.; Knudsen, K. G.; Jensen, A. D. *Appl. Catal. A-Gen* **2011**, *407*, 1-19.
113. Mortensen, P. M.; Grunwaldt, J.-D.; Jensen, P. A.; Jensen, A. D. *ACS Catal.* **2013**, *3*, 1774-1785.
114. Heck, J. G.; Napp, J.; Simonato, S.; Möllmer, J.; Lange, M.; Reichardt, H. M.; Staudt, R.; Alves, F.; Feldmann, C. *J. Am. Chem. Soc.* **2015**, *137*, 7329-7336.

Appendix of Supporting Information

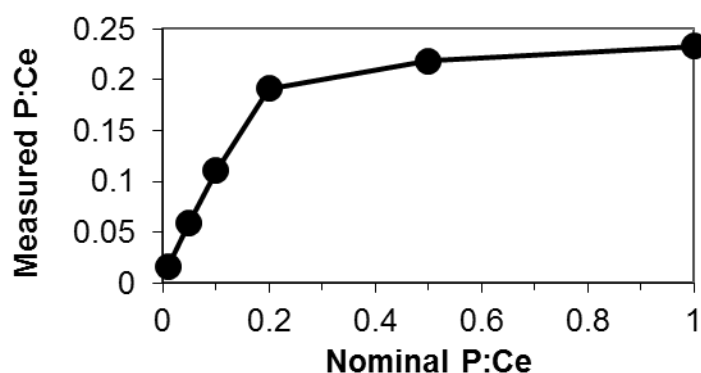


Figure S1. Measured P:Ce mole ratio after trimethylphosphate deposition onto CeO_2 followed by calcination versus the nominal P:Ce mole ratio.

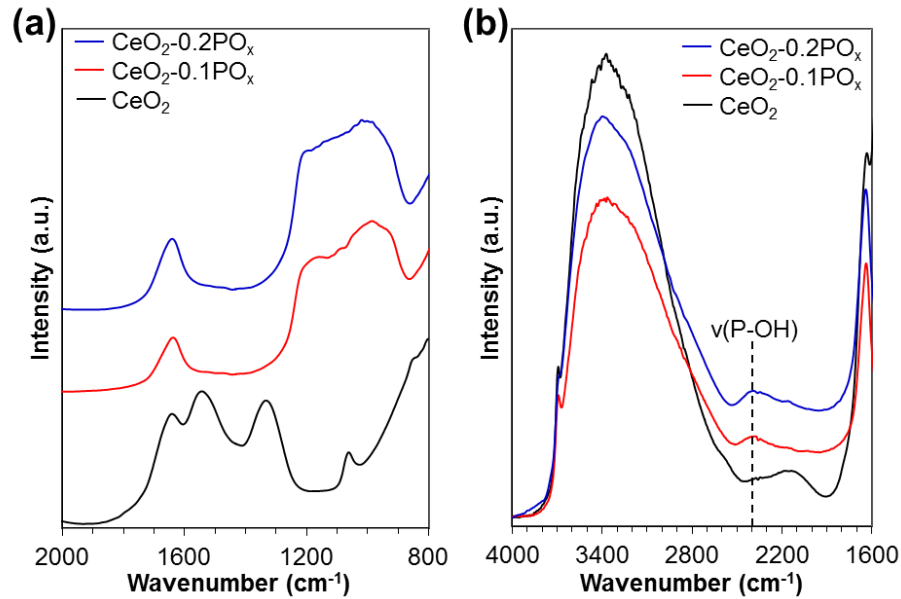


Figure S2. DRIFT spectra of the materials with no pretreatment (i.e. as-synthesized) and no baseline correction in the (a) carbonate/phosphate and (b) hydroxyl regions. The band around 2100 cm^{-1} for CeO_2 has been proposed as either an electron transition from donor levels located near the conduction band such as Ce^{3+} or oxygen vacancies or the forbidden ${}^2F_{5/2} \rightarrow {}^2F_{7/2}$ electronic transition of Ce^{3+} located at subsurface (or bulk) defective lattice sites.¹⁻³

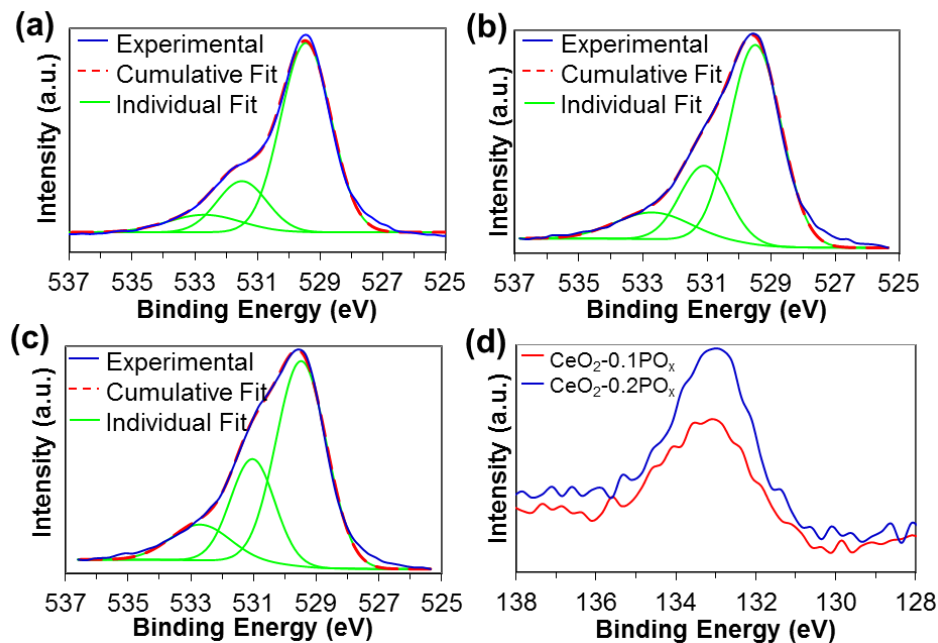


Figure S3. Deconvoluted XPS spectra in the O 1s spectral region for (a) CeO_2 , (b) $\text{CeO}_2\text{-}0.1\text{PO}_x$, and (c) $\text{CeO}_2\text{-}0.2\text{PO}_x$. (d) XPS spectra in the P 2p spectral region for phosphate functionalized materials.

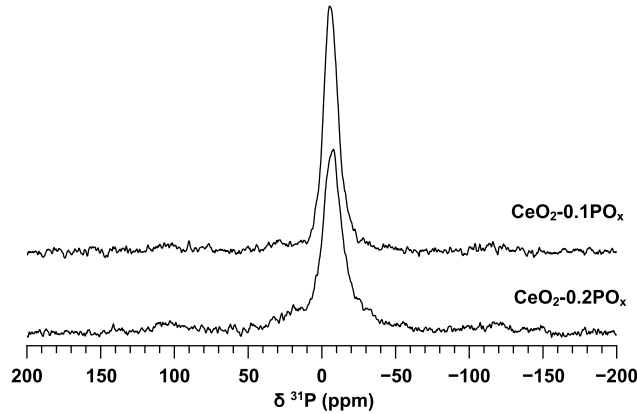


Figure S4. $^{31}\text{P}\{^1\text{H}\}$ CPMAS spectra of $\text{CeO}_2\text{-}0.1\text{PO}_x$ and $\text{CeO}_2\text{-}0.2\text{PO}_x$. The spectra were obtained using $\nu_R = 18$ kHz, $\square_{\text{CP}} = 2.1$ ms, $\nu_{\text{RF}}(^1\text{H CP}) = 96$ kHz, $\nu_{\text{RF}}(^{31}\text{P CP}) = 78$ kHz, $\nu_{\text{RF}}(^1\text{H SPINAL-64}) = 96$ kHz and 1024 scans.

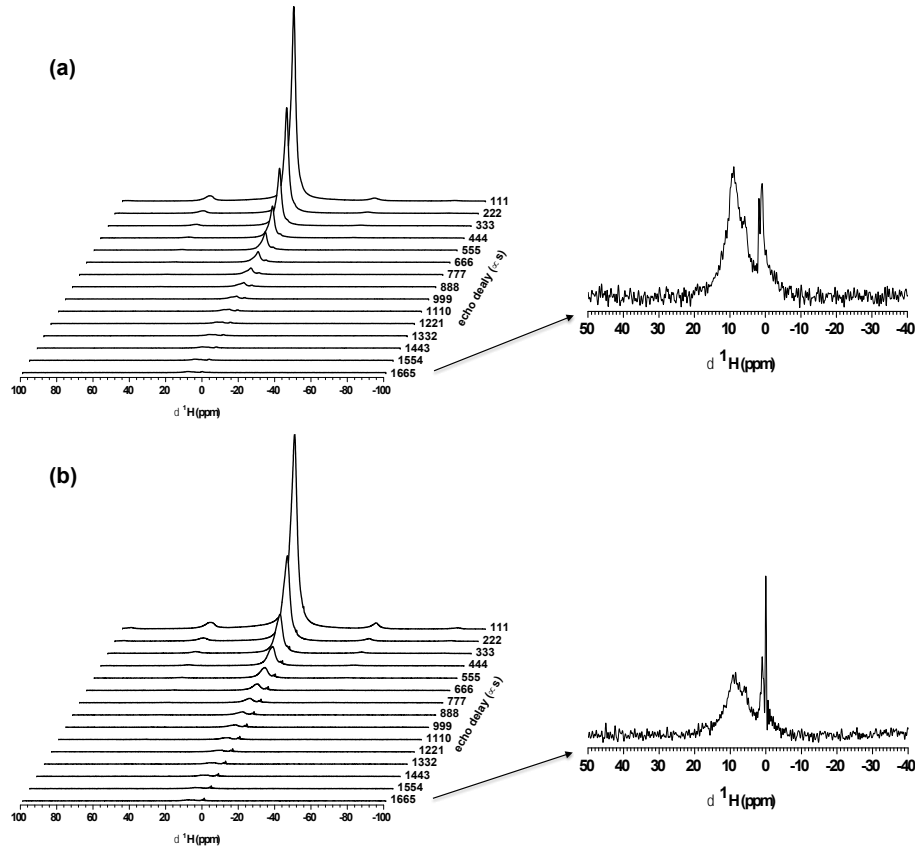


Figure S5. ^1H DPMAS Hahn echo spectra of (a) $\text{CeO}_2\text{-}0.1\text{PO}_x$ and (b) $\text{CeO}_2\text{-}0.2\text{PO}_x$. The spectra were obtained using $\nu_R = 18$ kHz, $\nu_{\text{RF}}(^1\text{H } 90^\circ) = 96$ kHz, $\square_{\text{rd}} = 7$ s, 64 scans/delay, and echo delays indicated in the figure.

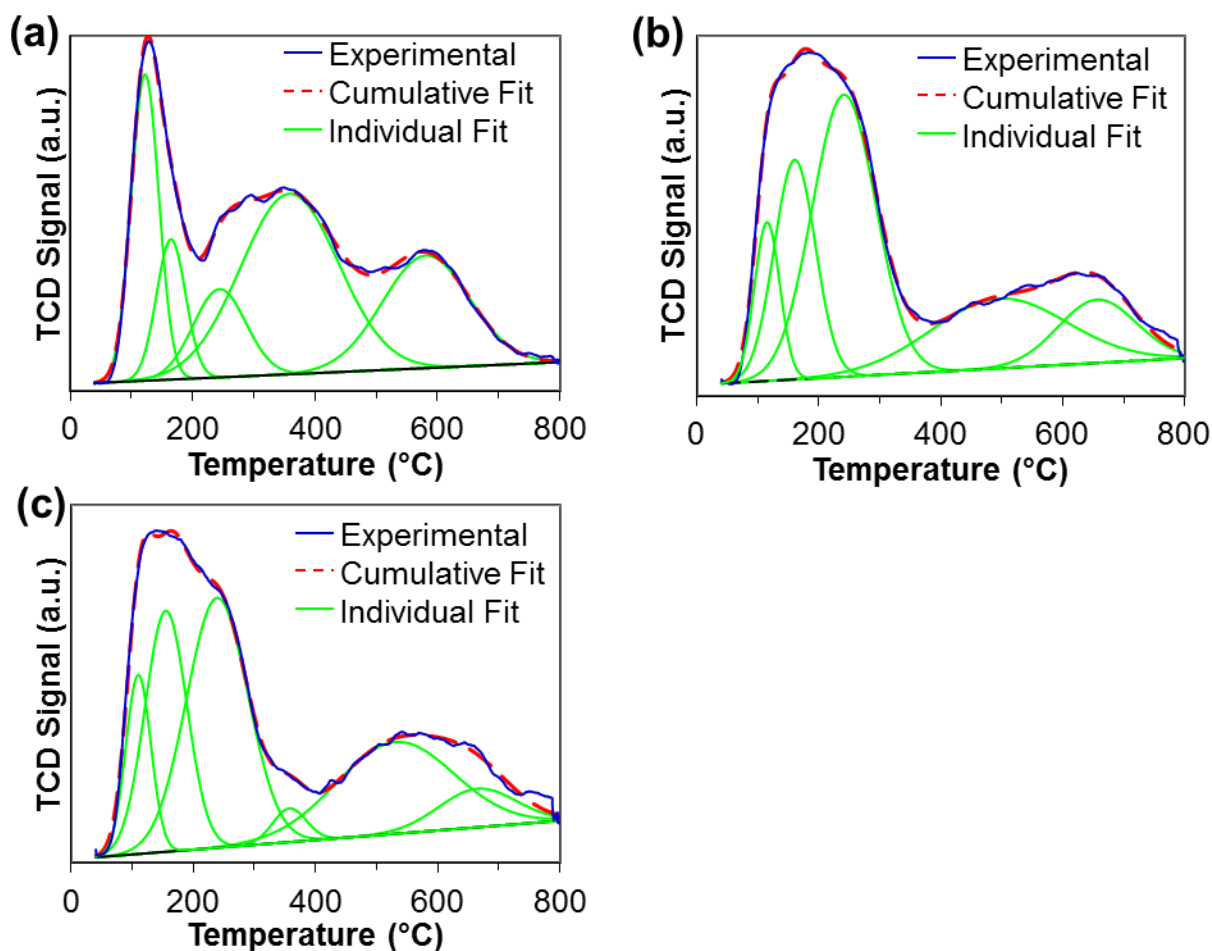


Figure S6. Deconvoluted NH_3 -TPD profiles for (a) CeO_2 , (b) $\text{CeO}_2\text{-}0.1\text{PO}_x$, (c) $\text{CeO}_2\text{-}0.2\text{PO}_x$, which correspond to NH_3 integrated values of 0.61, 0.57, 0.68 mmol g^{-1} , respectively.

The deconvoluted peaks with maxima around 110 °C and 160 °C (the two lowest temperature deconvoluted peaks) were common to all three materials. This indicates that the type of adsorbed NH_3 species is the same for all three materials and the low desorption temperature suggests they are multilayer and/or physisorbed species. These peaks were subtracted to determine the total number of acid sites. After correcting for physisorption, the acid site density for CeO_2 was 2.0 $\mu\text{mol m}^{-2}$. This value agrees well with prior studies using NH_3 adsorption microcalorimetry ($1.9 \pm 0.3 \mu\text{mol m}^{-2}$).⁴⁻⁷ The similarity between the corrected CeO_2 acid site

density to the literature values for ceria suggest this correction method is a good approximation to the true acid site density. The method was extended to the phosphate functionalized materials since the low temperature deconvoluted peaks are common to all materials. After correcting for physisorbed/multilayer NH_3 the integrated values for CeO_2 , $\text{CeO}_2\text{-}0.1\text{PO}_x$, and $\text{CeO}_2\text{-}0.2\text{PO}_x$ were 0.44, 0.41, 0.44 mmol g^{-1} , respectively.

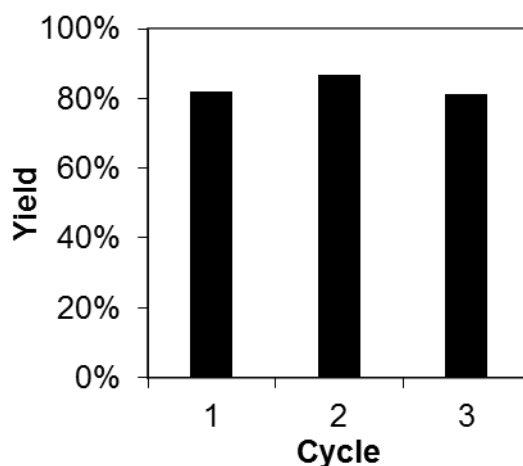


Figure S7. Recycling experiments using $\text{CeO}_2\text{-}0.2\text{PO}_x$ catalyst for the hydrolysis of propylene oxide. Conditions: ~ 40 mg catalyst, $T = 60$ $^\circ\text{C}$, D_2O (1 mL), propylene oxide = ~ 2.4 mmol, $t = 1$ h. The catalyst:substrate ratio was maintained at 16.7 mg mmol^{-1} .

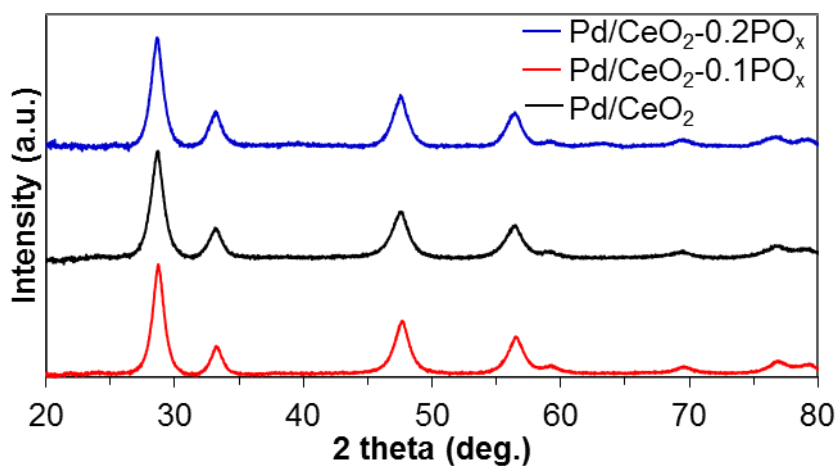


Figure S8. PXRD patterns of the catalysts used for eugenol hydrogenolysis reaction.

Table S1. Physicochemical properties of catalysts for eugenol hydrogenolysis.

Sample	BET Surface Area (m ² g ⁻¹) ^a	CeO ₂ Crystallite Size (nm) ^b	Pd Loading (wt. %) ^d
Pd/CeO ₂	121	7	1.0
Pd/CeO ₂ -0.1PO _x	111	9	1.0
Pd/CeO ₂ -0.2PO _x	112	10	1.1

^aSurface areas calculated using BET approximation. ^bObtained from PXRD data using Scherrer equation. ^cCalculated from H₂ chemisorption data. ^dLoadings obtained from ICP analysis.

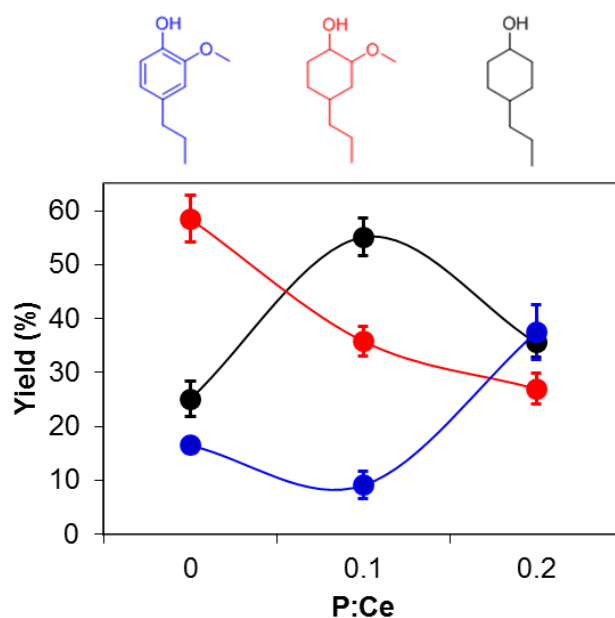
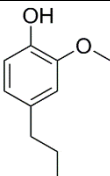
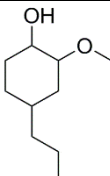
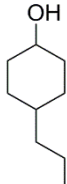


Figure S9. Product distribution for the hydrogenolysis of eugenol over Pd/CeO₂, Pd/CeO₂-0.1PO_x, and Pd/CeO₂-0.2PO_x. The error bars represent the standard deviation from three separate reactions. Conditions: T = 100 °C, t = 4 h, P_{H2} = 10 bar, Pd:Eugenol = 5 mol. %, 25 mL H₂O.

Table S2. Product distribution for the hydrogenolysis of eugenol over the three catalysts.^a

Catalyst	Reaction		
	Allyl hydrogenation	Allyl + aromatic hydrogenation	Allyl + aromatic + methoxy hydrogenation/lysis
	Product		
			
	4-propyl-2-methoxyphenol Yield (%)	4-propyl-2-methoxycyclohexanol Yield (%)	4-propylcyclohexanol Yield (%)
Pd/CeO ₂	16 ± 1	59 ± 4	25 ± 3
Pd/CeO ₂ -0.1PO _x	9.1 ± 2.5	36 ± 3	55 ± 4
Pd/CeO ₂ -0.2PO _x	37 ± 5	27 ± 3	36 ± 3

^aError bars represent the standard deviation from three separate reactions. Conditions: T = 100 °C, t = 4 h, P_{H₂} = 10 bar, Pd:Eugenol = 5 mol. %, 25 mL H₂O.

References.

1. Binet, C.; Daturi, M.; Lavalley, J.-C. *Catal. Today* **1999**, 50, 207-225.
2. Binet, C.; Badri, A.; Lavalley, J.-C. *J. Phys. Chem.* **1994**, 98, 6392-6398.
3. Bozon-Verduraz, F.; Bensalem, A. *J. Chem. Soc. Faraday Trans.* **1994**, 90, 653-657.
4. Stošić, D.; Bennici, S.; Rakić, V.; Auroux, A. *Catal. Today* **2012**, 192, 160-168.
5. Cutrufello, M. G.; Ferino, I.; Monaci, R.; Rombi, E.; Solinas, V. *Top. Catal.* **2002**, 19, 225-240.
6. Bonnetot, B.; Rakic, V.; Yuzhakova, T.; Guimon, C.; Auroux, A. *Chem. Mater.* **2008**, 20, 1585-1596.
7. Ge, X.; Hu, S.; Sun, Q.; Shen, J. *J. Nat. Gas Chem.* **2003**, 12, 119-122.

Chapter 6

Conclusions and Outlook

The data described in this thesis indicates ceria is a promising support, promoter, or catalyst for phenolic upgrading reactions and perhaps for biomass polymer degradation. Ceria activates phenolics for dearomatization through formation of surface phenoxy species and under certain conditions shows high yields to cyclohexanone. The amount of phenoxy species present on the surface is largely dictated by the type of solvent and the redox properties of ceria. The redox properties can be enhanced through modification of sodium and thus opens up a practical and facile method for redox enrichment of ceria for commercial applications. Ceria was shown to be an active support for transfer hydrogenation of phenol using secondary alcohols, but underwent reduction when using primary alcohols. The surface of ceria can be tuned with phosphates to afford multifunctional, redox-active materials capable of performing specialized tasks and tandem processes. The use of phosphates offers adaptability and compositional tuning in order to achieve desired catalyst properties.

Ceria is a unique rare earth oxide with interesting properties that have led to its widespread use for technological applications. Continued research and fundamental understanding of ceria should allow for more efficient design of materials exhibiting unique properties and enhanced activity. The facile ability to tailor the properties of ceria, as demonstrated here, will undoubtedly lead to its continued study.